Templated Synthesis of Graphene

Michael Tynan

A thesis presented for the degree of
Doctor of Philosophy

Durham University
Department of Chemistry
University Science Laboratories
South Road
Durham
2019

Abstract

Producing cost effective graphene remains difficult and is a large barrier to the material realising its full potential. Current techniques are either very expensive to scale requiring high temperatures and low pressures, or produce a product not suitable for many of the big marquee applications in electronics. This document proposes developments on the chemical vapour deposition process of producing graphene by using high surface area templating material. This allows the synthesis of larger quantities of high quality graphene.

The added benefits of the methods proposed here is an increased control in the morphology of the produced graphene. Studies have shown that changes in morphology of graphene have a large effect on the properties and allow for different applications.

In this document, four templating material are used to grow graphene. Two use a powdered catalyst of cobalt hydroxide hexagons and copper oxide cubes and both successfully catalyse and template the synthesis of carbon. On the cobalt hexagons, depending on conditions, curved graphitic materials would arrange into a hexagonal macrostructure or high quality graphene would be produced with little evidence of hexagonal shape. On the copper oxide cubes, three clear products could be produced depending on the conditions. Carbon nanofibers would either arrange themselves into cubes or fibrous "worm" like structures. Also thin carbon coatings could be produced on the cube.

The other two method were the templating the graphene on a foam template in order to synthesise graphene foams. Graphene foams have numerous applications including energy storage, gas storage and supports. The first method describes synthesis of graphene on a metal foam templated from a hydrogel. Two products were synthesised depending on the conditions - firstly a high quality graphene/graphite foam was synthesised. Also a foam macrostructure of closed graphitic structures was produced. The second method produced graphite foams from poly high internal phase emulsion template.

Contents

Chapter 1

Introduction

This project aims to synthesis graphene with a controlled morphology due to the shape dependent properties graphene has displayed. This chapter will introduce graphene giving a brief overview of its structure, properties and applications followed by a detailed review of how it is synthesised, focusing particularly on chemical vapour deposition as that is the main experimental technique used in this work. Following the introduction will be a section detailing the characterisation techniques used during the research and how they apply to carbon nanomaterials. Following that chapter are the experimental chapters. Firstly synthesis of graphene foams on a dextran templated metal foam. Then synthesis of graphene foams derived from metal doped poly high internal phase emulsions. Then synthesis of graphene on copper oxide cubes and lastly synthesis of graphene on cobalt hydroxide hexagons.

1.1 Graphene

Graphene is a 2D monolayer of sp^2 hybridised carbon atoms arranged in a honeycomb lattice. It forms the basis for all other graphitic materials: It is stacked to form 3D graphite, rolled into 1D carbon nanotubes (CNTs) and wrapped up into fullerenes. These three allotropes are shown in figure 1.1. The other crystalline carbon form is diamond which consists of sp^3 hybridised carbon. More disordered forms of carbon also exist, such as diamond-like carbon, amorphous carbon, glassy carbon, and others which all have there own wide ranging academic interest.[1–3]

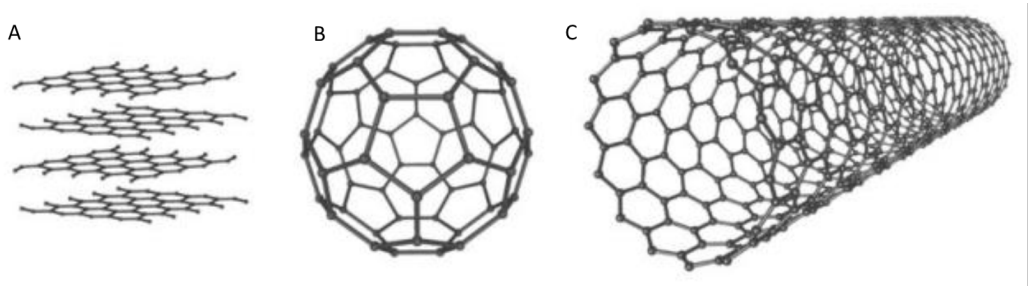

Figure 1.1: The three forms of graphitic carbon. A) Stacked to form graphite, B) wrapped to form fullerenes and C) rolled to form nanotubes.[4]

Graphene was first characterised in 2004 by Geim and Novoselov, this research won them the Nobel prize in Physics in 2010.[5] Although graphene's synthesis was documented as early as 1960 with $\approx$ 15 layers being produced,[6] Geim and Novoselov were the first to report of free standing, single-layer graphene. This was previously thought impossible due to the thermal fluctuations in a 2D material which lead to a large displacement in atoms, forcing the 2D crystallites to morph into a variety of 3D structures.[7] This theory was strongly supported by experimental observations that the melting point of thin films decreases with decreasing thickness, becoming unstable at approximately dozens of layers.[8] However, carbon - carbon bonds are strong enough that thermal fluctuations are not sufficient to destabilise graphene at room temperature.[7] Another viewpoint as to why 2D crystals are stable is due to the crumpling of the sheets in the Z axis. This 3D warping has been observed experimentally,[9] and leads to a gain in elastic energy and suppresses thermal vibrations.[7]

Since its discovery in 2004, graphene has attracted a large amount of interest,[10] and in 2017 the number of articles published on the subject reached over 80 per day. The interest for graphene has stemmed not only from its remarkable properties but also because graphene represents an ideal system for studying 2D materials. The study into graphene has paved the way for research into other 2D materials including hexagonal boron nitride and silicene.[11] Much research into graphene has been divided into the different morphologies that the graphene can take (platelets, films and 3D foams) as well as the method of synthesis. Graphene can be synthesised either through bottom-up processes, whereby the graphene is grown on a substrate, or top-down methods whereby graphene is derived from processing graphite.

This review will comment on the synthesis of the different morphologies of graphene, focussing primarily on bottom-up methods as it is more relevant to the work described here in. There will be only a brief mention of top-down methods.

1.2 Properties of Graphene

It is important to define exactly what is meant by graphene, literature often has a very broad definition but typically graphite should be considered graphene at less than 10 layers. This is because the electronic structure of graphene approaches that of graphite at approximately 10 layers.[12] There are many differences due to layer number in graphene before the 10 layer threshold is reached. Single-layer graphene (SLG) and bi-layer graphene (BLG) are both zero-gap semiconductors. However, for 3 or more layers, or few-layer graphene (FLG), the conduction and valence bands begin to overlap.[12] Transparency decreases with thickness with each additional layer of graphene resulting in an approximate decrease in transmittance of 2.3%.[13] Thermal conductivity has been shown to be very sensitive to thickness, where as few as four-layer graphene has a similar thermal conductivity to that of bulk graphite.[14] Hardness and elastic modulus have been observed to decrease linearly with increasing layer number up to four layers.[15] BLG and FLG can have different stacking arrangements, often depending on the way they are synthesised. These include AB (bernal stacking) which is most commonley found in natural graphite, ABC (rhombohedral stacking) as well as turbostratic stacking.[16] Turbostratic graphite, regardless of layer number, shares some properties with graphene as the layers are separated by a distance slightly larger than that of AB stacked graphite. It experiences the Dirac-like spectrum of free standing graphene, little doping, and exceptionally high electronic quality, $\mu \approx 250{,}000$ $cm^2V^{-1}s^{-1}$.[17] However, because an external electric field is screened within just a couple of near-surface layers, turbostratic graphite offers limited potential for electronics.[18] For the rest of this document, graphene will be referring to graphite with less than 10 layers.

It is the incredible properties of graphene which has led to the huge growth in literature over such a short period of time. Graphene has exceptional electronic properties.[5] It exhibits ballistic transport, the charge carriers behave as Dirac fermions meaning they have zero effective mass while prop-

agating through the honeycomb lattice, giving charge carrier mobilities up to 200,000 $cm^2V^{-1}s^{-1}$.[19] The charge carriers can also travel for micrometers without scattering at room temperature. This allows graphene to sustain current densities six orders of magnitude higher than that of copper.[20] Graphene also exhibits a room temperature quantum hall effect.[7]

It's not just the electronic properties that are exceptional in graphene, but also the mechanical, thermal and optical properties as well. Graphene has a breaking strength of ≈ 40 Nm^{-1} and a Young's modulus of ≈ 1.0 TPa.[21] Only diamond and SWNTs have recorded higher. Graphene is also flexible and can be stretched as much as 20 % more than any other crystal and has a bending radius of 2.3 mm.[21] It has a thermal conductivity of ≈ 5000 $Wm^{-1}K^{-1}$,[22] better than the next best thermal conductor diamond. SLG has a surface area value of ≈ 2630 m^2g^{-1} and is almost transparent, absorbing only 2.3 % of white light.[13] Unlike most other materials, graphene shrinks with increasing temperature.[23] Graphene is also impermeable to gases, including helium.[24]

It is important to note that these properties have been measured on near perfect graphene and measurements on bulk synthesised graphene are unlikely to be as exceptional. Experimental groups are synthesising graphene through micromechanical cleavage of bulk graphite. The same method which was used to isolate it for the first time where by scotch tape was repeatedly applied to highly ordered pyrolytic graphite (HOPG).[5] The technique has now been fine tuned and can achieve high-quality graphene flakes up to 100 microns. The same principle is applied but a fresh surface of the HOPG is simply rubbed against a solid substrate.[25] The vast majority of material produced via this method is graphite. What allows the detection of graphene was the observation that graphene is visible in an optical microscope if the substrate was silicon with a specific thickness of SiO_2 of 300 nm on the surface.[5] This method is unfeasable for any large scale synthesis but is preferred by research groups due to the small amount of defects imparted into the graphitic lattice. The presence of defects have been shown to have a negative impact on the properties of graphene and other methods of synthesis are likely to induce a higher density of defects.[26]

It is not just the number of layers where there is discrepancy about what is referred to as graphene. Materials with little in plane crystallinity which could also be classed as amorphous carbon is also labelled as graphene if the material is less than 10 layers. Examples of this can be seen with reduced grahene oxide (rGO), a graphene analogue discussed later in the

chapter that has lost much of the sp^2 hybridised carbon. Also, many of the low temperature synthesises of graphene do not have the in plane crystallinity expected of a graphitic material. These less crystalline materials however, still have many uses. Often the electrical quality that graphene is known for is lost with the loss of sp^2 carbon, as the extended π conjugated structure is destroyed. Typical conductivities recorded for rGO are ≈ 0.36 Sm^{-1},[27] much less than the ≈ 19 Sm^{-1} recorded for pristine graphene flakes.[28] These thin carbonacious materials do however still have properties making them worthwhile research areas, in particular, the presence of defects does act as areas which can be functionalised making the material more tunable and therefore better in composite materials.[29]

1.3 Applications of Graphene

More detailed reviews of all the potential applications for graphene exist,[30] and so they will only be briefly discussed here. The exceptional properties observed for graphene has lead to a host of potential applications being pursued, many of these are displayed in figure 1.2. Its exceptional electronic properties have led research groups to theorize that graphene could replace silicon, allowing for high frequency transistors.[7] However, the most limiting aspect of graphene in this regard is that the material is a zero-gap semi-conductor, and therefore for most logic applications, a band gap needs to be engineered into the graphene. This can be done is several ways: A small gap is induced in BLG.[7] For SLG, a gap can be induced by interaction with different substrates.[31] Controlling the aspect ratio of the graphene has also been shown to introduce a band gap, as demonstrated with graphene nanoribbons which have been successfully used in transistors.[32] The lack of band gap is less of an issue in analogue electronics. Ultrahigh frequency analogue transistors currently use GaAs - based devices, graphene could extend the operational range into terahertz frequencies.[33]

Many of the potential applications take advantage of the fact that graphene excels in many properties. The combination of its electronic and optical properties allow for use in optoelectronics,[35] graphene coatings could be a competitor to indium tin oxide (ITO), the transparent conductor used in such products as solar cells, liquid crystal displays, etc. The problem is that graphene films exhibit a resistivity of several hundred Ω for the standard transparency of ≈ 80 %.[36] This is two orders of magnitude higher than

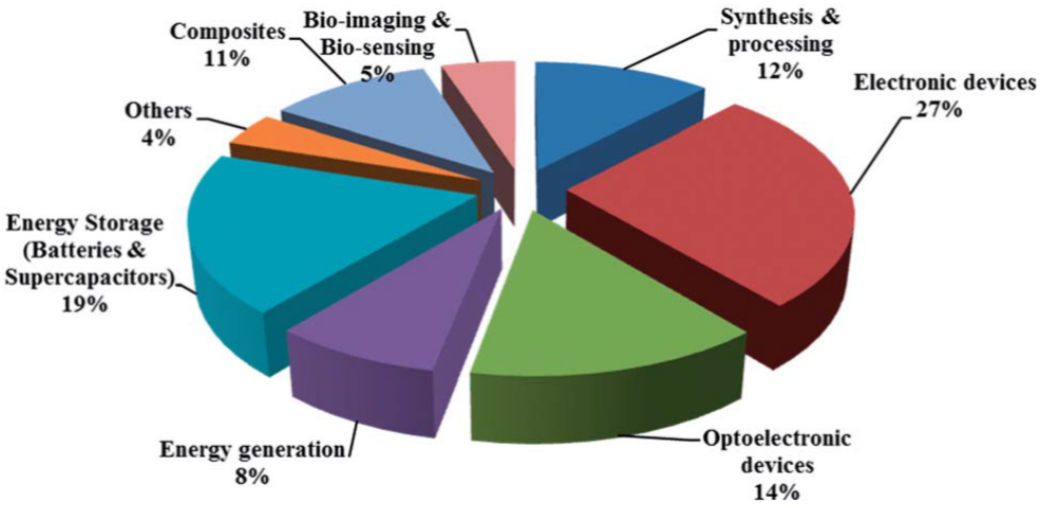

Figure 1.2: A pie chart showing the interest in graphene by number of publications for various applications.[34]

for ITO. Graphene does have advantages over ITO, it is chemically stable, flexible and robust, giving it use in bendable displays,[18] as well as more durable touch screens. An advantage graphene has over ITO in solar cells is that unlike ITO it is transparent to more wavelengths of light (from UV to NIR) and so should improve efficiency.[35,37]

The combination of high conductivity and strong mechanical properties gives graphene significant use in flexible electronics.[38] The high thermal conductivity gives rise to potential uses in heat management. The impermeability to gases gives graphene membranes a potential use as protection for metals against corrosion from oxygen and water.[24] Graphene has a very high sensitivity to anything adsorbed on its surface, and could allow for its use in sensors. A change in resistivity has been measured when only one atom was adsorbed onto a graphene sheet.[39] The combination of high surface area and conductivity is useful for energy storage applications such as capacitors and batteries.[40,41]

Graphene's remarkable properties have provoked wide interest in placing it into materials to make a composite. In paints it could be used to make the paint both thermally and electrically conductive, anti-static and also have gas barrier properties to protect against corrosion. Graphene could have similar effect when applied to polymers as well as increasing the polymers operating temperature and strength.[42]

When discussing applications, it is important to relate the nature of the synthesis and the morphology of the product to the potential applications. Depending on the synthesis and morphology, there will be large discrepancies in electronic, optical and surface area properties. Figure 1.3 shows a Venn diagram highlighting which macrostructure of graphene is best suited for which application.

Graphene films are best suited to electronic applications requiring the highest conductivities such as transistors and sensors, as the continuous film will minimise edge defects and contact resistances which both work to lower the conductivity of the device.[7,39] The greatest transparency will also be achieved in graphene films as less edges to scatter the light. Graphene foams, due to the high surface area and conductivity are suitable for energy storage applications,[43] while the high surface area and controllable porosity makes them suitable for catalyst supports,[44] and gas storage.[45] Many of these applications overlap with graphene platelets which too have a large surface area and conductivity. Platelets however have diminished conductivity compared to foams due increased number of edges and the contact resistance between each platelet. Also, less control of the porosity exists when platelets are agglomerated together. Instead, due to the relative ease of production, platelets are best suited for applications which require a lot of material, such as improving the properties of the material by making a composite.[42]

1.4 Synthesis of Graphene

Numerous methods exist for the synthesis of graphene each with their own set of pro's and con's. The methods can be broadly characterised into two groups, top-down and bottom-up synthesis. Top-down synthesis starts from graphite and then through various physical and chemical processes works to exfoliate the graphite by breaking apart the weak van der waal forces between the layers. Although the forces are weak, difficulty arises from damaging the sheets during exfoliation and preventing re-agglomeration of the graphene sheets.[46] Starting from graphite often means that these processes are more scalable and cheaper than their bottom-up equivalents. Bottom-up processes require growing graphene on a substrate using a carbon source other than graphite, usually a small hydrocarbon. In order to get the pristine sp^2 lattice seen in graphite, high temperatures are typically required making this a costly process. Also careful control of conditions are required to avoid carbon

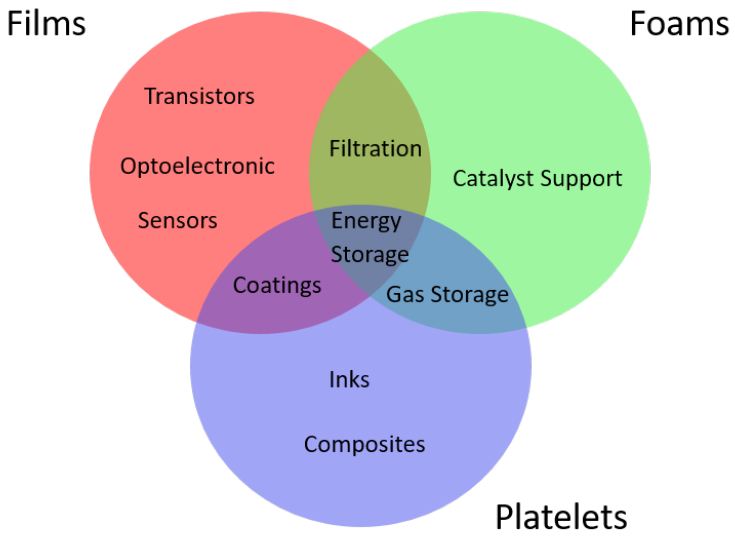

Figure 1.3: Venn diagram showing how the nature of the produced graphene relates to applications.

nanotubes. This section will primarily be discussing bottom-up processes as they were the used techniques in this thesis, with only brief mention of the various top-down methods.

1.4.1 Bottom-Up

Growth on silicon carbide

When silicon carbide (SiC) is heated to 1000 °C under a hydrogen atmosphere, the silicon sublimes leaving only carbon. The carbon left behind is graphitic.[47] A schematic of this is shown in figure 1.4. Two faces exist on SiC, SLG and BLG are typically grown on the Si-terminated face and multi-layer graphene (MLG) is grown on the C-terminated face. The MLG would be better described as turbostratic graphene as opposed to the Bernal stacking seen in graphite. The mobility values of graphene produced via this method are nearly that of graphene synthesised from the chemical vapor deposition method which will be discussed later. High quality wafer scale graphene with switching speeds of up to 100 GHz have been achieved with this technique.[48,49] The problem with this method is largely from the

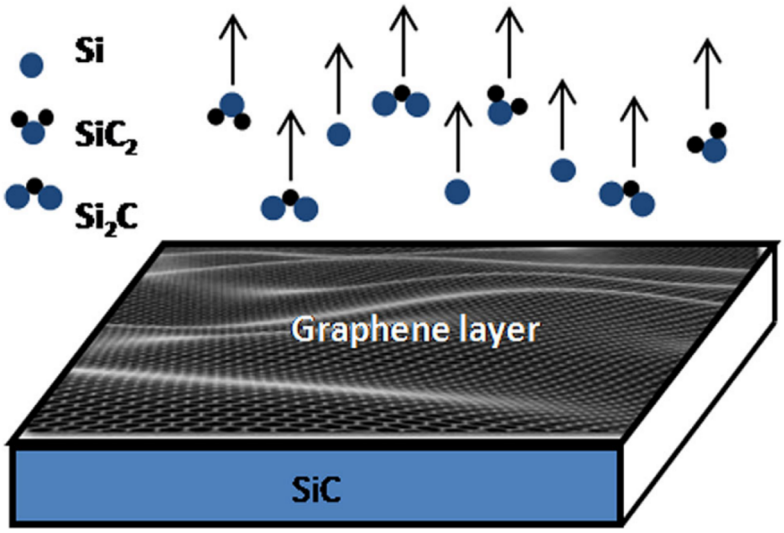

Figure 1.4: Schematic showing silicon subliming off the surface of SiC leaving behind graphene.[55]

cost of the SiC wafers and the high temperatures required and that typically there is a lack of continuity and uniformity in the graphene.[50] Methods exist in order to lower the temperature. By depositing a thin film of nickel on the silicon carbide wafer, temperatures as low as 700 °C can produce graphene. The nickel reacts with the silicon carbide forming nickel silicide leaving graphene behind.[51] Other methods include exposing the silicon carbide surface to chlorine gas, the gas reacts with the silicon forming $SiCl_4$ leaving carbon behind.[52] Graphene on SiC particles have been synthesised this way allowing the synthesis of graphene platelets.[53] Also graphene foams have been synthesised via this method whereby rather than SiC wafers, SiC foams are used.[54]

The work on silicon carbide has re-invigorated the field of carbide-derived carbons where a host of different carbides are treated thermally and chemically to produce carbon materials, including graphite, carbon nanotubes and graphene.[56] Some of the different carbides being looked at for graphene synthesis are Fe_3C,[57] and TiC.[58]

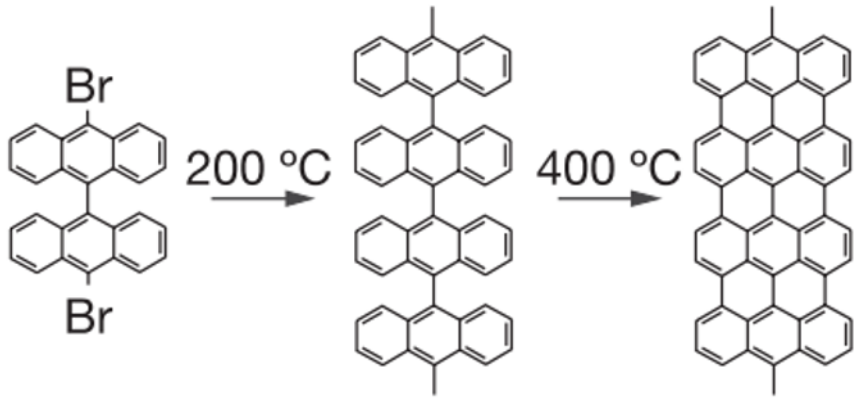

Figure 1.5: Schematic showing the reaction for the total organic synthesis of graphene nanoribbons.[59]

Organic Synthesis of Graphene

The organic synthesis of graphene-like polyacyclic hydrocarbons has been explored for decades. The advantages of such a method lies in the capability of simple functionalisation in order to improve the graphene's solubility. The difficulty has come in trying to preserve the planar structure. Many methods exist and are mostly performed by Klaus Müllen but one of the more interesting examples include a surface-assisted coupling of molecular precursors into linear polyphenylenes and their subsequent cyclodehydrogenation.[59] This is shown in figure 1.5. The monomer is sublimed onto a surface dehalogenating the monomers, then under heating, the monomers diffuse across the surface and undergo radical addition reactions to form linear polymer chains. An additional heating step then causes a surface-assisted cyclodehydrogenation to create the aromaticity. This produces graphene nanoribbons with very precise control over dimensions and edges.[59]

Unzipping Carbon Nanotubes (CNTs)

CNTs can be unzipped in order to produce graphene nanoribbons, as shown in figure 1.6. Several methods of unzipping exist including plasma etching,[60] laser irradiation,[61] and oxidative methods.[62] The widths of the ribbons can

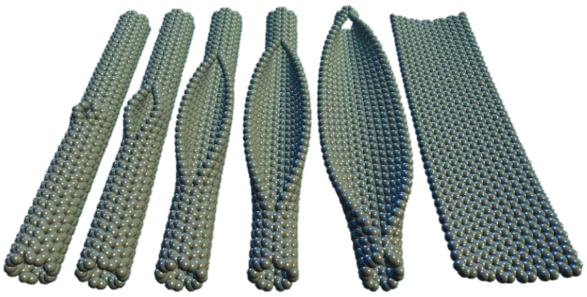

Figure 1.6: Cartoon showing the unzipping of a carbon nanotube.[62]

be controlled by the diameter of the CNTs. This is important as the graphene ribbons have different properties depending on their width and edge type.[63] The unzipping process occurs via breaking C - C bonds, which is often initiated at defect sites and can lead to irregular cutting.[64] More control has been offered in a new technique whereby flattened CNTs were unzipped. The unzipping occurs preferentially at the bent edges allowing for a much more consistent product.[65]

Chemical Vapour Deposition (CVD)

CVD is a process often used to grow thin films of material on a substrate. In the case of graphene synthesis, most typically a metal catalyst is heated to a high temperature while a carbon containing feed gas, mixed with hydrogen, is blown over the catalyst. The end result is a layer of graphene on the metal substrate. A diagram of a typical CVD set-up is shown in figure 1.7. Many variables have been changed in order to optimise the quality and layer number of the graphene, including carbon source, temperature, pressure and flow rates. These have been reviewed in depth elsewhere,[66] but will be briefly discussed here.

The chemistry of CVD carbon growth is nothing new, in fact, few-layered graphene materials have been synthesised on transition metal surfaces for nearly 60 years.[67] The first observation was thin films of graphite forming on nickel surfaces when the metal was exposed to hydrocarbons at high temperature.[67] Similar methods were also employed in the synthesis of carbon nanotubes whereby carbon containing gases are flown over metal particles or rough metal surfaces.[68] The field has been re-invigorated since the discovery of graphene where many groups are attempting to optimise the process for

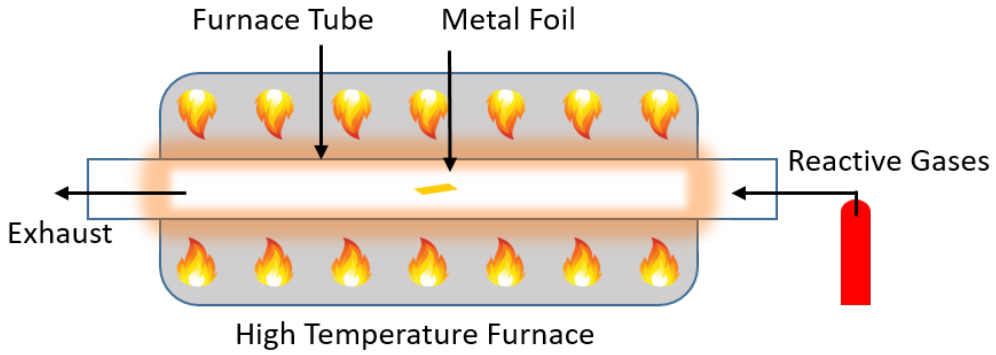

Figure 1.7: Diagram of a typical CVD set-up.

SLG.

Typically it is transition metals which catalyse the growth of graphitic carbon. Iron, nickel and cobalt are traditionally recognised as the best graphitisation catalysts.[69] Indeed, all three metals have been used to catalyse graphene synthesis,[38,70,71] with nickel experiencing the most attention. The catalytic ability of these transition metals arises from either partially filled d-orbitals or from the formation of intermediate compounds that adsorb and activate the reacting substances. The nickel - carbon phase diagram shows that nickel has a high carbon solubility at high temperatures which decreases when the temperature is lowered.[72] The formation of a metastable nickel carbide phase promotes the precipitation of carbon out of the nickel. Iron and cobalt show a similar phase diagram and so the catalytic behaviour is likely to be similar.[73] Interesting magnetisation studies have been done on nickel catalysts to confirm this mechanism for graphtic carbon formation. During the first 12 minutes of nickel exposure to a carbon source at temperature, a large decrease in magnetisation is observed. This is attributed to the formation of nonferromagnetic nickel carbide. After 12 minutes, the magnetisation is restored due to the decomposition of nickel carbide into metallic nickel and graphitic carbon.[74] Continuous few-layer graphene films have been grown on polycrystalline nickel foils and transferred onto plastic and Si wafers.[38,75] These films exhibit carrier mobilities up to 4000 $cm^2V^{-1}S^{-1}$.[38]

Copper, although not traditionally considered a graphitisation catalyst, has had a lot of success in graphene synthesis producing large graphene films with high mobilities.[76,77] Compared to the other traditionally used catalysts, copper has a much lower affinity for carbon, reflected in the fact that

it does not form any stable carbide phases and has a much lower carbon solubility. This is attributed to copper's full d - electron shell meaning copper can only form "soft" bonds with carbon via charge transfer from the π electrons in the sp^2 hybridised carbon to the empty 4s states of copper.[66] This means that rather than forming a solid solution with carbon, the carbon is limited to the surface of the copper. An interesting set of experiments were conducted by Ruoff *et al*,[78] to show the different mechanisms at work for nickel and copper. A conventional CVD was carried out using nickel and copper foils. The carbon source however, was sequential doses of $^{12}CH_4$ and $^{13}CH_4$. In the case of the nickel catalyst, the resulting graphene was a random mixture of ^{12}C and ^{13}C. This is because the two isotopes of carbon would be mixed in the solid solution and so upon cooling, when the carbon precipitates out, a mixture will occur. The resulting graphene on the copper however, was not a random mixture of ^{12}C and ^{13}C but was entirely made up of regions of ^{12}C and regions of ^{13}C. This is due to the carbon being limited to the surface of the copper and growing on the surface as and when the carbon comes into contact with the surface.[78] A schematic of the two experiments is shown in figure 1.8.[78] An experiment was conducted showing the graphene growth on copper at different times during the CVD,[77] it can be seen from figure 1.9 that after 1 minute there are independent graphene flakes which grow and eventually coalesce into a continuous layer. It can also be observed that the graphene domains grow over the grain boundaries of the copper.[77] It is thought that the weak interaction between graphene and the copper substrate allows the flakes to expand over the grain boundaries.[77]

As graphene growth on copper operates through a surface mechanism, it has been found to be easier to achieve SLG on copper than on nickel. Indeed 95% SLG coverage has been achieved on copper with the remaining 5% of the surface being covered with 2 - 3 layer material.[79] The deposition of a continuous graphene layer leads to passivation of the copper surface, hindering the growth of multi-layered material.[66] Growth on nickel on the other hand has a large tendency to grow MLG and requires careful control of the conditions to stop the growth at SLG. Typically the resulting material on nickel is much less homogeneous than on copper.[66] Graphene preferentially precipitates out at grain boundaries and so thicker material is present at these boundaries.[80]

Many studies have been conducted to deduce why MLG is able to form on a copper surface. The consensus is that the graphene grows on the copper, underneath the existing graphene layers.[81] Insight into how this occurs was given by the observation that SLG is favoured at low hydrogen

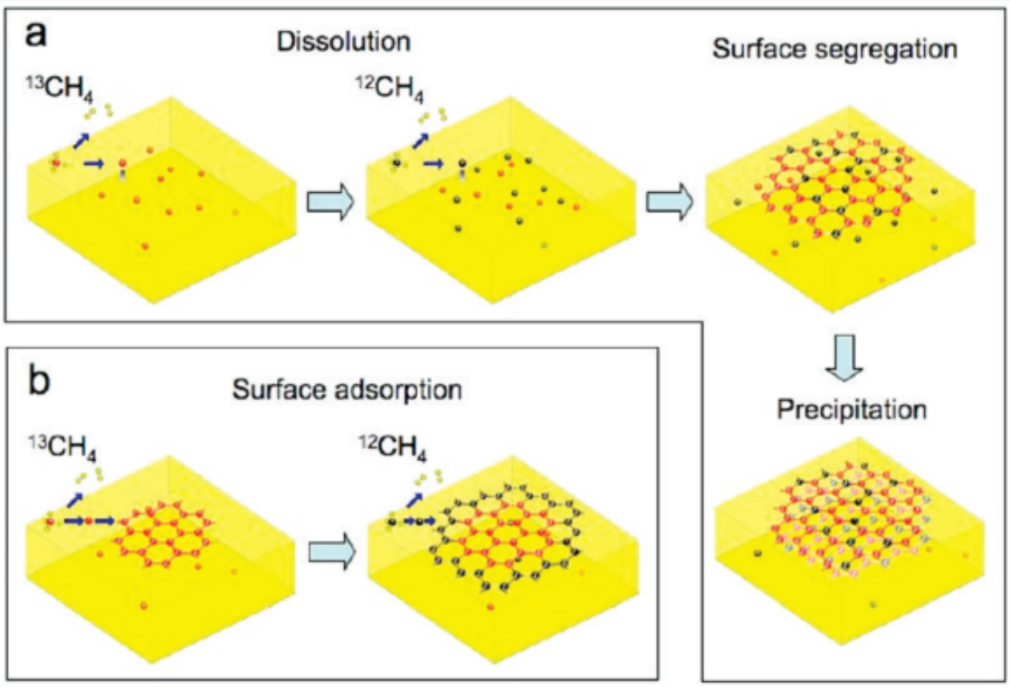

Figure 1.8: Diagram showing how the different mechanisms of graphene formation result in a different distribution of carbon isotopes after undergoing a CVD with a sequential input of different isotopes of carbon. A) Precipitation mechanism showing random distribution of isotopes. B) Surface mechanism showing distinct domains with different isotopes.[34]

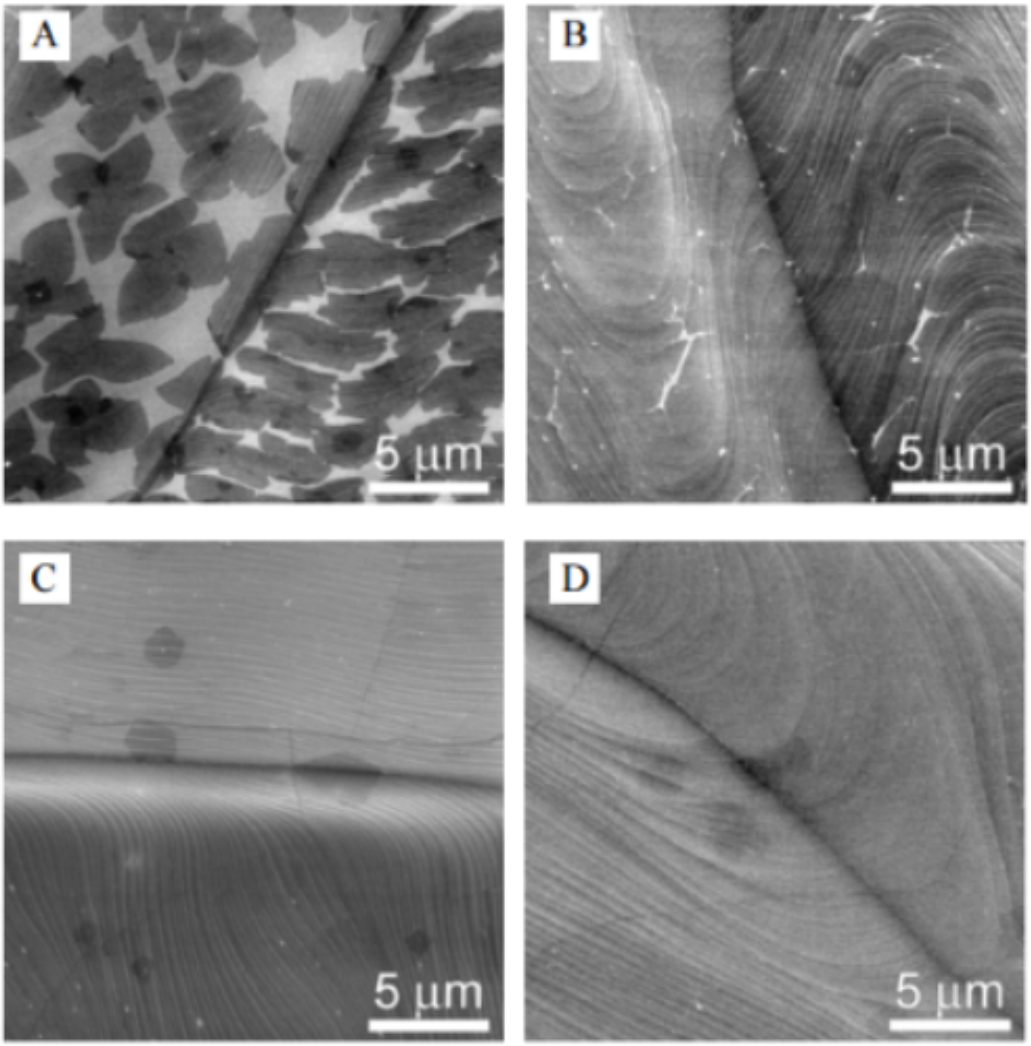

Figure 1.9: SEM images of graphene on copper with varying growth times of (A) 1 minute, (B) 2.5 minutes, (C) 10 minutes and (D) 60 minutes.[77]

concentrations while MLG was favoured at high hydrogen concentrations. At low hydrogen concentrations, the edge of the graphene tightly binds with the metal, preventing growth of additional layers. At high hydrogen concentrations, the edges of the graphene terminate with H and only loosely bind to the metal,[81] allowing methane to still have contact with the copper surface. Further evidence for this model comes from observations that in BLG, smaller domain sizes are present in the graphene in contact with the copper surface.[81,82]

The full impact of hydrogen on the CVD process is yet to be fully understood. Typically systems have hydrogen mix with the methane and then carried through with a carrier gas, usually argon. Hydrogen is thought to have many roles during the process depending on the metal used, studies have looked at copper and nickel catalysts. On copper, hydrogen diffuses into the Cu,[83] and then reacts with methane to form active species $(CH_3)_s$, $(CH_2)_s$, $(CH)_s$ or $(C)_s$ through a series of H-abstraction reactions (equation 1.1).[84]

$$(CH_4)_s + H_s <=> (CH_3)_s + H_2 \tag{1.1}$$

Density functional theory (DFT) calculations have shown that these reactions are not thermodynamically favourable in the absence of hydrogen.[85] The hydrogen also etches the graphene on the metal surface according to equation 1.2:

$$(H)_s + graphene <=> graphene - C + (CH)_s \tag{1.2}$$

This is an important process in achieving uniform coverage as the graphene grain density is greater at defects on the copper surface and the hydrogen etches smaller active carbonacious species allowing for larger graphene grain size.[84,86] On nickel, hydrogen recombines and gases off keeping sites on the nickel surface free for further dehydrogination of CH_x as well as aiding the dehydrogination of CH_x in the same way shown in equation 1.1.[83] Despite all this, studies have shown an improvement in yield and quality of SLG by excluding hydrogen from the system completely. It is thought that the hydrogen forms C-H bonds with the graphene, creating out of plane defects.[87] A wide variety of hydrogen concentrations have been used in order to firmly deduce its effect on CVD, from no hydrogen,[88] less hydrogen than methane,[89] and more hydrogen than methane.[90] each with differing results. Some groups have found that graphene cannot be grown in the absence of hydrogen or at very low methane concentrations,[84] while other groups have found a more pristine product in the absence of hydrogen.[88] Hydrogen has been shown to be vital during the annealing step in removing any residual oxide layer that might be present. If removed during the annealing step, a large amount of

oxide nanoparticles were formed on the surface.[91]

Some interesting variations have been attempted in order to grow large area, defect free graphene. Diagrams of these techniques are shown in figure 1.10. Very large graphene domains have been grown on liquid copper. By melting the copper, large single crystal domains form reducing the amount of grain boundaries, reducing the defect density in the graphene.[92] Nickel has been found to work as a promoter for CVD on copper. Improved surface coverage has resulted by placing nickel foil upstream of the copper foil. It is believed that the nickel generates carbon radicals that diffuse from the nickel onto the copper.[93] Ideas to reduce graphene nucleation and therefore increase graphene domain size include placing the copper foil inside a tube within the furnace tube with the upstream end closed. This increases the velocity of gas at the copper foil which results in less graphene nucleation.[94] Another method is to suppress copper evaporation during growth which roughens the surface. This is done by coating the inside of the tube with copper. Any evaporation of the copper would therefore be re-deposited, smoothing the surface.[95] Surface oxygen has been shown to inhibit graphene nucleation, larger graphene domain sizes have resulted from using an oxygen rich piece of copper.[96] Most CVDs are done on foils, but thin metal films deposited by e-beam,[97] or thermally evaporated onto a substrate,[98] have been used.

Although nickel and copper are by far the two most commonly used catalysts in CVD, likely because of their low cost and widespread availability, other metals have been attempted with success, including palladium,[99] ruthenium,[100,101] iridium,[102] platinum,[103] rhodium,[104] silver,[105] iron,[106] cobalt,[70,107] and gold.[108] Growth on the Ir(111) surface is interesting as the resulting material has a band gap, a very important characterisitic if graphene is to be used in transistor applications.[109] This was achieved by patterned adsorption of hydrogen atoms onto the graphene, this results in graphene-like clusters, presenting a barrier for electron mobility and opening up a band gap.[109] Ruthenium is an interesting case as it has a carbon solubility between that of nickel and copper, while also not forming a carbide. Growth of graphene on polycrystalline ruthenium has been achieved and was shown to have a mechanism similar to that of copper.[100]

The most common carbon source used for graphene synthesis through CVD is methane. This is a good source as it decomposes cleanly at high temperatures giving a highly crystalline graphitic product. Containing only one carbon atom also makes graphitic carbon more likely to form. It is also cheap and readily available. However, its flammability and high temper-

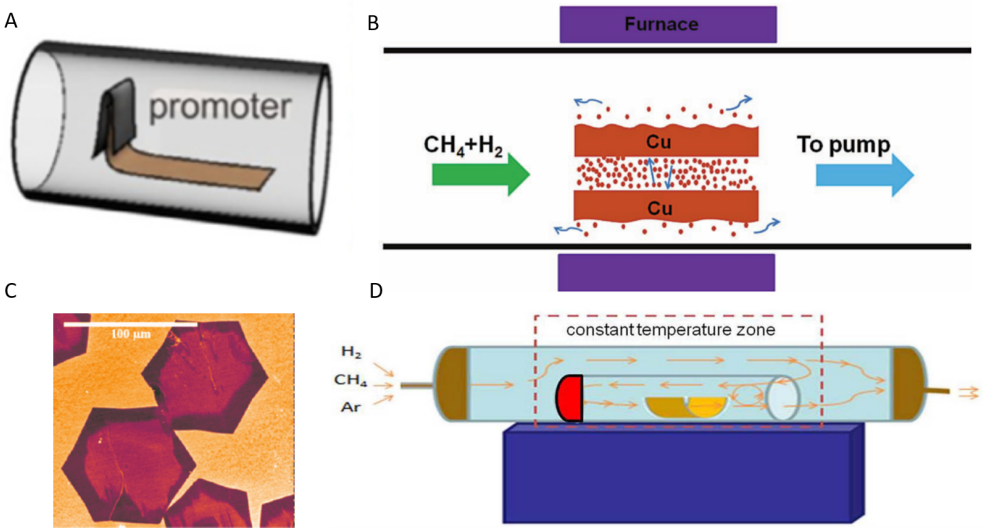

Figure 1.10: Diagrams showing variations of the CVD process. (A) Using nickel as a promoter,[93] (B) Coating the tube with copper foil,[95] (C) Large graphene domains on melted copper,[92] and (D) putting the foil inside a tube with in the furnace tube which has the upstream end sealed.[94]

ature requirements have led groups to research alternative carbon sources. One such source which has had a lot of use in the synthesis of CNTs is acetylene.[110] It has been sucessfully used to grow graphene on nickel foils at temperatures as low as 700 °C.[111] It is not just gaseous sources that have been used. Both liquid and solid source have effectively been used to grow graphene. Liquid sources include benzene,[112,113] toluene,[114] hexane,[115] methanol,[116] propanol,[116] and ethanol.[116] These sources all allow a lower temperature of CVD than the 1000 °C necessary with methane but does typically result in a lower quality material unsuitable for most electronic applications. However, they could facilitate the doping of graphene during synthesis by using nitrogen or boron containing organic solvents. Solid sources such as poly(methyl methacrylate) (PMMA),[112] polystyrene,[112] and camphor,[117] have been attempted and do work at low temperature but again at severely diminished quality. It has also been demonstrated that solid sources such as cockroach legs or cookies can produce high quality graphene on copper, so long as the high temperature is maintained.[118] This suggests that if the high temperature is maintained, any source which can decompose at that temperature is a good source for graphene growth on copper. This is because graphene growth on copper is largely self-limiting. This is not the case with

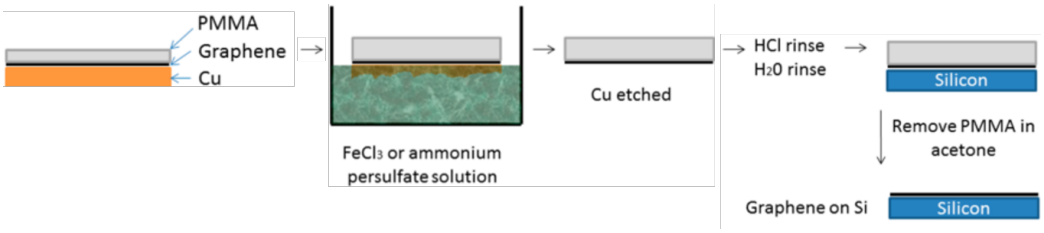

Figure 1.11: Schematic of the process of transferring CVD graphene to an insulating substrate.[122]

nickel and the other catalysts like nickel where a more careful control of the amount carbon introduced into the system is required.

Another condition which has proved important in CVD is the pressure of the system. Low pressure systems have typically yielded the best results with improved uniformity, thickness, surface coverage and better reproducibility.[79,95,119] Low pressure annealing has been shown to improve the smoothness of the metal surface.[88] Low-pressures also allow the reactive gases to approach the catalyst surface much closer than in an atmospheric pressure set up.[79,95,119]

For most electronic applications, it is important that the graphene is on an insulating substrate. Graphene produced on metal foils therefore needs to be transferred. This is most typically done by depositing a protective layer of PMMA onto the graphene film and then etching away the underlying metal. Once the metal is removed, the polymer coated graphene floats in the etchant solution and is strong enough to be handled and deposited onto an insulating substrate, usually silicon or silicon dioxide. The PMMA is then dissolved in acetone,[114,120,121] leaving graphene on the insulating substrate. This process is shown in figure 1.11. The transfer process often results in defects being introduced into the graphene. This has led to groups trying to deposit graphene directly onto insulating substrates. One such method was the deposition of a very thin layer of copper onto a silicon wafer, a normal CVD was then performed which causes much of the copper to evaporate and graphene ends up directly on the silicon wafer.[97]

The pre-treatment of the metal surface has been shown important for maximising the domain size of the graphene.[76,123] This has proven particularly true for growth on copper, as one might expect due to the surface orientated mechanism. The pre-treatment not only removes the native oxide

layer but it also has been shown that a flat surface morphology is imperative in gaining high quality SLG.[124] Impurities and defects on the metal surface have a large effect on the graphene, acting as nucleation sites, resulting in smaller graphene domain sizes.[125] Experiments have shown that there is a much higher graphene domain density at scratches and grain boundaries.[126] Surface defects may also result in more amorphous carbon. This is due to inhibited surface diffusion of the carbon atoms resulting in defected sp^3 networks upon termination.[124] It has also been shown that rougher surfaces give rise to MLG as growth rates on the surface become different.[88] The commonly used pre-treatment methods include extended annealing times, washing with acetic acid,[127] nitric acid,[128] mechanical polishing,[126] and electropolishing.[129] The annealing step is very important in increasing grain size and reducing surface defects of the metal.[66]

CVD growth is not just limited to graphene films. Graphene platelets and foams have also been synthesised through CVD. Graphene platelets are grown on small, platelet-like metal catalysts. Such examples from literature include: graphene nanoribbons on nickel nanobars,[130] copper ribbons,[131] and zinc sulphide ribbons.[132] Also graphene sheets have been synthesised from iron bars.[106] Difficulties with these processes come from the meting point depression experienced by small particles resulting in the particles balling up at the high temperatures required for methane CVD.[133] Therefore, ethanol typically needs to be used as the carbon source. CVD growth on small particles is also in direct competition with the synthesis of CNTs. Graphene foams have been synthesised through methane CVDs on nickel foams,[134] attempts were made to grow on copper foams but the graphene collapsed upon removal of the underlying metal. It is believed that thicker material is required in the graphene foam to support its structure.[135]

1.4.2 Top-down

Micromechanical Cleavage

This was the method used to isolate graphene in 2004 and uses an adhesive tape repeatedly applied to graphite unitl a single layer of graphene is achieved. Both SLG and FLG has been produced using this method. The resulting graphene is then applied to a substrate by gentle press of the tape to the substrate.[5] A heat treatment, such as 200 °C in hydrogen/argon for 1 hour is required once the graphene is on the desired substrate to remove

any glue residue left on the sample which could possibly limit electron mobility.[136] This method gets high quality graphene but is expensive and labour intensive so only suitable on a research scale.

Liquid exfoliation of Graphite

This is where graphite is dispersed into a solvent and then exfoliated via sonication,[137] or shear mixing.[138] The process rarely results in complete exfoliation so the graphene is separated from the graphite via centrifugation. The process works due to strong interactions between the solvent and the graphite reduce the energy penalty for exfoliation. The surface tension of the solvent should also serve to increase the interlayer separation of the graphite layers making them easier to exfoliate. Suitable solvents are those which the surface energy matches that of graphene. This has had most success in N-methyl-pyrrolidone (NMP),[137] but has been shown to work in other solvents.[137] Water has been used as the solvent with added surfactant. Yields as high as $\approx 40\%$ of the flakes having less than 5 layers and $\approx 3\%$ of flakes being SLG have been achieved when the surfactant sodium dodecylbenzene sulfonate was added and the solution sonicated. The surfactant is necessary as water has much too high of a surface energy to be a good exfoliate. The surfactant also helps prevent re-agglomeration of the graphene sheets.[136] Problems with these methods are that the sonication tends to shorten the flake size as well as add defects into the graphene lattice. Also, residual surfactant in the graphene has proved difficult to remove. Shear mixing as an alternative to sonication has been suggested. It has been shown that much less defects occur in the graphene lattice. However, the sheet size is shortened by the process and yields of SLG are poor.[138] Functionalisation of the graphite both covalently,[139,140] and non-covalently,[141] has ben shown to aid exfoliation. These methods however introduce structural and electronic disorder.[142,143]

Graphite Oxide

Graphite oxide can be used to synthesise a graphene analogue by exfoliating it to graphene oxide (GO) and then reducing it to reduced graphene oxide (rGO). Graphite oxide is made by the reaction of graphite with a mixture of potassium permanganate and concentrated sulphuric acid in the Hummers method.[144] There is much debate about what the structure of graphtie oxide

might be but the most well-known structure is the Lerf and Klinowski model shown in figure 1.12.[145] The interlayer separation of the graphite oxide is ≈ 0.65 - 0.75 nm depending on the amount of intercalated water. The water intercalates into the layers and stabilises the layered structure due to strong bonding with the layers. It is the increased interlayer separation due to the water along with the functional groups which makes exfoliation of graphite oxide into GO relatively easy. Thermal expansion and sonication are the two most common methods to exfoliate graphite oxide. Thermal expansion works by rapidly heating the graphite oxide, the functional groups decompose forming CO_2 which breaks apart the graphene oxide sheets.[146] The sonication method is usually performed in water as the oxygen groups make water a good solvent for graphite oxide.[145]

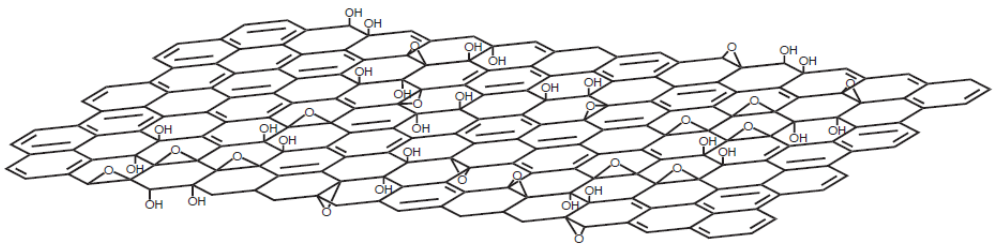

Figure 1.12: The Lerf and Klinowski model for GO.[145]

The GO is heavily functionalised with oxygen groups and so to give a good graphene analogue, it needs to be reduced. The reduction process is not complete and many defects in the sheets exist. It is therefore helpful to refer to the material not as graphene but instead as reduced graphene oxide (rGO). rGO does not have the remarkable properties associated with graphene but its synthesis is scalable and the material has found use in many applications.[147] Many reduction methods have been used including hydrazine,[148] thermal annealing,[35] vitamin C,[149] and HI.[150] It is also possible to apply thermal shock to exfoliate and reduce the GO at the same time.[146] GO lacks the long range conjugation of graphene and so reduction methods not only have to remove lattice defects but also restore the long range conjugation of the graphitic lattice.[151] Complete reduction of GO has proved difficult because the layers become less hydrophilic as they get reduced and tend to aggregate and precipitate.[152] rGO is not just limited to the synthesis of graphene platelets. 3D macroporous graphene foams have been synthesised through the self-assembly of graphene oxide.[153–155]

Graphite Intercalation Compounds (GIC)

GICs are compounds consisting of positive or negative layers of graphite with counter ions intercalated between the layers. The intercalated compounds cause the interlayer separation to increase making it easy to exfoliate the layers and achieve graphene.[156] One group has found that by sonicating oleum intercalated graphite in DMF and then centrifuging to separate out the graphene, a suspension where 90% of the flakes are SLG is achieved.[157] There is a drawback to sonicating in that it will reduce the size of the graphene flakes, this has led to development of a synthesis using an alkali GIC which spontaneously exfoliates in NMP to yield graphene sheets and nanoribbons.[158]

Electrochemical Exfoliation

Exfoliation of graphite by electrochemical means has had success where the graphite is used as an electrode and then placed in different electrolytes and then a current applied. Use of poly(sodium-4-styrenesulphonate) as an electrolyte has achieved SLG and FLG, it is thought that the $\pi - \pi$ interactions between the graphene surface and the aromaticity of eletrolyte is what allows for exfoliation.[159] Another electrochemical method has been to use a lithium complex as the electrolyte, the current makes one of the graphite electrodes negatively charged at which point the Li complex intercalates causing the graphite to expand. The graphite can then be exfoliated by sonication. This method has reported greater than 70% yield of FLG.[160] Electrochemical methods are desirable as processes have a large potential to be scaled up and made continuous.[159]

1.5 Synthesis and its Relationship to Applications

The term graphene has encompassed a wide range of different materials such that not all of the graphene produced by the different methods are suitable for each application. Some applications require a large quantity of material and electronic quality is less important. For other applications, small amounts of highly pristine graphene is preferred. Not just quality and yield

are important, but also the form of the graphene; 3D graphene or graphene foams are finding there own niche set of applications with which they are best adapted for, while there has already many potential applications for graphene platelets. The different synthesis methods above are all best suited to produce different "types" of graphene. Table (1.1) outlines some of the most suitable applications depending on the synthesis method. This topic has been reviewed elsewhere.[152]

Method of Synthesis	Nature of Product	Potential Applications
CVD	Films, platelets or foams	Electronic, optoelectronic, energy storage and sensors
Epitaxial Growth on Silicon Carbide	Films and platelets	Electronics
Unzipping nanotubes	Ribbons	Transistors
Organic Synthesis	Ribbons	Transistors
Micromechanical Cleavage	Platelets	Research
Solvent Exfoliation	Platelets	Composites and conductive inks
Graphite Oxide	Platelets and foams	Composites, conductive inks and energy storage
Graphite Intercalation Compounds	Platelets	Composites and conductive inks
Electrochemical Exfoliation	Platelets	Composites and conductive inks

Table 1.1: Table showing the best suited applications of graphene depending on the synthesis method.

1.6 Summary

Graphene is an exciting material which has many potential applications depending on the morphology and synthesis method of the graphene. Large scale production of graphene platelets with poor electronic quality has been achieved and indeed graphene is already starting to make its way into composite materials and even energy storage devices. The big marque appli-

cations in electronics are still absent. The challenge remains making large quantities of very high-quality graphene. Progress is being made and much literature is published every year, especially on the CVD process.

The aim of this PhD was to synthesise graphene with a control over the morphology. Controlling the morphology gives influence over the properties and therefore the potential applications to which the carbon material can be used for. Films, foams and platelets all have unique applications and this thesis will focus on the synthesis of foams and platelets.

There are numerous methods of synthesis of graphene but the technique most appropriate for templating the growth of graphene is CVD. A large quantity of literature exists in controlling the morphology of metals or building 3D metal foams and CVD has had much success on growing graphene on metals. The only other technique which might offer a similar level of control in morphology is the growth on silicon carbide, but the synthesis is expensive, reliant on defect-free silicon carbide and the literature on controlling the morphology of silicon carbide is much more sparse. This body of work will therefore focus on controlling the morphology of metal catalysts and then growing carbon on the metal catalysts.

Chapter 2

Characterization Methods

This chapter will introduce many of the key characterisation techniques used to gain insight into the materials produced in this research. A brief introduction to the technique will be given but the focus will be on how the technique is useful for the characterisation of carbon nanomaterials.

2.1 Powder X-ray Diffraction

X-ray diffraction (XRD) is used for phase identification of a crystalline material and provides information on unit cell dimensions. X-rays fired at a sample interact with the electron cloud surrounding the atoms of the solid and constructively interfere when conditions satisfy Bragg's law (equation 2.1):

$$n\lambda = 2d\sin\theta \tag{2.1}$$

where λ is the wavelength of the incident X-rays, θ is the scattering angle and d is the lattice spacing. The diffracted X-rays are then detected and counted giving a diffraction pattern. From Bragg's law, the d-spacing can be obtained and then compared with a database of materials.

For carbon nanomaterials, powder X-ray diffraction (PXRD) is used where the sample is ground into a fine powder and average bulk composition is

determined. The first piece of information that can be obtained qualitatively is how crystalline the material is. A crystalline material has a repeating unit cell and so sharp peaks occur in the diffraction pattern. When the repeating structure is only short range, broad peaks occur as the diffracted X-rays are detected over a wider range of angles. For graphite-like materials, the most intense peak will come from the interlayer separation, labelled as the (002) and is usually 3.35 Å. This number is increased for turbostratically stacked graphite and non-existant for graphene due to none or only a few layers being present. The 2nd order of the (002), the (004) peak is also commonly observed. The other commonly observed peaks for graphite, although much less intense are the (110) and the (100) at 1.23 Å and 2.12 Å respectively and are planar spacings shown in figure 2.1.

In figure 2.2, commonly observed XRD patterns are shown for graphite, graphite oxide and graphene. The graphite pattern shows the (002) as the most prominant, and is often the only peak seen in such patterns. The graphite oxide pattern only has a (002) down shifted due to the much larger interlayer separation between graphite oxide and graphite. No (002) peak can be observed in graphene as there is no long range crystalinity in this direction due to the few number of layers.

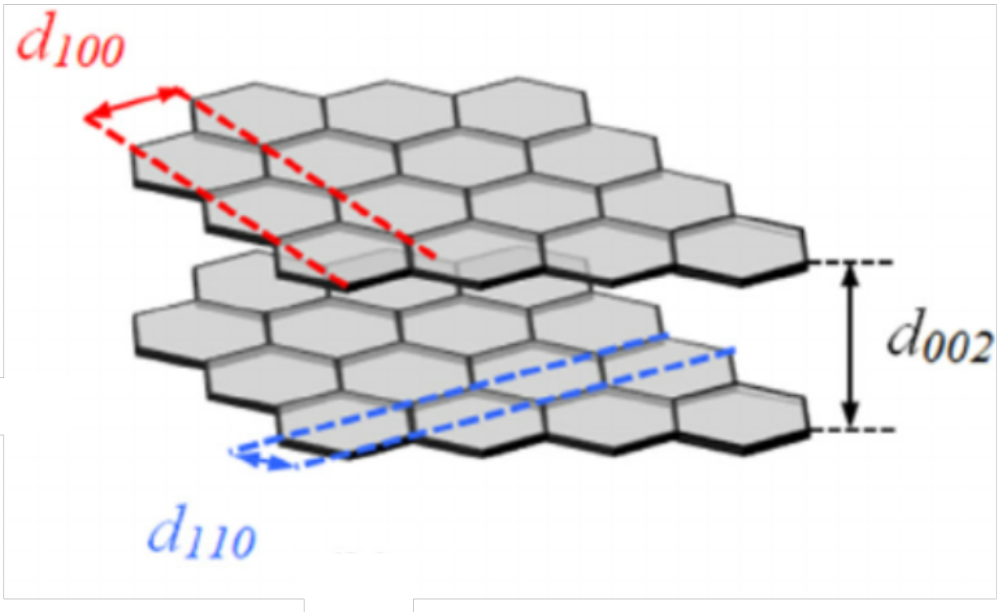

Figure 2.1: Image showing the commonly observed lattice spacings of graphite.[161]

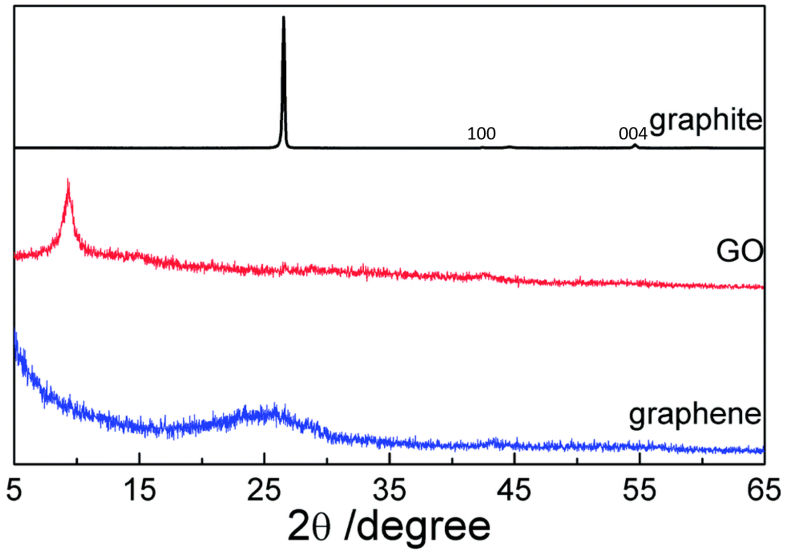

Figure 2.2: Commonly seen XRD patterns for graphite, graphite oxide and graphene.[162]

2.2 Electron Diffraction

Electron diffraction (ED) is very similar to X-ray diffraction with the same information being gathered. Electrons have wavelengths according to the de Broglie equation:

$$\lambda = \frac{h}{mv} \tag{2.2}$$

where λ is the wavelength of the electrons, m is the mass of the electrons, h is Planks constant and v is the velocity of the electron. Due to the wave-like nature of the electrons, diffraction occurs when electrons pass through the crystal lattice of a material.

For carbon nanomaterials, electron diffraction is most commonly carried out inside a transmission electron microscope (TEM). An ideal ED pattern for graphene is shown in figure 2.3. The selected area chosen for diffraction produces a set of diffraction spots, lattice parameters can then be extracted from the distances of the spots from the centre of the electron beam. A single set of spots at each spacing show the material is single crystalline and

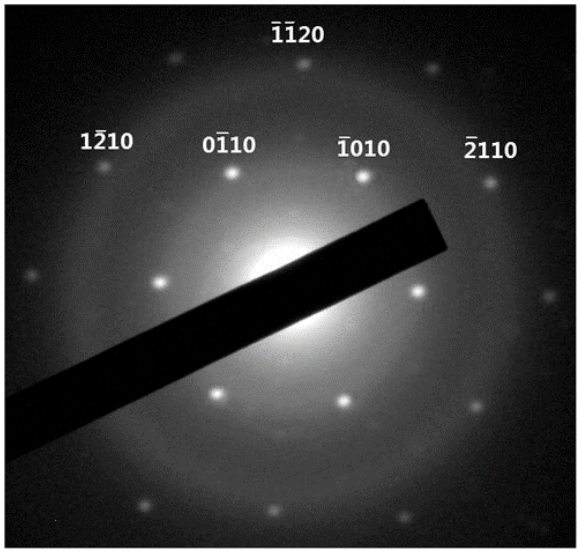

Figure 2.3: Electron diffraction pattern of graphene showing the $(0\bar{1}10)$ and $(1\bar{2}10)$ indices.[163]

each additional set of spots shows further crystalline domains been observed. With polycrystalline materials, so many sets of dots become indistinguishable and rings appear. Like in XRD, graphene will show no (002) set of diffraction spots and only the reflections at 0.212 nm and 0.123 nm corresponding to the $(0\bar{1}10)$ and $(1\bar{2}10)$ indices respectively will appear.[9] These can be seen in the electron diffraction pattern shown in figure 2.3. Amorphous carbon structures typically appears as diffuse rings in the diffraction pattern due to the nano sized crystalline domains. These rings appear at $\approx 1.2\,\text{Å}$, $2\,\text{Å}$ and $3.5\,\text{Å}$.[164]

Relative intensity of different spots has been used to distinguish between single and multi-layer graphene. Previous studies have shown that for few-layer graphene and graphite with Bernal (AB) stacking the intensity ratio of $\frac{I_{1100}}{I_{2110}}$ is less than 1, whereas monolayer graphene $\frac{I_{1100}}{I_{2110}}$ is greater than 1.[9,137]

2.3 Raman Spectroscopy

When light is shone onto a material, several processes can occur. The material can reflect, transmit, absorb or scatter the light. Most of the scattered light is scattered with no change in energy (elastic scattering) and this is known as Rayleigh scattering. However, a small proportion of the light will be Raman scattered where by either a loss in energy (stokes) or a gain in energy (anti-stokes) occurs. This is demonstrated in figure 2.4.

The change in energy occurs due to the interaction of the light with molecular vibrations, similar to infra-red spectroscopy. For a vibrational mode to be Raman active, there must be a change in polarisability of the molecule during the vibration. This is in contrast to IR active modes which require the vibration to cause a change in dipole moment. Raman spectroscopy therefore gives information regarding the vibrational modes in a material by producing a spectra of the stokes (or anti-stokes) shift of the material. That is the difference between the absorbed photons and the emitted photons. The virtual state describes a very short lived energy state that exists only when the sample is excited by the laser.

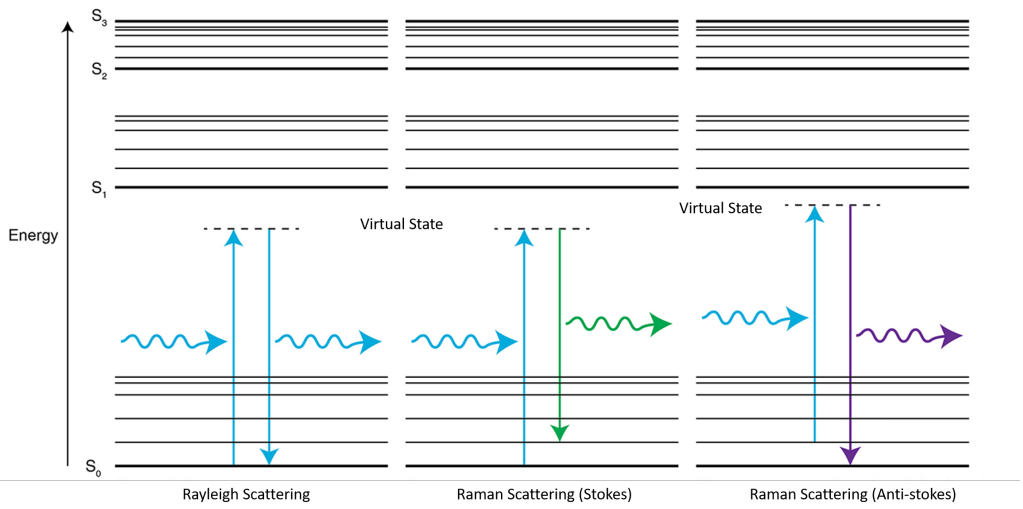

Figure 2.4: Schematic showing the different transtions making up Rayleigh, Stokes and Anti-stokes scattering. Image taken from: http://www.renishaw.com/en/raman-spectroscopy-in-more-detail–25806

Raman spectroscopy has been a very popular tool for carbon based materials. This is due to the technique being most sensitive to symmetric covalent bonds with little or no natural dipole moment. The carbon - carbon bonds that make up carbon nanomaterials fit this criterion. It is particularly good for sp^2 hybridised systems due to resonance effects when using a 532 nm laser, increasing the number of Raman scattering events. It is also very sensitive to molecular morphology of the material as every band in the Raman spectrum corresponds to a specific vibrational frequency of a bond. Therefore, the allotropes of carbon all have a different Raman signature.

The Raman spectrum of pristine diamond is composed of a single peak at approximately 1332 cm^{-1} representing the tetrahedrally bonded sp^3 hybridised carbon. When the diamond starts to become less crystalline, the peak starts to broaden and a second peak becomes apparent at $\approx$ 1600 cm^{-1} representing sp^2 hybridised carbon, known as the G peak. With increased disorder and amorphicity, a D peak might become apparent at 1350 cm^{-1} - the breathing mode of sp^2 carbon. Due to sp^2 hybridised carbon being more polarisable than sp^3 carbon, only a very small amount of sp^2 carbon needs to be present to dominate the spectrum.[165]

The many different types of fullerene also have there own distinctive Raman spectrum. C_{60} has a sharp peak at $\approx$ 1450 cm^{-1} due to having only one type of carbon bond, while C_{70}, which is much less symmetrical than C_{60}, has many more Raman active bands.[166]

Graphite has the most prominant peak at $\approx$ 1600 cm^{-1} known as the G band. Graphene has a very prominent peak at $\approx$ 2700 cm^{-1} - known as the 2D band or the G' band. These peaks can be seen in figure 2.5. The G band is an in-plane vibrational mode involving sp^2 hybridised carbon and corresponds to the high frequency E_{2g} phonon shown in figure 2.6 A). In pristine graphene, the shift of the G peak can be used to determine layer number. As layer number increases, the band shifts to lower energies due to a softening of the bonds. As with many of the properties of graphene, the band stops shifting after $\approx$ 10 layers is reached.[167] It is often impractical to use shift values by themselves as evidence of anything as they are very sensitive to a great many of factors including temperature, doping and strain in the material. It is important to note that he G mode arises from the stretching of any pair of sp^2 sites, not just limited to sp^2 rings. At $\approx$ 1350 cm^{-1}, the D band can often be observed. This band is often referred to as the defect band, represents a ring breathing mode from sp^2 hybridised carbon rings shown in figure 2.6 B). The ring must be next to a graphene

edge or defect in order to be present. A large D band relative to the G band is therefore indicative of many defects in the material.[168] The 2D band is the second order of the D band and is the result of a two phonon lattice vibrational process. It does not need to be activated by the presence of a defect. The 2D band gives information in regards to number of layers of graphene, both from its intensity and its shape.[75,169,170] This is because the resonant Raman mechanism that gives rise to it is linked to the electronic band structure, the band structure changes with the the number of layers and the layer orientation.[171]

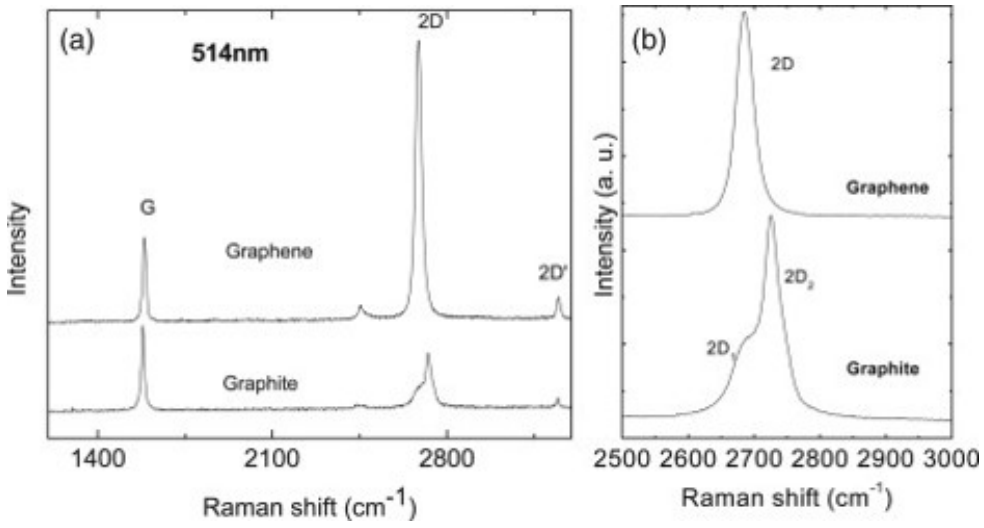

Figure 2.5: Raman spectra of graphene and graphite.[172]

For single layer graphene, the 2D band is a single symmetric peak with a full-width half maximum (FWHM) of ≈ 30 cm^{-1}. Adding successive layers to the graphene causes the 2D band to split into several overlapping peaks which interfere to form a broad, asymmetric peak in the Raman spectrum. This distinction between the 2D band shape in graphene and graphite can be seen in figure 2.5. The nature of the stacking influences the asymmetry of the peak, turbostratic stacked graphite will always have a singular, narrow 2D peak. The I_G/I_{2D} ratio is used to determine layer number for graphene while the I_D/I_G ratio is indicative of defects.[75,169,170] Pristine graphite has no D peak and a sharp G band, as crystallite size is reduced, the D peak appears and increases in intensity. I_D/I_G ratio reaches a maximum for a nanocrystalline graphite sample while still only containing sp^2 hybridised carbon rings. Further disorder would be to add in sp^2 carbon chains and sp^3 carbon into the rings, creating amorphous carbon. However, as the amount

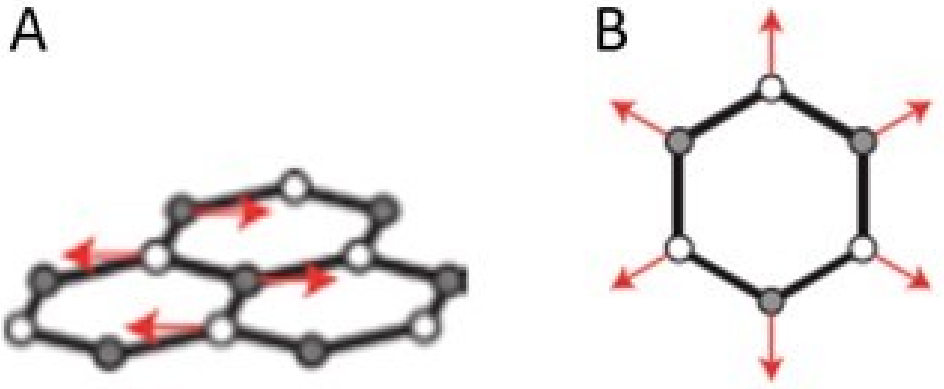

Figure 2.6: Vibrational modes giving rise to A) the G peak and B) the D peak.[171]

of carbon rings decrease, so too does the D band and I_D/I_G starts to decrease, until one very broad G band remains for amorphous carbon.

Carbon nanotubes have different Raman spectra depending on whether they are single-walled carbon nanotubes (SWCNTs), double-walled carbon nanotubes(DWCNTs) or multi-walled carbon nanotubes(MWCNTs). The Raman for SWCNTs looks very similar to that of graphite with a G band at $\approx$ 1600 cm^{-1}, a 2D band at $\approx$ 2700 cm^{-1} and a D band at $\approx$ 1350 cm^{-1}. Unlike graphite however, the D band will always be present in SWCNTs due to the disorder induced from the curved structure of the tube, more defective tubes will however have a more intense D peak. SWCNTs have a unique set of bands at sub 200 cm^{-1} known as the Radial Breathing Modes (RBM). They correspond to the expansion and contraction of the tubes.[173] The frequency of these bands can be correlated to the diameter of SWCNTs and also provide information as to the degree of aggregation. MWCNTs are similar but the RBMs are not present as the outer tubes restrict them. Typically the D band increases as the number of layers increase.[174]

Raman mapping has become a useful tool in studying carbon materials. By taking successive Raman spectra after movement of the sample by a small increment. Maps can be generated detailing where chemical features are located. This is very useful when studying heterogeneous materials so as the overall nature of the material can be determined.[175]

2.4 Microscopy

2.4.1 Scanning Electron Microscopy

In scanning electron microscopy (SEM), a focused beam of electrons are scanned across the sample. These electrons then interact with the sample and an image is generated. The nature of the interaction can vary between forming back scattered electrons (BSE) and secondary electrons (SE). SE are emitted from the sample due to excitation by the focused electron beam and are most sensitive to topography. Typically greater resolution is achieved with SE as the electrons are emitted from very close to the surface of the sample. BSE are beam electrons elastically scattered by the sample and emerge from deeper locations from the sample. BSE detection mode is best used for gaining information about the composition of the sample due to the sensitivity of BSE on atomic number.

SEM has been used extensively on carbon nanomaterials. The study of individual nanomaterials is best suited for other techniques such as transmission electron microsocpy (TEM) but for large macrostructures such as CNT bundles and forests, agglomerated graphene oxide, graphene foams and expandable graphite, SEM can give information about the macro structure and overall morphology. SEM can also be used to see individual graphene grains on a substrate, such as graphene on metals grown through CVD. Some example SEM images are shown in figure 2.7. Due to the large field of view available in SEM, an indication can be gained as to the homogeneity of any produced nanomaterial. BSE detection will give compositional information about the sample, useful for looking at residual metals which are often present in the bottom-up synthesis of carbon nanomaterials.

2.4.2 Energy Dispersive X-ray Spectroscopy

Energy dispersive X-ray spectroscopy (EDX) is the analysis of the X-rays emitted from a sample upon excitation by an electron beam. Upon excitation, a core electron can be emmitted and X - ray flourescence occurs when an electron from an outer shell moves to replace the ejected core electron. The energy of emitted X-ray is characterisitc of the atomic number of the atom it came from. EDX has therefore become a useful tool for elemental analysis identifying impurities in carbon nanomaterials and compositional

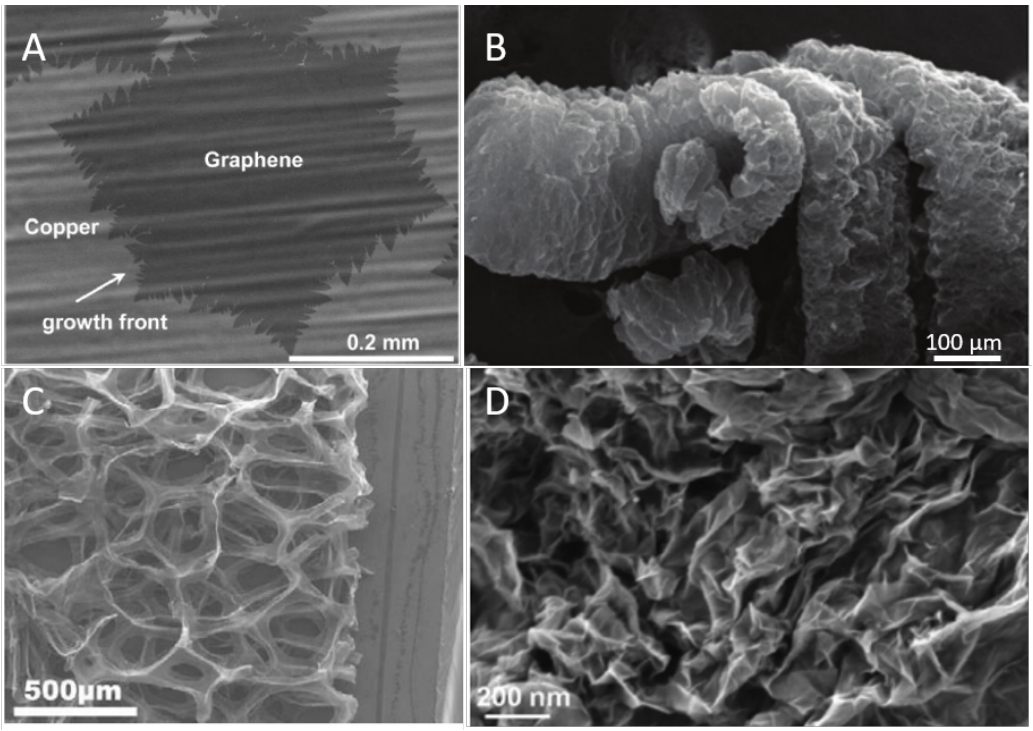

Figure 2.7: SEM images of A) CVD graphene domain on copper,[176] B) expandable graphite,[177] C) graphene foam,[178] and D) agglomerated graphene oxide.[179]

information for composite materials.

2.4.3 Transionsmission Electron Microscopy

Transmission electron microscopy (TEM) is a technique whereby a thin section of material is exposed to a high energy beam of electrons. The electrons penetrate the sample and are scattered. These scattered electron are then detected on the other side of the sample giving insight as to the structure of the material.

A limitation of this technique with carbon nanomaterials has been the high voltages required for TEM imaging, usually 80 - 200 kV. These high voltages result in substantial damage to the carbon. Despite this however, high resolution images of graphene have been obtained. A single sheet of graphene is shown in figure 2.8 B) while individual graphene layers can be seen and counted at the edge of a multi-layer graphitic sheet where it curls upwards(figure 2.8 C). Atomic resolution has also been achieved by using low-voltage aberration corrected TEM (figure 2.8 A). The technique has also been very useful for the analysis of multi-walled carbon nanotubes, where

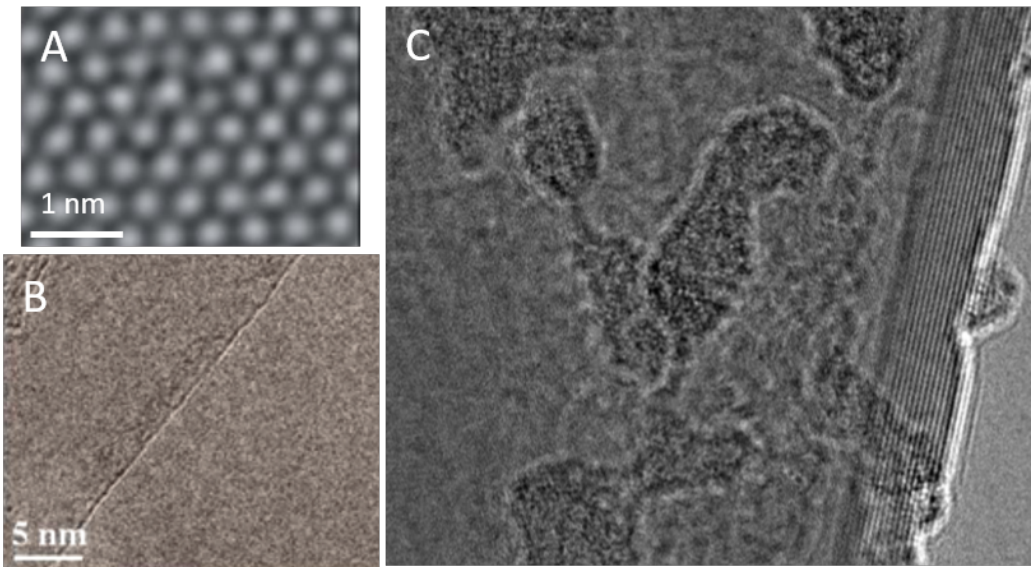

Figure 2.8: A) Atomic resolution TEM image of graphene,,[180] B) TEM image of single graphene sheet,[118] and C) TEM image of multi-layer graphene.

the number of walls can be counted, and the type of tube can be discerned.

2.4.4 Electron Energy Loss Spectroscopy

Electron energy loss spectroscopy (EELS) utilises the electrons scattered inelastically by the sample to gain chemical information. Electrons which pass through the sample causes electronic transitions to occur, therefore electrons lose the equivalent energy. By measuring the energy lost, the transitions can be deduced, these transitions are unique to different elements.[181] The technique can also be used to measure the thickness of the sample by relating it to the energy loss at different beam energies.[181]

2.5 Thermogravimetric Analysis

Thermogravimetric analysis (TGA) is the monitoring of the mass of a sample while changing the temperature. Mass plots are returned as a function of temperature or time and give an indication of the thermal stability of the material. The atmosphere that the sample is heated up in can be changed to observe the different reactivities of the material.

For carbon nanomaterials, the onset of thermal decomposition in air gives information as to the crystallinity of the carbon material, since defect sites are more prone to thermal oxidation.[182] The onset of thermal oxidation has also been shown to decrease upon exfoliation of graphite, due to the reduced interlayer interactions between exfoliated sheets and the sheets of graphite.[183] The nature of the carbon material can also be deduced from TGA by the different thermal onsets, for instance amorphous carbon burns at a much lower temperature than graphite.[184] Figure 2.9 shows this with graphite having the highest onset, graphene having a reduced onset at around 500 °C due to the reduced interlayer interactions and graphite oxide having a further reduced onset due to both reduced interlayer interactions and in plane defects. Graphite oxide has two onsets due to the presence of water between the layers burning off before the carbon burns.

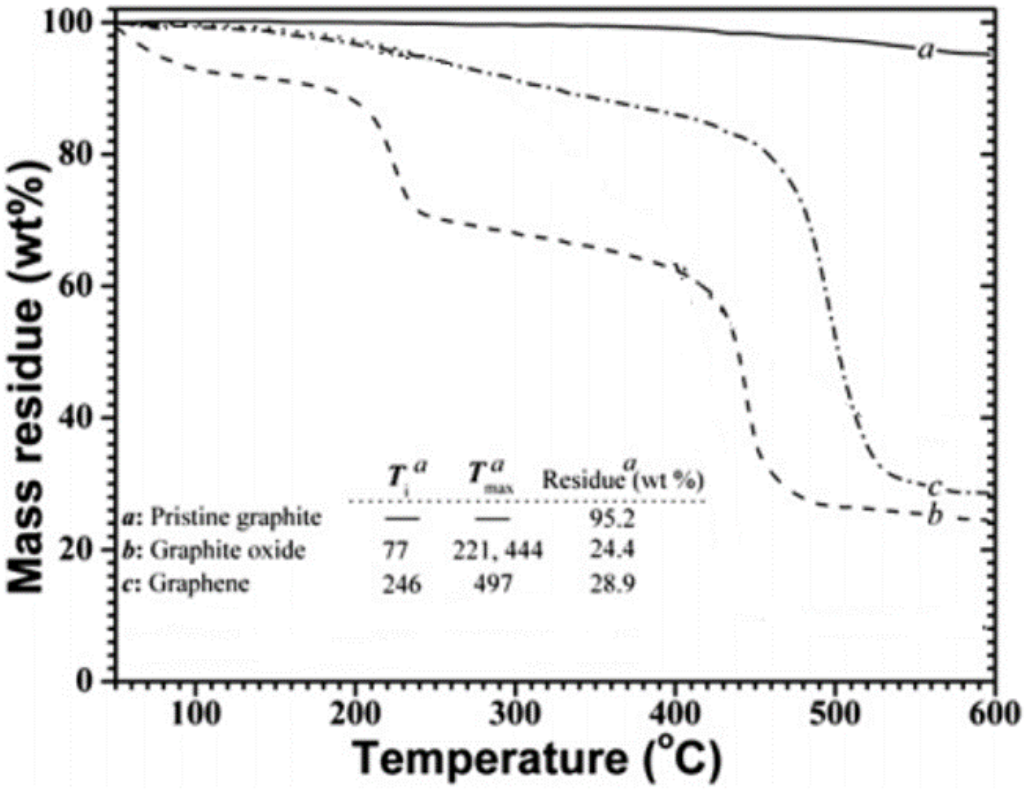

Figure 2.9: TGA curves of pristine graphite, graphite oxide and graphene and the initial degradation temperature (T_i) and the maximum mass loss temperature (T_{max}).[185]

Chapter 3

Porous Carbon Materials

3.1 Introduction

Porous carbon material is a term used to describe a host of carbonaceous materials, typically referring to high surface area carbons. This includes materials such as carbon nanotubes, activated carbon and carbon onions. The materials all make use of their high surface areas for use in many potential applications, including gas storage,[186] gas separation, as catalyst supports, supercapacitors and for use in Li-ion batteries.[44] Porous carbons are often produced through several methods. One such method is the carbonisation of biomass such as wood, shells and sugars at temperatures around 600 °C and activation usually by KOH.[187] Another method is the carbonisation of polymer resins or carbon aerogels at around 900 °C.[188,189] These tend to give very high surface area carbons with values reaching as high as 3400 m^2g^{-1}.[190]

Energy storage is an application receiving much attention at the moment. For this application, it is desirable to have both a high surface area and a high conductivity. Much work has recently been done on graphitic porous carbon due to its higher conductivity, well-developed crystalline structure, thermal stability and oxidation resistence at low temperature.[40,41] Methods to induce graphitisation have been to heat the porous carbons to around 3000 °C.[191] This is a prohibitively high temperature for many commercial applications. Also, by inducing graphitisation in this manner, there is a limitation to the carbon source that can be used. Only graphitisable carbons would be able to be graphtised in this way.[69] Recent developments have

involved catalysing the graphitisation using metal catalysts such as nickel, iron or cobalt. These are traditionally recognised as the best graphitisation catalysts due to their partially filled d-orbitals.[69] By catalysing the graphitisation, lower temperatures can be used of around 800 - 1200 °C. Also, any carbon source can be used for the initial carbon template. The most common method of catalysing the porous carbon growth is making metal-doped carbon xerogels through a sol-gel polymerisation carried out in a metal salt solution.[192–194] Other methods include pyrolysing carboxyl containing polymer particles which have undergone an ion exchange with transition metals,[40] doping saccharides with metal salts,[195] and graphitising thermoset resins based on metal organic salts.[196] Literature also exists on the metal doping of carbon aerogels to graphitise them.[197] Advantages of carbon aerogels are controlloble pore sizes, high surface areas and high conductivity attributed to its monolithic structure composed of covalently bonded small carbonaceous particles.[197,198] It has proven difficult to combine high conductivity and high surface area with developed mesoporosity.[199] The surface areas for the porous materials after graphitisation tend to be only around 200 - 600 m^2g^{-1}.[191,197,200]

Recent work has looked into making porous macrostructures or foam like materials. Porous macrostrucutres are materials which have a 3D framework and have been used in electrodes,[201,202] conducting frameworks for polymer thermosets,[135,178] and filtration/pollution control.[203,204] These applications all have the shared requirement for easily accessible pores. In applications where electrical conductivity is important, such as electrode materials, the continuous conducting network of a monolith can be more desirable than a discontinuous powder electrode.[43] Macroporous graphene is most commonly produced from either the self-assembly of graphene oxide,[153–155] or from graphene growth on a "hard" porous continuous metal template.[75,77] The popularity of graphene oxide centres on the cheap and scalable production methods. However, the oxidation and exfoliating processes introduce defects into the graphene structure disrupting the delocalised sp^2 network, adversely affecting its physical and electrical properties and decreasing its chemical stability. By contrast, the 'hard' template approach typically involves chemical vapour deposition (CVD) onto commercially available nickel foams with an average pore size in excess of 50 µm.[178,205–207] The templated CVD graphene produced typically has much higher electrical conductivity than that of graphene derived from graphite oxide, however, yields are much lower than those found in graphene oxide self-assembly routes.[38] An alternative route to graphene foams via the sintering of metal oxide particles followed by CVD has been reported.[208,209] The materials produced, although

low density and high surface area, have relatively low levels of overall graphitisation. Similarly, the sintering of metal salt crystals can also be used to produce high density graphene foams.[210]

Here we propose two methods of porous carbon synthesis. The first method for carbon foam production is a templated CVD method and the second method discussed is an attempt to remove a step in the initial process where a metal - doped dextran hydrogel is carbonised.

3.2 Synthesis of Graphene Foams from Soft Templated Metal Monoliths

3.2.1 Synthesis of Catalyst

Graphene has been synthsised on metal foils by CVD. If the metal foil is replaced with a metal foam, graphene can be grown in a foam like structure to closely follow the macrostructure of the underlying metal. The difficulties of this process are having the graphene hold its shape once the metal foam is removed and also ensuring that the metal foam can catalyse graphene growth. The metal foils typically used for graphene growth are highly polished with very large domains. This is harder to achieve for metal foams. The metal foams used here were synthesised by heating metal/dextran hydrogels in air to form metal oxide foams. This metal oxide foam was then reduced *in situ* during the CVD process, allowing the metal to catalyse graphene growth, as shown in figure 3.1. Unlike graphene growth on hard metal foams, the soft-templated metal framework procedure described herein requires no cleaning of the metal substrate prior to use, works at atmospheric pressure and has a low sensitivity to changes in conditions.

This is the first time that a soft-templated metal framework has been employed for the CVD synthesis of graphene.

The formation of porous metal frameworks by templating has long been an area of study for those working in the fields of catalysis, filtration and electrochemistry.[211–216] Such materials can be produced by a variety of routes involving either soft or hard templates.[217,218] The use of so-called soft templates was first developed by Mann *et al*,[212] who demonstrated that dextran hydrogels could be used as sacrificial templates for production

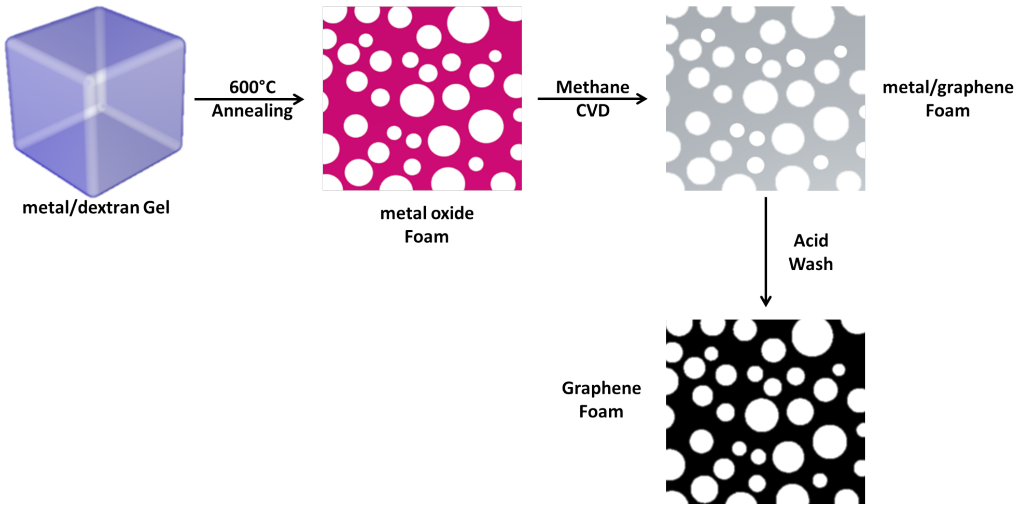

Figure 3.1: Scheme showing the process of growing graphene from a metal/dextran gel.

of copper oxide, silver and gold metal monoliths.[211] The principle advantages of soft-templating include the facile, scalable and benign nature of the chemistry used. In addition, soft-templating can offer a degree of control over the macrostructure properties including mechanical strength and pore size.[212,219,220]

Four different metal foams were synthesised: Copper, nickel, cobalt and iron. Nickel and copper are very commonly used catalysts for graphene synthesis but operate by different mechanisms. Copper is typically considered the best graphene catalyst as it operates via a surface mechanism and is therefore often self-limiting to monolayer graphene.[66] However, this means it is very sensitive to surface morphology and typically undergoes an extensive polishing prior to CVD,[221] it therefore might not be suitable as a foam template. Nickel, cobalt and iron have all being used for graphene synthesis.[70,222] Cobalt and iron less so than nickel, but they all have had extensive use catalysing other carbon materials such as carbon nanotubes and carbon nanofibers.[223–226] They all operate through a bulk mechanism whereby the carbon dissolves into the catalyst.[73] This makes precise control of layer number more challenging but it should be less sensitive to surface morphology and therefore better suited to the synthesis on foams.

The metal/dextran hydrogels were synthesised according to a modified procedure first outlined by Mann *et al.*[212] They synthesised copper ox-

ide, silver and gold foams. The method was adapted for the synthesis of copper oxide, but modified so as to synthesise cobalt, nickel and iron oxide foams. Briefly, metal salt was dissolved into water followed by addition of the surfactant Triton X-45. This solution was then combined with a highly concentrated dextran solution. This mixture was then stirred at 60 °C for 30 minutes. The resulting gel was then allowed to age for 4 days prior to use. A photo of the metal gels are shown in figure 3.2

Dextran is used as a sacrificial template for the formation of porous metal oxide structures. Dextran is chosen due to its large water solubility allowing its dissolution into more concentrated metal solutions and therefore resulting in larger metal loadings in the metal hydrogels. Dextran also contains reductive aldehyde groups which will reduce the metal ions.[211] The amount of metal in each of the gels was determined by ICP-OES and was shown to be 3.80%, 4.11%, 5.47% and 4.59% for iron, nickel, copper and cobalt respectively. The hydrogels were then annealed at 600 °C in air in order to create metal oxide foams. This dehydrates the gel and then subsequently burns off the dextran. During this process the metal salt is oxidised and forms a continuous metal oxide monolith. SEM images of the structures are shown in figure 3.3.

The SEM images clearly show a porous structure with pore size of approximately 20 µm for the cobalt oxide and copper oxide foams (figure 3.3 top left and right respectively). Although still macroporous, this is an order of magnitude smaller than those of commercial nickel foams which have pore

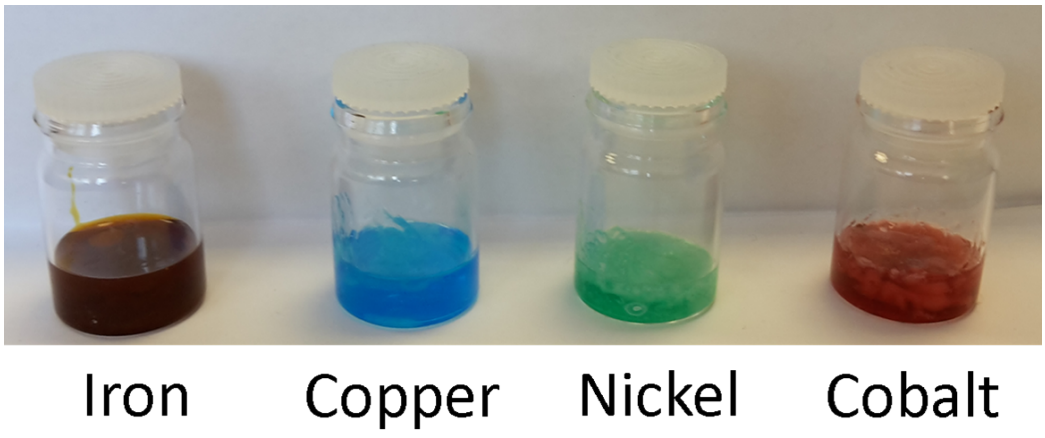

Figure 3.2: Photo showing the dextran/metal salt gels.

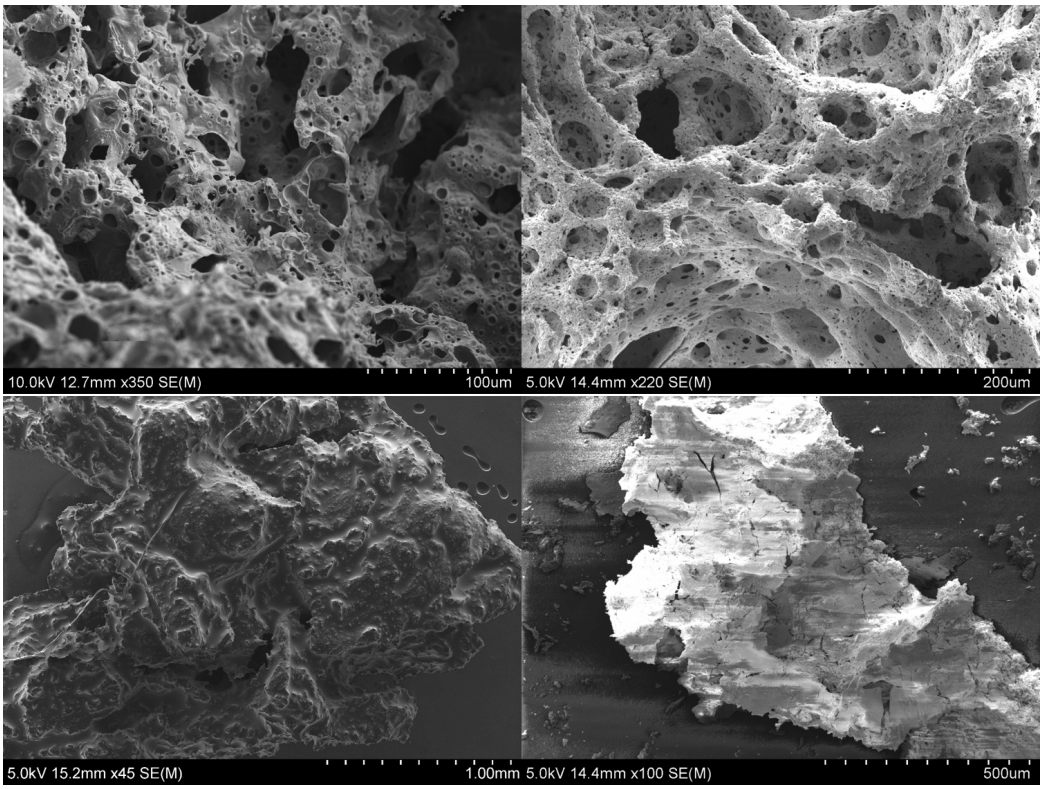

Figure 3.3: SEM images of (top left) cobalt oxide, (top right) copper oxide (bottom left) nickel oxide and (bottom right) iron oxide. Images taken at 10.0 kV, 5.0 kV, 5.0 kV and 5.0 kV respectively using the SE detector.

sizes in excess of 100 µm. It is believed that the pores originate from the controlled outgassing of CO_2 bubbles into the viscous surfactant matrix.[212] One of the advantages of this soft templating method to a metal foam is that there are numerous adaptations to both increase and decrease the pore sizes in the structure.[212] The nickel oxide and iron oxide (figure 3.3 bottom left and right respectively) show a much more closed structure. It appears that the synthesis did not work nearly as well for these materials as the foams were much less monolithic than the cobalt and copper material, appearing more like a powder than a foam.

In order to prove that the porous structure would be retained upon reduction of the metal oxide foam. A test run was conducted where no carbon source was added and the metal oxides were reduced to elemental metal. The metal oxides were heated to 1000 °C in a hydrogen/argon atmosphere. Images of the resulting structures are shown in figure 3.4. It appears that the pore

size decreases upon reduction to the metal for the cobalt metal where pore size is around 5 µm (figure 3.4 (top left)). The pore size remains consistent for the copper at around 20 µm (figure 3.4 (top right)). The nickel and iron structures are opened up after the heat treatment and some porosity can be observed (figure 3.4 (bottom left and right respectively)). Grain boundaries are clearly visible in the polycrystalline cobalt structure.

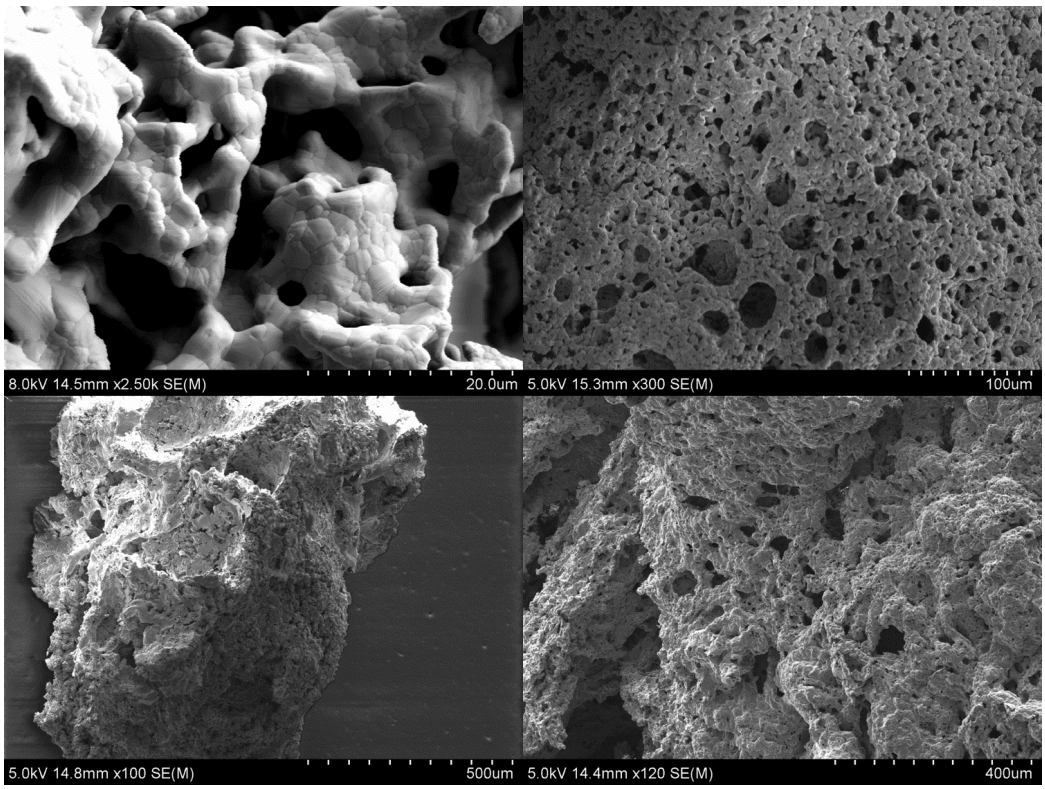

Figure 3.4: SEM images of the metal oxide after being heated to 1000 °C in a reducing atmosphere. (top left) cobalt, (top right) copper, (bottom left) iron and (bottom right) nickel. Images taken at 8.0 kV, 5.0 kV, 5.0 kV, and 5.0 kV respectively using an SE detector.

3.2.2 Synthesis of Graphene

A conventional atmospheric pressure methane CVD was performed on the metal oxide foams. The metal oxide foams were placed in an alumina boat inside a quartz furnace tube inside a furnace. The foams were then heated

to 1000 °C in an argon/hydrogen atmosphere. At 1000 °C, methane is briefly introduced into the gas stream. The system is then allowed to cool under just argon and hydrogen. A schematic of this process is shown in figure 3.5.

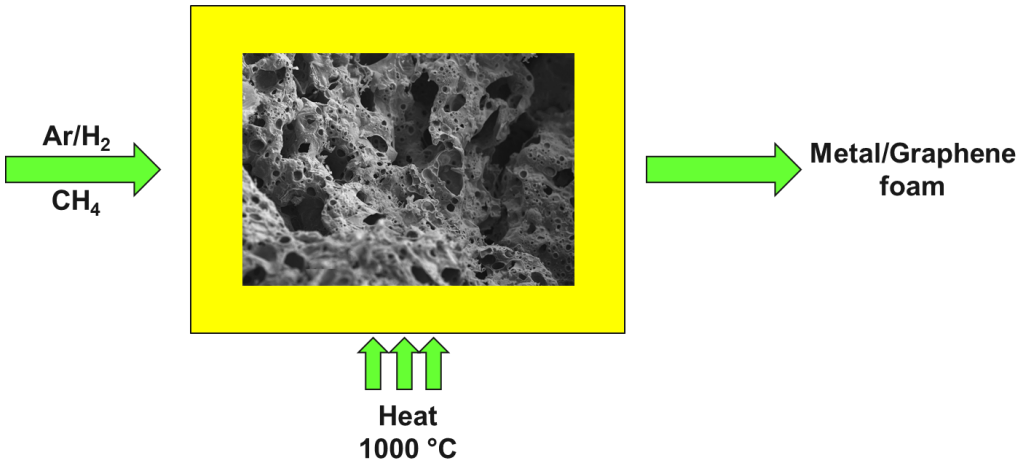

Figure 3.5: Scheme showing the CVD set up of growing graphene on the metal oxide foams. Inside the furnace is an SEM image of cobalt oxide foam.

The CVD process was performed with all the different metal foams to produce copper graphene foam (CuGF), nickel graphene foam (NiGF), iron graphene foam (FeGF) and cobalt graphene foam (CoGF) . The materials taken out of the furnace were small and fragile macroporous foams. In the case of the metals nickel and iron; carbon from the methane precursor is thought to dissolve into the metal forming a solid solution and then precipitate upon cooling.[78] Graphene has been shown to form this way with nickel,[78] and the same mechanism is thought to apply to cobalt due to similar solubility of carbon in both the nickel and cobalt.[70,107] With copper, the mechanism is thought to be limited to the surface as the methane dissociates into carbon and graphene forms on the surface of the copper. This was discussed in section 1.4.1. SEM images were taken to get an idea of the structure of these foams (figure 3.6). Two images are displayed for each of the different metal/graphene foams. Cobalt, (figure 3.6 (A) and (B)) nickel,(figure 3.6 (E) and (F)) iron (figure 3.6 (C) and (D)) and copper (figure 3.6 (G) and (H)) The size and stability of the foams produced varies across the metals. Cobalt, (Figure 3.6 (A) and (B)) nickel,(Figure 3.6 (E) and (F)) and copper (Figure 3.6 (G) and (H)) showed stable and large porous structures, while iron (Figure 3.6 C and D) was observed to be the least stable, both in handling where it would crumble to a powder and on both visual observation

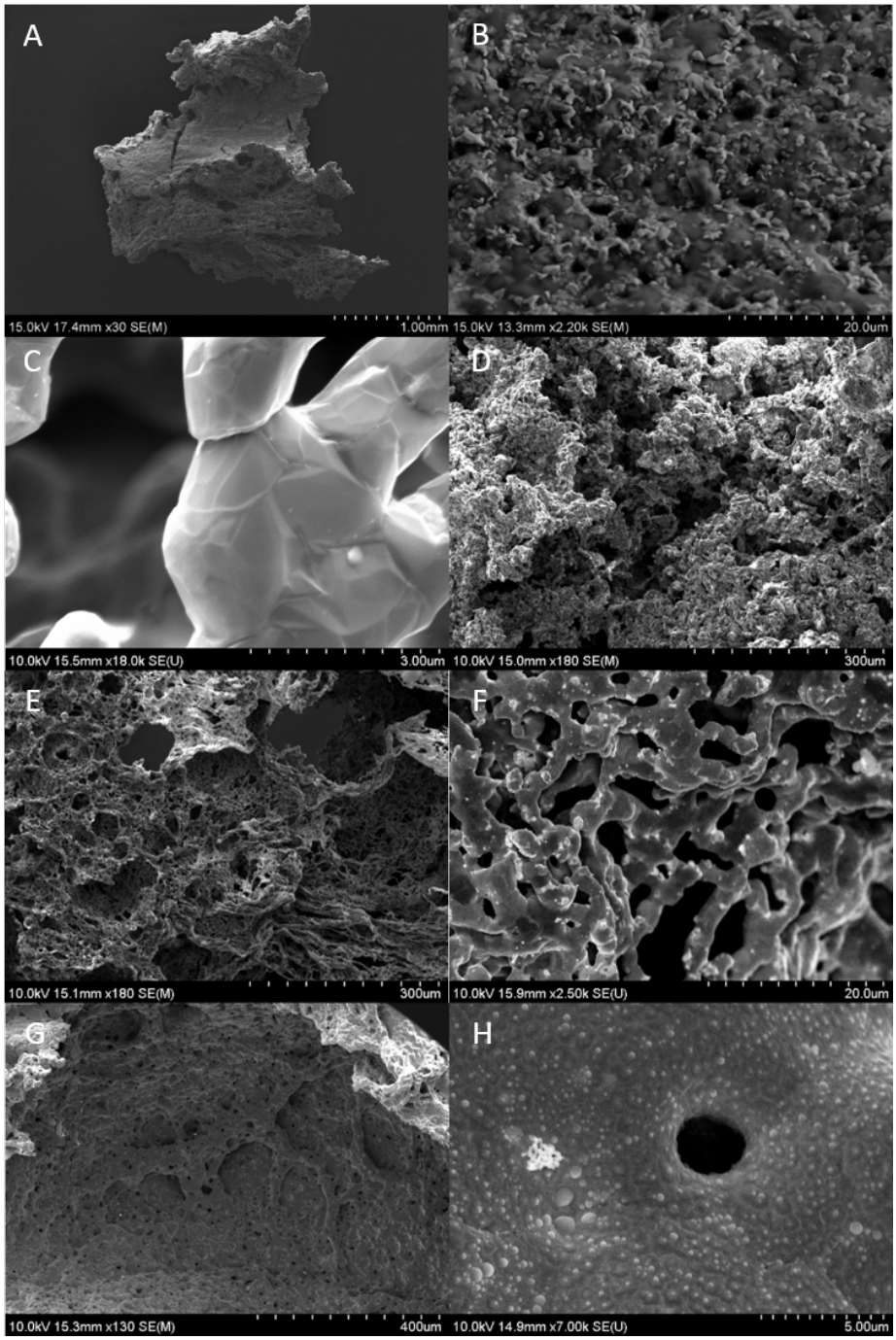

Figure 3.6: SEM images of the material produced after CVD on the metal oxide foam. A) and B) cobalt derived material. C) and D) iron derived material. E) and F) nickel derived material. G) and H) copper derived material. Images taken at 15.0 kV for the CoGF and 10.0 kV for the other materials using the SE detector.

and in the SEM. This is in contrast to the other metal/graphene foams in which large macrostructures a few millimeters in size could be handled without breaking. The CuGF, NiGF and CoGF were open pore structures with a pore size of approximately 2 microns. The copper had a much lower pore density than the other metals.

The CoGF, FeGF and NiGF show regions of two distinct contrasts in the SEM. There are many reasons why varying contrast can occur in an SEM but a common one is differing elements. An EDX map was taken of the CoGF to determine the origin of the different contrasts. The map is shown in figure 3.7. Cobalt was detected through out the sample, so a map was taken to display carbon intensity. It can be clearly seen that there are regions of more carbon (red) and regions of less carbon (green) in the sample. These can be attributed to differing layer numbers of the graphene/graphite produced in the sample. The high contrasting material in the SEM images is the cobalt.

Raman was taken determine the quality of carbon produced on each of the samples. Copper was by far the worst quality of carbon produced. The Raman spectrum for the CuGF is shown in figure 3.8 The Raman spectrum contains the characteristic peaks for graphitic material with a G band at 1577 cm^{-1}, a 2D band at 2695 cm^{-1} and a D band at 1346 cm^{-1}.[167] The G band originates from in-plane vibrations of sp^2 hybridised carbon atoms and the 2D is a second order of the D band and provides information about

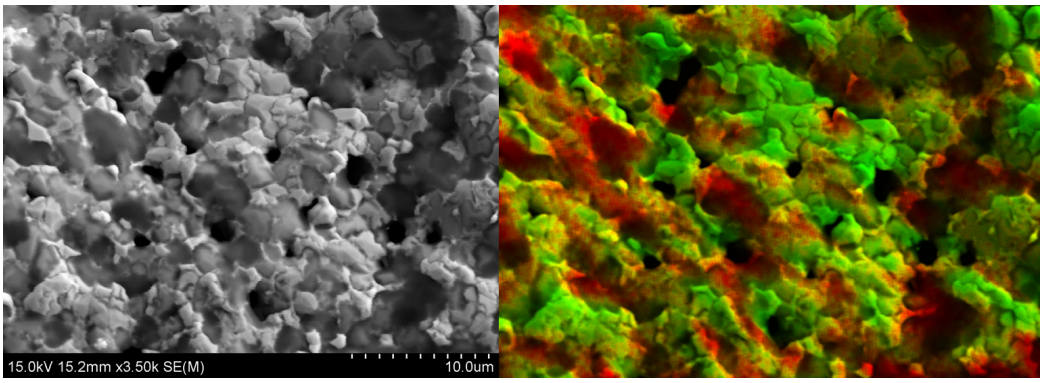

Figure 3.7: (A) SEM image of the cobalt graphene foam (CoGF) pre-acid wash and (B) carbon intensity EDX map showing regions of high carbon signal (red) and low carbon signal (green). Images taken at 15.0 kV with the SE detector.

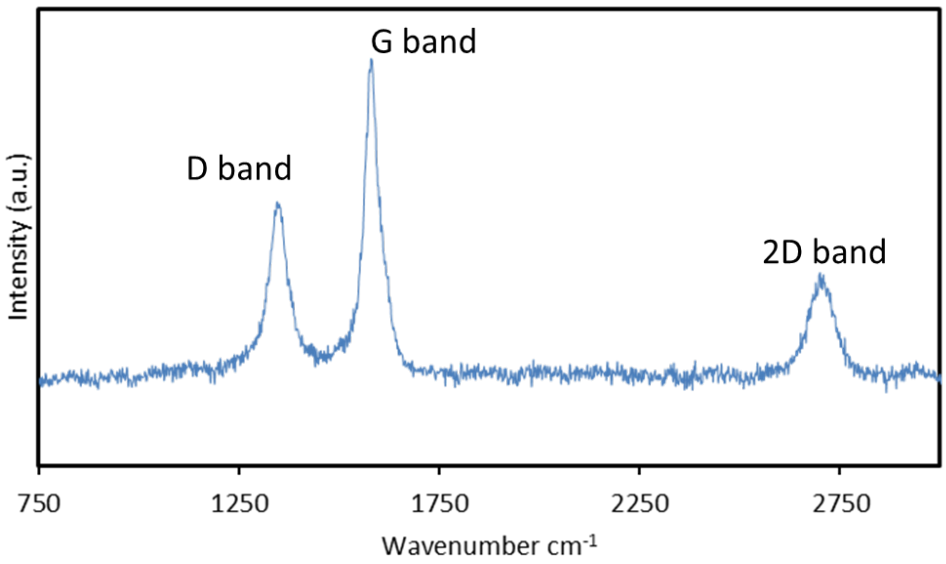

Figure 3.8: Raman spectrum of the CuGF.

layer number. The D band is often due to defects or nanocrystalline domain sizes.[168] Using the equation:[227]

$$L_a(nm) = (2.4 \times 10^{-10})\lambda^4(\frac{I_D}{I_G})^{-1} \tag{3.1}$$

where La is average crystallite size, λ is laser excitation wavelength and I_D/I_G the ratio of intensities of the D and G band. The average crystallite size of the graphene on the copper foam was found to be 42.5 nm (SD = 8.4), averaged over 307 spectra. A histogram of this data is shown in appendix A figure 8.1. The very small domain size of graphene on the copper is unsurprising. Graphene growth on copper typically requires the foil to undergo an intensive pre-treatment, often with a mixture of mechanical and electrochemical polishing.[228] The pre-treatment has been proven to improve the domain size of the synthesised graphene. Copper catalyses the growth of graphene via a surface mechanism, this makes the growth much more sensitive to surface roughness and curvature. It is likely that copper is not suitable for the growth of graphene foams. The formation of highly defective graphene/graphitic material is likely to be as a consequence of the surface roughness and poor crystallinity of the underlying 3D copper catalyst

monoliths.

Raman spectra of the material grown on the Ni, Co and Fe is shown in figure 3.9. Interestingly no D band was observed with the other metals. This suggests that the material is much less defective or has larger domain sizes than that of the material grown on the copper. As the EDX map in figure 3.7 shows, the carbon was not uniform. Raman maps were therefore taken of the samples in order to get a clear indication on the homogeneity of the material.

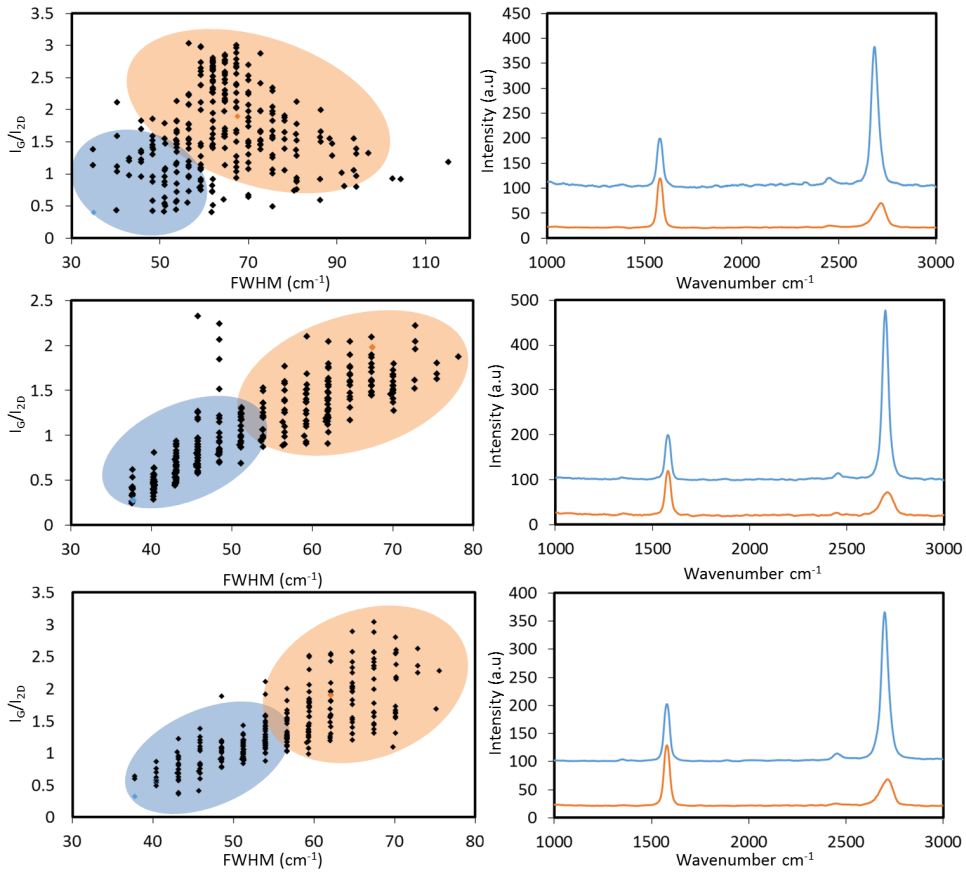

Figure 3.9: Scatter plots of I_G/I_{2D} ratio vs FWHM of the 2D peak for (A) NiGF, (B) FeGF and (C) CoGF. Adjacent the scatter plots are individual spectra of the coloured points from the scatter plots. The orange and blue regions give a rough indication of >3 layer material and 1 - 3 layer material respectively.

Figure 3.9 shows scatter plots of I_G/I_{2D} vs FWHM of the 2D band for the NiGF, CoGF and FeGF taken for approximately 300 spectra for each. Copper is not included as it is a much less crystalline, although more uniform so provides a less informative scatter plot when compared to the other metals. The 2D band is a second-order overtone of the in-plane vibration, D. It has been shown that for CVD graphene there is a correlation between the ratio of the intensities of the G and the 2D band (I_G/I_{2D}) and graphene layer number.[75,169,170] The maps show that there are a range of values for the FWHM and the I_G/I_{2D} ratio and therefore a range of layer numbers. A I_G/I_{2D} ratio of approximately 0.2 - 1.3 suggest a graphene layer number of 1 - 3 layers respectively. FWHM of the 2D peak also gives a rough indication of layer number. FWHM's of around 40 cm $^{-1}$ suggest 1 - 2 layers. The FWHM increases largely for 3 layers to around 70 cm $^{-1}$. The scatter plots were divided into two regions, areas of 1 - 3 layers (blue) and area of greater than 3 layers (orange). Representative spectra of the two regions are shown on the right hand side. All three metals show a mixture of thick and thin graphene as agreed by the EDX in figure 3.7. The NiGF had the widest variety in material and doesn't show the linear relationship between I_G/I_{2D} and FWHM which would be expected as both correlate to layer number. The CoGF and the FeGF both show a large proportion of few-layer graphene (1-3 layers). The heterogeneity of the graphene thickness could be due to the increased precipitation of carbon at grain boundaries in the metal foam.[229] This has been observed with metals such as nickel on foils. Another reason for the heterogeneity in the material could be due to growing on a foam. The irregularity of the foam will mean that different parts of the foam will experience a different flow profile than other regions of the foam and therefore a different material would grow. The results suggest that the material grown here is of similar crystallinity to other groups growth via CVD and much more crystalline than the material produced through the other methods of graphene/graphite production. Other groups have demonstrated the production of graphtie in addition to graphene on nickel foams,[207] but no other group has mapped their graphene and so it is hard to deduce the homogeneity of the different materials.

A more clear comparison of the different materials synthesised on the different metals can be observed in the histogram in figure 3.10 showing the frequency of different I_G/I_{2D} ratios. Copper clearly showed the worse material with a very small 2D band. Nickel had a very broad distribution of I_G/I_{2D} ratios with still a large proportion of graphite. Cobalt and iron show a large proportion of very thin material but since cobalt held the foam like structure much better than the iron, CoGF will be the focus for the rest

of the analysis. The conditions chosen for this CVD are based on a large quantity of literature which all come to differing conclusions on the optimum set of conditions. It is coincidental that the conditions chosen are best suited for iron and cobalt over nickel. An alternative set of conditions likely exist in which nickel gives the thinnest, most uniform material.

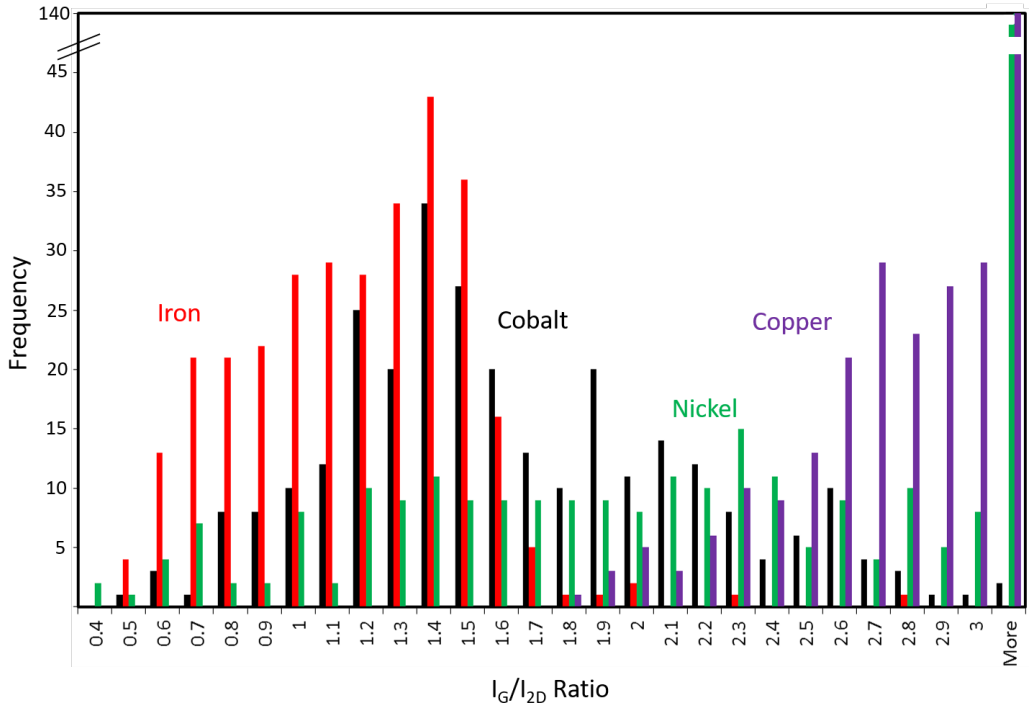

Figure 3.10: Histogram displaying the frequency of different I_G/I_{2D} ratios for each of the metals.

TGA was also taken of the materials to gain further insight into how graphitic the structure is (figure 3.11). By looking at the onset of when the material starts to burn in air, information is gained on the quality of the carbon. The high onset of the NiGF, CoGF and FeGF materials (700 - 800 °C) is further evidence of their graphitic structure. The low onset of the CuGF is also in agreement with the Raman in suggesting a less graphitic material. Generally, owing to their crystallographic order, graphitic carbons are more stable against air oxidation than amorphous carbons.[182] The rises in mass observed are likely due to the oxidation of metals.

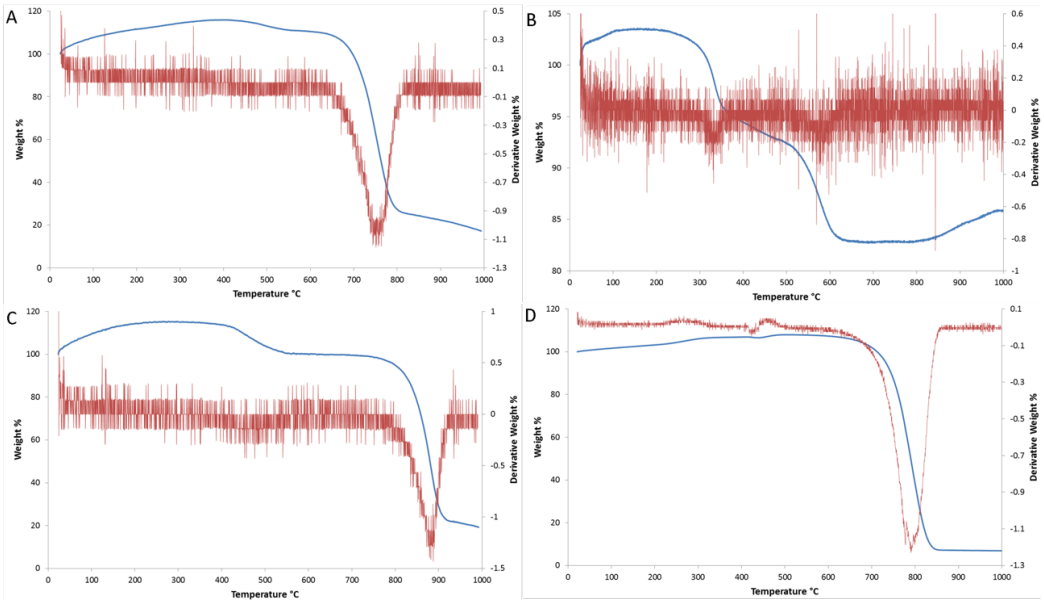

Figure 3.11: TGA (blue) and first derivative plots (red), recorded in air from ambient to 1000 °C at 10 °C min^{-1} of (A) iron graphene foam, (B) copper graphene foam, (C) nickel graphene foam and (D) cobalt graphene foam showing onsets at 675 °C, 303 °C, 816 °C and 715 °C respectively.

XRD was also taken of the graphene/graphite grown on the different metals and is shown in figure 3.12. The XRD for the NiGF, CoGF and FeGF show the peaks associated with graphite including the peak arising due to the interlayer spacing, the (002). This is to be expected as despite the large amount of graphene in the sample, the graphite will dominate giving the sharp (002) peak. The CuGF material gave no discernible graphite peaks due to non-crystalline nature of the material.

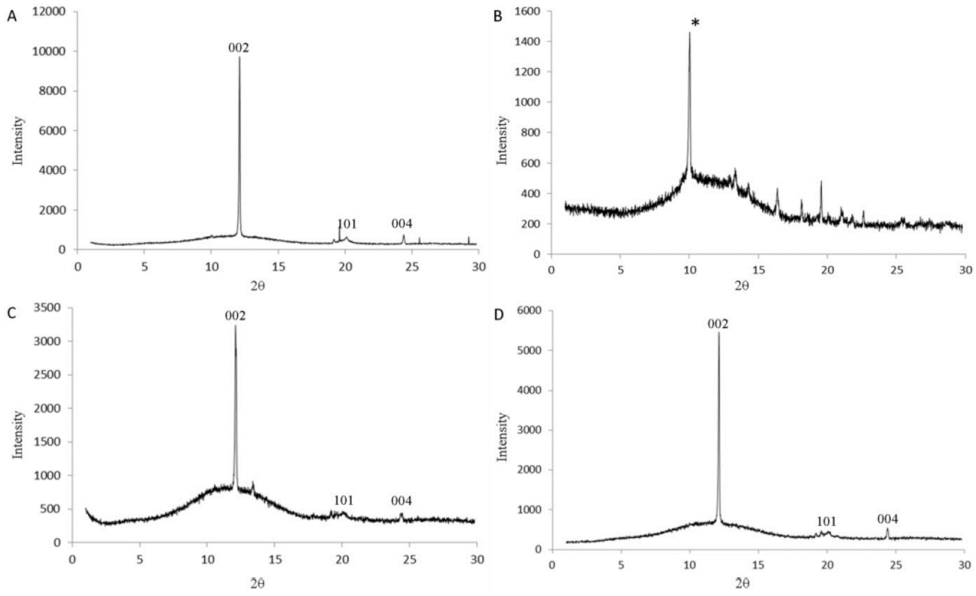

Figure 3.12: PXRD patterns of (A) iron graphene foam, (B) copper graphene foam, (C) nickel graphene foam and (D) cobalt graphene foam; showing the characteristic peaks for graphitic carbon of (002), (101) and (004). Mo Kα1,2 Xray source, $\lambda = 0.7093$ Å.

The CoGF was washed in 6 M HCl for 4 days to remove the cobalt metal. SEM images were then taken of the post washed material and are shown in figure 3.13. Figure 3.13 (A) shows that the macrostructure was preserved upon removal of the cobalt. Figure 3.13 (A) and (B) show that the pore structure was retained with pore sizes of 1 - 2 microns. Figure 3.13 (B), (C) and (D) show numerous graphene sheets on top of each other and that the graphene material is very sheet like while (B) and (D) shows that the sheets are wrinkled. Wrinkles are thought to be present due to the difference in thermal expansion coefficients of the cobalt and the graphene.[230] The high level of transparency observed for the graphene material in the SEM images suggests that the sheets are very thin. BET surface area measurements of the 3D graphene foam grown on cobalt gave values between 60 and 120 m^2 g^{-1}. EDX spectra was taken over the entirety of figure 3.13 A and showed no cobalt present (appendix A figure 8.2) although TGA for the CoGF showed some residual mass most likely due to cobalt oxide (figure 3.11).

To gain further information on the graphene sheets making up the macroporous structure, the CoGF was bath sonicated in N-methylpyrolidone

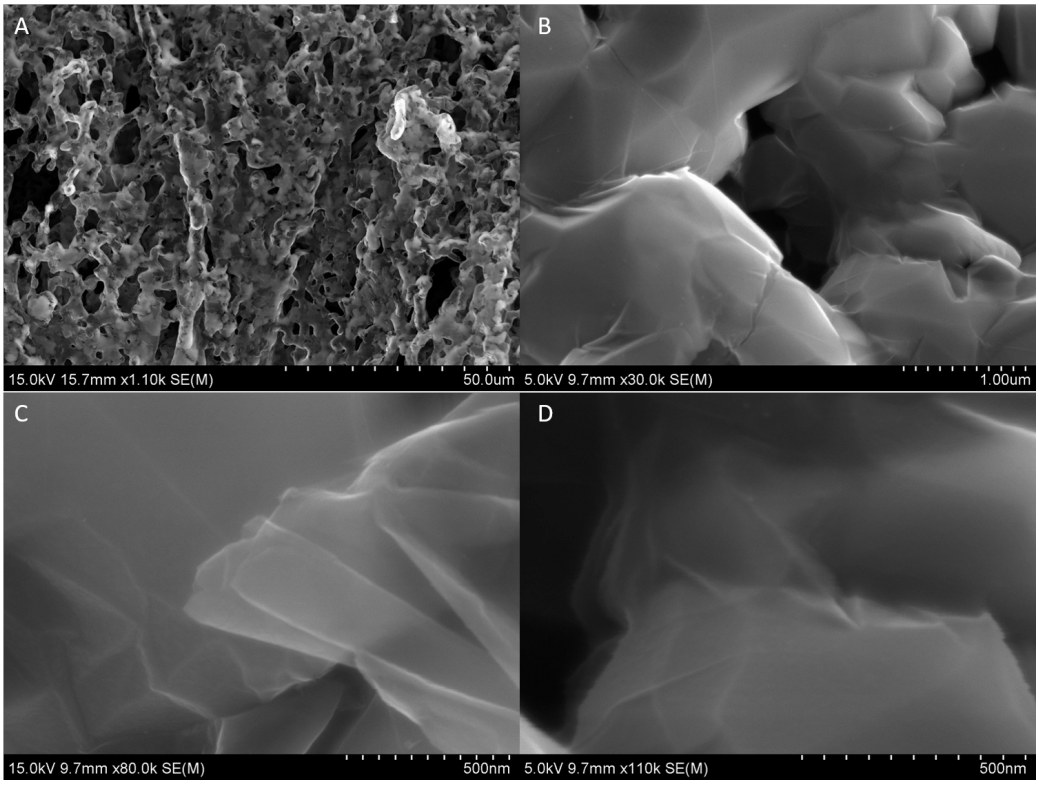

Figure 3.13: (A)–(D) SEM (SE) images of the cobalt graphene foam (CoGF) after HCl wash

(NMP) to break up the monolitihic structure and then dropped onto lacey carbon TEM grids. These images are shown in figure 3.14. The material was shown to be thin and entirely graphene like, with no other carbon based structures present. In agreement with the Raman and SEM data, the graphene sheets were observed to be single (figure 3.14 (B)) and multi-layerd (figure 3.14 (C). Figure 3.14 (D) shows a frequency histogram of the distribution of single- few- and multi-layer sheets observed in the TEM. The normal-incidence selected area electron diffraction (SAED) pattern (figure 3.14 (F) taken from the marked region in figure 3.14 (E) shows the typical six-fold symmetry for graphene with reflections, at 0.212, 0.123 nm which correspond to the $(0\bar{1}10)$ and $(1\bar{2}10)$ indices respectively.[9] The multiple hexagonal patterns present suggest a number of graphene sheets are lying on top of each other. Three sets of spots are clearly visible in the diffraction pattern indicating that three sheets are stacked on top of each other, the offset of the spots relative to the most intense shows that the second and third sheet are

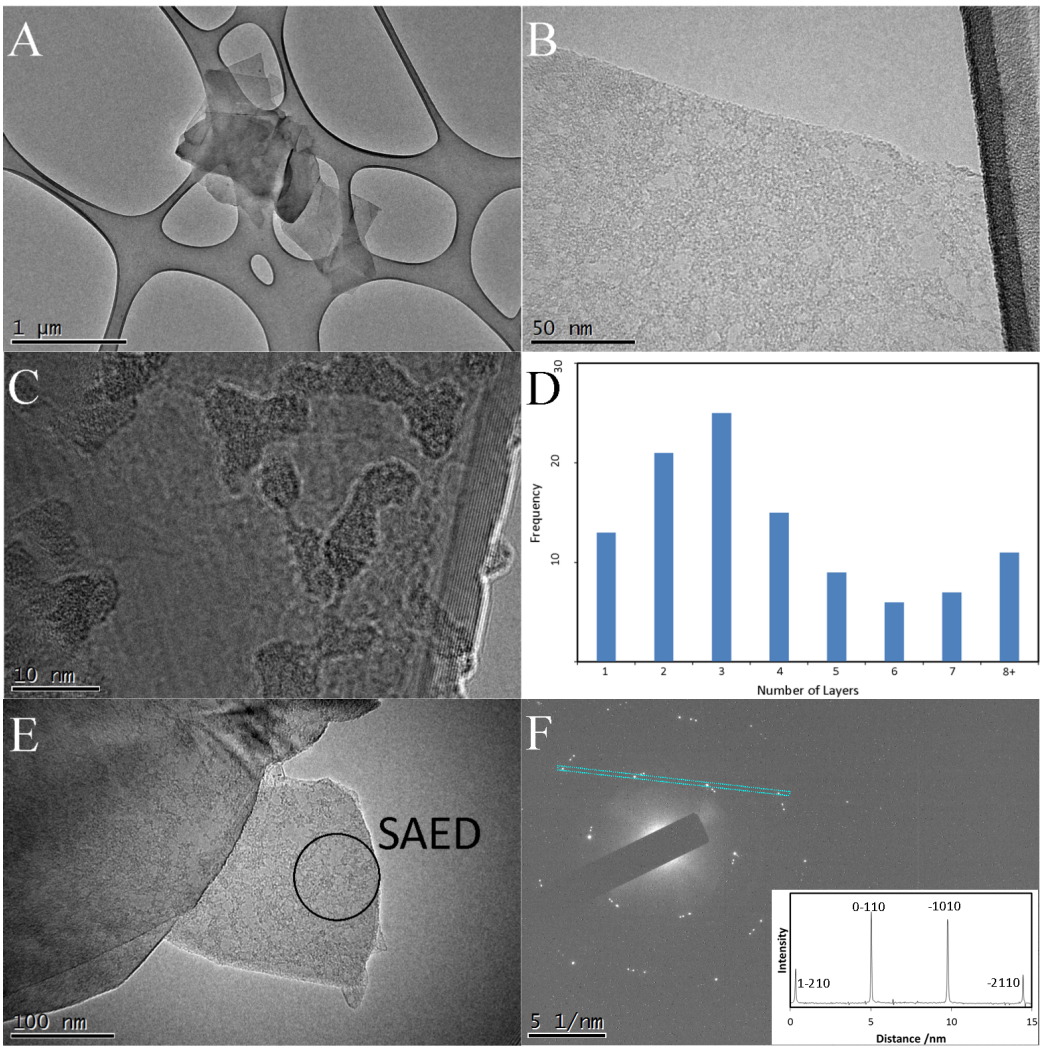

Figure 3.14: (A) Low magnification TEM image of graphene sheets from the cobalt graphene foam (CoGF). (B) HRTEM image of a single graphene sheet. (C) HRTEM image of a multi-layer graphitic sheet. (D) Histogram of the number of layers observed for the graphene in the TEM across 107 images. (E) TEM image of graphene and the region where the SAED pattern was taken. (F) SAED from region shown in (E) and intensity profile inset.

rotated approximately 5° and 7° respectively. The intensity of the dominant reflections can be used to provide information on any stacking that may be present. Previous studies have shown that for few-layer graphene and graphite with Bernal (AB) stacking the intensity ratio of $\frac{I_{1100}}{I_{2110}}$ is less than 1, whereas monolayer graphene $\frac{I_{1100}}{I_{2110}}$ is greater than 1.[9,137] The intensity profile (figure 3.14 (F) inset) shows that the intensity of the $(0\bar{1}10)$ and $(\bar{1}010)$ are significantly greater than $(1\bar{2}10)$ and $(\bar{2}110)$, indicating monolayer graphene. Sheet resistance of filter cakes of the CoGF were measured across 3 different films using the four-point-probe method and were found to be between 500 - 600 Ω sq $^{-1}$ across several samples for an approximately 120 µm thick films and is comparable to other synthetic graphene materials.[231] SEM images proving sample thickness is shown in appendix A figure 8.3.

3.3 One-step Synthesis of Graphitic Foams

In order to try and make the synthesis of graphitic foams more efficient, a step was removed from the process described above. Once the dextran/metal gel had been synthesised, rather than anneal it in air to produce the metal oxide foam, the dextran/metal gel was heated in a reducing atmosphere. The idea was that the reducing atmosphere might generate a metal foam which can catalyse graphitic carbon growth while dextran can act as the carbon source. Dextran should be an effective carbon source as many sugar materials have been used to grow graphitic carbon.[195,232] The graphitic foams were then washed in HCl to remove the metal catalyst. This is most similar to the work carbonising metal - doped xerogels.[192–194] All four metal-dextran hydrogels were carbonized in addition to a dextran hydrogel with no metal present. This was done in order to ascertain the effect of metal in catalysing the formation of graphitic carbon.

After the heat treatment, black foam like structures were pulled from the furnace and then analysed by SEM. The material with no metal present is shown in figure 3.15 in a photo and SEM image. The photo shows a glossy and brittle glassy carbon monolith while the SEM image shows very large macro pores. The copper, iron and nickel based carbon materials are shown in figure 3.16 rows 1 - 3 respectively. Figure 3.16 is split into three columns. Column 1 shows SEM images of the unwashed foam structure pulled straight from the furnace for the three different metals. Column 2 shows the results of mixing the BSE and SE signals on unwashed material

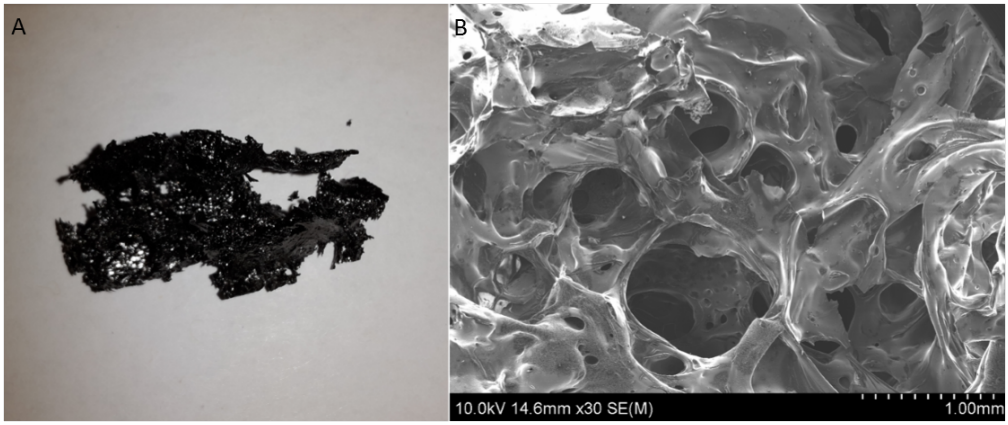

Figure 3.15: (A) Photo and (B) SEM image of carbonized hydrogel with no metal present. Image taken at 10.0 kV with the SE detector.

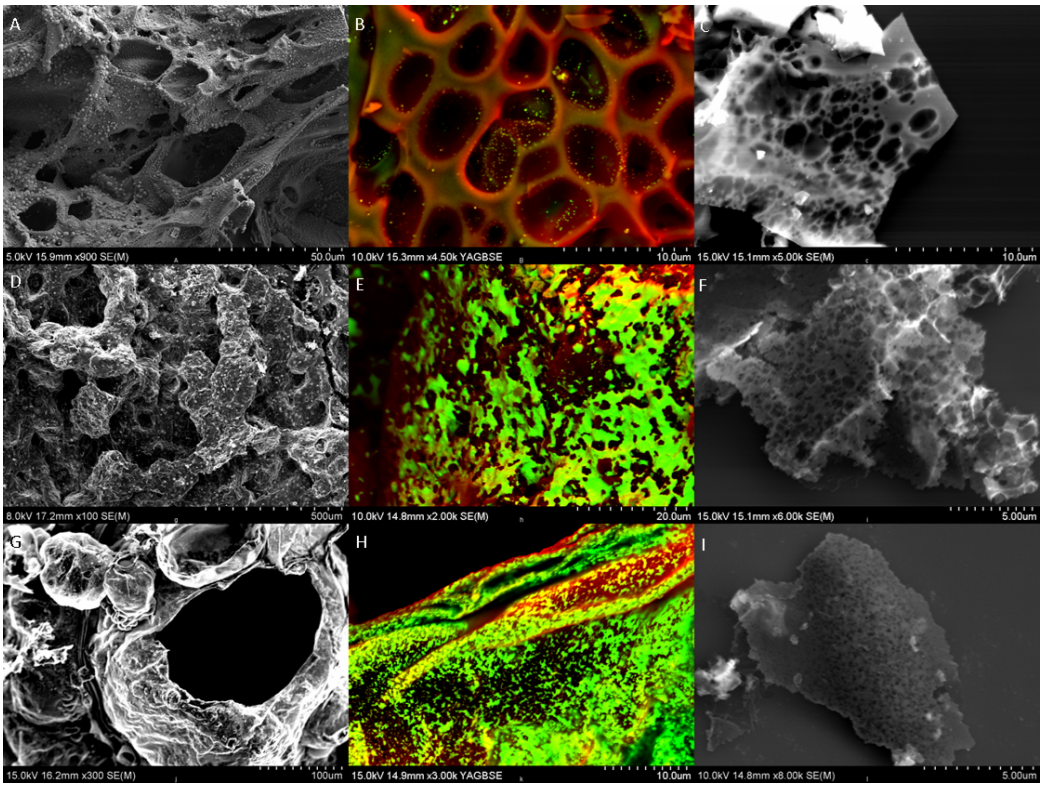

Figure 3.16: SEM images of the post carbonized material. Lines 1 - 3 showing the copper, iron, and nickel material respectively. Column 2 is the a mixture of SE (red) and BSE (green) signals and column 3 shows the material having undergone an acid wash. Images in columns 1 and 3 were taken with the SE detector while images in column 2 was taken using both the SE and BSE detector. Images taken at a range of accelerating voltages from 5.0 kV to 15.0 kV.

with metal (high BSE signal) shown in green and carbon (high SE signal) shown in red. The images clearly show the metal intermixed with the carbon sheets, this is in agreement with column 3 displaying the post acid washed material. The removal of the metal results in pores and voids appearing in the carbon sheets. After acid washing all the macrostrucutre of the foams was lost and the material collapsed into a powder.

The cobalt based material (figure 3.17), still retained some large foam monoliths after the acid wash. These foam monoliths were very fragile and break under pressure. It is clear that the metal particles are vital in holding the structure together. The cobalt derived material showed the

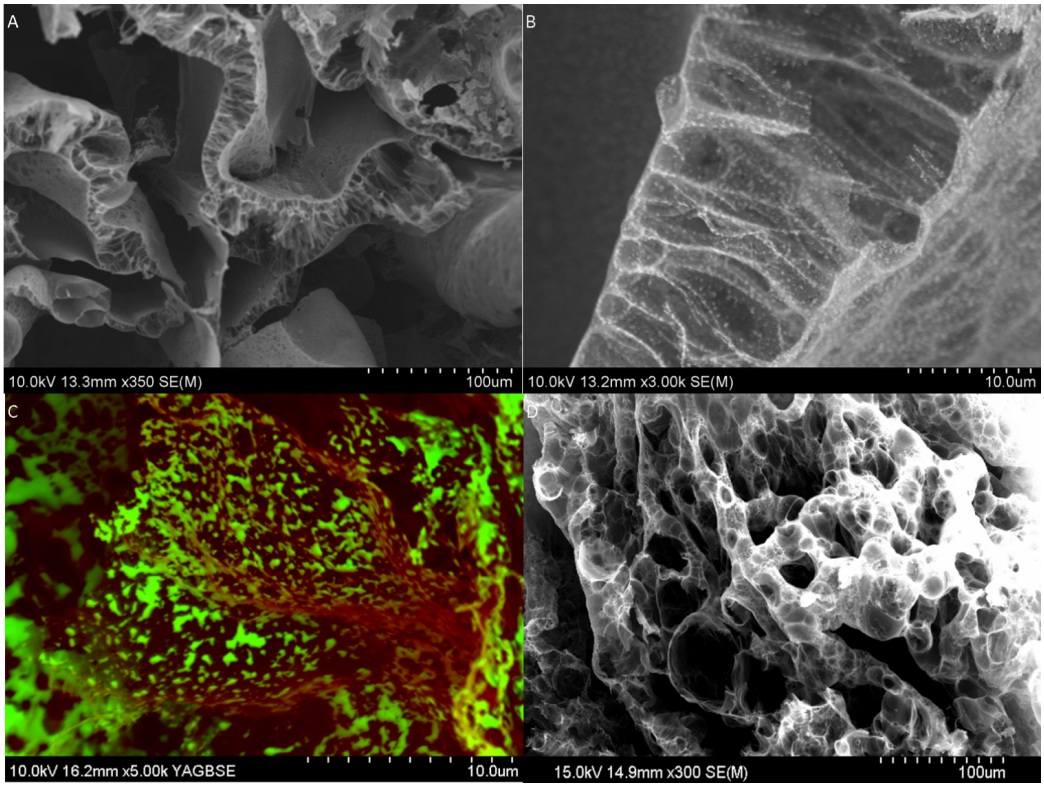

Figure 3.17: SEM images of the post carbonized cobalt/dextran hydrogel (A) and (B) before an acid wash, (C) before and acid wash but mixing the SE and BSE signals, green showing high BSE intensity and red showing high SE intensity, and (D) after an acid wash. Image (A), (B) and (D) were taken at 10.0 kV, 10.0 kV and 15.0 kV respectively using the SE detector. Image (C) was taken at 10.0 kV using both the SE and BSE detector.

most interesting structure and so further images are shown in figure 3.17. The Co/graphitic carbon material in figure 3.17 (A) and (B) show a very interesting porous macrostructre and like the other metals cobalt is located within the carbon sheets. Unlike the other metals, the material still shows a porous macrostructure upon removal of the cobalt with an acid wash (figure 3.17). EDX was taken across the entirety of the region shown in figure 3.17 (D) and shows no cobalt peaks (appendix A figure 8.4). In order to deduce the amount of metal in post washed material, the samples were heated to 500 °C in a water atmosphere for four hours to burn away all the carbon. The residue was then washed with 6M HCl and ICP-OES was performed and the % of metal remaining in the post washed samples were 0.83% and 0.26% for the cobalt and nickel respectively. Data could not be included for the iron and copper as the treatment did not remove the entirety of the carbon for those metals.

An EDX map was also taken of some of the pre-wash cobalt material (figure 3.18), this confirms the presence of cobalt particles located within the carbon sheets. It is therefore perhaps not surprising that the stability of the macrostructure is reliant on the metal particles.

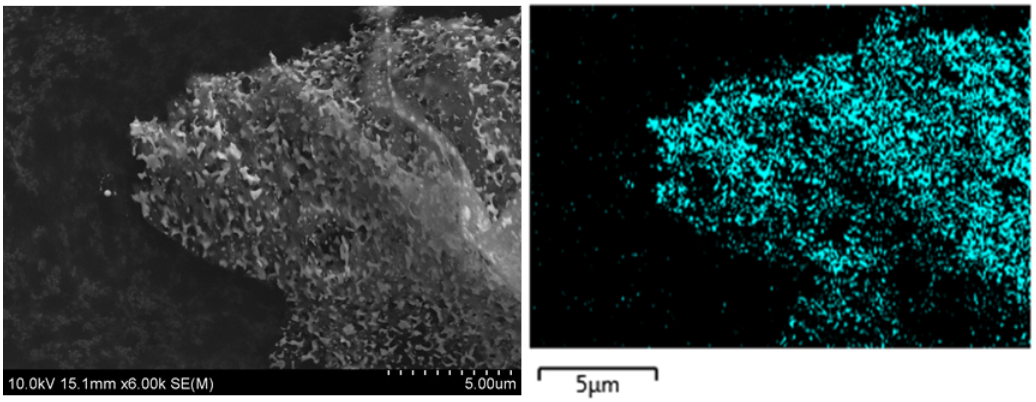

Figure 3.18: EDX map showing the presence of cobalt (blue) in the carbon sheet. Image taken at 10.0 kV using the SE detector.

Characteristic raman spectra for the different metal/carbon foams is shown in figure 3.19. There are three apparent peaks in the spectra, all typical of graphitic carbon. The D peak at $\approx$ 1300 cm^{-1}, the G peak at $\approx$ 1600 cm^{-1} and the 2D peak at $\approx$ 2700 cm^{-1}. These have been discussed before but briefly: The D peak is considered to be due to disorder and is a

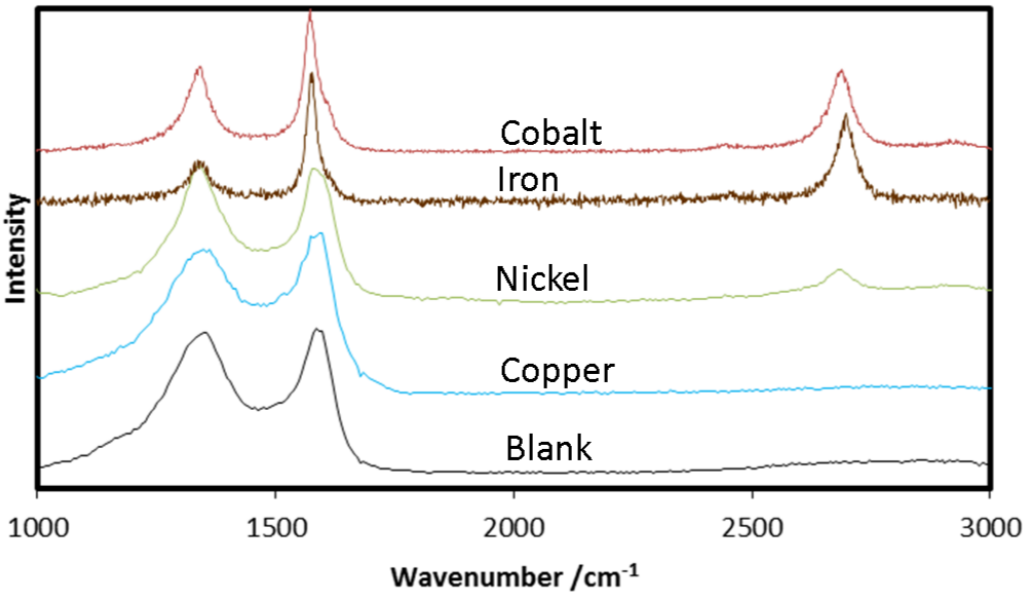

Figure 3.19: Raman spectra of the resulting carbon material for the four metals and the blank run.

Raman inactive mode that becomes active when defects in the system are present.[168] The G band is present in all sp^2 hybridised carbon and arises from the E_{2g} vibrational mode. The 2D peak is a second harmonic of the D peak and arises due to long range order in the graphitic structure. The difference in Raman for the different experiments is very interesting. Cobalt and iron produced very good results with an intense G and 2D which would be expected when using such well known graphitisation catalysts. What is surprising is how much worse the nickel based material is. The overlapping D and G and smaller 2D suggest a much less crystalline structure. Nickel is also a very well used graphitisation catalyst and has had better results with similar materials.[233] The sample which contained no metal, labelled blank, appears to be fairly amorphous with the broad, overlapping D and G bands and small 2D band. What is also very interesting, is that the copper based material, not a common but certainly not unknown graphitisation catalyst,[234] has less long range order than the blank material. Looking at the structure of the material produced in the blank, it looks very similar to glassy carbon, both in the Raman,[235] and in physical appearance (glossy and brittle) as shown in figure 3.15. The copper material is not glossy but looks more similar to the other metal based materials in being a matt black powder.

The I_D/I_G ratio gives information on the defect density in the material. The average I_D/I_G for the metals used and the blank are 0.77, 0.91, 1.00, 0.93 and 0.66 for the cobalt, copper, nickel, blank and iron respectively. Raman maps were taken over approximately 1000 spectra for each of the samples and the data plotted as a histogram showing the frequency of different I_D/I_G ratios appearing for each of the metals and the blank (figure 3.20). Also shown are colour maps of the intensity of the I_D/I_G ratio. Red showing high I_D/I_G ratios and blue showing lower I_D/I_G ratios. The iron has low I_D/I_G ratios but quite a diverse range suggesting a less defective material but also a heterogeneous material. The other materials also show a more defective structure than the iron but are far more uniform. It is important to note that the high D peak in the copper compared to the nickel means slightly different things. The well defined 2D peak in the nickel suggests that the carbon is sp^2 hybridised and so the large D originates from nanocrystalline domains. With the copper, the absence of the 2D suggests that the carbon is amorphous, with a mixture of sp^2 and sp^3 carbon.[2] It is unsurprising in this case that the D band might be smaller relative to the G band with amor-

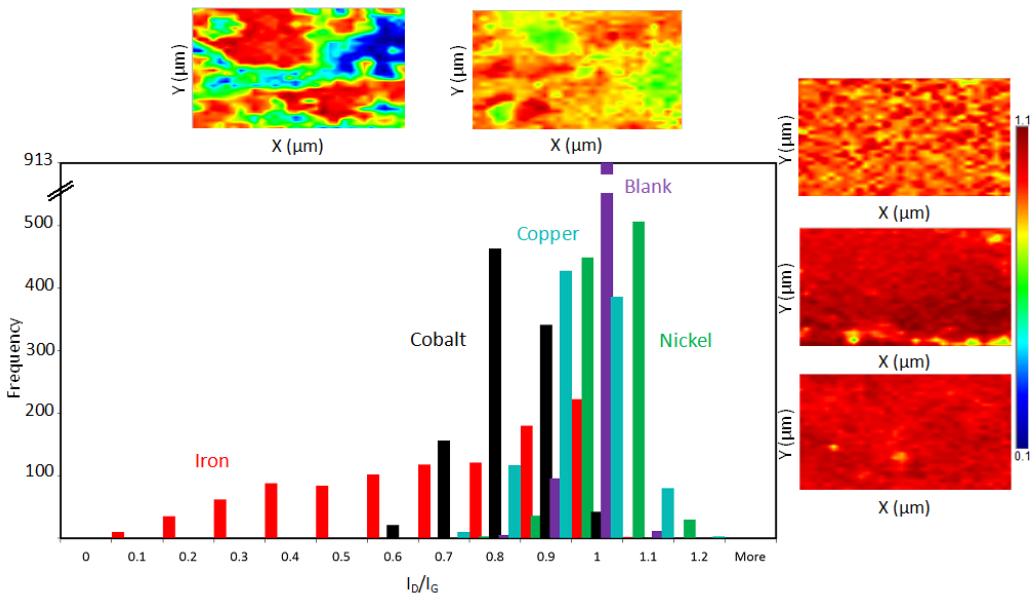

Figure 3.20: Histogram showing the frequency of different I_D/I_G ratios for each of the different metals. Also intensity maps (**top**: iron and cobalt left to right, **right hand side**: copper, blank, nickel top to bottom) of the I_D/I_G for each of the metals where red corresponds to large I_D/I_G ratios and blue corresponds to small I_D/I_G ratios.

phous carbon. The D band originates from defects in sp^2 rings, as a smaller proportion of amorphous carbon is rings, the D band will decrease. The G band originates from pairs of sp^2 carbon and so remains unchanged.[168]

In plane crystal length can also be calculated from this ratio using equation 3.1,[194,236] and are calculated to be 14.79, 17.51, 19.22, 18.04 and 12.68 nm for the cobalt, copper, nickel, blank and iron respectively. Due to the absence of a D band for the cobalt, iron and nickel material created in section 3.2.2, no comparison can be made. Crystal size was calculated for the CuGF to be 42.5 nm, significantly larger than the crystallite sizes of the one pot material, as to be expected from the differing synthesis methods.

A histogram was also produced displaying the frequency of different I_G/I_{2D} ratios accompanied by corresponding image maps (figure 3.21). Red shows large values of I_G/I_{2D} while Blue shows small values. The copper derived material was not included in the histogram as there was no discernible 2D band. Cobalt shows the highest I_G/I_{2D} ratio consistently, followed by iron, nickel and then the blank. Looking at the previous data, it's not surprising that the nickel is worse than the iron. The iron's I_G/I_{2D} ratio is inhomogeneous much like its I_G/I_D ratio. 2D typically gives information in regards to number of layers and 3D crystallinity with lower I_G/I_{2D} ratios indicating thinner material.[75] The average I_G/I_{2D} values are 1.40, 4.28, 3.15 and 4.54 for the cobalt, nickel, iron and blank respectively.

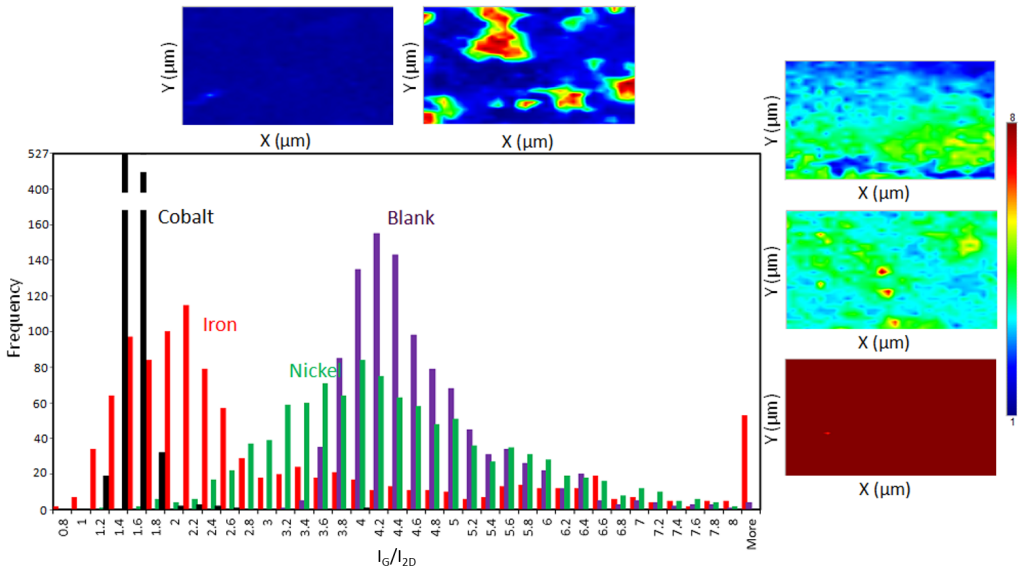

Figure 3.21: Histogram showing the frequency of different I_G/I_{2D} ratios. Also maps (**top**: cobalt and iron left to right, **right hand side**: nickel, blank, copper top to bottom) showing the intensity of the I_G/I_{2D} ratio with red being a high I_G/I_{2D} ratio and blue being a low I_G/I_{2D} ratio.

Information can be gathered by looking at the burn profile of the different carbon materials (figure 3.22). The blank, cobalt and nickel materials have the characteristic burn onset for glassy carbon and graphitic carbon (700 °C).[237] The iron shows a wide onset from 500 - 700 °C. This was to be expected when looking at Raman spectra as the material is very heterogeneous. The copper shows a very early burn profile at approximately 300 °C. This is typical of amorphous carbon. It is interesting to have such a clear onset for the cobalt and nickel materials at ≈ 600 °C. The work done on carbonising xerogels often find that their material is a mixture of amorphous and graphitised carbon. This is due to the carbon close to the metal graphitising while the material further away from the metal is not experiencing any catalysing effect.[238] The iron based material shows features more similar to this as the burn profile is over a large range of temperatures.

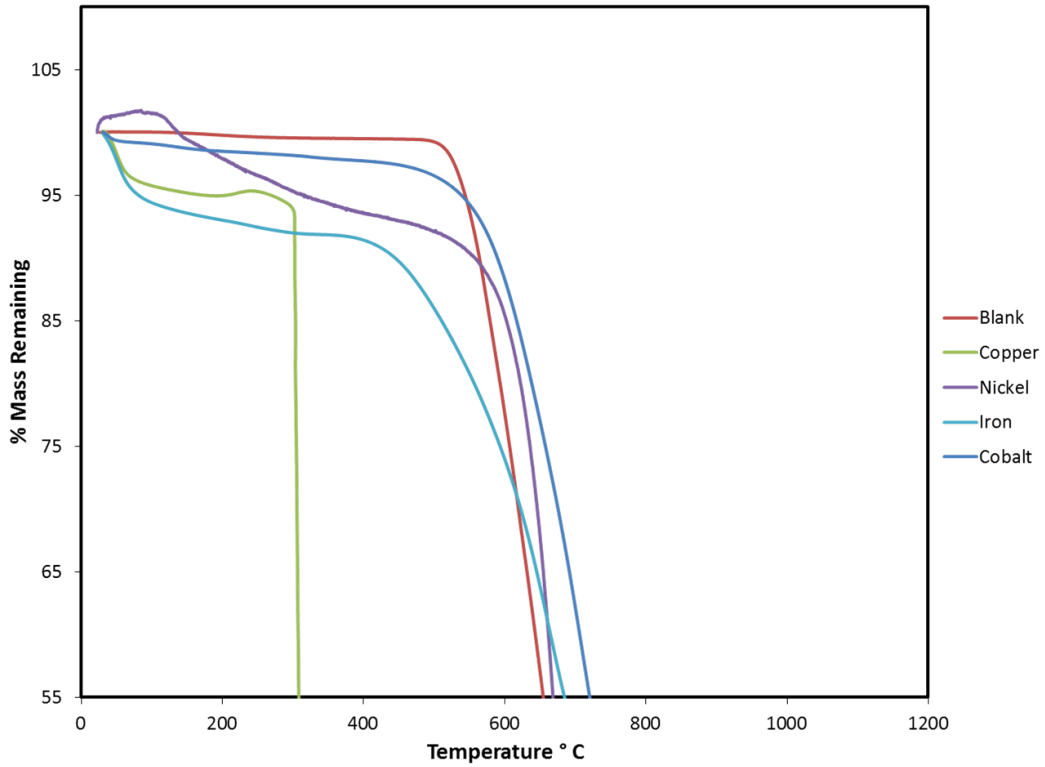

Figure 3.22: Thermogravimetric analysis of the different products heated in air to 1000 °C at 20 °C/min.

An *in situ* TGA was done of the cobalt dextran gel and the blank gel (figure 3.23). This was where the gels were heated to 1000 °C inside a TGA in an argon/hydrogen atmosphere. At around 100 °C the water comes off and 40 % mass loss is observed. The water comes off at lower temperature with the blank, this could be due to the boiling point elevation of water when adding salt to the solution as in the cobalt gel. The next significant mass loss comes at approximately 200 °C and is due to the decomposition of dextran into different products. The mass then stabilises at about 12 % for the cobalt gel and 8 % for the blank gel. It is to be expected that the cobalt gel will have a larger residual mass as residual cobalt will remain in the pan.

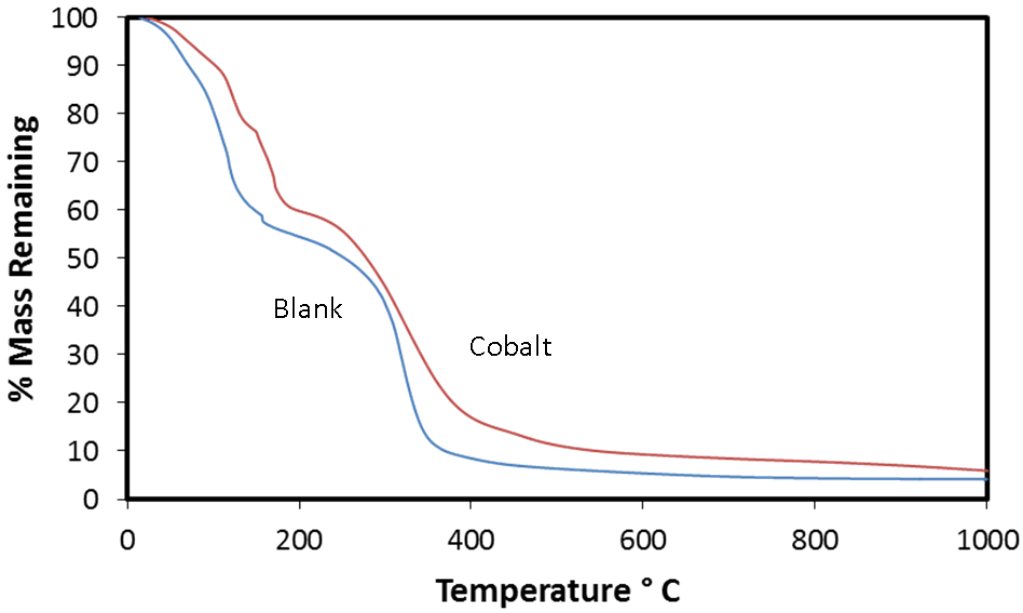

Figure 3.23: TGA's were taken of the cobalt and blank gels heated at 20 °C/minute to 1000 °C in an argon/H_2 atmosphere.

TEM images were taken of each of the metal derived carbons post acid wash after sonicating the material in ethanol and dropping them onto a TEM grid. Figure 3.24 shows TEM images of the copper ((A) and (B)), iron ((C) and (D)) and nickel ((E) and (F)). Representative TEM could not be obtained for the blank material as the material was too brittle to get into a smaller enough form for deposition. The cobalt material is shown in more depth in figure 3.25. The copper material also shows mostly amorphous material, although some graphitic regions could be found. An ED is shown in appendix A figure 8.5 The iron and nickel materials show porous graphitic sheets and is confirmed by the ED (appendix A figure 8.6 and 8.7). On closer inspection of these sheets, it can be seen that the sheets are made up of curved graphitic structures. This too is seen in the cobalt material in figure 3.25. Figure 3.25 (A) shows the material before an acid wash. The cobalt particles can be clearly seen in the graphitic sheet. The material after an acid wash can be seen in figure 3.25 (B) where pores are visible in which the cobalt had previously occupied. Higher resolution images of the material show the curved graphitic sheets visible in the iron and nickel based material. It is also shown that the heavily curved material is not the only carbonaceous material present in the sample but a more sheet like graphite material is also apparent. High resolution images and electron diffraction (inset) of this material also

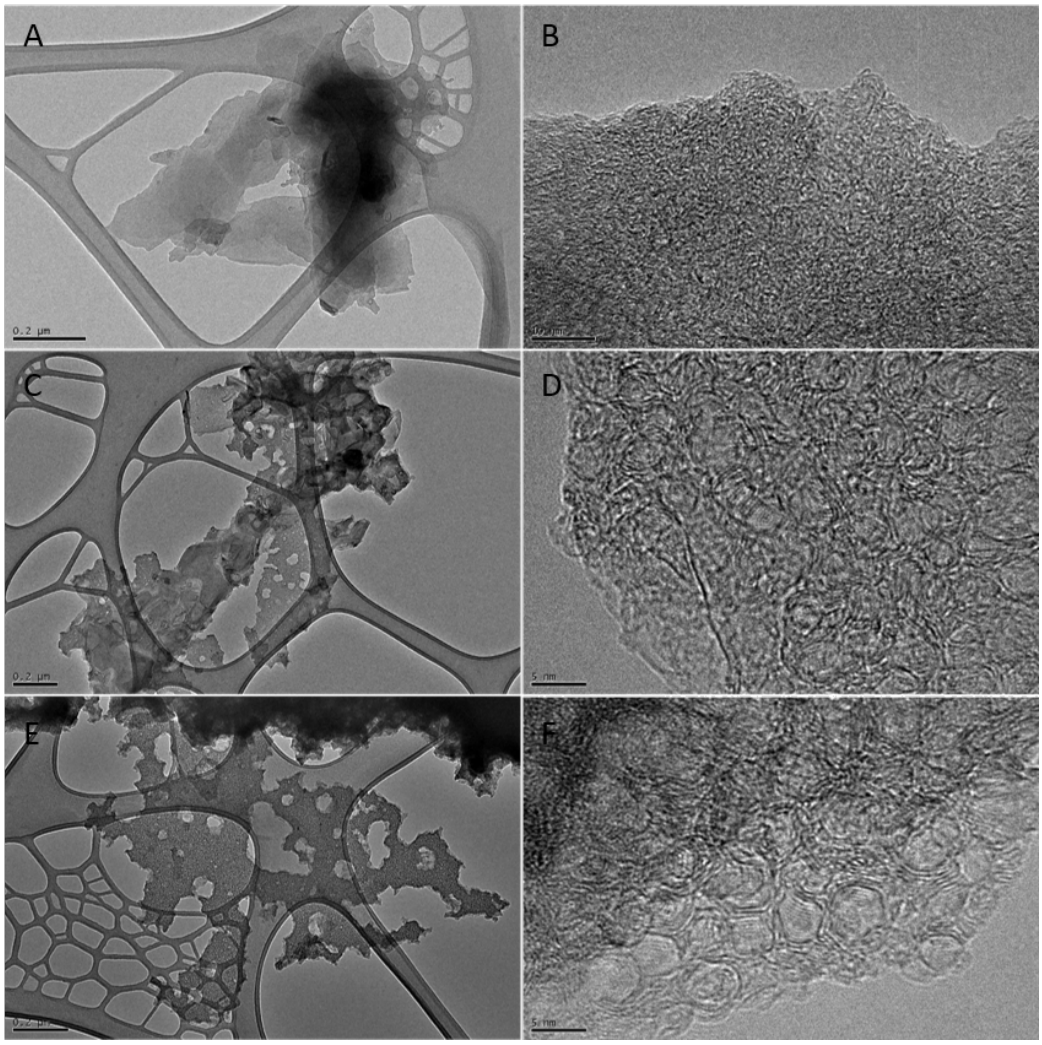

Figure 3.24: TEM images of the material after an acid wash taken at 80 kV. (A) and (B) copper based material, (C) and (D) iron based material and (E) and (F) nickel based material. Images taken at 80.0 kV.

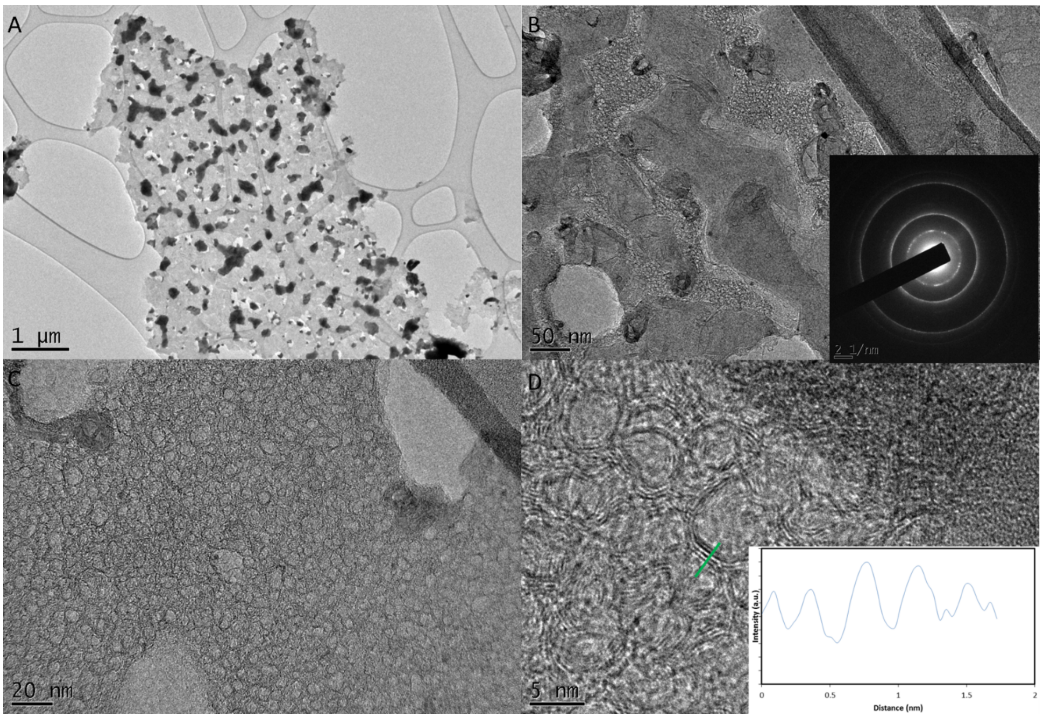

Figure 3.25: TEM images of the cobalt based material (A) pre acid wash and (B), (C) and (D) post acid wash. Inset (B) is an electron diffactogram of the region in (B). Inset (D) is a line profile of the region shown in (D). Images taken at 80 kV.

show that it is graphitic with distinct rings with lattice spacings appropriate for graphitic material. The two different structures of carbon could be due to proximity of the metal catalyst during the graphitisation step. Line profiles of the number layers of the curved material was taken for the nickel, iron and cobalt samples and were found to be between 4 and 6, with no significant difference between the number of layers for each of the different materials. An example of this is shown inset in figure 3.25 (D). Electron diffraction was taken of the material and is shown inset in figure 3.25 (B) and shows the (002), (100) and (110) lattice spacings giving d spacings of 0.34, 0.21 and 0.12 nm respectively. Mesopores(2 to 50 nm) and nanopores (100 nm) can both be clearly seen in the images. It is believed that the nanoporosity is due to the metal particles contained within the carbon sheets, evidence for this comes from figure 3.25 (A) where metal particles can be clearly seen within the sheets. The mesoporosity appears to come from the voids created from the curvature of the graphitic material which can be clearly seen in

figure 3.25 (C) and (D). BET surface area measurements were taken of the cobalt material after an acid wash and were found to be 140 m^2g^{-1}. This is comparable with other graphitised porous carbons.[191,197,200]

3.4 Conclusions and Future Work

Two synthetic methods were shown as novel ways of growing porous graphitic materials. The first method was a traditional CVD synthesis growing graphene onto a porous metal foam. Four different metals were attempted with graphene material being produced on the nickel, iron and cobalt metals while copper seemed to produce a more defective and less crystalline material. The graphene foams were able to hold their shape reasonably well after the removal of the metal. It is believed that this is due to the large amount of graphite present in the foam supporting the structure. The process is not optimised and in the future we could look into trying to improve the proportion of material that is single-layer graphene by changing parameters such as carbon loading in the gel, temperature, flow rates and cooling rates. Much literature exists looking at the effect of these different conditions on the quality of material produced, mostly for nickel and copper catalysts. Doing the experiment under low pressure conditions may also improve quality. It is important to note that any increased proportion of few-layer graphene compared to graphite is likely to hamper the structural stability of the foam. Other groups have got round this by coating in PMMA before etching the metal away, leaving a graphene/PMMA foam composite.[207]

Trying to get results from the copper catalyst could be worthwhile. Growth on copper foils tend to require intensive pretreatment of the copper in order to maximise surface smoothness and grain boundary size.[239] Such methods that could be employed for this synthesis is longer annealing times or perhaps synthesising the copper foam then electropolishing it before performing the CVD. It might be the case that copper just isn't feasable for growth of macroporous graphene's. Chen *et al*,[178] attempted CVD on copper foams but due to the growth on copper being self-limiting to single layer, any attempt to etch the underlying copper foam away resulted in the graphene foam collapsing.

One of the advantages of doing a soft templated route to the metal foams is that a greater control of pore size can be achieved. Mann *et al*,[212] have demonstrated this in the synthesis of metal foams and so future work

might involve the synthesis of macroporous graphene with different pore sizes. The control of pore size is important in supercapacitor applications. Demonstration of an application for the macroporous graphenes should also be performed in future work. The graphene foam could be used as a 3D electrode and the capacitance then measured.

The second method discussed in this chapter was a synthesis of porous graphitic material where a metal doped dextran hydrogel was carbonized at 1000 ℃ in an inert atmosphere. Free-standing foams were produced that would collapse into powder upon washing of the metal. This leaves curved graphitic material with large holes in the sheets from where the metal particles had been washed away. This was done for four different metals: cobalt, iron, nickel and copper. This process was also not optimised and work could be done to improve the crystalinity and uniformity of the material such as changing flow rates and temperature. A lower temperature of 800 ℃ was tried on the cobalt hydrogel and gave a much inferior result in regards to Raman spectroscopy (Appendix A figure 8.8).

Testing the material in different applications could be worthwhile. The material is high surface area and graphitic and so should be suitable in energy storage applications such as supercapacitors and some powder electrodes should be produced and capicitance measured. Porous carbon sheets might also make a suitable filtration material. The defective nature of the sheets and the high surface area should make for good interaction with a polymer matrix and might improve the mechanical properties of a composite material.

Being synthesised from a gel gives potential to mould the material into desirable shapes. This is particularly encouraging for use as free-standing electrodes in supercapacitor applications. Attempts were made to mould the material but it is believed that the water comes off the gel too violently when heating up for the shape to be maintained. This could be controlled by altering the heating rate of carbonisation. Another method was to freezedry the gels prior to carbonization inside a cylindrical crucible. A picture is shown in figure 3.26 of a post carbonised freeze dried gel. Other methods of trying to mould the material could be to use a much slower heating rate. The material would collapse upon removal of the metal. The presence of the metal might improve the capacitance properties due to acting as a pseudocapacitor, this material should therefore be tested as free-standing electrode. Methods could be employed to try and get the carbon structure to hold its shape better after the removal of the cobalt such as sulfonation, adding sodium

chloride or adding silica nanoparticles.[240]

Figure 3.26: Photo of a carbonized freezedried cobalt hydrogel on a dandelion.

Chapter 4

PolyHIPE's as Templates for Carbon Growth

4.1 Introduction

As stated in the previous chapter, 3D graphene has attracted much interest in applications such as electrodes,[201,202] conducting frameworks for polymer thermosets,[135,178] and filtration/pollution control.[203,204] 3D graphene is well suited to these applications due to its high surface area and its high thermal and electrical conductivities.[40,41] Important features required of the 3D graphene in order to maximise its ability to perform these applications are physical stability, control of pore size, high surface area and good quality graphitic material to allow for the high electrical and thermal conductivity.

In this chapter an alternative method to 3D graphene is proposed. The last chapter referred to methods of either carbonizing hydrogels or CVD on porous metal catalysts. Limitations of those methods are a lack of stability in the carbon foam where the foam would collapse upon the addition of a small amount of force, and that the resultant material had a non-uniform macropore structure. The method put forward in this chapter is the carbonization of polyHIPE's (poly high internal phase emulsions), a well known stable porous material with a very regular pore structure.

High internal phase emulsions (HIPEs) have been known for many years and have seen applications in food preparation, cosmetics, fuels and oil

recovery.[241] Their characterizing feature is that at least 74 % of the volume of the emulsion is comprised of droplets (volume ratio (Φ) = 0.74).[241] This number represents the maximum efficiency packing of non-deformed spheres. Greater percentage volume of droplets can be achieved but droplets are of non-uniform size or deformed.[241] HIPEs have been used as templates for highly porous structures. Such materials are formed by curing the continuous phase of the the emulsion to form polyHIPEs, where the continuous phase is solidified and the droplets are embedded into the resulting material.[241] The internal phase and surfactant are then removed giving the porous structure. A scheme of the synthesis of carboHIPEs is shown in figure 4.1, whereby the aqueous phase is added to the organic phase forming an emulsion, the mixture is then polymerised with the aqueous droplets embedded into the material. The droplets are then removed with heating, leaving behind pores. The resulting polyHIPE can then be carbonized to form a carboHIPE.

PolyHIPEs are typically synthesised by the addition of monomer to crosslinker and surfactant while slowly adding the droplet phase. The resulting mixture is then cured. Advantages of using polyHIPEs as porous materials is having a well documented control over the morphology and the ability to tune pore size.[242] The macromorphology can be varied by simply

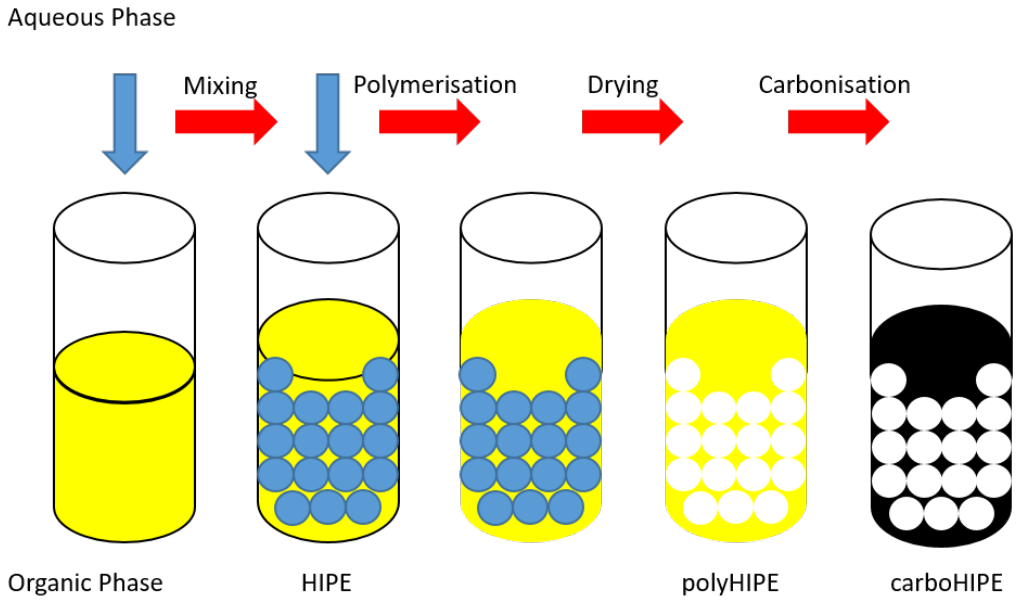

Figure 4.1: Scheme showing the synthesis of a carboHIPE.

changing the vessel within which the polyHIPE is cured in, while pore size can be changed by adjusting the volume of the emulsion comprised by droplets.[241]

The carbonization of polyHIPEs has received attention for use as supercapacitors,[243] batteries[244,245] and as reinforcements for composites.[246] The carbonized polyHIPEs are known as carboHIPEs. CarboHIPEs are produced by first synthesising a polyHIPE, and then treating with sulfuric acid to sulfonate the polyHIPE. The sulfonated polyHIPE is then heated to 500 °C - 900 °C.[243,244,247–249] Sulfonation has been proven a necessary step in the production of carboHIPEs prior to carbonization in order to provide stabilisation for the polyHIPE against depolymerisation during heating. This is due to the strongly interacting sulfate moieties stabilizing the polymer through the initial stages of carbonization.[249] The results of missing out that step can be seen in figure 4.3 B where no macrostructure is retained post carbonization. Silica nanoparticles have also been used to stabilisie the carbHIPEs during carbonization. The silica is believed to act like a scaffold, and the shape of the polyHIPE is maintained after removal of the silica.[250] CarboHIPEs have been synthesised from polyHIPEs of DVB/styrene and resorcinol/formaldehyde,[242,249,251–253] with most research been done on the resorcinol/formaldehyde carboHIPE.[253] Advantages of using carboHIPEs for these applications come from the large surface area increases upon carbonization. Such increases as 9 m^2g^{-1} to 445 m^2g^{-1} have been observed.[249] This suggests that carbonization introduces nanoporosity into the sample. Surface areas as high as >1400 m^2g^{-1} have been achieved by activating the polyHIPE with KOH during the carbonization step.[247] CarboHIPEs produced thus far have very little graphitic character as shown by Raman spectra of the produced materials.[240,243,247] In this chapter, a method of producing carboHIPEs with a graphitic character is described. The increased proportion of sp^2 hybridised carbon in the 3D foams should increase the conductivity, making the material better suited for applications in energy storage.

4.2 Synthesis of Graphitic CarboHIPEs

4.2.1 Synthesis of PolyHIPE's

PolyHIPE's with a continuous phase consisting of styrene and divinylebenzene (DVB) were chosen for this work due to the large amount of literature available on such polyHIPEs.[254] Briefly, the polyHIPE's were prepared by

mixing azobisobutyronitrile (AIBN) as the initiator and SPAN 80 as the surfactant to a styrene/DVB solution. The AIBN acted as a free radical initiator to polymerise the continuous phase. To make metal doped polyHIPEs, metal salt was dissolved into the aqueous phase. Cobalt and nickel salts were chosen with most focus on cobalt due to the lessons learnt in the previous chapter. This aqueous phase was then added dropwise to the continuous phase. The mixture was cured in an oven overnight. Three different porosities of polyHIPE were synthesised by varying the ratio of the continuous phase to the overall volume. Continuous phase to volume ratios of 80%, 85% and 90% were chosen. SEM images of the polyHIPE's with and without metal doping are shown in figure 4.2. It can be seen that the doping of metals has little effect on the structure of the polyHIPE's. PolyHIPEs typically have a hierarchical pore structure present, large voids which are present due to the removal of the droplets in the emulsion, interconnecting windows between the voids and lastly, the pores within the polymer walls and struts that comprise the solid phase of the material.[241] A rough estimate of the pore sizes from the images in figure 4.2 give average sizes of 3 µm, 3 µm, 4 µm, 5 µm, 10 µm and 6 µm for figure 4.2 A) -F) respectively. Measurements were made across 20 pores for each image, note that due to exceeding the 74% threshold for sphere packing the pores were of irregular shapes.

4.2.2 Carbon Growth Templated from PolyHIPE's

The six different polyHIPE's were carbonized by heating to 1000 °C and holding for two hours. 1000 °C was chosen as it is a commonly used temperature for CVD growth of graphene. The polyHIPEs were heated in an argon/hydrogen atmosphere in order to reduce the metal salt to metal so it can catalyse the graphitisation. Photos of the pre and post carbonized polyHIPEs are shown in figure 4.3. Figure 4.3 A and B show that the blank polyHIPEs lose all macrostructure and a large amount of volume upon carbonization. This is in direct contrast to the metal doped polyHIPEs (figure 4.3 C) and D)) whereby the macrostructure is retained and only a small loss of volume is observed. No differences can be observed between the different porosities.

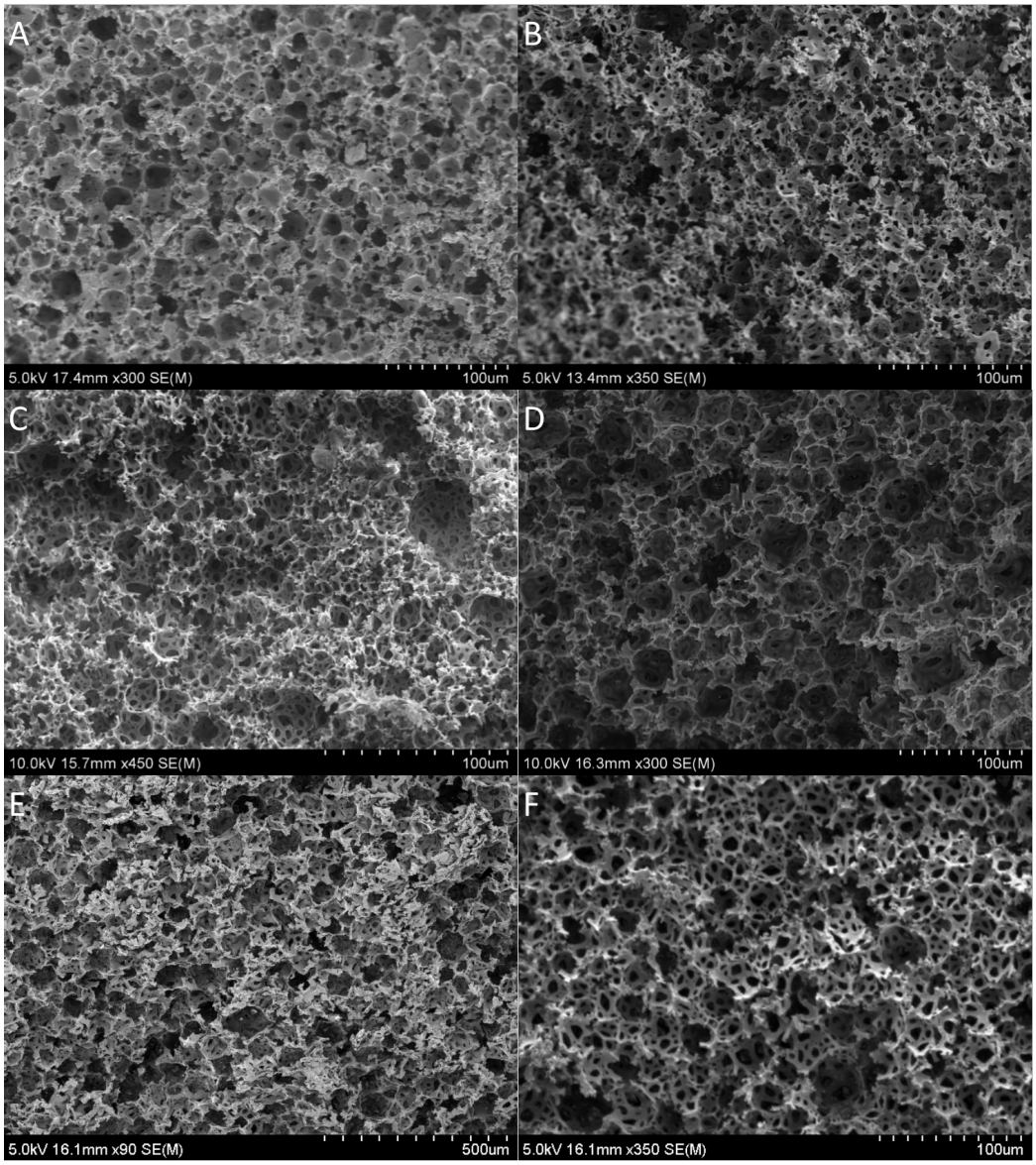

Figure 4.2: SEM images of A) and B) 80% polyHIPE with and without cobalt, C) and D) 85% polyHIPE with and without cobalt and E) and F) 90% cobalt with and without cobalt.

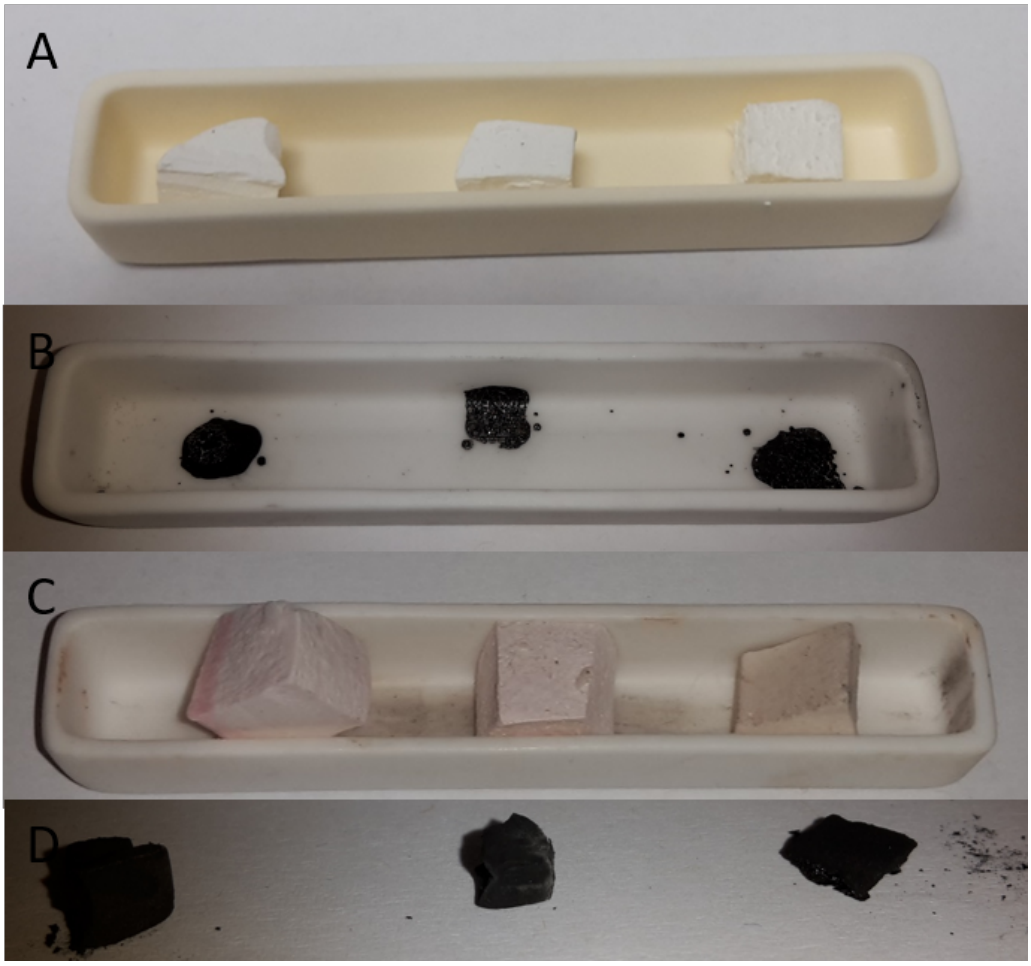

Figure 4.3: Photographs of A) blank polyHIPE's, B) blank carboHIPE's, C) Co doped polyHIPE's and D) Co doped carboHIPE's. 80%, 85% and 90% poly/carboHIPE's shown left to right.

SEM images of the undoped carboHIPE's (figure 4.4) and doped carboHIPE's (figure 4.5) agree with figure 4.3 whereby the blank carboHIPEs in figure 4.4 have lost all porosity when compared with the metal doped carboHIPEs in figure 4.5. The doping of the metal is clearly necessary for the stabilisation of the polyHIPE macrostructure, this could be due to the metal forming a scaffold during the carbonization adding to the stability, much like the observations of Woodward *et al* when using silica nanoparticles prior to carbonization.[240]

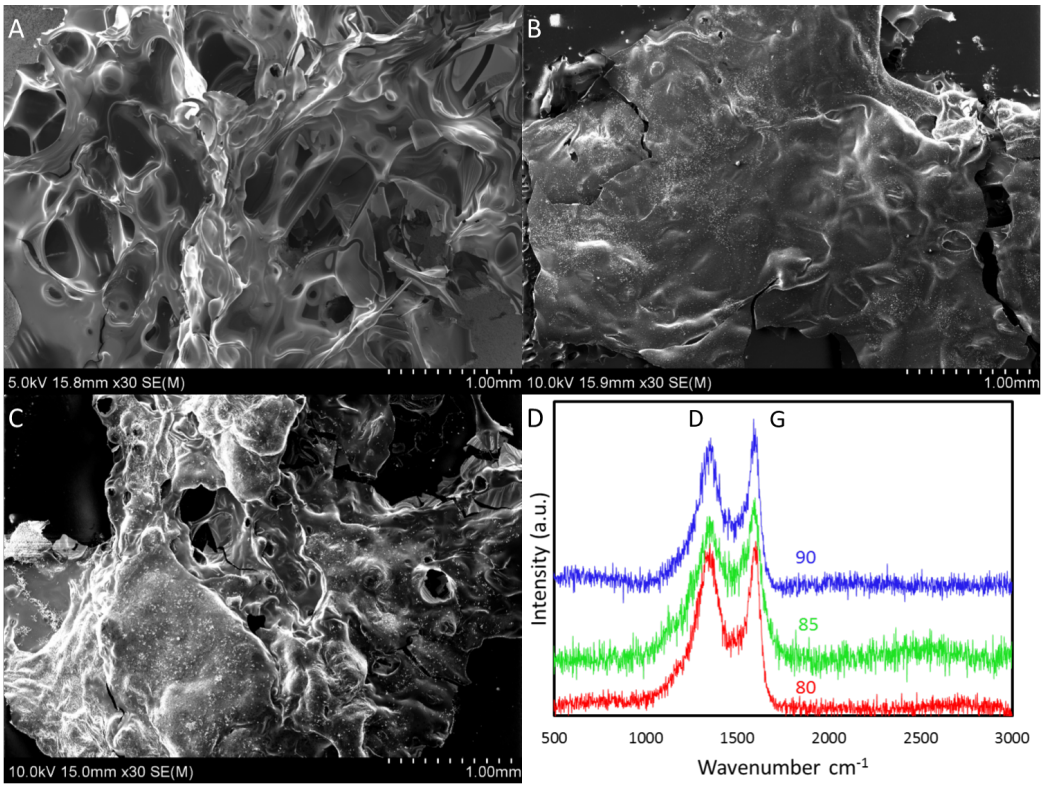

Figure 4.4: SEM images of A) 80%, B) 85% and C) 90% undoped carboHIPE and D) Raman spectra of the three carboHIPE's.

The SEM images in figure 4.4 clearly show that the macrostructure of the carbonized blank polyHIPE has collapsed due to the heat treatment and all porosity has been lost. Raman spectra shown in figure 4.4 D is typical of what would be seen from amorphous carbon with an overlapping D and G band ($\approx$ 1300 cm^{-1} and 1600 cm^{-1} respectively) with an approximate I_D/I_G of 1. The absence of a 2D band ($\approx$ 2700 cm^{-1}) also suggests no crystallinity in the sample. The formation of amorphous carbon is to be expected

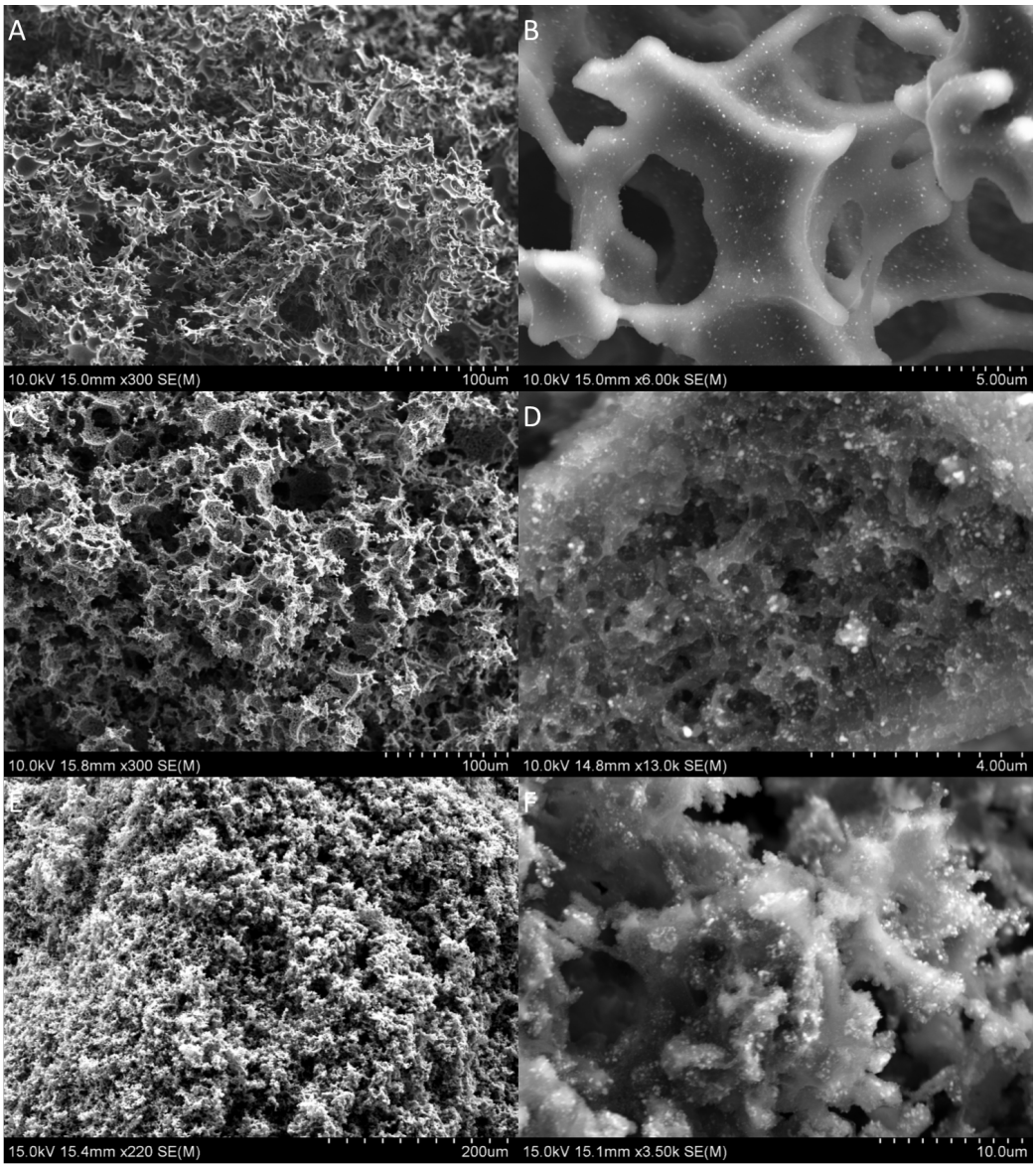

Figure 4.5: SEM images of the Co doped carboHIPE's. A) and B) - 80% carboHIPE. C) and D) 85% carboHIPE and E) and F) 90% carboHIPE.

when carbonization occurs at such a low temperature of 1000 °C without the presence of a graphitisation catalyst. This is typical of the Raman spectra commonly observed in the carboHIPE literature whereby amorphous carbon structures are produced.[247] There is no discernible evidence that the porosity of the polyHIPEs have an effect on the the Raman spectrum with similar I_G/I_{2D} and I_G/I_D ratios observed for all three carbonized polyHIPEs.

On comparison of the blank carboHIPEs in figure 4.4 with the SEM images of the Co doped carboHIPEs shown in figure 4.5, the difference in structure can clearly be observed. The metal allows the macrostructure to be retained and a 3D carbon/metal monolith to be obtained. On further comparison with the metal-doped polyHIPEs shown in figure 4.2, it can be seen that porosity does remain but its nature is different to that of the starting material with the voids much less apparent. This can be attributed to the carbon dissolving into the metal at high temperature and then precipitating out. Such is the mechanism for the catalytic graphitic carbon formation from cobalt.[69] It can be seen in the higher magnification images in figure 4.5 that the carbon produced is rough and that metal particles are embedded throughout the material. The presence of the metal is confirmed in the EDX shown in figure 4.6 where a very prominent carbon peak can be observed along with a small cobalt peak. The difference in the porosities starts to become apparent in the SEM images in figure 4.5. Semblance of the starting materials seen in figure 4.2 can be seen in the 80 % and 85 % porosity but much less so in the 90 % porosity which appears to have lost much of the characteristic polyHIPE structure. This is unsurprising as it was deduced earlier that the metal is vital in maintaining the structure of the carboHIPE. The 90 % porosity polyHIPE has the least metal present.

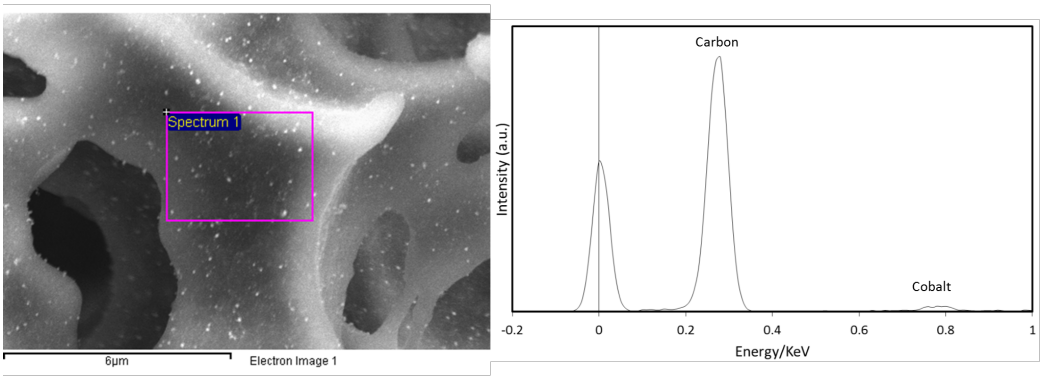

Figure 4.6: SEM image (left) of Co doped 80% carboHIPE and EDX spectra (right) of the region shown.

In order to remove the metal and obtain a standalone carbon monolith, the carboHIPE's were washed in 6 M HCl for 24 hours. SEM images and EDX was then taken of the carboHIPE's to determine if any loss of structure occurred and if the metal particles have been successfully removed. The resultant data is shown in figure 4.7. It can be seen from the SEM images in figure 4.7 that the macrostructure was retained after the acid wash. This is however, most likely due to the ineffectiveness of the acid wash in removing the cobalt. The EDX in figure 4.7 D, and the observation of the charged particles in the SEM images, show that the cobalt still remained in the sample. It appears that the carbon has coated the metal particles, making it very difficult for the acid to access it and etch it. Even with agitation, it proved impossible to remove all of the metal.

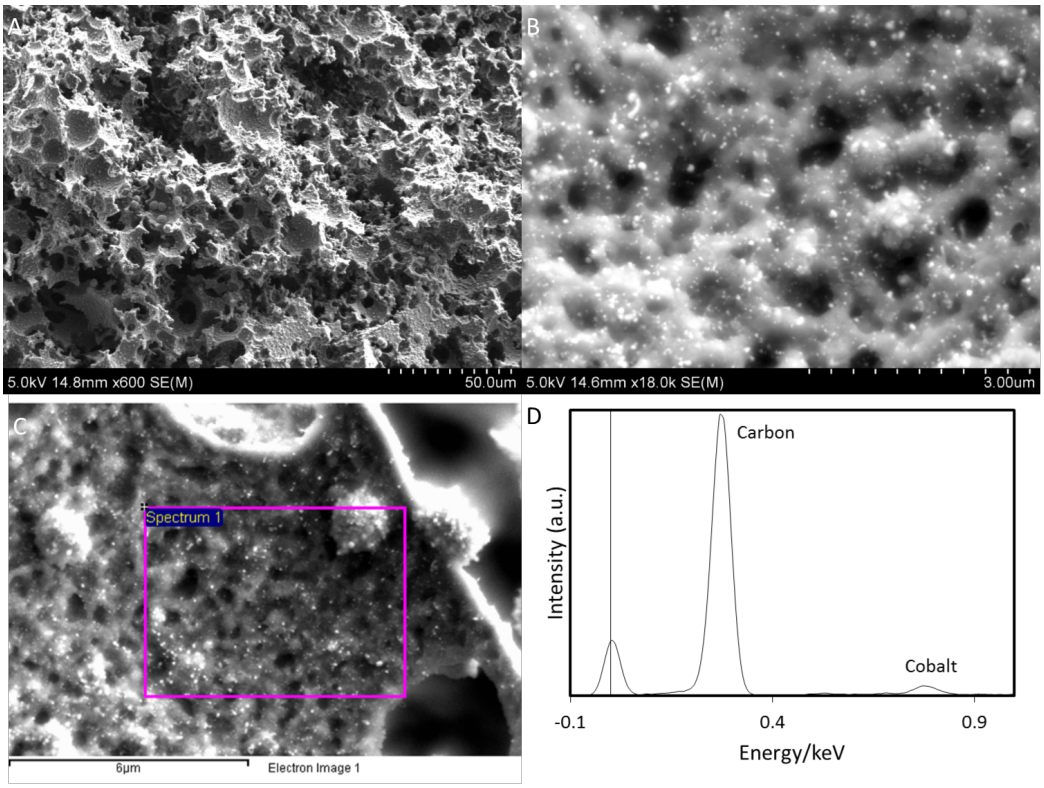

Figure 4.7: A), B) and C) SEM images of the Co doped 80% carboHIPE after an acid wash and D) EDX spectra of the region shown in C).

In order to prove that the synthesis could be adapted to other metals, a nickel carboHIPE (figure 4.8) was also synthesised at 90% porosity and can be seen to be very similar to the cobalt carboHIPEs. In fact, the nickel carboHIPE maintained it's structure much better that the 90% cobalt carboHIPE. Figure 4.9 shows that the Raman and XRD is similar for both the nickel and cobalt carboHIPEs, with similar I_G/I_{2D} and I_G/I_D observed with both metals.

Representative Raman spectra of all the porosities of carboHIPE and the nickel derived carboHIPE are shown in figure 4.9 B. They show the typical peaks associated with graphitic carbon of a D, G and a 2D band. The high D band is indicative of defects in the sheets while the 2D band being only approximately half that of the G band suggests graphite. The sharp and distinct G and D band is also indicative of crystalline material. These carboHIPEs are much more graphitic than those produced without metal-doping. Raman spectra taken of carboHIPEs from the literature,[240,243,244,247]

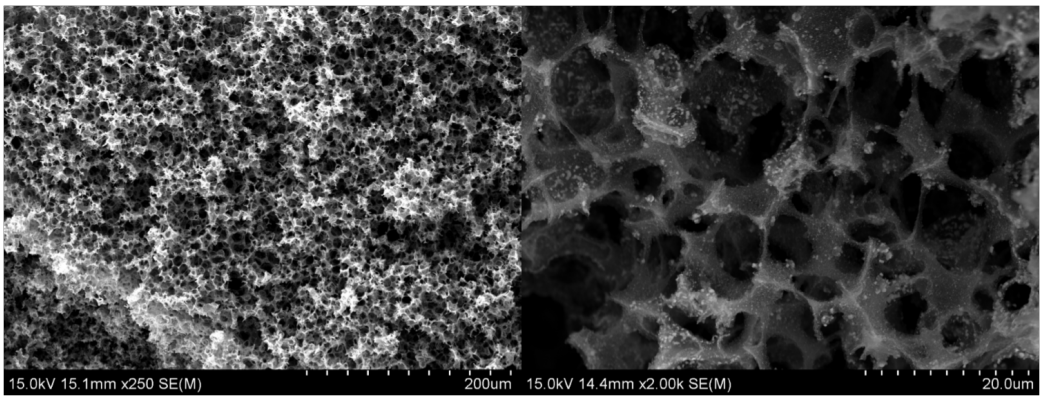

Figure 4.8: SEM images of Ni doped 90% carboHIPE

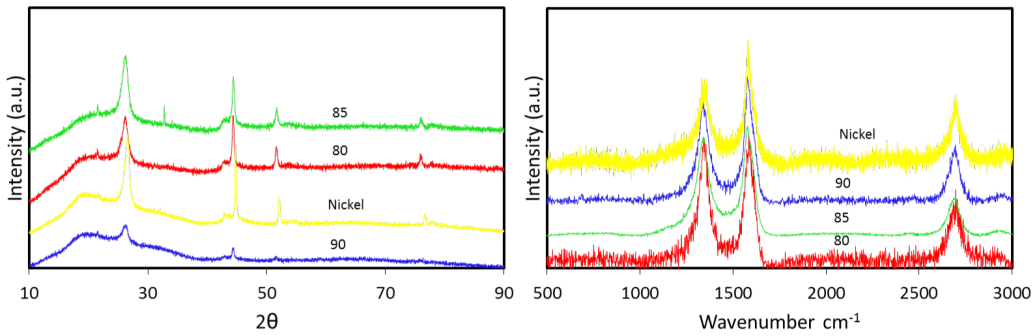

Figure 4.9: XRD (left) and Raman spectra (right) of metal doped carboHIPE's with different porosity.

are much less crystalline as shown by the absence of a 2D peak and by the heavily overlapped D and G band.

The XRD pattern in figure 4.9 shows the most prominant peak associated with graphitic carbon - the (002) spacing at $\approx$ 26.6 °. All other peaks in the diffractogram are associated with residual metal or the silicon used as a support.

Raman maps were taken of the different metal doped carboHIPE's, mapping 504 points. In order to determine the overall quality of the material, ratios of the G to 2D band intensity and ratios of the D to G band intensity were compared. Blank carboHIPE data was included for the 85 % porosity for comparison but due to the absence of a 2D peak for the blank carboHIPE, it was not included in that histogram. The results are shown in

histograms in figure 4.10. As described in previous chapters, I_D/I_G ratio is indicative of defect density or the relative proportions of amorphous carbon to sp^2 hybridised carbon. Figure 4.10 B clearly shows that the 90% porous material is the most defective material with the highest I_D/I_G value. The 80% and 85% have similar I_D/I_G ratios, lower than that of the 90% porosity material. This trend is continued when looking at the I_G/I_{2D} ratios. I_G/I_{2D} ratio is again indicative of graphitisation and is correlated to Z axis crystillinity. On observation of figure 4.10 A the 90% porosity is again significantly less graphitic than the other two porosities, as shown by the higher I_G/I_{2D} ratio. This is likely due to the 90% porosity containing less metal than the other two porosities resulting in less catalytic activity and so therefore less graphitisation.

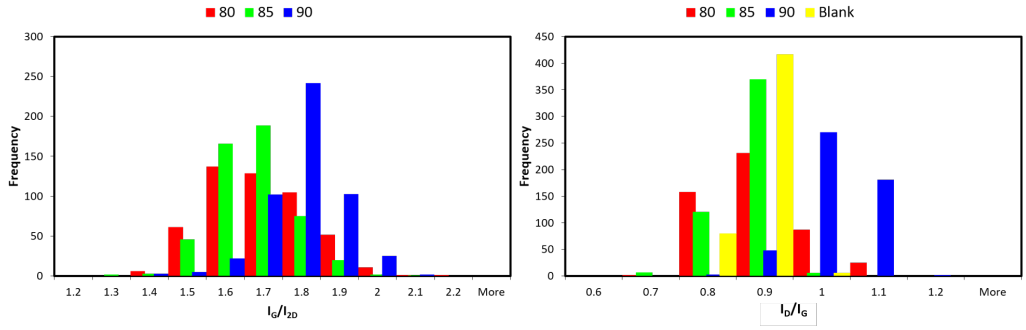

Figure 4.10: Histogram showing frequency of different I_G/I_{2D} (left) and I_D/I_G (right) ratios of Co doped carboHIPE's with different porosity.

The TGA in figure 4.11 shows the blank carboHIPEs have an onset of 500 °C - 600 °C while the metal-doped carboHIPEs have an onset of 550 °C - 610 °C. This was to be expected as graphitic carbon is more stable than amorphous carbon. There does appear to be some residual material left in the pan for the blank carboHIPEs. This could be alumina from the boat that was used as the vessel to carbonize the polyHIPEs. The material was etched onto the boat and had to be scraped off in order to remove it for analysis, some alumina may well have been taken with it. The residual in the metal-doped polyHIPEs is likely to be metal. They follow the expected trend of the 90% porosity having the least metal and therefore least metal residual followed by the 85% and then the 80%.

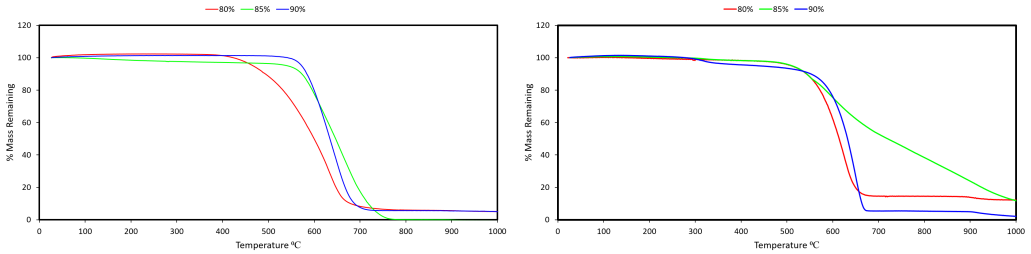

Figure 4.11: Thermogravimetric analysis of blank carboHIPEs (left) and cobalt doped carboHIPEs (right) heated in air to 1000 °C at 20 °C/min.

TEM images were taken of each of the different porosity of carboHIPEs and are shown in Figure 4.12. Material was prepared for TEM by sonicating in ethanol and then dropping onto a holey carbon TEM grid. Images A and B show the 80% porosity carboHIPE before an acid wash while the remaining images show the 80% (C and D), 85% (E and F) and 90% (G and H) porosity cobalt carboHIPEs after an acid wash.

Figure 4.12 A and B clearly show the presence of large metal particles within the carbon sheet and when compared with the TEM images from the acid washed material, it is clear that the acid washing does remove the majority of the metal. Figure 4.12 C - H show very little difference between the porosities while the HRTEM on the right hand column show that for each porosity graphitisation has occurred and the layers could be counted. It is clear that the thickness of the material is consistently greater than 20 layers. The nature of the graphitic material appears to be curved, onion like structure which likely occured as the carbon grew around the metal particles which were embedded in the lattice prior to the acid wash.

These onion like structures can be seen more clearly in figure 4.13 which shows further TEM images of the 85% polyHIPE after the acid wash. The pore sizes were measured across 20 images and were shown to range between 15 - 30 nm. Figure 4.13 also shows amorphous carbon was present in the sample. This is likely to be due to some polymer not being in contact with the surface of the cobalt and so not experiencing any catalytic effect. Electron diffraction (figure 4.13 D) was also taken of the area shown in figure 4.13 C. The rings can be indexed giving the characterisitic lattice spacings of graphite: (002), (100) and (110) giving a d spacing of 0.34, 0.22 and 0.13 nm respectively.

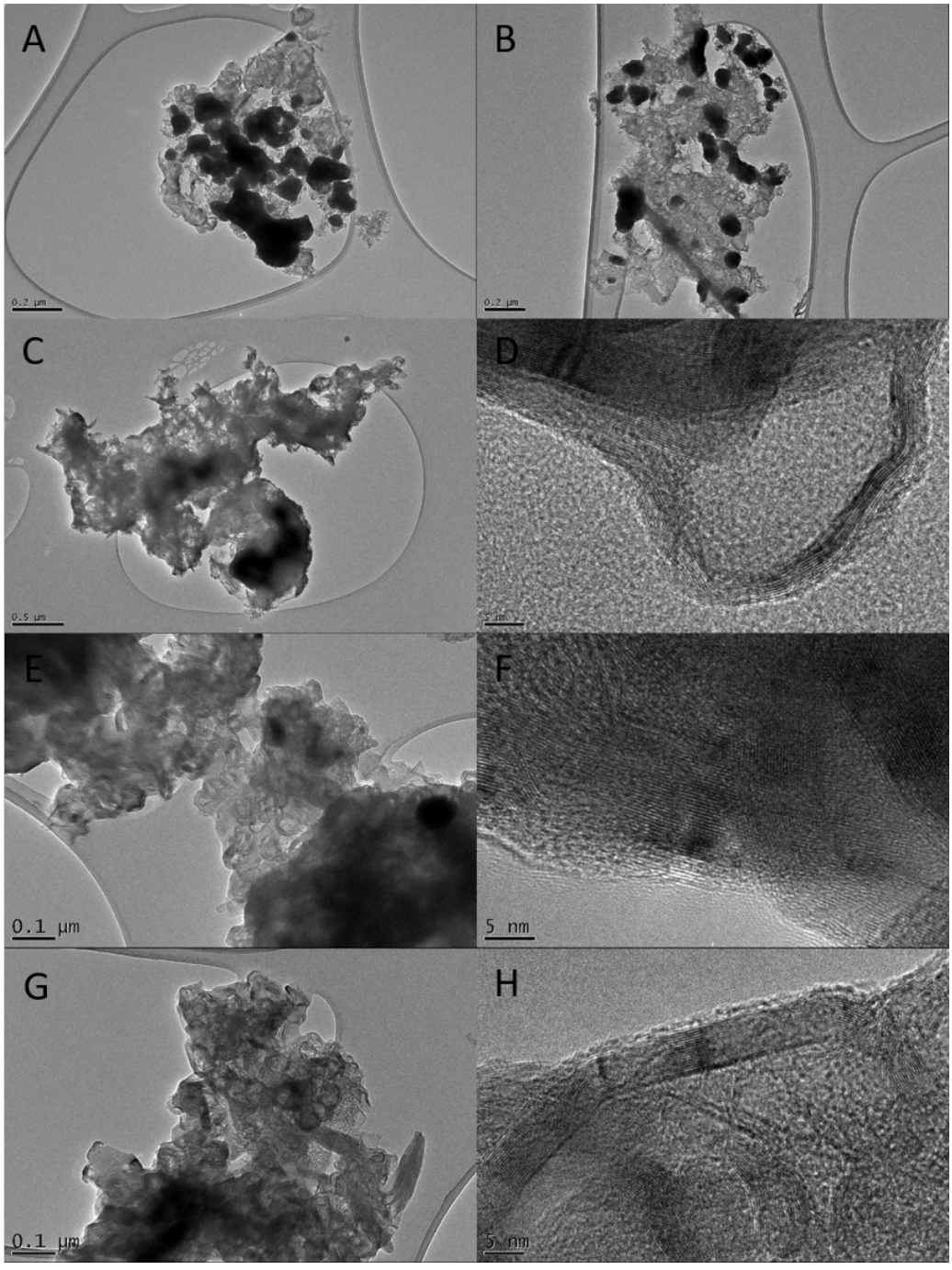

Figure 4.12: TEM images of A) and B) Pre acid wash Co doped 80% carboHIPE, C) and D) post acid wash 80% carboHIPE and E) and F) post acid washed 85% carboHIPE and G) and H) post acid washed 90% carboHIPE.

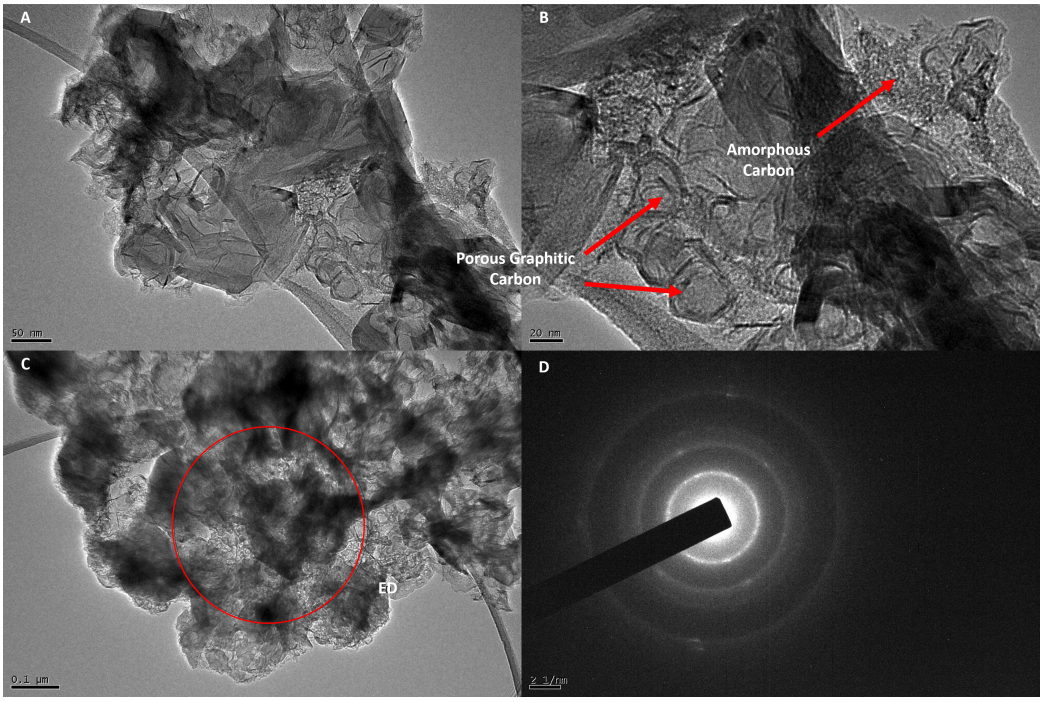

Figure 4.13: A) - C) TEM images of metal doped 85% carboHIPE and D) electron diffraction of region shown in C).

For comparison, figure 4.14 shows the 80% blank carboHIPE. It can be cleary seen that the carbon has no graphitic character and that the structure was largely destroyed in the carbonization process.

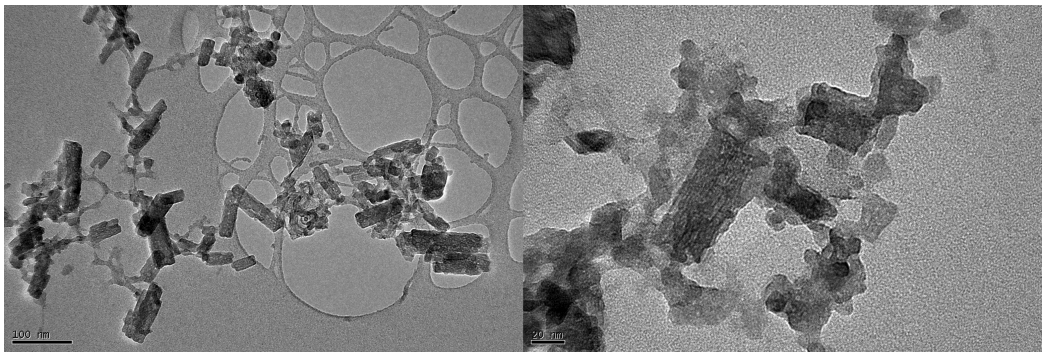

Figure 4.14: TEM images of 80% blank carboHIPE.

4.3 Metal PolyHYPE Annealed in Air to Generate Metal Foam followed by CVD

A similar methodology to that used in section 3.2 was used to produce graphene from a cobalt polyHIPE. First, a cobalt polyHIPE was synthesised as done previously in this chapter. This cobalt polyHIPE was then annealed in air at 600 ℃ for 4 hours. This produced a cobalt scaffold shown in figure 4.15 A and B. A methane CVD was then conducted on the cobalt scaffold (figure 4.15 C) and the carbon produced was characterised by Raman spectroscopy (figure 4.15 D). Cobalt was the only metal used for these experiments as that is the metal which had most success in chapter 3.

Figure 4.15 A and B show that a cobalt scaffold was created with a regular macrostructure. The SEM images also show that the surface of the cobalt foam is very rough and therefore likely to inhibit the growth of graphitic carbon. Figure 4.15 C shows that even after the cobalt foam undergoes the high temperature of the CVD process, the surface remains rough. The Raman spectra in figure 4.15 D is more indicative of graphite as shown by the I_G/I_{2D} ratio of approximately 1.9 and a FWHM of 80 cm^{-1}.[75] The absence of the D peak, which is indicative of defects, sugests that the graphite is pristine and it is likely with careful control of conditions, graphene could be synthesised.

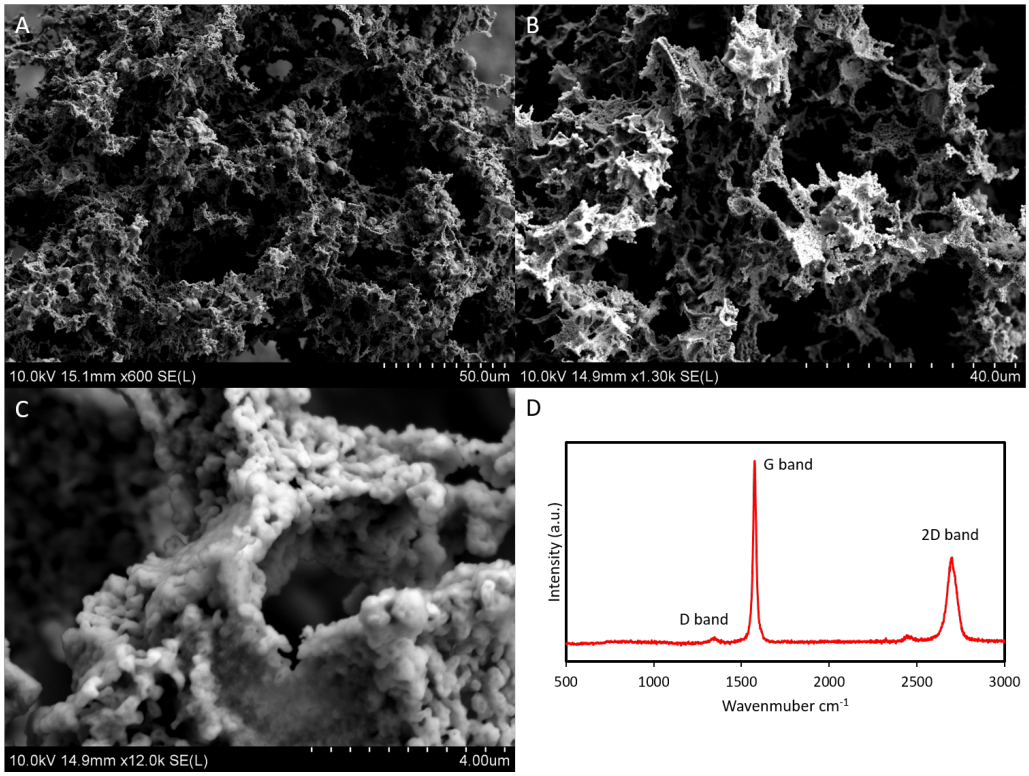

Figure 4.15: SEM images of A) and B) polyHIPE derived Co foam, C) polyHIPE derived Co foam after CVD and D) Raman spectra after CVD on polyHIPE derived Co foam.

4.4 Conclusions and Future Work

Porous graphitic foams were produced through a novel method of doping polyHIPEs with metal particles. Three different porosities of polyHIPE were prepared by varying the amount of continuous phase relative to droplet phase and the effect on the structure was apparent. This change in structure was translated into the carboHIPEs. The effect of the metal was twofold, it can be clearly seen that the metal particles are imperative in maintaining the structure of the foam while also graphitising the carbon. Figure 4.10 shows that the degree of graphitisation is increased in the lower porosity materials, owing most likely to having a greater proportion of metal present in the sample. Methods in the literature have managed to produce carboHIPEs which were not graphitic through primarily the use of sulfonation prior to carbonization, in order to maintain the stability of the foam.

The excitement surrounding carbonizing polyHIPEs is largely due to the control over pore size and porosity available in the polyHIPEs. Only one method of controlling the pore size was utilised in this chapter. Alternative methods for controlling the porosity of the starting polyHIPE includes using different organic porogenic solvents. It was found that by changing from toluene to 2-chloroethylbenzene produced an increase in BET surface area from 350 m^2g^{-1} to 550 m^2g^{-1}.[241] By changing the solubility parameter of the solvent closer to that of the polymer, phase separation occurs later during the polymerisation, producing smaller microgel particles with smaller pores between them.[255]The void diameter can be increased by adding water-miscible organic species to the HIPE aqueous phase, promoting Ostwald ripening.[255] In the case of styrene/DVB HIPE, increasing the ratio of DVB causes the void diameter to decrease. This was attributed to the droplet diameter decreasing because of the increased hydrophobicity of DVB compared to styrene. Changing surfactant has also shown to have a large effect on porosity for similar reasons. Increasing surfactant concentration stabilises the emulsion allowing smaller droplets to exist, decreasing void diameter size.[241]

The use of polyHIPEs to template the growth of metal scaffold, which could then undergo a traditional CVD was only briefly looked into. This is much like the use of a metal doped hydrogel to produce a metal scaffold described in chapter 3. Very high quality graphene was produced in that section and by optimisation of the CVD conditions and metal catalyst, similar results could be achieved with a polyHIPE derived metal scaffold with the advantage of increased control over porosity as described above. The SEM images in figure 4.15 suggest that the biggest prohibiter for the growth of pristine graphene from these metal scaffolds is the surface roughness. Surface roughness has been shown to promote multi-layer growth.[88] Parameters could be optimised to smoothen the surface such as pretreatment of the metal scaffold, increased annealing times and changing hydrogen concentration.[66,127] All of these have been shown to affect the surface roughness of metal foils.

Parameters in the above synthesis could be optimised. Using cobalt catalysts mean that it is unlikely to require temperatures as high as 1000 °C and similar degrees of graphitisation with such a catalyst has been acheived at temperatures as low as 700 °C.[256] The choice of metal could be varied, cobalt was chosen as that had most success in chapter 3, however, the few experiments conducted on nickel derived carboHIPEs looked promising and so iron may well show equal promise. It is unlikely that copper would be an effective catalyst for the same reasons concluded in chapter 3. The role

of hydrogen in formation of graphitic carbon is not conclusive and it may well be possible that more graphitic material is produced in the absence of hydrogen.

Testing the material in electrochemical applications would be worthwhile. The material in its current form is not strong enough to form a free standing electrode but it could be coated onto a current collector and electrochemical data collected through that method. Efforts could be made to make it strong enough to act as a free standing electrode including sulfonation.[243,244,247–249] Initial experiments to sulfonate metal-doped polyHIPEs however were not successful in achieving the desired graphitisation seen without the sulfonation step, as shown by Raman spectroscopy.

+

Chapter 5

Templated Carbon Growth on Copper Oxide Polyhedra

5.1 Introduction

Templated carbon growth is the synthesis of materials where the structure of the synthesised carbon copies that of the template material, usually a catalyst. Templating the growth of graphene should allow a greater control over its properties. It has been shown that the shape of the graphene effects electronic structure with graphene nanoribbons having a band gap.[257] Differing sizes of graphene sheets have also been found to have different composite reinforcing effects.[258] Another advantage is being able to grow graphene on a powder, this should provide a larger surface area and therefore a greater yield of material. So far, bottom-up synthesis of graphene has been performed on metal foils and so a very small amount of graphene has been produced. Synthesis on a powder might allow for the bulk production of bottom-up graphene.

Numerous examples of templated growth exist in the literature, particularly for the synthesis of graphene. These include graphene nanoribbons on nickel nanobars,[130] and on copper ribbons,[131] mesoporous graphene nanoballs from polystyrene beads,[259] graphene nanoballs from nickel nanoparticles,[260] graphene nanotubes on nickel and copper nanotubes,[261] graphene sheets from iron bars,[106] and the formation of few-layer graphene nanoribbons by growth on zinc sulphide ribbons. These were grown through a con-

ventional methane CVD and the resulting graphene ribbons mirror the zinc sulphide catalyst near perfectly and can be isolated from the catalyst.[132] Although, not a common catalyst for carbon growth, zinc has been used in the growth of carbon nanotubes.[132,262]

These methods have substantial drawbacks and difficulties. The quality of the graphene produced from polystyrene beads and copper ribbons was of poor quality.[131,259] This could be due to not being able to achieve the high temperatures required for graphitisation. A common problem with small particles is that they experience a large melting point depression, and often deform at the high temperatures required for graphitisation.[263] This effect was observed in the synthesis on copper nanotubes, where the copper nanotubes would collapse,[261] or become deformed, passing on these defects to the synthesised graphene. Poor quality also results when growing on small particles as only small graphitic domains will result, the material produced will therefore have more domain boundaries and a greater proportion of edges. Another problem, which was observed during the synthesis on iron bars, is the production of CNTs. Small particles, particularly of nickel and iron, have always favoured the synthesis of CNTs.

Alternative methods to grow templated graphene exist. One such method is patterning the metal foil into the desired shapes and then performing a conventional CVD. Areas of the foil are removed and so no graphene grows in these regions.[38,101] Another method of producing graphene nanoribbons has been to deposit nickel onto a silicon wafer and then carry out a standard CVD. The nickel can then be etched away leaving a ribbon of graphene.[264] These methods both suffer from being very low yielding and hard to scale. Another solution to the problem of templated growth is using a carburisation step at low temperature. Graphene nanoballs have been synthesized by the carburisation of nickel nanoparticles in ethylene glycol followed by a high temperature anneal to graphitise the carbon.[265] Since the carburisation occurs at a low temperature of 250 °C, the morphology of the nickel particles is protected. This however adds an extra step, it also appears that the graphitisation step requires a higher temperature than that used for normal CVD.

The first step in designing a new system for templated graphene growth is finding a suitable templating catalyst. A wide range of literature exists in controlling the morphology of metal particles due to their applications in catalysis. The criteria required was a catalytically active metal (iron, nickel, cobalt or copper) with a large flat face in which graphene could

grow. The catalyst would ideally be microns in dimensions as nanoparticles could make the synthesis of CNTs more likely. Metal oxides are acceptable as the graphene synthesis occurs in a reducing atmosphere, however, it is likely that this process will result in a change in morphology. Here we propose to grow graphene on a copper catalyst, which should provide the highest quality graphene, in the shape of square platelets. This is outlined in figure 5.1. We synthesised copper oxide cubes which then underwent a CVD process that would reduce them to copper metal, hopefully retaining the cube shape for subsequent graphene growth. Copper is an ideal choice of catalyst material as the graphene growth is self limiting to the monolayer due to the surface based mechanism.[266]

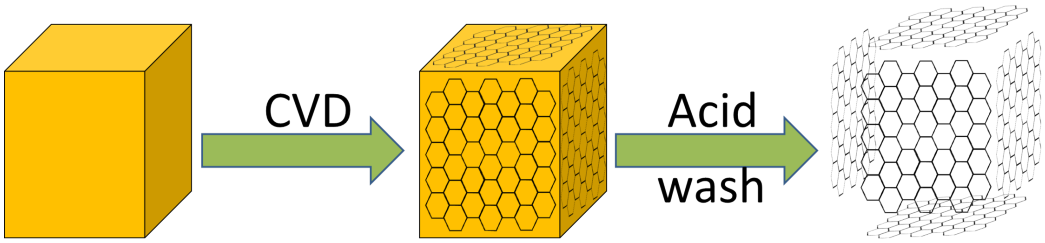

Figure 5.1: Scheme showing the synthesis of graphene from a copper cube catalyst. First, the copper cube undergoes CVD, where graphene grew on each of the faces of the cube. The underlying copper cube is then etched away, leaving graphene.

5.2 Synthesis of Templated Carbon from Copper Oxide Polyhedra

5.2.1 Synthesis of Cu_2O Polyhedra

Cu_2O microcubes were synthesised according to a process described by Liu *et al.*[267] Briefly, an aqueous solution of copper acetate was refluxed with sodium hydroxide before glucose is added and the solution is allowed to cool. The resulting solid was then separated by centrifugation and dried in a vacuum oven at 60 °C. SEM images and pXRD of the resulting material is shown in figure 5.2.

The SEM image in figure 5.2 shows that truncated edge cubes were

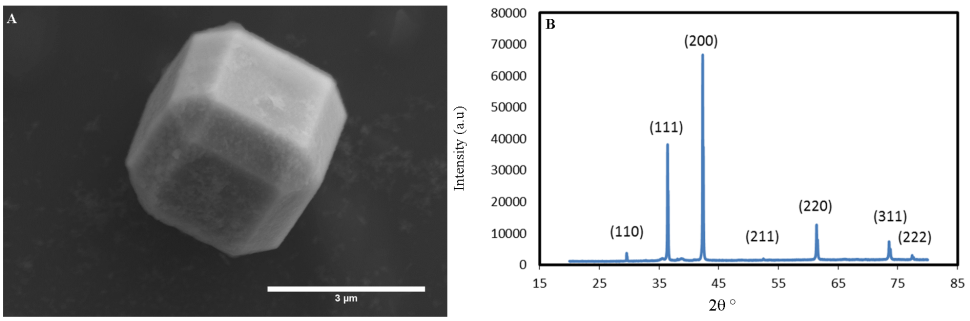

Figure 5.2: A) SEM image of Cu_2O microcube and B) XRD pattern of Cu_2O microcubes.

produced with approximately three micron sized square faces which should be suitable to grow graphene on. The faces are of the orientation {100} which has been shown to be suitable in the growth of graphene before.[268] The Cu_2O cube also contains six pairs of {110} facets and four pairs of {111} facets. The diffraction peaks are indexed according to the standard cubic structure of Cu_2O (space group: $Pn3\overline{m}$). No impurities such as copper or copper (II) oxide were detected in the sample. The synthesis of the truncated-edge polyhedra required very precise control of the conditions. Very small changes in temperature or reagent concentrations resulted in very different morphologies of product.[267]

The following reactions are believed to take place in the Cu_2O synthesis:

$$\mathrm{Cu^{2+} + 2\,OH^{2-} \longrightarrow Cu(OH)_2}$$
$$\mathrm{Cu(OH)_2 + 2\,OH^{2-} \longrightarrow [Cu(OH)_4]^{2-}}$$
$$\mathrm{2\,[Cu(OH)_4]^{2-} + C_6H_{12}O_6 \longrightarrow Cu_2O + C_6H_{12}O_7 + 4\,OH^{-} + 2\,H_2O}$$

NaOH is used as a coordinating agent and the concentration of OH^- affects reaction rate and therefore the morphology of the resulting product. The glucose acts as a mild reductant. The use of acetate as the copper salt is important as it is believed that the CH_3COO^- plays a role in both adsorbing onto different faces of the Cu_2O seeds inhibiting growth in that direction, and also etching some specific sites in the {100} facets, leading to the appearance of {110} facets at higher temperature.[267] The CH_3COO^- preferentially adsorbs onto different sites due to the sites differing properties. For instance the {100} facet is polar surface while the {111} facet is a

non-polar surface.[267]It is thought that the CH_3COO^- ions selectively adsorb onto the {111} facets due to there lower surface energy and stabalise them, confining growth in that direction.[267] By varying the ratio of growth rate in the {111} and {100} directions, a variety of shapes can be made. When the {100} direction is growing faster than the {111} direction, octahedrons are produced. While if the growth in {111} direction is faster, cubes result.[267] It is also thought that the CH_3COO^- oxidatively etches specific sites on the {100} facet resulting in the appearence of some {110} facets.

Although the CVD reactions will be performed well below the melting point of the copper. It is known that smaller particles have depressed melting points,[133] and are likely to deform and agglomerate at lower temperatures due to the higher surface energy of the the nanoparticles.[263] To test the morphological resistance of the Cu_2O template to heat, experiments were performed heating the catalyst up to various temperatures with no carbon source and observing how their shape changed. Another comparison to make is the effect of hydrogen on the polyhedra. Hydrogen would be necessary to reduce the copper oxide polyhedra to copper metal, an active catalyst for carbon growth. The hydrogen for the carbon growth is generated *in situ* from the decomposition of ethanol.[269] Indeed, copper oxide has been shown to be reduced with a flow of argon/ethanol.[270] In order to test if there is any morphological change upon the reduction, blank runs were carried out with and without hydrogen. Figure 5.3 clearly shows that there are no major morphological differences between the two temperatures and that the cube shape is maintained reasonably well, especially when no hydrogen is introduced into the gas stream. This suggests that any difference in products between the two temperatures will likely be due to either the difference in the break down of ethanol at these temperatures or the interaction between the copper oxide and ethanol at the different temperatures. Control runs were also tried at 1000 °C and the Cu_2O catalyst disintegrated into very small fragments (appendix B figure 8.9). This ruled out using a higher temperature.

5.2.2 Ethanol CVD on the Cu_2O Polyhedra

Carbon was grown onto the catalyst particles using CVD. This process is described in detail in the section 1.4.1, but briefly, it is where a carbon containing feedstock is blown over the catalyst at high temperature. The catalyst then facilitates the decomposition of the feedstock into elemental carbon which then graphitises.

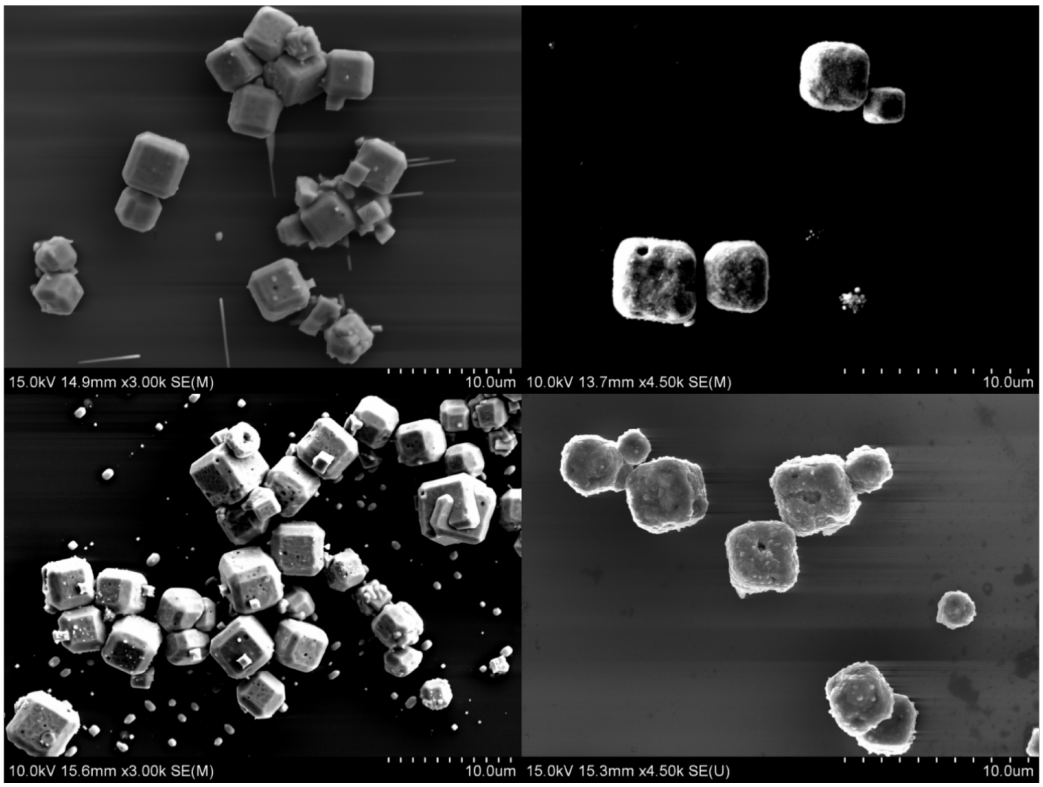

Figure 5.3: Top: SEM images of Cu_2O catalyst heated to 750 °C under a flow of left) argon and right) argon and hydrogen. Bottom) SEM images of Cu_2O catalyst heated to 820 °under a flow of left) argon and right) argon and hydrogen.

The Cu_2O catalyst was spin-coated onto a silicon wafer in order to maximise separation between particles and to minimize agglomeration of the catalyst particles. Ethanol was used as the carbon source by blowing the carrier gas (argon) through absolute ethanol over the catalyst. The catalyst on the silicon wafer was placed in the centre of a quartz furnace tube inside a furnace and then treated at different temperatures. A schematic of the set up is shown in figure 5.4. Ethanol was chosen as the carbon source as it has been used previously to grow carbon nanomaterials on copper, including graphene,[116,271,272] carbon nanotubes,[270] and carbon nanofibers.[273] It is also the most widely used carbon source for CVD outside of methane but has some advantages over methane. It is less explosive, while also decomposing at a lower temperature than methane which is important as the catalyst is destroyed at high temperature. Ethanol CVD has been performed at tem-

peratures as low as 650 °C.[116] Much work on the decomposition of ethanol has been done in relation to the cracking of it in order to make hydrogen. The predicted decomposition products for ethanol at high temperatures and when catalysed by copper are:[269,274,275]

$$\begin{gathered}
C_2H_5OH \longrightarrow C_2H_4 + H_2O \\
C_2H_5OH + H_2O \longrightarrow CO + CO_2 + 5\,H_2 \\
C_2H_5OH \longrightarrow CO + CH_4 + H_2 \\
C_2H_5OH \longrightarrow C_2H_4O + H_2 \\
CO + H_2O \longrightarrow CO_2 + H_2 \\
2\,C_2H_5OH \longrightarrow (C_2H_5)_2O + H_2O
\end{gathered}$$

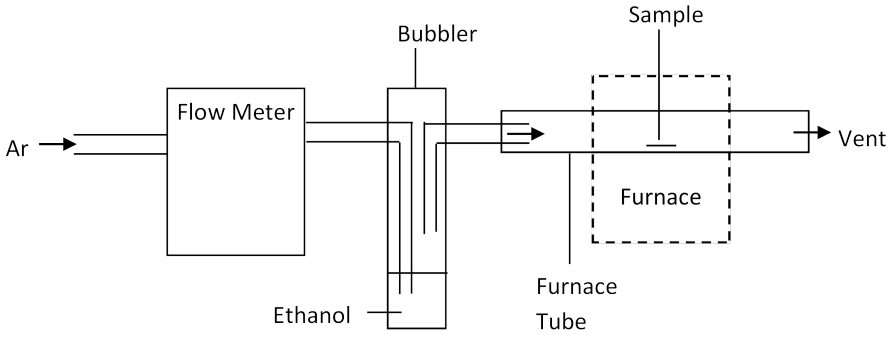

Figure 5.4: Scheme of the ethanol CVD setup used to grow carbon on the Cu_2O polyhedra.

After performing the ethanol CVD on the catalyst particles and analysing the results, two distinct products were observed depending on temperature the CVD was carried out. When the CVD was performed At 750 °C, carbon cube structures were primarily synthesised, while at 820 °C the major product were these fibrous like structures which will be referred to as carbon rings. At temperatures between 750 °C and 820 °C a mixture of both products were formed.

5.2.3 Carbon Cubes

By undergoing the ethanol CVD described above at 750 °C and dwelling there for 60 minutes, carbon cubes were synthesised as shown in the SEM

images in figure 5.5.

Figure 5.5 shows clearly that carbon cubes were produced from the copper catalyst while the copper catalyst deforms into a more rounded shape. By mixing signals from the BSE and SE detector, images can be collected which give an insight to the elemental composition of each structure. This is shown in figure 5.5 (B). This shows the heavier elements which dominate the SE detector as red (copper and the silicon substrate) while the lighter elements (carbon) appear green. This can also be observed with the EDX map in figure 5.5 (C, D and E) where the cube like structure is predominantly carbon (blue) while the higher contrast material is shown to be copper (red). It is interesting to note that while the carbon is cube like in shape, much like the starting Cu_2O catalyst, the copper has consistently deformed into a smoother more spherical structure. The EDX point spectra did not detect any oxygen (0.5 KeV) over the cube, suggesting that the copper oxide has been fully reduced to copper metal. These carbon structures are unlike anything which has been reported previously.

The Raman spectra shown in figure 5.6 (B) shows the typical bands for carbon with a D, G and a broad 2D band. The high D peak indicates the defective nature of the carbon, which may originate from distorted hexagonal sp^2 carbon,[167] strain induced effects,[276] and small particle sizes.[227] This will be exacerbated by the small size of the laser spot. The spot size of the laser beam is approximately 1 µm, not much smaller than the catalyst particles. It is therefore likely that the signal would be dominated by edges and contribute to the large D band. The very small and broad 2D band can be explained by a nonplanar structure of the carbon material.[277] The broad region is likely composed of multiple peaks, including the 2D and D + G bands at 2694 and 2901 cm^{-1} respectively. The D + G originates from the strained structure.[278,279] The presence of amorphous carbon or highly defective graphitic material is not surprising as the temperature used is far too low to encourage graphitisation on a copper catalyst. X-ray diffraction (XRD) was taken of the sample on the silicon wafer and the diffractogram can be seen in figure 5.6 A). The silicon peaks and copper metal peaks are highlighted. No copper oxide peaks were observed suggesting that all the catalyst is reduced to copper metal. No carbon could be detected in the XRD. This was expected as only a small amount was present on the silicon wafer and the carbonacious material was not particularly crystalline, as confirmed by the Raman.

TEM grids were prepared by sonicating the silicon wafers in ethanol for 15 minutes and then dropping the solution onto holey carbon TEM

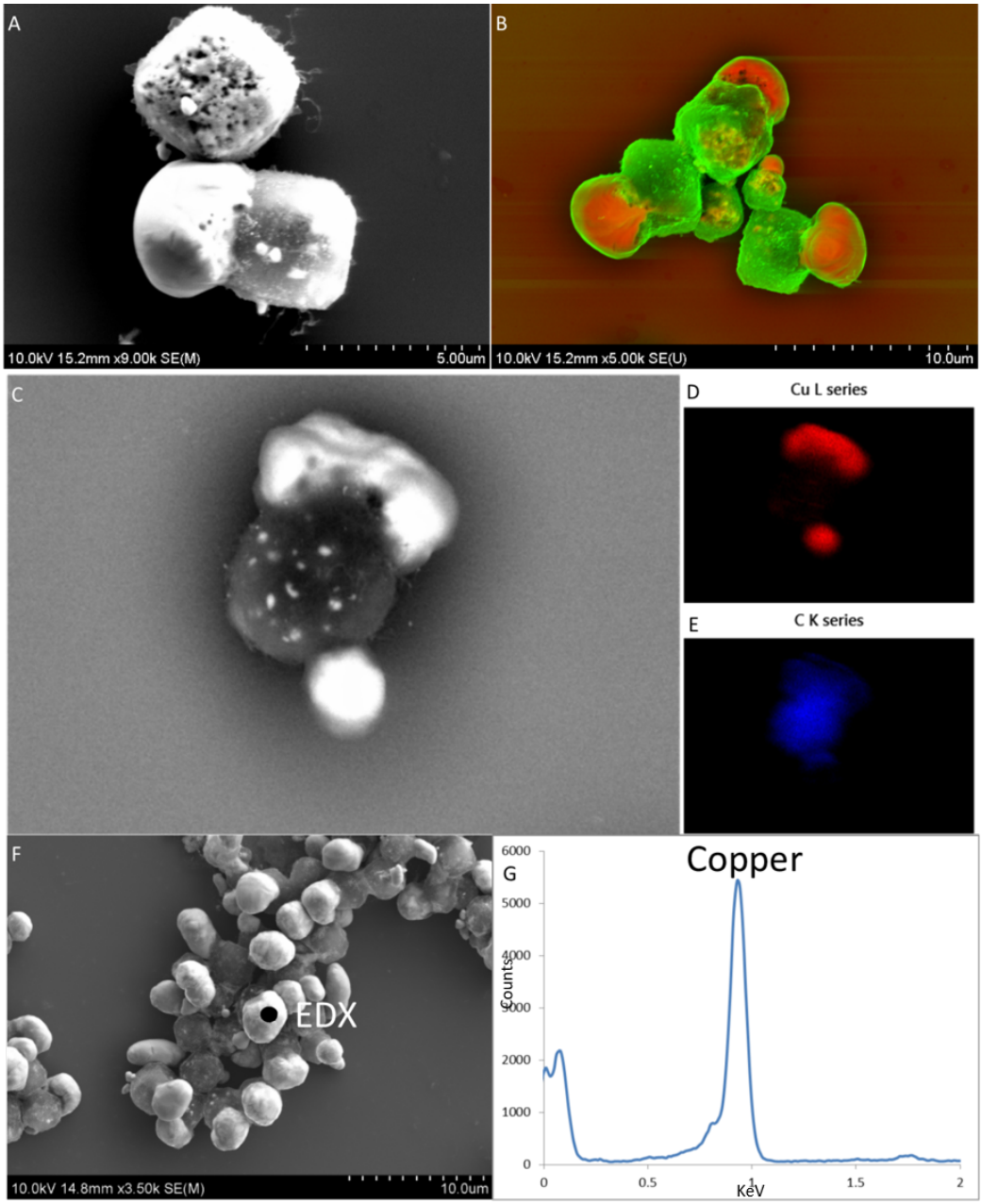

Figure 5.5: A) SEM image of carbon cubes and copper catalyst and B) SEM image of carbon cubes and copper catalyst after mixing the SE and BSE signals. Copper shown in red, carbon in green. D) and E) EDX maps taken of the image in C) where D) shows the copper and E) shows the carbon. F) Image of the copper catalysts and carbon cubes and G) EDX spectra of the region indicated in F)

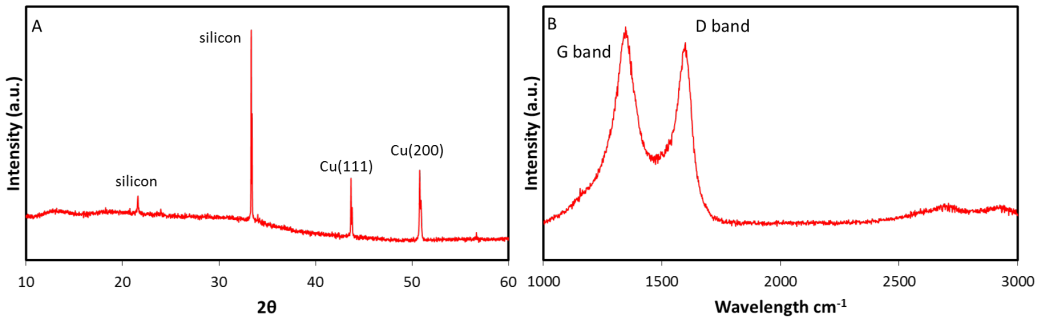

Figure 5.6: A) XRD pattern and B) Raman spectra taken of the carbon cubes produced at 750 °C on a a silicon wafer substrate.

girds. The TEM images (5.7) show what looks to be carbon nanofibers (CNFs).[280,281] As far as we are aware, the arrangement of CNFs into such a macrostructure as observed in figure 5.5 has never been reported before. Carbon nanofibers have been grown on copper catalysts before,[282 283] typically however, it has been iron or nickel catalysts used for the synthesis of carbon nanofibers.[74] This is because many of the theorised mechanisms for CNF synthesis require the carbon to dissolve into the metal catalyst. Copper has a much lower carbon solubility than nickel and iron.

The mechanism for CNF and CNT growth has been widely discussed. Traditionally the vapor-liquid-solid mechanism,[284,285] has been applied whereby the carbon containing feedstock gas dissociates and the carbon dissolves into the liquid catalyst. The carbon then migrates through the bulk of the catalyst and precipitates out on the other side. It has even been applied

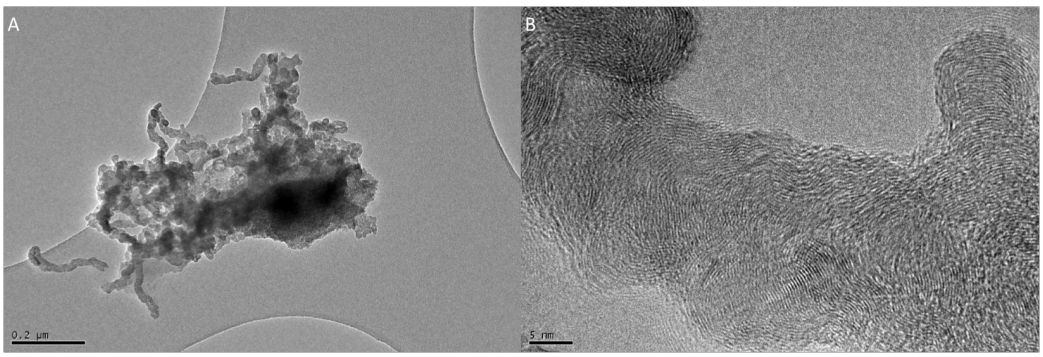

Figure 5.7: A and B) TEM images of the carbon cubes taken at 80 kV.

to the synthesis of CNTs from copper, despite coppers very low carbon solubility.[270] This mechanism has been challenged when CNTs and CNFs were grown on catalysts well below their melting point, however the mechanism is still possible due to the melting point depression experienced by nanoparticles.[133] The observation of CNFs from our catalyst particles however, put the VLS mechanism in further doubt as micron sized particles are unlikely to experience the same melting point depression experienced by nanoparticles.

An alternative mechanism is one where the catalyst particle remains solid and the carbon feedstock dissociates on the surface of the particle, and then migrates, either on the surface or through the bulk to the other end of the catalyst, where it then precipitates out.[286] The process is usually terminated when the exposed face of the metal catalyst is coated in carbon,[287] deactivating it. It is a concentration gradient which drives the migration and it is a temperature gradient, arising from the decompostion of feedstock gas being exothermic, which results in the carbon precipitating at the other end of the catalyst.[288,289]

The HRTEM image in figure 5.7 B) shows some degree of graphitic character and is in agreement with the Raman. The lines which can be observed arise due to graphitic planes folding upwards in the TEM. By measuring the distance between those lines the interlayer separation between the graphitic planes can be deduced. The value is 0.36 nm, slightly more than the 0.34 nm expected for graphite. CNFs have been reported to be more disordered than graphite and have an extended interlayer separation.[286] This agrees with the Raman spectra in figure 5.6.

To try and get an insight into the structure and perhaps the mechanism for the formation of these carbon cubes, the sample was cut in halve using a focused ion beam (FIB) so the cross section could be imaged. In collecting these images, the material is coated in platinum in order to protect it while manoeuvring the ion beam. The ion beam then mills through the sample and then the cross section is imaged. Figure 5.8 A) shows this cross section, on the left is the carbon cube and it can be seen that it has a porous structure with some copper still remaining in the carbon structure. As far as we are aware, this is the first instance that CNFs have arranged themselves in such a porous macrostructure, the only similar material we have come across is a dense network of CNFs.[290] The dense network is due to numerous strands of fibres growing off every facet of their nickel catalyst, it is described as an octopus-growth mode and occurs for the growth on larger nickel particles.[290]

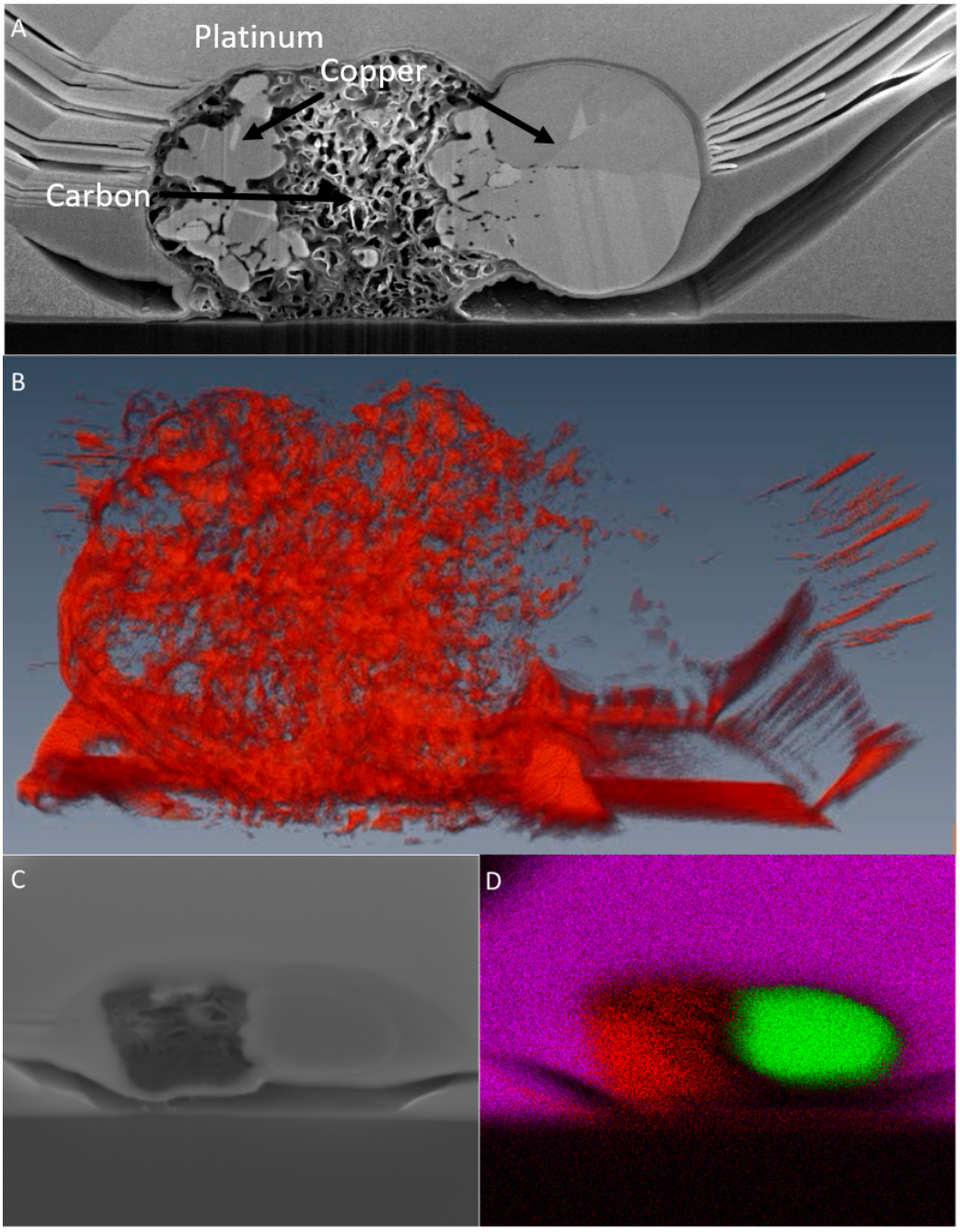

Figure 5.8: A) SEM image of a cross section of the carbon cube and catalyst. B) Reconstruction of the carbon appearing in image A) built up from 200 cross sections of the region using AMIRA software. C and D) SEM image and EDX map of the a cross section of the carbon cube and catalyst. Platinum in pink, carbon in red and copper in green.

The copper can be clearly distinguished from the platinum and carbon due to the appearance of the grain boundaries. The presence of copper inside the carbon cube might give evidence that the carbon is dissolving into the copper. However, according to the Cu-C phase diagram, carbon does not dissolve into copper in significant quantities until the temperature is in excess of 1100 °C. However, the continuous observation of copper catalysing the growth of carbon nanotubes,[270,291] has led to the belief that carbon can dissolve into copper nanoparticles at these temperatures. It is known that smaller particles, due to the high surface to volume ratio, have increased solid solubility.[133] In our case however, it is micron, not nanoparticles that are in use.

By milling 108 different slices of the material and then taking an image after each slice, a 3D structure of the carbon cube can be built up. This is shown in figure 5.8 B). This 3D reconstruction of the carbon cube clearly shows the porous structure of the carbon cube. An EDX map of the image in figure 5.8 C) is shown in figure 5.8 D) showing the platinum in pink, the carbon in red and the copper in green.

Figure 5.9 shows a potential timeline for the formation of the carbon cubes. All images were taken from the same sample. Line 2 shows BSE images of the sample with copper appearing with a high contrast and carbon a much lower contrast. line 4 displays cross sections produced with the FIB of the images in line 3. Line 2 and 3 in stage 1 both show primarily what is a copper cube. The cross-section in line 4 agrees with this showing mostly a copper cube with some carbon apparent, primarily at the edge. At stage 2, all three lines show the copper begin to separate, lines 2 and 3 show the carbon cube begin to form with the much smaller and smoother copper slightly protruding out of the cube. Line 4 clearly shows large copper domains beginning to form at the other end to where the carbon cube is beginning to take shape. Stage 3 shows further separation between the copper and carbon cube in all three lines. Line 4 shows us that some residual copper still remains inside the carbon cube. Line 1 is a schematic of the process. The idea of the metal particle being squeezed out of a carbon structure is not a novel one. For CNFs synthesised from nickel catalysts during a methane CVD, it is believed that nickel carbide is formed, this carbide phase then decomposes into metallic nickel and graphite that encapsulates the nickel particle. Pressure then builds up due to the formation of graphite layers at the internal surface of the nickel and graphite, forcing the nickel catalyst out. This nickel catalyst then continues to catalyse more CNF formation.[286] This is not what is happening here, as the newly exposed copper metal

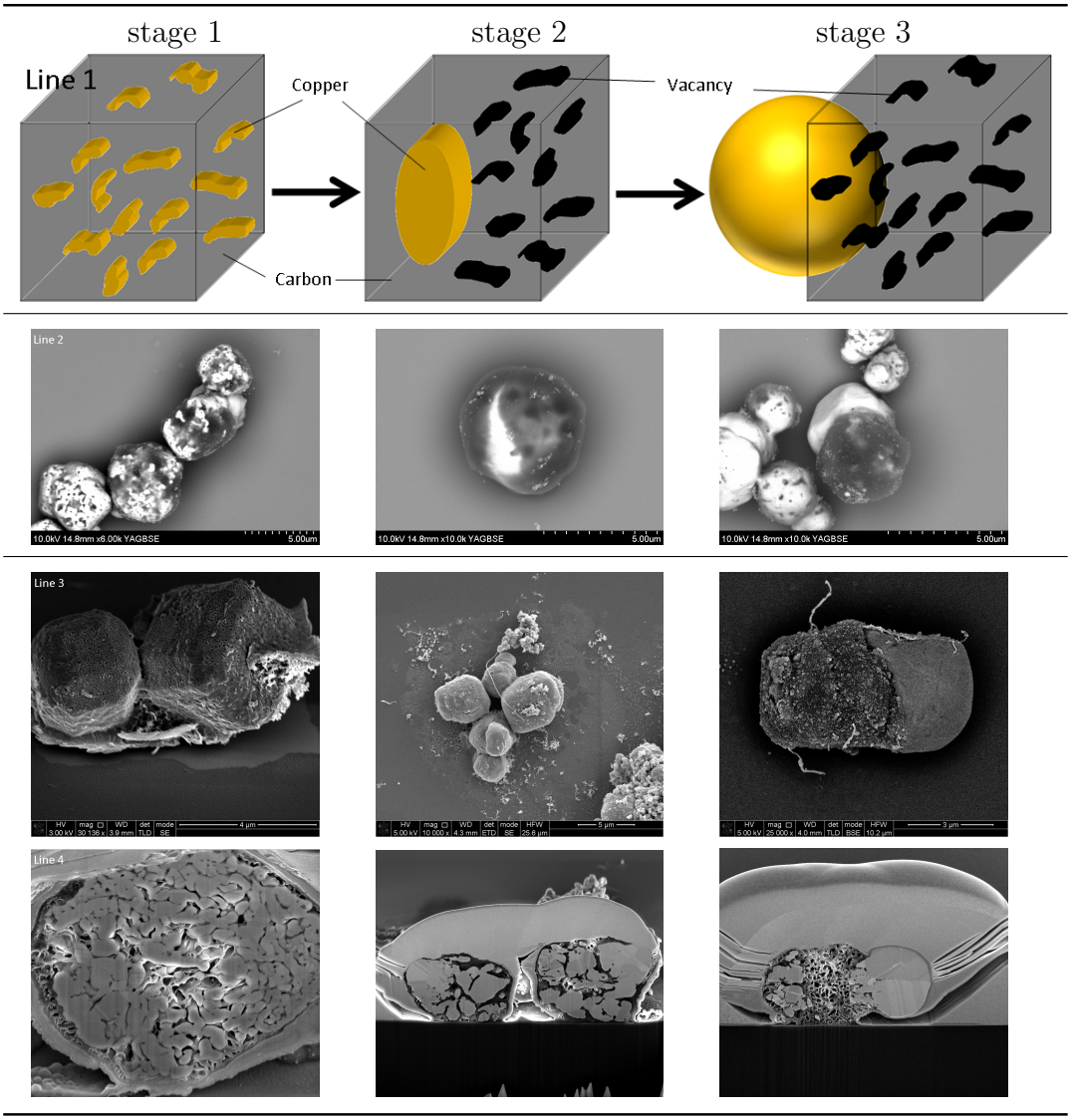

Figure 5.9: Theorized mechanism for the synthesis of carbon cubes, line 2 - 4 showing SEM images of three stages, stage 1, mixing of the carbon and copper. Stage 2, segregation of the carbon and copper then stage 3, extrusion of the copper leaving the carbon cube. Line 2 is BSE images. Line 4 is SEM images of the cross sections of the images in line 3. Line 1 is a schematic of the three stages.

is not catalysing any more carbon growth. This suggest that it is upon cooling, when no more ethanol is reacting, that the cubes form and the copper becomes exposed.

5.2.4 Solitaire Rings

By increasing the temperature at which the CVD was carried out from 750 °C to 820 °C, but maintaining the dwell time at 60 minutes, a very different product could be observed. SEM images in figure 5.10 shows a helical ring like structure. The EDX map in figure 5.10 C,D and E shows carbon growing out from the catalyst particle on both sides. BSE images of the product (figure 5.10 G) also show this with the red showing material with high BSE signal (copper and silicon) while green shows material with much less of a BSE signal (carbon). A close up the carbon material (figure 5.10 F) shows that is a very fibrous like structure. A small amount of carbon nanotubes can also be observed, these are formed from very small copper fragments produced during the high temperature treatment.

An extensive literature search has deduced that the material produced is most similar to helical carbon nanofibers or carbon belts.[292] Carbon nanofibers commonly form microcoils as defects in the graphene layers bend the fiber round.[86] It is believed that fibres grow from each of the facets of the metal particle and entangle, giving the rope like appearance.[292] Microcoils have been synthesised via a range of techniques including aerosol chemical vapour deposition from a benzene/ferrocene solution,[293] growth on copper nanoparticles,[294–298] growth on nickel nanoparticles,[86,299,300] and growth on iron catalysts.[293,301]

Numerous studies have suggested that changing temperature of the CVD,[293,302] or morphology of the catalyst,[86,293,294,299,303] has a large effect on the product. The decomposition products of ethanol will be slightly different at the different temperatures, it is likely that more hydrogen would be produced at the higher temperature.[274] Hydrogen reduces the amount of carbon atoms formed and can therefore prevent encapsulation and deactivation of the catalyst.[86] This allows the catalyst to be active for longer and may be responsible for the vast increase in carbon seen at 820 °C.[86] If the C-atoms are formed too quickly on the surface, faster than they can diffuse through the catalyst, the surface will become coated and no clean metal surface is available to dissociate the feed gas and the catalyst becomes deactivated.[86]

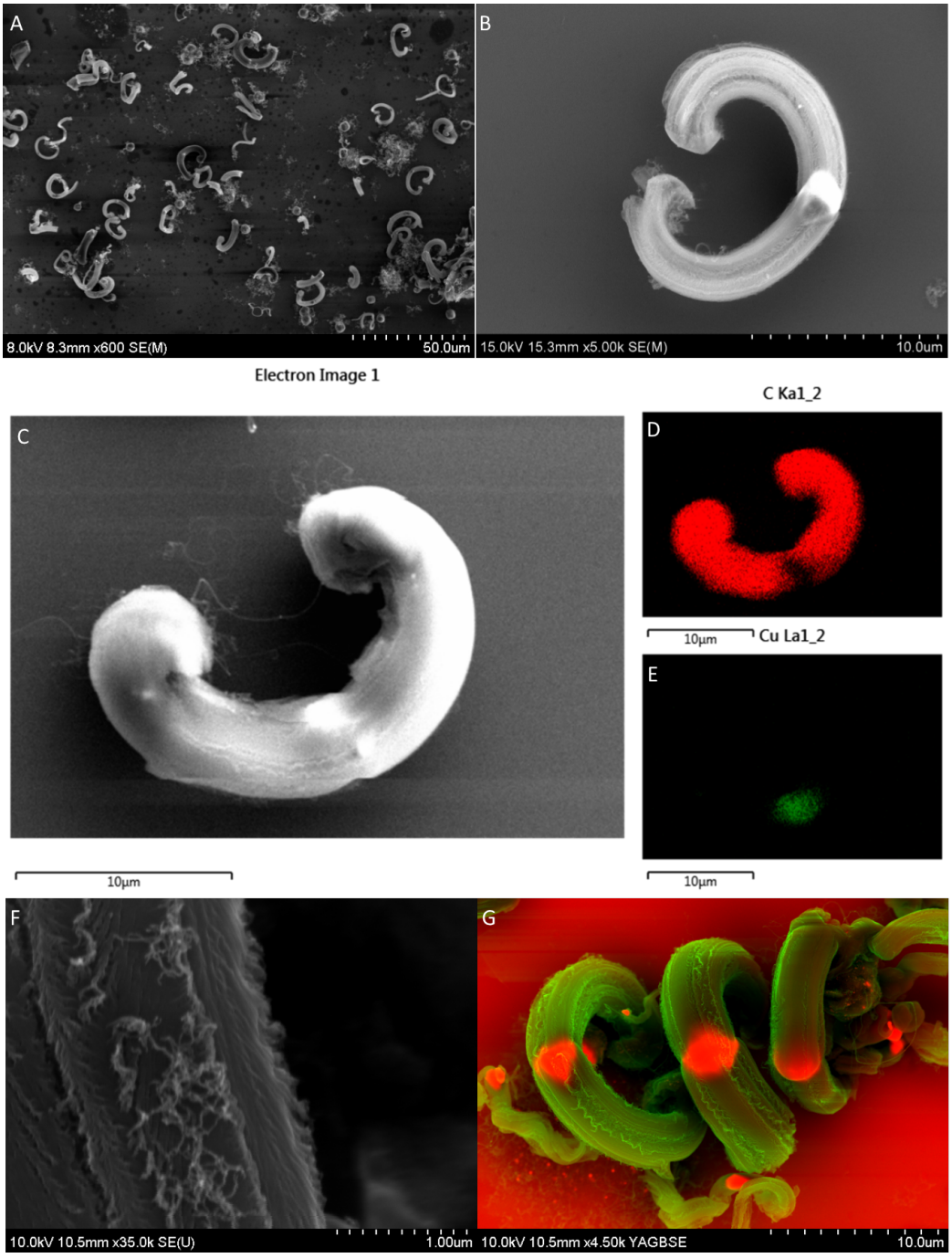

Figure 5.10: A and B) SEM images of carbon rings D and E) EDX maps showing where the copper (green) and carbon (red) are loacted in image C), F) SEM image showing the fibrous carbon structure and G) SEM image after mixing the SE and BSE signals. Copper shown in red, carbon in green.

Another observation made is that more spherical particles are more able to break down feed gases. This is due to more active surfaces being present in the particle.[86] It is likely that the higher temperature causes the copper catalyst to deform more allowing it to break down more of the ethanol, producing more hydrogen.

Figure 5.11 shows a cross section of the ring like macrostructure. This was performed in the same way as in figure 5.8 (A) with the focused-ion beam. It appears that there is a stream of copper dissecting the carbon structure through the middle. The porous carbon structure looks very similar to that observed with the carbon cubes. This suggests the same material is being produced but just a different macrostructure is observed.

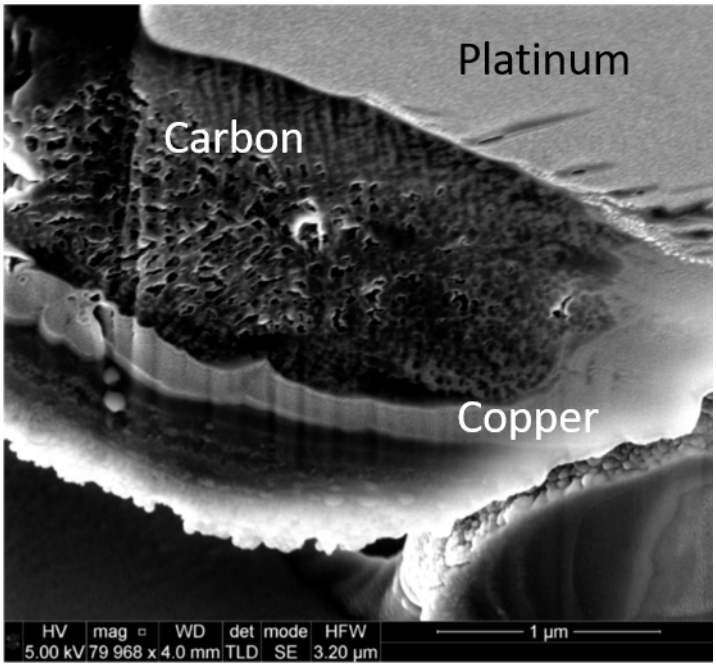

Figure 5.11: SEM image of a cross section of the carbon rings after being cut with a FIB.

For TEM, the samples were prepared the same way as those for the carbon cubes. The slicon wafer containing the carbon rings was sonicated in ethanol for 10 minutes. Drops of this solution was then placed on a holey TEM grid. The results are shown in figure 5.12. The sonication clearly broke up the large ring like macrostructure into the constituent CNFs,[280,281] which, just like the carbon cube material, look like a mostly amorphous carbon with

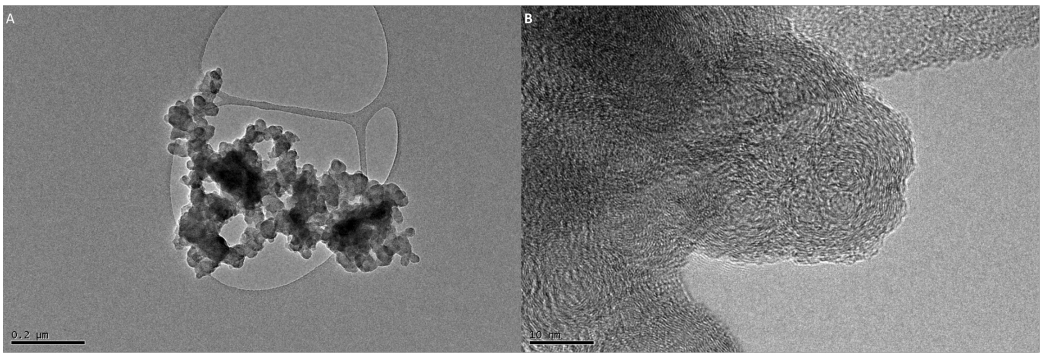

Figure 5.12: A and B) TEM and HRTEM images of the carbon ring structure.

some more graphitic domains present. No intact macrostructure was found in the TEM suggesting that the structure is very weakly bound. HRTEM shown in figure 5.12 (B) suggest that a slightly less graphitic structure than what was observed for the carbon cubes in figure 5.7. This agrees with the Raman spectra in figure 5.13 (B) where unlike for the carbon cubes in figure 5.6, no 2D band is observed suggesting no Z axis order in the structure. It is surprising that this sample is less graphitic than the carbon cubes. Typically, higher temperatures are associated with more graphitisation.

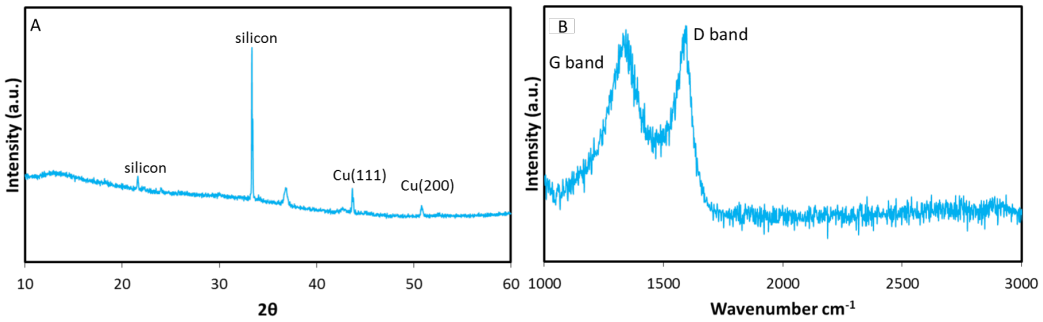

Figure 5.13: A) XRD and B) Raman of the carbon rings taken on a silicon wafer.

The Raman in figure 5.13 B) shows a D and a G band typical of carbon. The D band is again very high, indicative of a highly defective structure. Raman spectra such as this is unsurprising due to the low temperature used. Raman and XRD analysis from literature show that CNFs have a predominantly disordered graphitic structure. The graphite layers however, are short ordered with an inter-layer spacing greater than 0.34 nm.[286] Typically

the crystallites are less than 2 nm.[304] The XRD in figure 5.13 shows that the copper is completely reduced with no sign of oxide impurities.

5.2.5 Carbon Rings vs Carbon Cubes

To gain more information about the potential mechanism for the synthesis of these carbon structures, an experiment was performed at 800 °C for 60 minutes as it is between 750 °C and 820 °C. SEM images from this experiment are shown below:

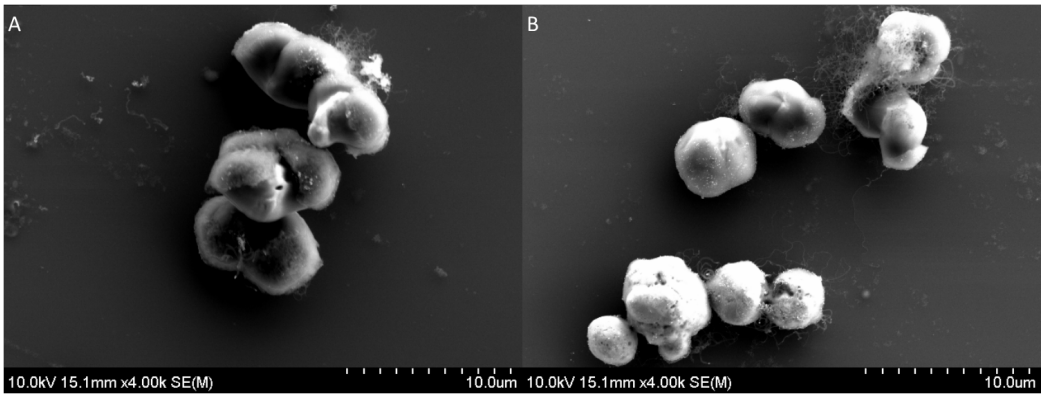

Figure 5.14: SEM images of the material prodiced after an ethanol CVD taken at 800 °C showing the formation of partial solitaire rings.

It can be seen from figure 5.14 that partial rings or smaller solitaire rings are produced, these conditions also yielded complete rings and a small quantity of carbon cubes. It is likely that temperature control is vital for the synthesis of the carbon rings, possibly due to increased carbon solubility in the copper catalyst or a change in morphology of the copper catalyst at the higher temperature.

Temperature is not the only condition this product is sensitive to. All materials produced so far have been produced by adding ethanol to the gas flow stream during the heating phase. If this is replaced with just argon, or an argon/hydrogen mixture, and ethanol only added during the dwell step, the carbon cubes are not formed, no matter how long the dwell with ethanol would last. The same cannot be said for the ring structure, as the material could be reproduced after a 60 minute dwell but not after a 30 minute dwell. This is shown in figure 5.15.

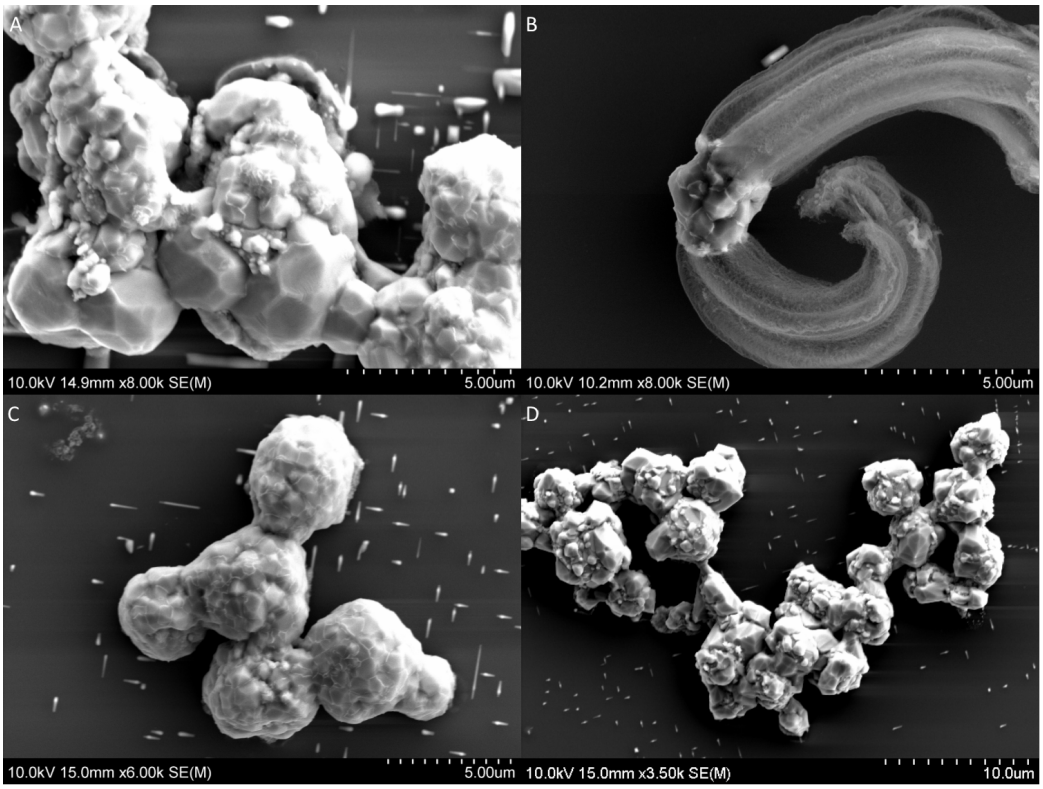

Figure 5.15: SEM images of ethanol CVD where ethanol was only added at various temperatures for different lengths of time. A) 820 °C for 30 minutes. B) 820 °C for 60 minutes. C) 750 °C for 60 minutes and D) 750 °C for 120 minutes.

Figure 5.15 shows experiments where the samples were heated up in just an argon atmosphere. Once the furnace reached temperature, ethanol was introduced into the stream. It can be clearly seen that the morphology of the polyhedra is lost to a much greater extent than when ethanol is included during heating. Similar observations have been made before,[277] and can be attributed to a carbon shell forming at lower temperatures and protecting the original morphology of the copper. As can be seen, no visible carbon is produced at 750 °C while by dwelling for 60 minutes, the solitaire ring structure can be reproduced. One possible explanation for the synthesis of the carbon cubes is that during heating, the copper and the carbon form a solid solution. The carbon/copper cube product is saturated at 750 °C, but also deactivated due to a carbon shell across the surface. Upon cooling, the carbon begins to precipitate out, forcing the copper to extrude out of the

carbon cube shell. At 820 °C, increases in carbon solubility reactivate the copper catalyst as the surface encapsulation dissolves, and solitaire rings can form from a more traditional mechanism of carbon forming at the surface, migrating through either bulk or surface diffusion, and then depositing at another face of the catalyst.

5.2.6 Templated Sheets

A consequence of not flowing ethanol during the active heating phase is that a reducing environment is no longer present. To test the importance of the reducing atmosphere a run was conducted using hydrogen and argon gas The cubes were heated up in an argon/hydrogen atmosphere, and then at 750 °C, hydrogen stopped and the argon directed through ethanol for 120 minutes.

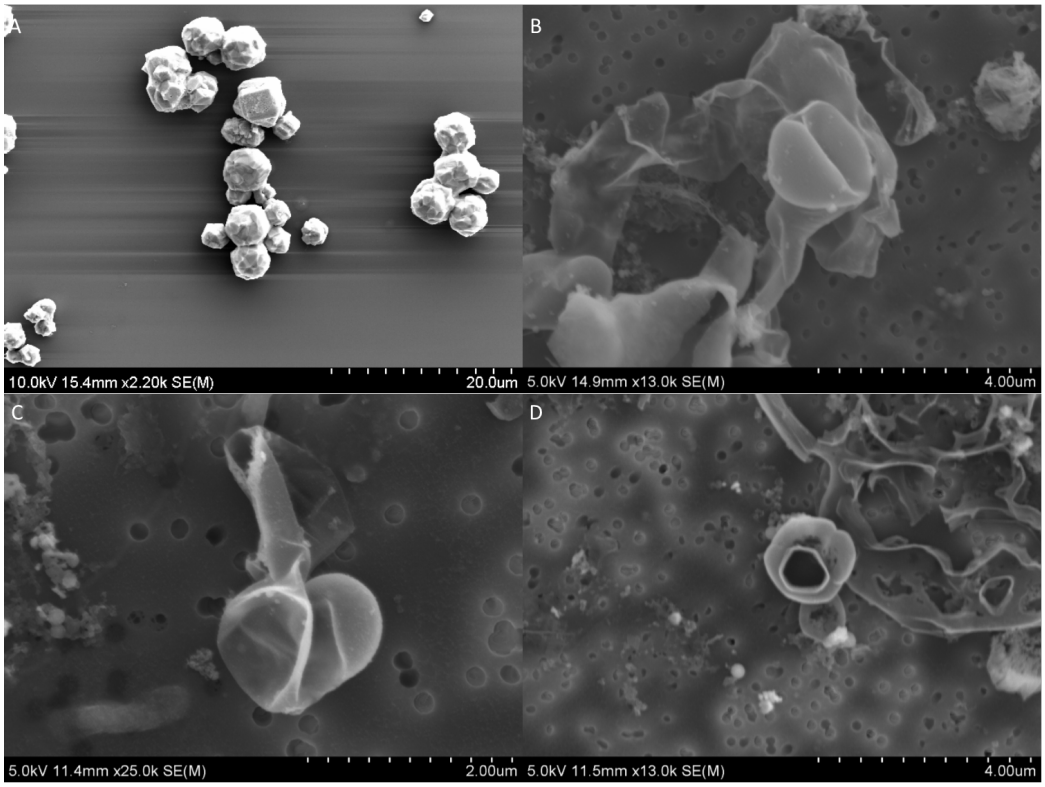

Figure 5.16: A) SEM image of copper catalyst having undergone an ethanol CVD, heated in the presence of hydrogen. B, C and D) SEM images of the carbon material left after the copper was etched away in $FeCl_3$ solution.

Figure 5.16 (A) shows that the product appears very similar to figure 5.15 and that therefore hydrogen while heating has little effect on the product. Figure 5.16 (B), (C) and (D) show the results after the catalyst was etched away with an $FeCl_3$ solution. The catalyst particles are clearly observable in figure 5.16 (A), with only a slight loss in the cube like morphology. Upon etching, figure 5.16 (B), (C) and (D) show that carbon shells remain. These carbon shells look to be hollow and to mimic the shape of the underlying copper catalyst structure. This is similar to what was originally intended with the catalyst particles as shown in figure 5.1 where a thin layer of graphene would cover the surface of the catalyst which could then be etched away leaving just graphene. It appears that rather than just growing on the faces, giving graphene sheets, the carbon has encompassed the entire catalyst. This could be due to the loss of sharp edges in the catalyst particle upon heating. It can be observed from figure 5.16 that the catalysts have become more spherical. Similar structures have been observed on spherical copper nanoparticles whereby the copper was coated with a thin layer of carbon.[277]

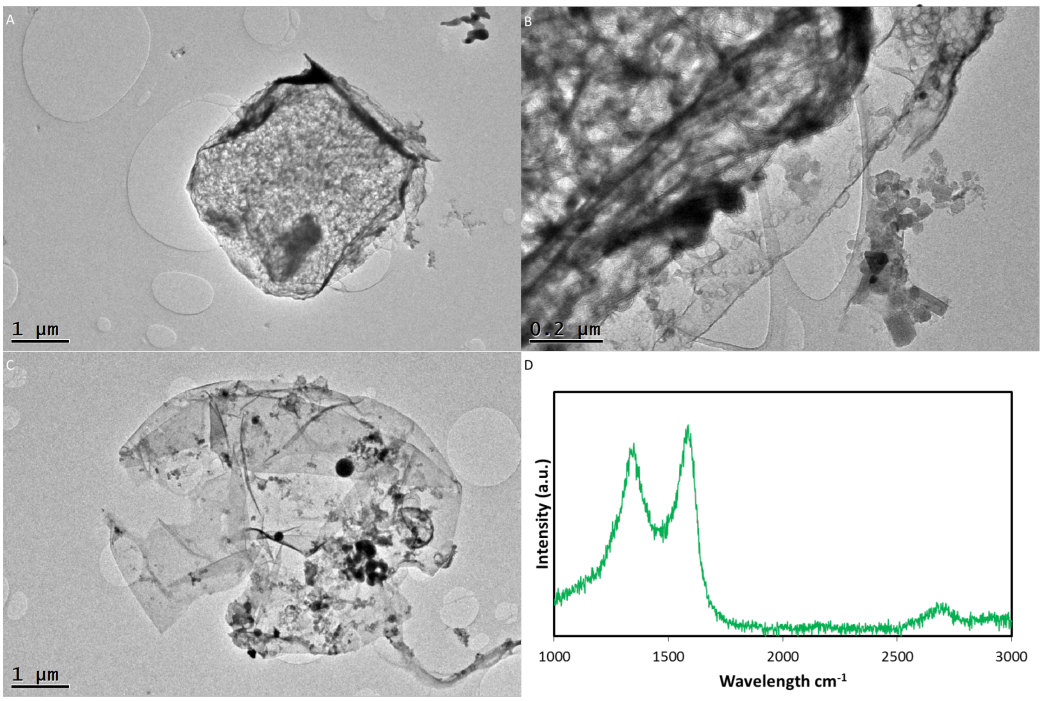

Figure 5.17: A - C) TEM images of carbon after the copper catalyst had undergone an ethanol CVD, heated in the presence of hydrogen and then etched with $FeCl_3$ solution. D) Raman spectra of the carbon material.

The TEM image shown in figure 5.17 (A) shows what was clearly a cube and how the sheets have folded back on themselves. Figure 5.17 (B) show how sheet like the materials is and how thin it is. Figure 5.17 (C) shows what must have been the carbon shell over a particle which became more spherical upon heating. The Raman in figure 5.17 (D) gives an indication of the graphitisation, the large D and small 2D show that the sample is not particularly graphitised. This is to be expected when using such a low temperature. The small size of the sheets will also increase the D band and reduce the 2D band.

5.3 Conclusions and Future Work

Novel CNF based structures were synthesised on a copper oxide cube catalyst. At 750 °C CNFs would arrange themselves into porous carbon cubes while at 820 °C the CNFs would arrange themselves into rope like structures. Experimental conditions were varied in order to deduce a possible mechanism for the synthesis of the different products. For the carbon cubes, firstly the ethanol would dissolve into the copper cubes until saturation. The cube would then be encapsulated by carbon, this carbon would take on the cube shape while also deactivating the catalyst to further reactions with the carbon. Upon cooling, the carbon would precipitate out of the cube, forcing the copper to extrude out. What would be left is a carbon shell with a porous interior. The porosity is due to voids left behind from the copper extruding out. For the carbon rings, a similar mechanism must occur as both carbons produced share the same porous interior structure as shown in figure 5.11 and figure 5.8. At the higher temperature, the catalyst elongates while the carbon is still dissolving into it. The continuous elongation and contraction of the catalyst keeps reactivating the catalyst allowing more carbon to form.[305] The porous carbon is a result of the copper again extruding out of the carbon as the carbon precipitates out. The templated sheets are a result of the carbon encapsulation occurring before any carbon dissolves into the catalyst. More experiments could be performed to get a better idea of the mechanism, such as doing a wider variety of dwell times and temperatures. Schemes of the mechanisms are displayed in figures 5.18, 5.19 and 5.20.

CNFs have many uses such as additives in polymers,[306] gas storage,[307] catalyst support materials,[308,309] and as catalysts.[310,311] Since the materials synthesised are so novel it would be worth measuring their proper-

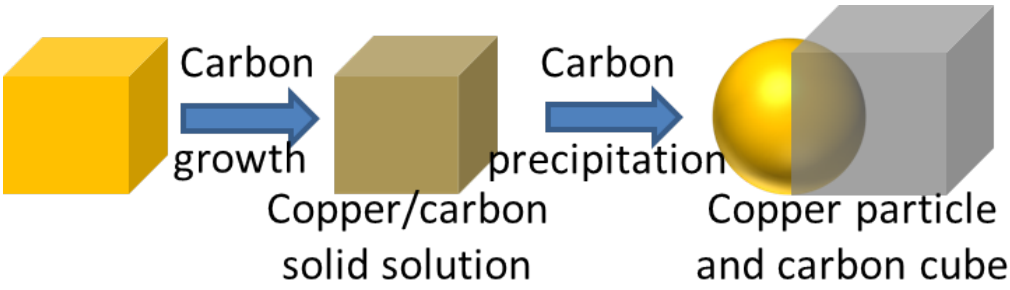

Figure 5.18: Scheme showing the synthesis of carbon cubes.

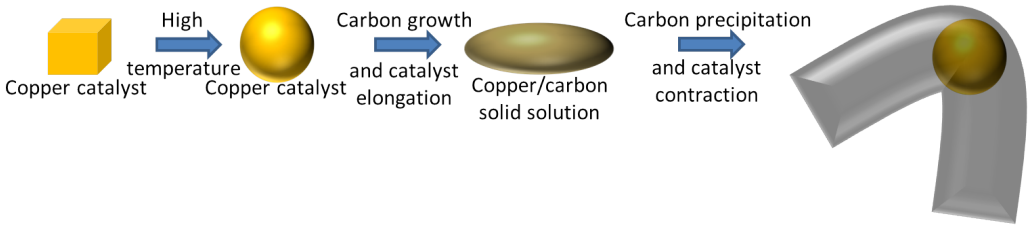

Figure 5.19: Scheme showing the synthesis of carbon rings.

ties, both mechanical and electrical. The porous nature of the macrostructure might give potential uses in energy storage due to a high surface area. This will also contribute to its interaction with a polymer matrix and might improve the mechanical properties of any polymer composite.

A set of conditions were found in order to match the initial aims where the catalyst was heated to 750 °C in a hydrogen/argon atmosphere before adding ethanol. Graphene like sheets were produced matching the shape of the initial catalyst. The sheets however, were not particular graphitic and work could be done trying to improve this such as by increasing the temperature or perhaps performing a pre-carburisation of the catalyst and then graphitisation. It would also be worth measuring the properties of the graphene platelets for electrical conductivity and whether they improve the mechanical properties in polymer composites.

All these experiments were performed on a silicon wafer, severely limiting the amount of material which could be produced. There are several methods in order to scale the synthesis. The catalyst particles could be

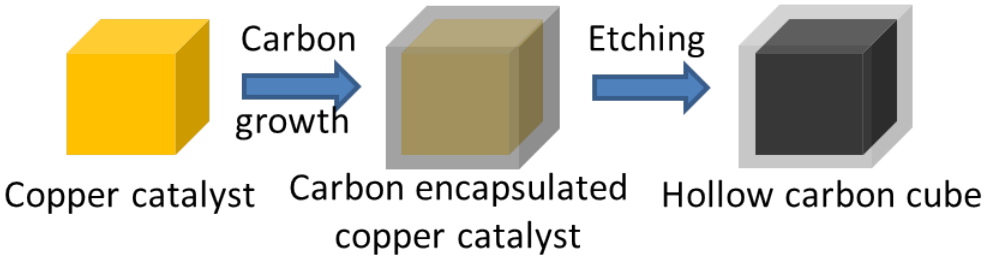

Figure 5.20: Scheme showing the synthesis of templated sheets.

embedded into a three dimensional support such as MgO. This would allow a large amount of powder to be added to the CVD chamber. The best method would be to use a fluidised bed reactor. This is where the gas flow agitates the particles so they behave as a fluid and remain in motion during the CVD. This allows all surfaces of the catalyst to be exposed and should prevent agglomeration of the catalyst giving a more uniform product.

Chapter 6

Templated Carbon Growth on Cobalt Hydroxide Catalyst

6.1 Introduction

The desire to produce templated graphene sheets has been discussed in the previous chapter, but will briefly be reiterated here. The production of templated graphene sheets has attracted much interest due to the unique properties different morphologies can impart on the produced graphene. For example graphene nanoribbons have been shown to have a band gap,[257] so should improve its use in the semi-conductor industry whilst different sizes of graphene sheets have been found to have different composite reinforcing effects.[258] Another advantage is to synthesise graphene from a powder catalyst. Typically metal foils are used in the production of high quality graphene, this however results in a very low yield of carbon. Using a powder catalyst rather than a foil should allow for a much greater yield of carbon material due to the much larger surface areas of the powder.

Existing methods for templated graphene growth include: Growth of graphene nanoribbons on nickel nanobars,[130] and copper,[131] and zinc sulphide ribbons.[132] Mesoporous graphene nanoballs have been prepared from polystyrene beads,[259] graphene nanoballs from nickel nanoparticles,[260] graphene nanotubes on nickel and copper nanotubes,[261] and graphene sheets from iron bars.[106] Metal foils can be patterned into shapes and then graphene grown on the surface using a CVD approach.[38,101] Unfortunately, these meth-

ods have substantial drawbacks and difficulties including producing poor quality material,[131,259] carbon nanotube synthesis in addition to graphene,[106] low yielding and hard to scale.[38,101]

The previous chapter discussed attempts to grow graphene templated from copper cubes. In this chapter the methods discussed will involve templating from cobalt hexagons. Cobalt has a large advantage over copper as a catalyst for these types of experiments. The melting point of copper is 1,085 °C while the melting point of cobalt is 1,496 °C. The higher melting point of the cobalt means it's more likely to maintain its morphology at the high temperatures required for CVD providing a more unifrom structure for the graphene to grow on. In our own experience, cobalt is a superior catalyst for graphene growth as shown in chapter 3. This does not agree with literature which suggests copper is better. We attribute this to the lack of pre-treatment, such as polishing, that is standard practice for synthesis on foils but is difficult to replicate for our catalyst particles. This makes the synthesis on particles inherently worse for the surface based mechanism occurring on a copper catalyst. Much more success has been observed in our experiments by using a catalyst which goes through a dissolution-precipitation mechanism. Being hexagonal should be more desirable than cubes for the synthesis. In attempts to grow graphene on the faces of the cubes, the carbon material would either dissolve into the catalyst and precipitate out as carbon nanofibers rather than graphene (section 5.2.4) or the carbon would coat the entire particle, giving graphene like shells rather than graphene sheets (section 5.2.6). The hexagons are flat platelets and should be too thin to allow significant carbon dissolution while also having no edges for the graphene to grow over.

The potential downsides of using a cobalt catalyst is its propensity to catalyse the growth of other carbon materials such as carbon nanofibers (CNFs), carbon onions and carbon nanotubes (CNTs). Smaller cobalt particles tend to catalyse these materials so it is important to synthesise particles large enough that graphene synthesis is favoured over other carbonaceous materials. The synthesis of graphene materials on nickel nanobars,[130] nickel nanoparticles,[260] and iron bars,[106] suggest that graphene growth can be encouraged over other carbon materials just by careful control over the conditions, as these too are very good catalysts for CNTs, CNFs and onions. Controlling the number of layers of graphene has also been an issue with growth on these types of catalysts before, this can be alleviated by again carefully controlling the growth conditions and also by using thin catalysts.

Here we propose a method to template the synthesis of graphene on cobalt hexagons. Firstly, cobalt hydroxide hexagons were synthesised. These were then placed inside a furnace and CVD was undertaken. The cobalt hexagons were reduced to cobalt metal during the CVD process. Graphene grows on the surface of the hexagons and follows the morphology of the underlying catalyst. The cobalt can then be etched away leaving graphene hexagons. An idealistic scheme of this process is displayed in figure 6.1.

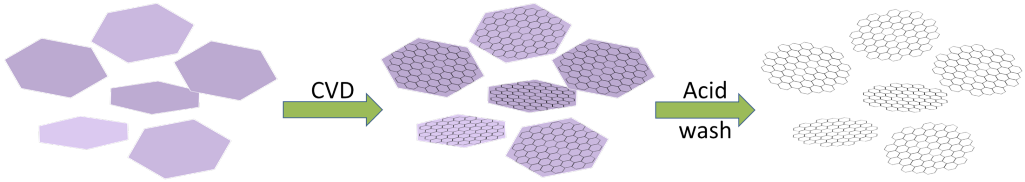

Figure 6.1: Idealised scheme for the templated growth of graphene on CoOH hexagons giving graphene hexagons.

6.2 Synthesis of Templated Carbon from Cobalt Hydroxide Hexagons

6.2.1 Synthesis of Cobalt Hydroxide Hexagons

CoOH hexagons were synthesised by the method outlined by Liu *et al.*[312] Briefly, cobalt chloride and hexamethylenetetramaine (HMT) were dissolved in a water/ethanol mixture. The solution was heated to 90 °C under reflux for one hour. The resulting product was then isolated by filtration and dried in air. The HMT acts as a hydrolysis agent. SEM images and XRD pattern of the resulting product are displayed in figure 6.2.

The SEM images show near perfect hexagons with sizes of approximately 3 - 4 µm. The sample is also remarkably uniform with no other shapes or structures present. The XRD pattern can be indexed as the hexagonal cell of brucite-like β - $Co(OH)_2$ with lattice constants a = 3.182 Å and c = 4.658 Å (space group $P\bar{3}m1$). These are consistent with the values in the literature (JCPDS card, No. 74-1057). The sharp reflections suggest a highly crystalline structure. The high crystalinity and large structures are

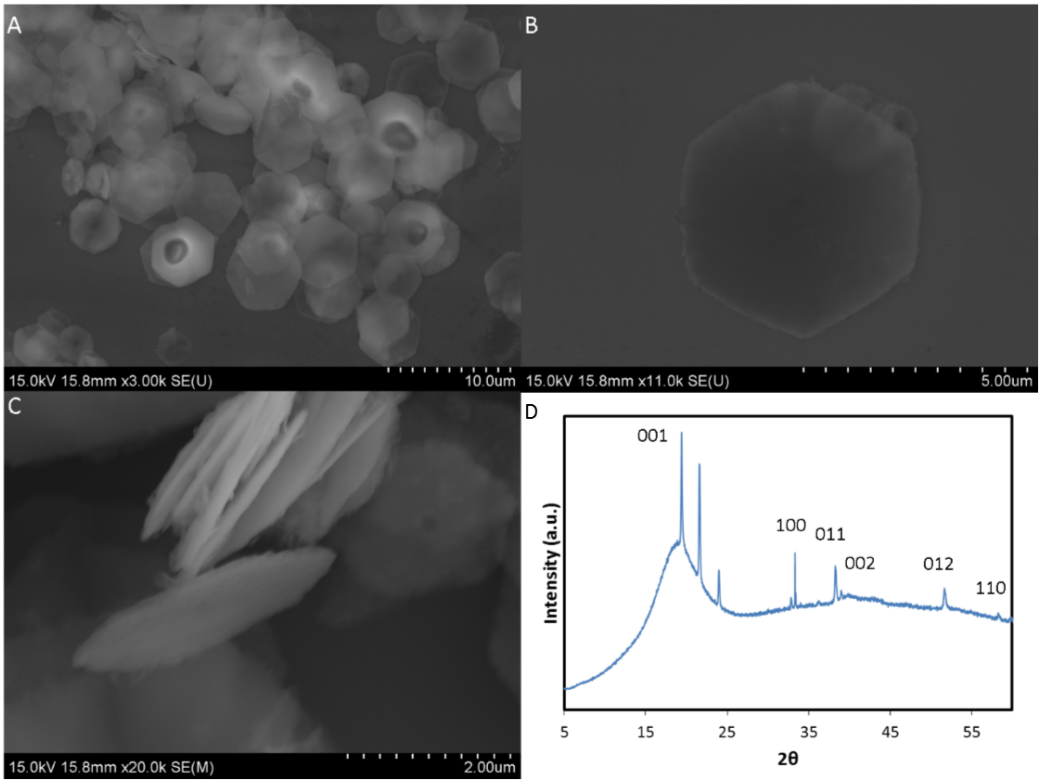

Figure 6.2: A), B) and C) SEM images of CoOH hexagons and D) XRD pattern of CoOH hexagons. SEM images taken at 15.0 kV using the SE detector.

attributed to the slow rate of nucleation. The initial slope in the pattern is due to not much material being analysed.

The cobalt hydroxide catalysts are thin enough in order to prepare for TEM. The particles were dispersed in water and then dropped onto lacey TEM grids. The results are shown in figure 6.3. Image A shows a TEM image of the CoOH hexagon. It is clear that a thin, approximately 3 micron hexagon is produced. The hexagon appears to have some surface roughness. This roughness might be passed through to the graphene produced adding defects to the sheets. High temperature treatment however can often smooth metal surfaces. SAED was taken of the hexagon in image A and is shown in image C. The first two sets of spots in the ED can be indexed to the (001) and the (110) respectively. A thickness map using electron energy loss spectroscopy (EELS) was taken of the region shown in image B. This was done by taking the ratio of zero-energy loss electrons to the total transmitted

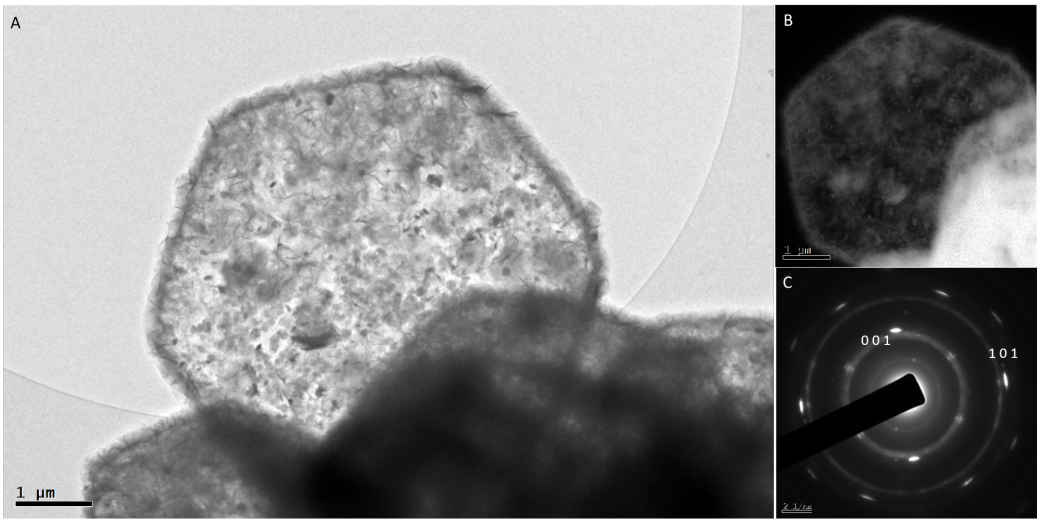

Figure 6.3: A) and B) TEM images of CoOH and C) electron diffraction pattern of CoOH hexagons. Images were taken at 200 kV.

intensity. This is then compared with a reference which is the amorphous carbon substrate on the TEM grids. The material is approximately 30 nm thick. The hexagons being so thin should make the growth of single layer graphene easier as it should limit the amount of carbon that can dissolve into the catalyst. However, it is worth noting that during CVD of thin nickel foils the high temperature results in the nickel decomposing into particulates which can result in discontinuous graphene layers.[111]

6.2.2 Ethanol CVD on Cobalt Hydroxide Hexagons

Ethanol has been a common carbon source in the synthesis of graphene with numerous reports of it being used to grow graphene on copper, and a few reporting its use on nickel.[313,314] It has the advantages of being less flammable and therefore safer as well as decomposing at lower termperatures than the more traditionally used methane. The downside is that it is difficult to control the growth of graphene from carbon precursors with more than one carbon atom in them.[315] The higher reactivity of ethanol also means that the system becomes saturated with carbon.[271]

Ethanol CVD was performed on the cobalt hydroxide catalyst using a similar method described in section 5.2.2. Briefly, the CoOH hexagons were

dispersed in water and then spin coated onto a silicon wafer. This silicon wafer was then placed into the centre of a furnace. The catalyst deposited on Si was then heated in an argon atmosphere before the gas stream was diverted through a modified dreschel bottle with a glass sinter at the bottom, filled with ethanol. This saturates the gas with ethanol. A scheme of this is shown in figure 6.4. The ethanol will decompose into a variety of products as described in section 5.2.2, one of which will be hydrogen. This hydrogen will then reduce the cobalt hydroxide to metallic cobalt so it can catalyse carbon growth.

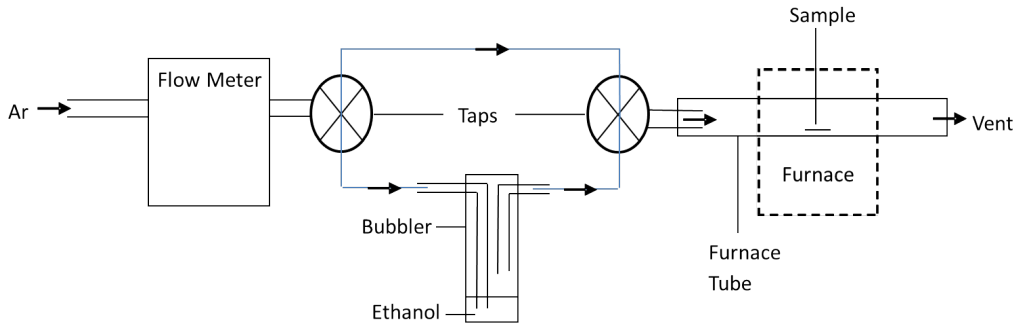

Figure 6.4: Scheme showing the apparatus used to perform the ethanol CVD on the cobalt hydroxide hexagons.

An initial experiment was performed at 800 °C which shows the catalyst completely deformed with no resemblance of hexagons remaining as well as far too much carbon in the system. SEM images of this are shown in figure 6.5.

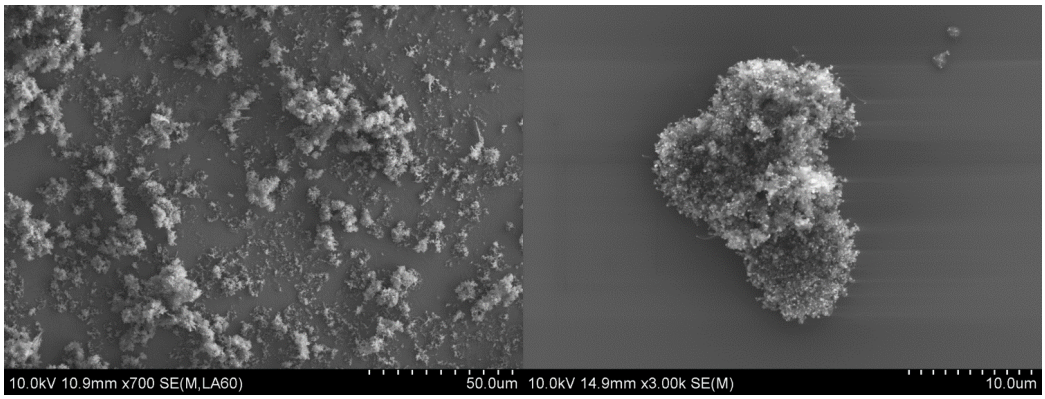

Figure 6.5: A) and B) SEM images of the hexagons having undergone an ethanol CVD at 800 °C. Images were taken at 10.0 kV using the SE detector.

In order to have the catalyst maintain its morphology better, the CVD was carried out instead at 600 °C for a range of dwell times. The results are shown in figure 6.6

The SEM images shown in figure 6.6 shows that the hexagon shape was maintained after being treated at 600 °C. No difference could be observed in the structure of product when varying the time the catalyst was exposed to ethanol. Raman spectra are shown in figure 6.6 (E) and show the characteristic bands for graphite of a D, G and 2D band. The intense 2D band is characteristic of a large degree of crystallinity, despite the relatively low temperature being used, although cobalt has catalysed the synthesis of carbon nanotubes at temperatures as low as 500 °C.[316] The large D band in the spectra show that the material is defective or nanocrystalline.

PXRD was taken with the material on the silicon wafer and showed no sign of graphitic carbon. This was to be expected when measuring such a small amount of material. Interestingly, the only cobalt phase present was a cobalt carbide phase (JCPDS 005-0704). It seems likely that a solid solution of cobalt and carbon are forming at temperature which at saturation then forms cobalt and graphite. Upon cooling, cobalt reacts with the graphitic carbon to form cobalt carbide.

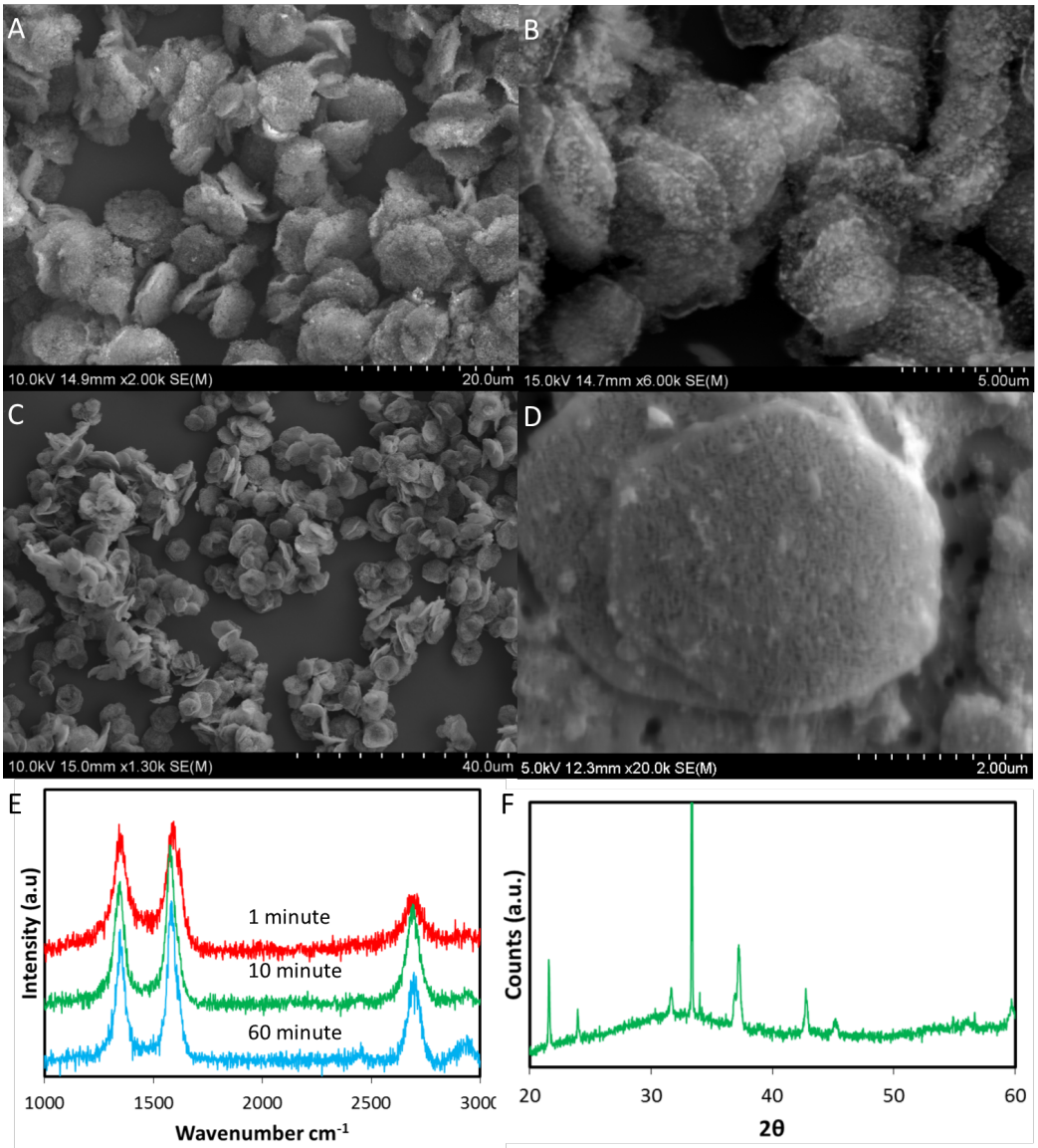

Figure 6.6: A) SEM images after 1 hour EtOH B) 10 minutes EtOH C) and D) 1 minute EtOH E) Raman spectra for each ethanol time E) XRD pattern for 1 minute ethanol run. SEM images taken at 10.0 kV, 15.0 kV, 10.0 kV and 5.0 kV respectively using the SE detector.

Further SEM images were taken of the sample which was treated to ethanol for 1 minute after having the cobalt etched by 6M HCl. The images are shown in figure 6.7. The images show clearly that the hexagon shape is maintained but that the surface is very rough. EDX (figure 6.8 D) shows that a small amount of cobalt still remains in the sample and this might be responsible for the hexagon shape being maintained. Carbon nanotubes can be seen on the surface of the hexagon. This will likely be due to the interaction of ethanol with the cobalt roughening its surface. The formation of carbon nanotubes is a common occurrence on cobalt particles.[317] If the surface of the hexagon becomes rough enough, it will effectively act like a particle and carbon nanotube growth would be preferred over graphene.

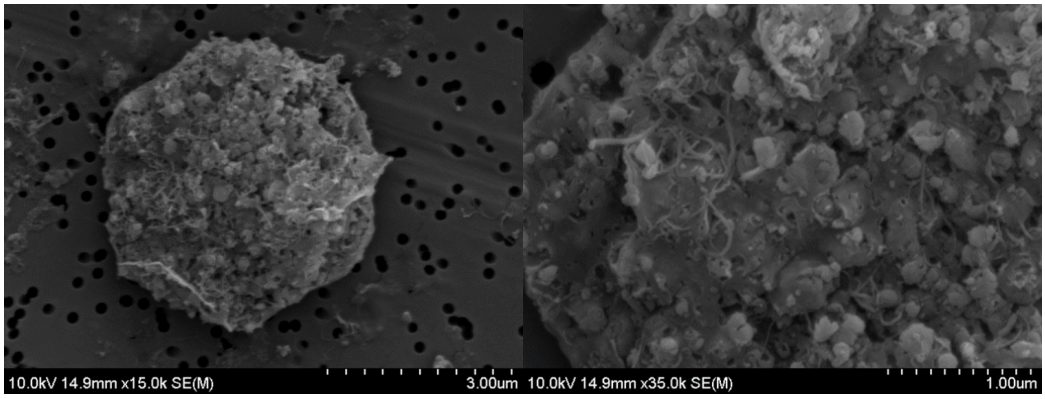

Figure 6.7: A) and B) SEM images of the catalyst treated to 1 minute of ethanol after undergoing an acid wash to remove the cobalt.

The post acid washed material was prepared for TEM by sonicating the material in ethanol and dropping onto lacey TEM grids. The images are shown in figure 6.8. The TEM images in (A) and (C) show that carbon hexagons were formed. The carbon however, seems to be an agglomeration of closed graphitic structures. The graphitic structure can clearly be seen in image (B). The ED inset in (C) also confirms the presence of graphitic carbon. The SAED pattern was indexed showing rings according to the graphitic planes of (002) and (100). The EDX in (D) shows the presence of some cobalt which may be responsable for the hexagonal morphology being maintained. The copper peak is due to the TEM grid while the silicon peak is likely due to contamination from the silicon wafer or the quartz tube during the CVD. The carbon is clearly templated with its macrostructure following the hexagonal shape of the catalyst. The material is also graphitic despite being produced at such a low temperature. The macrostructure however, is an agglomeration of

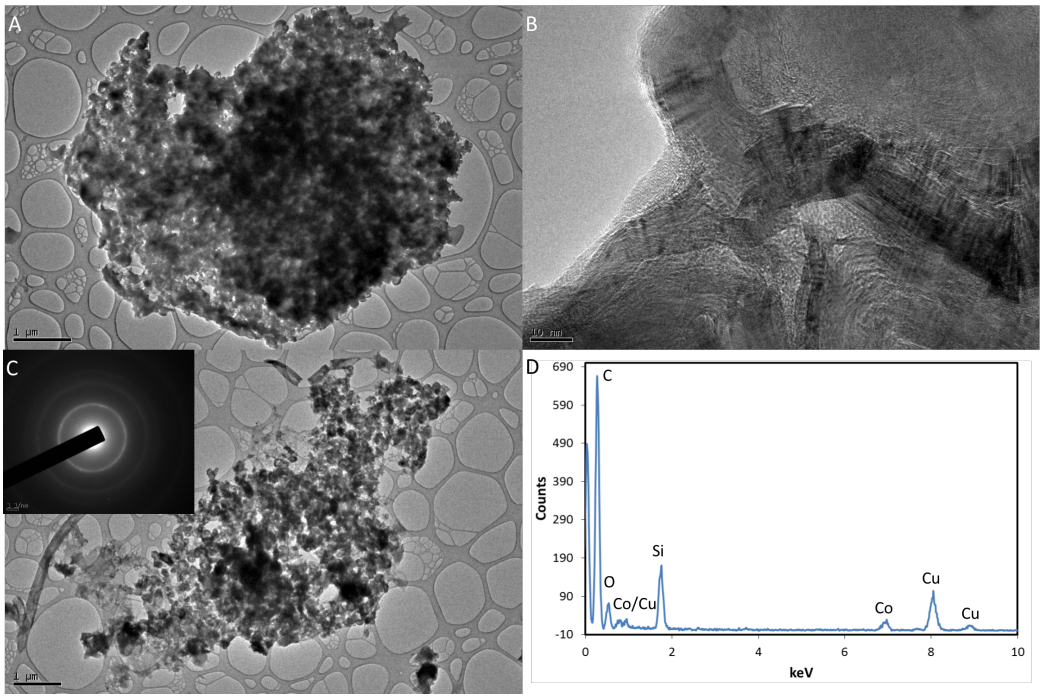

Figure 6.8: A) and B) TEM images of carbon hexagons C) HRTEM image of carbon hexagon and D) EDX pattern across the entire region of A). SAED pattern of image B) inset. TEM images were taken at 80 kV.

carbon materials, none of which appear to be graphene. In order to encourage graphene growth over other carbon structures, an alternate carbon source will be used. Ethanol has traditionally had much success catalysing the growth of carbon nanotubes or carbon onions and so a source which decomposes at higher temperatures might limit the amount of carbon entering the system and encourage graphene growth.

6.2.3 Acetylene CVD on Cobalt Hydroxide Hexagons

Experiments were done using acetylene as the carbon source. Acetylene has been used as a carbon source for CVD growth of graphene and provides a lower temperature alternative to that of methane. Indeed, it has been successfully used to grow graphene on nickel foils at temperatures as low as 700 °C.[111] The proposed mechanism for the growth on nickel, which will very likely be similar for the growth on cobalt, is that the acetylene adsorbs onto

the metal surface and initially decomposes to ethynyl (CCH) and hydrogen.[318] The system will then dehydrogenate and the C-C bond will break. The barrier for breaking the C-C bond is lower than for C-H bonds, this could explain the lower growth temperature for graphene with acetylene as the source gas compared to methane as the source gas.[319] The carbon atoms then dissolve into the bulk of the metal foils forming a solid solution. Then during cooling, the segregation of the carbon atoms leads to formation of graphene layers.[38,320]

Low pressure CVD (LPCVD) has advantages over atmospheric pressure CVD (APCVD). These advantages include an improved uniformity of thickness, increased purity and better reproducibility. The disadvantage typically is a lower deposition rate, however, this is less of an issue when wanting the growth to stop at a monolayer, i.e. graphene synthesis. The improved uniformity and homogeneity is achieved due to the ratio of the mass transport velocity and the velocity of reaction on the surface. The velocity of the mass transport depends on the reactant concentration, diffusion and thickness of the border layer. With lower pressures, the diffusion decreases and the velocity of mass transport will decrease and the gases can approach the substrate more closely, giving a better result. Indeed, LPCVD set-ups have proven the optimum set up for graphene growth in terms of graphene domain size and uniformity of coverage.[79,95,119] A schematic of the set-up used for the following experiments is shown in figure 6.9. LPCVD was proven necessary after an APCVD with acetylene was attempted where even at low flow rates and dwell times too much carbon was deposited (appendix C figure 8.10).

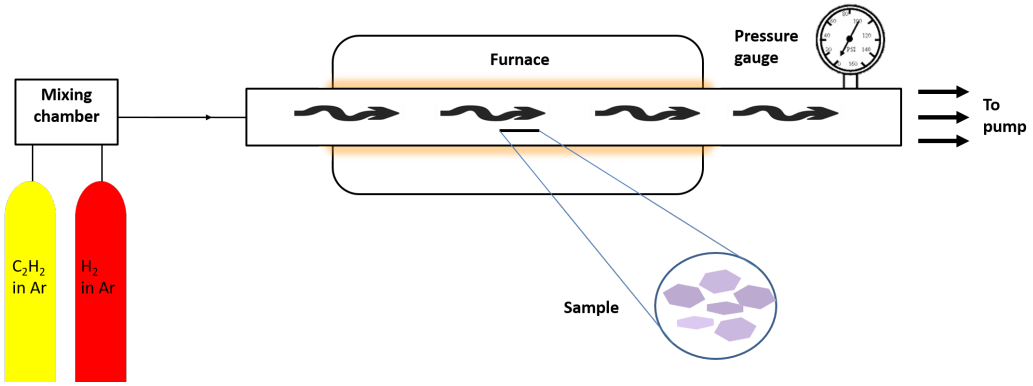

Figure 6.9: Schematic of LPCVD set-up for acetylene CVD over cobalt hydroxide catalysts.

The CoOH hexagons were spin coated onto a silicon wafer which

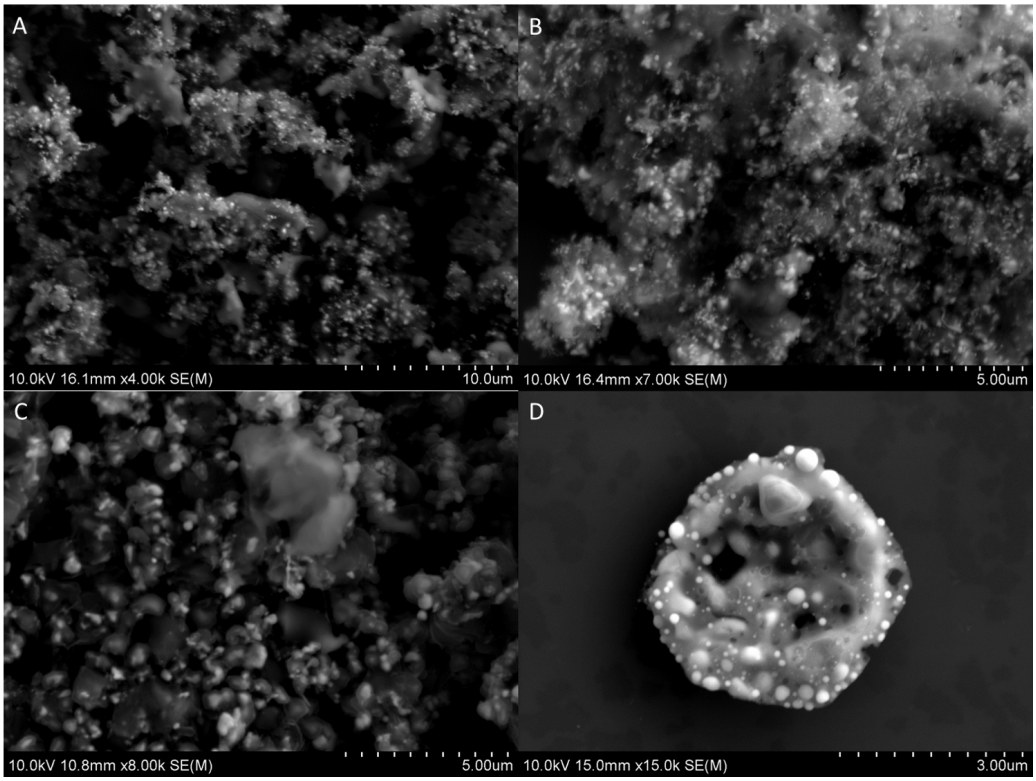

Figure 6.10: SEM images of the cobalt hydroxide catalyst having undergone LPCVD with acetylene for A) 3 hours, B) 1 hour, C) 10 minutes and D) 1 minute. Images taken with an SE detector at 10.0 kV

was placed in the centre of a furnace. The furnace was then evacuated to 25 mbar. 160 ml/min of a 5% hydrogen in argon mixture was introduced into the system which was then heated to 420 °C, held there for one hour before being heated to a higher temperature. The system was initially held at 420 °C as this has been shown to achieve complete reduction of cobalt hydroxide to cobalt metal.[321] At the higher temperature, 160 ml/min of 2000 ppm acetylene in argon was introduced into the flow for varying amounts of time.

The SEM images in figure 6.10 show the acetylene LPCVD performed at 1000 °C for varying amounts of time. When the acetylene was added for extended periods of time (figure 6.10 (A) - (C)) all hexagonal structure was lost and the system was saturated with carbon. Much of this degradation of the catalyst could be attributed to the excess of carbon in the system. When acetylene is only flown for 1 minute (figure 6.10 (D)) the hexagon shape is retained to a much greater extent, although it is still

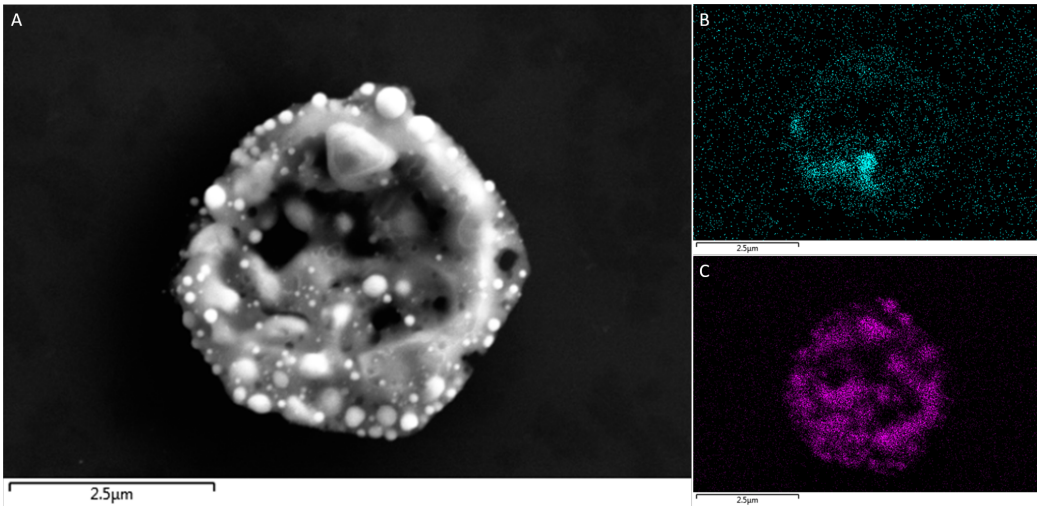

Figure 6.11: (A) SEM image of CoOH hexagon having undergone acetylene CVD, (B) and (C) carbon and cobalt EDX maps over the image shown in (A). Image taken at 10 kV with the SE detector.

apparent that some degradation has occurred with cobalt clearly migrating and agglomerating forming cobalt particles on the hexagon surface.

Carbon and cobalt EDX maps were taken of the cobalt/carbon hexagons from when acetylene was only flown for 1 minute. Figure 6.11 shows that the cobalt, under the high temperature has agglomerated and concentrated at certain regions on the hexagon shown by the varying intensity of cobalt signal across the sample. This is also the case with the carbon where there is a non-uniform distribution of carbon throughout the hexagon.

Raman taken of the acetylene CVD experiments are shown in figure 6.12 and show that a highly graphitic carbon is produced. The very small I_G/I_{2D} values of approximately 0.55, 0.74, 0.91 and 1.00 for 1, 10, 60 and 180 minutes respectively suggests that the material is few-layer graphene.[75] The ratio increases with dwell time as more carbon is deposited, increasing the layer number of graphene. The very small or non-existant D peak suggests that the domains are large and have a low defect density. XRD shows cobalt (JCPDS 015-0806) proving that the conditions reduce the cobalt hydroxide to cobalt metal, an active catalyst for graphene growth. The XRD pattern does not show any carbon in the system, as to be expected when such a small amount of material is produced.

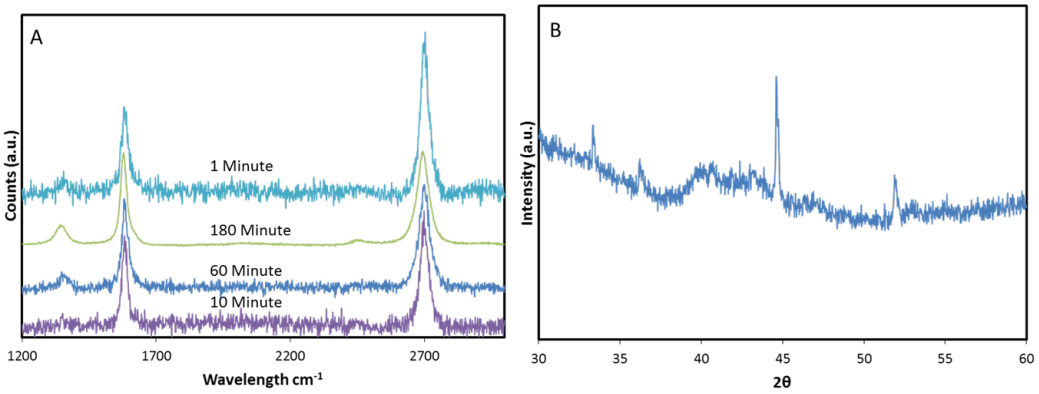

Figure 6.12: (A) Raman spectra of the cobalt hydroxide hexagons after CVD with different acetylene growth times and (B) XRD pattern of the material after 1 minute acetylene dwell.

The samples which were treated to 10 minutes and 1 minute of acetylene were washed with 6M HCl in order to remove the cobalt and then prepared for TEM. The images are shown in figure 6.13. The sample treated to 10 minutes acetylene (figure 6.13 (A) and (B)) showed much smaller pieces of material than that treated to 1 minute of acetylene (figure 6.13 (C) and (D)). However, both samples showed no sign of retaining the hexagonal morphology. This was to be expected when looking in the SEM even for the 1 minute sample as the carbon was in-homogeneously deposited through out the hexagon as shown from the EDX in figure 6.11. It was possible to identify areas of very thin and crystalline material from the TEM of the 1 minute sample, this is in agreement with the Raman shown in figure 6.12.

In order to have better retention of the hexagon shape as shown in figure 6.14. Acetylene LPCVD was performed at 800 °C. The SEM images confirm that a much better shape retention occurred, however, depositing carbon at this temperature proved challenging. When the gas was introduced into the system for 1 minute, no carbon was detected. However, when introduced for 10 minutes, carbon could be detected. The Raman gave little indication that the material was graphitic with only a G band and only a very small 2D band (figure 6.14).

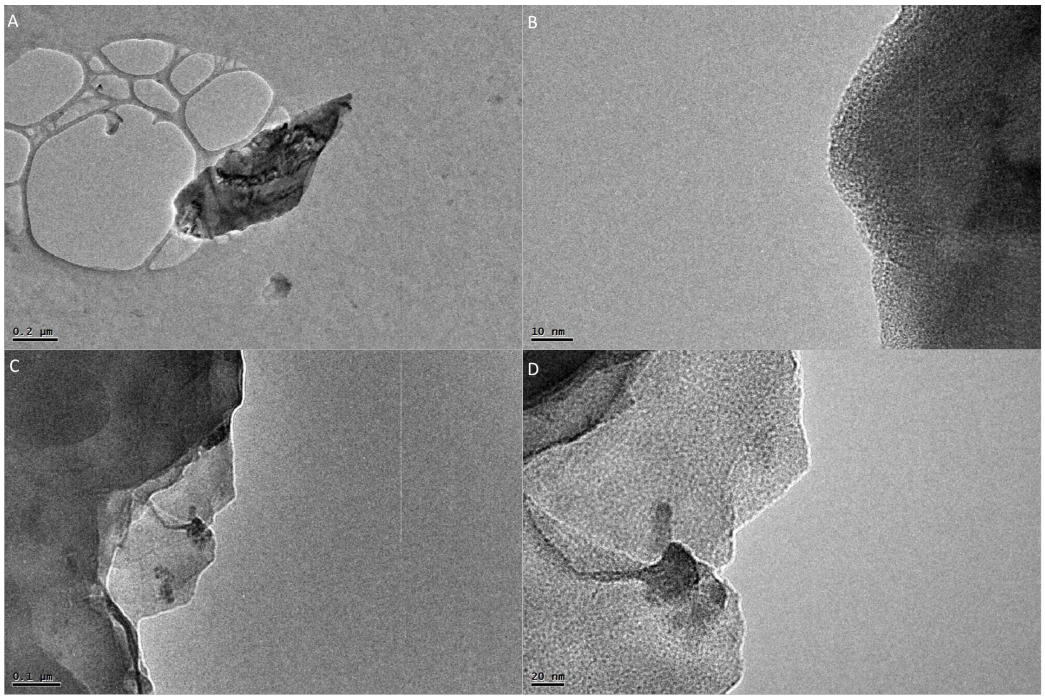

Figure 6.13: (A) and (B) 10 minute acetylene dwell and (C) and (D) 1 minute acetylene dwell. Images taken at 80 kV.

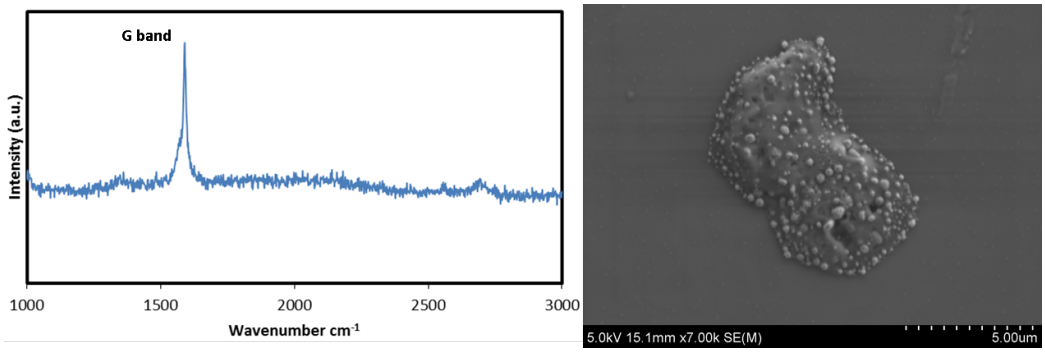

Figure 6.14: A) Raman spectrum and B) SEM image of CoOH after acetylene LPCVD at 800 °C. SEM image taken at 5.0 kV using the SE detector.

6.3 Conclusions and Future Work

CVD was performed on cobalt hydroxide hexagons in order to produce hexagonal graphitic carbon structures. Two carbon sources were used in order to

get the best conditions for graphene growth while maintaining the hexagonal shape. A careful balance was required between high temperature in order to encourage the carbon to graphitise but not so high that the catalyst particles deform beyond recognizable hexagons.

Ethanol CVD allowed deposition of carbon at the lowest temperatures. APCVD at 800 °C produced large amounts of carbon but the catalyst particles did not resemble hexagons. Experiments conducted at 600 °C show that the catalyst particles retained their hexagonal shape when only a small amount of carbon (1 minute flow time) was introduced into the system. Raman spectra showed that the material was highly graphitic while TEM showed that the graphitic material produced shell like materials agglomerated into hexagons rather than discreet sheets. This is the first example of the growth of graphitic material with a hexagonal macrostructure. To the best of our knowledge it is also the largest templated structure produced, growth of other templated carbons has been on nanoparticles. The strucutre is also much more graphitic than many of the other templated carbon materials produced which tend to be amorphous or have nanocrystalline domains.

In an attempt to improve the morphology of the graphite material produced, LPCVD was performed using acetylene as a carbon source. Best results were attained when performing the reaction at 1000 °C where Raman spectra suggests 1 - 3 layer graphene was synthesised. However, the hexagonal shape was not retained. Temperatures were lowered to 800 °C resulting in a large drop in the crystallinity of the carbon but the hexagonal shape was much better maintained. It is clear that there is a trade off between crystallinity of the carbon and the retention of the morphology. Although it was difficult to obtain the hexagonal shaped graphene, this was a successful synthesis of CVD quality graphene through a powdered catalyst and could mean a scalable route to high quality graphene. Typically there is a trade-off between quality of graphene and scalability of production. Graphite oxide is the most scalable route to graphene but the product is of poor quality while CVD offers high quality material but with low yields. This could be a method which bridges this gap and work should therefore be done attempting to scale up these reactions. The experiments above were performed with the CoOH isolated on a surface, but adding the catalyst to a high surface area support or performing the reaction in a fluidised bed should allow a larger quantity of catalyst material into the furnace while also minimising agglomeration.

A set of future experiments could be to synthesise the alpha-phase CoOH. Although the crystals are typically smaller than the beta-phase syn-

thesised here, TEM images suggest they are much smoother which should encourage more crystalline graphene growth.[312] The alpha-phase CoOH has been intercalated with organic materials. It may be worth attempting to use these organic materials as the carbon source for graphene growth as the amount of carbon introduced into the system then should be optimal for very few-layer growth.[312]

Chapter 7

Conclusion

To conclude, 4 new catalyst template materials were synthesised and then a host of conditions were attempted in order to produce graphene. Each had varying degrees of success at producing graphene but all were able to template the synthesis of carbon nanomaterials.

The first experimental chapter described the synthesis of metal foams based on dextran hydrogels. 4 traditional CVD catalysts were synthesised in this way and then conventional methane CVD was performed on the metals. This produced high quality graphene/graphite foams as shown by TEM and Raman spectroscopy. This synthesis was then amended to use dextran as the carbon source rather than methane. This resulted in a significantly different product, instead producing closed graphitic structures arranged into a foam-like macrostructure.

The second experimental chapter also aimed to produce graphene foams but instead templated from metal doped polyHIPEs. The polyHIPE was used as the carbon source in this synthesis and graphitic carbon foams were produced. Raman and TEM studies suggest that the material is more similar to the closed graphitic structures produced in the "one-pot" synthesis described in the previous chapter. The metal-doped polyHIPEs were also able to produce graphite foams by burning of the polyHIPE in air creating a metal foam which was then used as the template in a conventional methane CVD.

The third experimental chapter aimed to synthesise square graphene

platelets on a copper oxide cube catalyst particle. This was particularly sensitive to conditions with numerous different ethanol CVDs being performed. Three structures were produced - at higher temperature CVD, carbon solitaire rings were produced and at lower temperatures, carbon cubes were produced. TEM show both these structures to be agglomerations of carbon nanofibers. By altering the heating regime, a third product was produced which was more similar to the initial aim - carbon sheets that clearly had encapsulated the copper cube prior to etching the cube away, giving a collapsed cube morphology. Although sheet like carbon and very thin, Raman studies show that much of the sp^2 hybridisation had been lost. The growth of carbon nanofibers on copper microparticles challenges current understanding and mechanisms for the growth of carbon nanofibers from metals.

The final experimental chapter aimed to synthesise graphene with a hexagonal shape on a cobalt hydroxide hexagonal catalyst. Firstly, ethanol CVD was performed and produced hexagonal macrostructures of closed graphitic carbon. Low pressure acetylene CVD was also performed on the cobalt and produced high quality graphene - the temperature required for this however meant that much of the hexagonal morphology of the cobalt was lost and the graphene had no discernible shape. Despite the morphology not being transferred to the graphene, this was synthesis of high quality graphene on a powdered catalyst and indicative of potentially scalable CVD graphene.

Chapter 8

Experimental Section

8.1 Characterisation Methodology

8.1.1 Raman Spectroscopy

Raman spectra were obtained on a Horiba LabRam Evolution using a 532 nm laser and a x 50 long working distance objective lens. The instrument was calibrated against a silicon reference. Spectra were background corrected and normalized to the G band using the Horiba Labspec 6 software. Samples were placed on glass slides for measurement.

8.1.2 Scanning Electron Microscopy

For SEM, materials were mounted on a metal stup with silver paint. SEM images were collected using a Hitachi SU-70 FEG SEM or FEI Helios Nanolab 600 using both SE and BSE detectors.

8.1.3 Energy Dispersive X-ray Spectroscopy

EDX was taken inside the SEM and collected using an Oxford Instruments EDX system (INCA x-act LN_2-free analytical Silicon Drift Detector), and

the data analysis performed on the proprietary INCA software.

8.1.4 Transmission Electron Microscopy

For TEM, samples were prepared by bath sonicating material in NMP or ethanol for 15 minutes to form a dispersion. The samples were then deposited onto lacey or holey carbon TEM grids (Agar Scientific) by drop casting. Samples were then allowed to dry overnight prior to imaging. Imaging was carried out on a JEOL 2100F FEG TEM.

8.1.5 X-ray Diffraction

PXRD was recorded on a Bruker AXS d8 Advanced X-ray powder diffractometer operated at 40 kV and 40 mA using either Mo K$\alpha_{1,2}$ X-ray source (λ = 0.7093 Å) or a Cu K$\alpha_{1,2}$ X-ray source (λ = 1.5506 Å). Samples were loaded into a glass capillary or sieved onto a glass slide for analysis.

8.1.6 Conductivity Measurement

Sheet resistance was measured using a Keithley 2602 Source Measure Unit (SMU) and a Guardian SRM-232 SP4-62.5-45-TC-FH R = 10 MIL 4-point, in-line probe head. Samples were dispersed in NMP (1 mg mL^{-1}) by sonication and then made into thin films by vacuum filtration onto polycarbonate membranes (0.45 µm, Millipore). Voltage was swept between -1.5 V to 1.5 V and correction factors were applied to correct for sample geometry. SEM was used to prove films were $<$ 400 µm thick.

8.1.7 Thermogrivimetric Analysis

TGA was carried out using a Perkin ELmer Pyris I. Samples were exposed to the chosen gas and the temperature increased from ambient to 1000 °C at 10 °C min^{-1}.

8.1.8 Brunauer-Emmett-Teller Surface Area Analysis

BET surface area measurements were taken using a Micromeritics ASAP 2020 nitrogen porosimeter. Samples were dried on the instrument at 300 °C until pressures of <10 mmHg were achieved and held for 2 h. BET surface areas were measured by nitrogen adsorption at 77 K using 1/2 inch glassware fitted with a filler rod, sealed frit and isothermal jacket.

8.1.9 Elemental Analysis

Elemental analysis was carried out on a Horiba Jobin Yvon Ultima 2, which uses Inductively Coupled Plasma, Optical Emission Spectroscopy (ICP-OES) to determine weight percentages of the constituent elements. Samples of the metal containing material were prepared by acid digestion in the concentrated nitric acid.

8.2 Experimental Synthesis

All chemicals were purchased from Sigma Aldrich, BOC or Fischer and used as received.

8.2.1 Synthesis of Metal Doped Hydrogels

Metal doped hydrogels were synthesised by dissolving 10 g of metal salt (cobalt(II) nitrate hexahydrate(98 %), nickel(II) nitrate hexahydrate (98 %), copper(II) sulphate pentahydrate(99 %) or iron(III) chloride(99 %)) into 15 ml of high purity water. 10 g of Triton X-45 was then added. In a separate vessel, dextran (10 g, 1500 - 2800 kDa) was mixed with 10 ml high purity water. The two solutions were then combined and stirred for 30 minutes at 60 °C. The gel was then allowed to age for 4 days prior to use.

8.2.2 Synthesis of Metal Oxide Foams

The metal doped hydrogel was placed in an alumina boat placed inside a quartz furnace tube. The system was heated insed a tube furnace up to 600 °C in air at 5 °C min^{-1} and held there for 2 hours.

8.2.3 Synthesis of Metal Foam

Metal oxide foam was placed in an alumina boat inside a quartz work tube inside a tube furnace. The system was then purged with argon (48 l h^{-1}) for 30 minutes. Hydrogen (8 sccm) was then added to the flow and the furnace ramped up to 1000 °C at 20 °C min^{-1} and held at temperature for 2 hours. The system was then allowed to cool under the flow of argon and hydrogen.

8.2.4 CVD on Metal Oxide Foam

Metal oxide foam was placed in an alumina boat inside a quartz work tube inside a tube furnace. The system was then purged with argon (48 l h^{-1}) for 30 minutes. Hydrogen (8 sccm) was then added to the flow and the system was then ramped up to 1000 °C at 20 °C min^{-1} and held at this temperature for 1 hour before methane (5 sccm) was introduced to the flow for 10 minutes. The methane was then stopped and the furnace was held at temperature for another 50 minutes. The system was then allowed to cool under a flow of argon and hydrogen. The metal/graphene foam was then washed in 6 M hydrochloric acid for 19 hours to remove the metal, filtered and dried in a vacuum oven at 60 °C under a reduced pressure (10^{-1} Pa).

8.2.5 Synthesis of One-pot Carbon Material

An alumina boat was half filled with metal doped hydrogel. The alumina boat was then placed inside a quartz worktube inside a tube furnace. The system was then purged with argon (48 l h^{-1}) for 30 minutes. Hydrogen (8 sccm) was then added to the flow and the system was then ramped up to 1000 °C at 20 °C min^{-1} and held at this temperature for 2 hours. The resultant carbon/metal foam could then be washed in hydrochloric acid for 24 hours to remove the metal.

8.2.6 Synthesis of PolyHIPEs

Styrene (5.5 ml, 47.4 mmol), divinylbenzene (1.3 ml, 9.2 mmol), Azobisisobutyronitrile (52 mg) and SPAN 80 (2.0 g, 4.67 mmol) were mixed together to form the organic phase. The aqueous phase was made by mixing high purity water (27.2, 38.5 and 61.2 ml to form 80, 85 and 90% porosity respectively) with potassium persulfate (0.1 g, 0.37 mmol). The organic phase was placed in a two funnel round bottom flask and the aqueous phase was added dropwise, mixing at 350 rpm to form an emulsion. The emulsion was placed in an oven at 60 °C for 18 hours at a reduced pressure (10^{-1} Pa). To synthesis metal doped polyHIPEs, cobalt nitrate hexahydrate (1.1 g) or nickel nitrate hexahydrate (1.1 g) was dissolved into the aqueous phase.

8.2.7 Carbonization of PolyHIPEs

PolyHIPEs were placed in an alumina boat inside a quartz worktube inside a tube furnace.The system was then purged with argon (48 l h^{-1}) for 30 minutes. Hydrogen (8 sccm) was then added to the flow and the system was then ramped up to 1000 °C at 20 °C min^{-1} and held at this temperature for 2 hours.The resultant carbon/metal foam could then be washed in hydrochloric acid for 24 hours to remove the metal.

8.2.8 Synthesis of PolyHIPE Derived Metal Oxide Foam

The metal doped polyHIPE was placed in an alumina boat placed inside a quartz furnace tube. The system was heated insed a tube furnace up to 600 °C in air at 5 °C min^{-1} and held there for 2 hours.

8.2.9 CVD on PolyHIPE Derived Metal Oxide Foam

PolyHIPE derived metal oxide foam was placed in an alumina boat inside a quartz work tube inside a tube furnace. The system was then purged with argon (48 l h^{-1}) for 30 minutes. Hydrogen (8 sccm) was then added to the flow and the system was then ramped up to 1000 °C at 20 °C min^{-1} and held

at this temperature for 1 hour before methane (5 sccm) was introduced to the flow for 10 minutes. The methane was then stopped and the furnace was held at temperature for another 50 minutes. The system was then allowed to cool under a flow of argon and hydrogen.

8.2.10 Synthesis of Copper Oxide Polyhedra

Copper acetate (0.724 g) was dissolved in 40 ml of high purity water with constant stirring at 70 °C. 5 ml of 6 M NaOH was then added dropwise. After 5 minutes 0.2 g of D-glucose was added. After a furthur 3 minutes the solution heating is stopped and the solution allowed to cool. The particles are cleaned and separated with repeated centrifugation with high purity water and ethanol. The polyhedra are then dried in a vacuum oven at 60 °C under a reduced pressure (10^{-1} Pa).

8.2.11 Ethanol Chemical Vapour Deposition on Copper Oxide Polyhedra

Copper oxide polyhedra were spin coated onto a piranha cleaned [0 0 1] silicon wafer placed in the centre of a quartz work tube inside a tube furnace. Argon could be diverted through a glass sinter at the bottom of a Dreschler bottle containing ethanol in order to saturate the gas. The system was purged for 30 minutes with just argon before being heated to 750 - 820 °C with the argon diverted through the ethanol at various temperatures. The system was then allowed to cool in either argon or argon saturated with ethanol.The resultant carbon/metal material could then be washed in hydrochloric acid for 24 hours to remove the metal.

8.2.12 Synthesis of Cobalt Hydroxide Hexagons

Cobalt chloride hexahydrate (1.190 g) and hexamethylenetetramine (8.411 g) were dissolved in 1 L of a 9:1 mixture of deionised water:ethanol and heated with stirring at 90 °C. Heating was stopped after approximately 1 hour when a pink precipitate was evident. The particles were filtered, washed with deionised water and then dried in a vacuum oven at 60 °C under a reduced pressure (10^{-1} Pa).

8.2.13 Ethanol Chemical Vapour Deposition on Cobalt Hydroxide Hexagons

Cobalt hydroxide hexagons were spin coated onto a piranha cleaned [0 0 1] silicon wafer placed in the centre of a quartz work tube inside a tube furnace. The system was purged in 10 L/h of argon before being heated to 600 - 800 °C under the same flow of argon. At temperature, the flow is diverted through a glass sinter at the bottom of a Dreschler bottle containing ethanol in order to saturate the gas. The furnace is held at temperature for 1 - 60 minutes before cooled under just argon.The resultant carbon/metal material could then be washed in hydrochloric acid for 24 hours to remove the metal.

8.2.14 Low Pressure Acetylene Chemical Vapour Deposition on Cobalt Hydroxide Hexagons

Cobalt hydroxide hexagons were spin coated onto a piranha cleaned [0 0 1] silicon wafer placed in the centre of a quartz work tube inside a tube furnace. The system was evacuated down to 0.02 bar for 30 minutes before adding a flow of 160 ml min^{-1} 5 % hydrogen in argon and heating to 420 °C, holding for 1 hour and then heating to 1000 degree C at 10 °C min^{-1}. The furnace was held at 1000 °C for 1 - 180 minute under a flow of 160 ml min^{-1} 5% hydrogen/argon and 160 ml min^{-1} 3000 ppm acetylene/argon flow. The system was then cooled with just the hydrogen/argon flow and the clam shell of the furnace was opened to cool the system rapidly.

Bibliography

[1] J. Robertson, *Advances in Physics*, 1986, **35**, 317–374.

[2] J. Robertson, *Materials Science and Engineering: R: Reports*, 2002, **37**, 129–281.

[3] P. K. Chu and L. Li, *Materials Chemistry and Physics*, 2006, **96**, 253–277.

[4] R. B. Hudson and A. Sinha, *Vibration of carbon nanotubes with defects: order reduction methods*, 2018, vol. 474, p. 20170555.

[5] K. S. Novoselov, A. K. Geim, S. V. Morozov, D. Jiang, Y. Zhang, S. V. Dubonos, I. V. Grigorieva and A. A. Firsov, *Science (New York, N.Y.)*, 2004, **306**, 666–669.

[6] H. Fernandezmoran, *Journal of Applied Physics*, 1960, **31**, 1840.

[7] a. Geim, P. Kim, K. Novoselov, Z. Jiang, H. Stormer, Y. Zhang, S. Morozov and U. Zeitler, *APS Meeting Abstracts*, 2007, **293**, 40002.

[8] J. A. Venables, G. D. T. Spiller and M. Hanbucken, *Reports on Progress in Physics*, 1984, **47**, 399.

[9] J. C. Meyer, a. K. Geim, M. I. Katsnelson, K. S. Novoselov, T. J. Booth and S. Roth, *Nature*, 2007, **446**, 60–63.

[10] N. Savage, *Nature*, 2012, **483**, S30—-S31.

[11] S. Z. Butler, S. M. Hollen, L. Cao, Y. Cui, J. a. Gupta, H. R. Gutiérrez, T. F. Heinz, S. S. Hong, J. Huang, A. F. Ismach, E. Johnston-Halperin, M. Kuno, V. V. Plashnitsa, R. D. Robinson, R. S. Ruoff, S. Salahuddin, J. Shan, L. Shi, M. G. Spencer, M. Terrones, W. Windl and J. E. Goldberger, *ACS nano*, 2013, **7**, 2898–2926.

[12] B. Partoens and F. Peeters, *Physical Review B*, 2006, **74**, 1–11.

[13] R. R. Nair, P. Blake, a. N. Grigorenko, K. S. Novoselov, T. J. Booth, T. Stauber, N. M. R. Peres and a. K. Geim, *Science*, 2008, **320**, 1308.

[14] S. Ghosh, W. Bao, D. L. Nika, S. Subrina, E. P. Pokatilov, C. N. Lau and A. a. Balandin, *Nature materials*, 2010, **9**, 555–558.

[15] Y. Zhang and C. Pan, *Diamond and Related Materials*, 2012, **24**, 1–5.

[16] K. F. Mak, J. Shan and T. F. Heinz, *Physical Review Letters*, 2010, **104**, 176404.

[17] M. Orlita, C. Faugeras, P. Plochocka, P. Neugebauer, G. Martinez, D. K. Maude, A. L. Barra, M. Sprinkle, C. Berger, W. A. De Heer and M. Potemski, *Physical Review Letters*, 2008, **101**, 1–5.

[18] a. K. Geim, *Science (New York, N.Y.)*, 2009, **324**, 1530–1534.

[19] J.-H. Chen, C. Jang, S. Xiao, M. Ishigami and M. S. Fuhrer, *Nat. Nanotechnol.*, 2008, **3**, 206–209.

[20] X. Du, I. Skachko, A. Barker and E. Y. Andrei, *Nature nanotechnology*, 2008, **3**, 491–495.

[21] C. Lee, X. Wei, J. W. Kysar and J. Hone, *Science (New York, N.Y.)*, 2008, **321**, 385–388.

[22] A. a. Balandin, S. Ghosh, W. Bao, I. Calizo, D. Teweldebrhan, F. Miao and C. N. Lau, *Nano letters*, 2008, **8**, 902–907.

[23] W. Bao, F. Miao, Z. Chen, H. Zhang, W. Jang, C. Dames and C. N. Lau, *Nature nanotechnology*, 2009, **4**, 562–566.

[24] J. S. Bunch and S. S. Verbridge, *Nano letters*, 2008, **8**, 2458–2462.

[25] A. K. S. Novoselov, D. Jiang, F. Schedin, T. J. Booth, V. V. Khotkevich, A. K. Geim, T. M. Rice, K. S. Novoselov, D. Jiang, F. Schedin, T. J. Booth, V. V. Khotkevich, S. V. Morozovt and A. K. Geim, *Proceedings of the National Academy of Sciences of the United States of America*, 2005, **102**, 10451–10453.

[26] S. D. Sarma, S. Adam and E. Rossi, *Reviews of Modern Physics*, 2011, **83**, 407–470.

[27] Z. J. Li, B. C. Yang, S. R. Zhang and C. M. Zhao, *Applied Surface Science*, 2012, **258**, 3726–3731.

[28] A. Fahimi, I. Jurewicz, R. J. Smith, C. S. Sharrock, D. A. Bradley, S. J. Henley, J. N. Coleman and A. B. Dalton, *Carbon*, 2013, **64**, 435–443.

[29] X. Huang, X. Qi, F. Boey and H. Zhang, *Chemical Society reviews*, 2012, **41**, 666–686.

[30] Y. Zhang, L. Zhang and C. Zhou, *Accounts of Chemical Research*, 2013, **46**, 2329–2339.

[31] C. Berger, Z. Song, X. Li, X. Wu, N. Brown, C. Naud, D. Mayou, T. Li, J. Hass, A. N. Marchenkov, E. H. Conrad, P. N. First and W. a. de Heer, *Science (New York, N.Y.)*, 2006, **312**, 1191–1196.

[32] L. A. Ponomarenko, F. Schedin, M. I. Katsnelson, R. Yang, E. W. Hill, K. S. Novoselov and a. K. Geim, *Science*, 2008, **320**, 356–358.

[33] Y.-M. Lin, K. A. Jenkins, A. Valdes-Garcia, J. P. Small, D. B. Farmer and P. Avouris, *Nano letters*, 2009, **9**, 422–426.

[34] X. Zhang, B. R. S. Rajaraman, H. Liu and S. Ramakrishna, *RSC Advances*, 2014, **4**, 28987–29011.

[35] X. Wang, L. Zhi and K. Müllen, *Nano letters*, 2008, **8**, 323–327.

[36] M. F. Craciun, T. H. Bointon and S. Russo, *IET Circuits, Devices & Systems*, 2015, **9**, 403–412.

[37] W. S. Koh, C. H. Gan, W. K. Phua, Y. A. Akimov and P. Bai, *IEEE Journal of Selected Topics in Quantum Electronics*, 2014, **20**, 36–42.

[38] K. S. K. S. Kim, Y. Zhao, H. Jang, S. Y. Lee, J. M. Kim, K. S. K. S. Kim, J.-H. Ahn, P. Kim, J.-Y. Choi and B. H. Hong, *Nature*, 2009, **457**, 706–710.

[39] F. Schedin, a. K. Geim, S. V. Morozov, E. W. Hill, P. Blake, M. I. Katsnelson and K. S. Novoselov, *Nature Materials*, 2007, **6**, 652–655.

[40] A.-h. Lu, W.-c. Li, E.-l. Salabas, B. Spliethoff and F. Schu, *Chem. Mater.*, 2006, **18**, 2086–2094.

[41] B. Y. Xia, J. N. Wang, X. X. Wang, J. J. Niu, Z. M. Sheng, M. R. Hu and Q. C. Yu, *Advanced Functional Materials*, 2008, **18**, 1790–1798.

[42] K. S. Novoselov, V. I. Fal'ko, L. Colombo, P. R. Gellert, M. G. Schwab and K. Kim, *Nature*, 2012, **490**, 192–200.

[43] S. Chabi, C. Peng, Z. Yang, Y. Xia and Y. Zhu, *RSC Adv.*, 2014, **5**, 3999–4008.

[44] T. Burchell, *Carbon materials for advanced technologies.*, 1999.

[45] S. Gadipelli and Z. X. Guo, *Progress in Materials Science*, 2015, **69**, 1–60.

[46] Y. Zhang, J. P. Small, W. V. Pontius and P. Kim, *Applied Physics Letters*, 2005, **86**, 73104.

[47] I. Forbeaux, J.-M. Themlin and J.-M. Debever, *Physical Review B*, 1998, **58**, 16396–16406.

[48] Y.-M. Lin, C. Dimitrakopoulos, K. a. Jenkins, D. B. Farmer, H.-Y. Chiu, A. Grill and P. Avouris, *Science (New York, N.Y.)*, 2010, **327**, 662.

[49] C. Virojanadara, M. Syväjarvi, R. Yakimova, L. Johansson, a. Zakharov and T. Balasubramanian, *Physical Review B*, 2008, **78**, 1–6.

[50] T. Ohta, F. El Gabaly, A. Bostwick, J. L. McChesney, K. V. Emtsev, A. K. Schmid, T. Seyller, K. Horn and E. Rotenberg, *New Journal of Physics*, 2008, **10**, 23034.

[51] E. Escobedo-Cousin, K. Vassilevski, T. Hopf, N. Wright, A. O'Neill, A. Horsfall, J. Goss and P. Cumpson, *Journal of Applied Physics*, 2013, **113**, 114309.

[52] V. Presser, M. Heon and Y. Gogotsi, *Advanced Functional Materials*, 2011, **21**, 810–833.

[53] T. Peng, H. Lv, D. He, M. Pan and S. Mu, *Scientific reports*, 2013, **3**, 1148.

[54] S. A. Ganiyu, O. Muraza, A. S. Hakeem, K. Alhooshani and M. A. Atieh, *Chemical Engineering Journal*, 2014, **258**, 110–118.

[55] N. Mishra, J. Boeckl, N. Motta and F. Iacopi, *Physica Status Solidi (a)*, 2016, **13**, 1–13.

[56] V. Presser, M. Heon and Y. Gogotsi, *Advanced Functional Materials*, 2011, **21**, 810–833.

[57] S. Dimovski, A. Nikitin, H. Ye and Y. Gogotsi, *Journal of Materials Chemistry*, 2004, **14**, 238.

[58] T. Peng, Z. Kou, H. Wu and S. Mu, *Scientific reports*, 2014, **4**, 5494.

[59] J. Cai, P. Ruffieux, R. Jaafar, M. Bieri, T. Braun, S. Blankenburg, M. Muoth, A. P. Seitsonen, M. Saleh, X. Feng, K. Mullen and R. Fasel, *Nature*, 2010, **466**, 470–473.

[60] L. Jiao, L. Zhang, X. Wang, G. Diankov and H. Dai, *Nature*, 2009, **458**, 877–880.

[61] P. Kumar, L. S. Panchakarla and C. N. R. Rao, *Nanoscale*, 2011, **3**, 2127–2129.

[62] D. V. Kosynkin, A. L. Higginbotham, A. Sinitskii, J. R. Lomeda, A. Dimiev, B. K. Price and J. M. Tour, *Nature*, 2009, **458**, 872–876.

[63] M. Fujita, K. Wakabayashi, K. Nakada and K. Kusakabe, *Journal of the Physical Society of Japan*, 1996, **65**, 1920–1923.

[64] S. Cho, K. Kikuchi and A. Kawasaki, *Carbon*, 2011, **49**, 3865–3872.

[65] C. Y. Kang, L. L. Fan, S. Chen, Z. L. Liu, P. S. Xu and C. W. Zou, *Applied Physics Letters*, 2012, **100**, 251604.

[66] C. Mattevi, H. Kim and M. Chhowalla, *Journal of Materials Chemistry*, 2011, **21**, 3324.

[67] B. C. Banerjee, T. J. Hirt and P. L. Walker, *Nature*, 1961, **192**, 450–451.

[68] M. Kumar and Y. Ando, *Journal of Nanoscience and Nanotechnology*, 2010, **10**, 3739–3758.

[69] A. Oya and H. Marsh, *Journal of Materials Science*, 1982, **17**, 309–322.

[70] H. Ago, Y. Ito, N. Mizuta, K. Yoshida, B. Hu, C. M. Orofeo, M. Tsuji, K.-i. Ikeda and S. Mizuno, *ACS nano*, 2010, **4**, 7407–7414.

[71] Y. Xue, B. Wu, Y. Guo, L. Huang, L. Jiang, J. Chen, D. Geng, Y. Liu, W. Hu and G. Yu, *Nano Research*, 2011, **4**, 1208–1214.

[72] P. Franke and N. Neuschütz, *Binary systems. Part 2: Elements and Binary Systems from B – C to Cr – Zr*, Springer Berlin Heidelberg, 2004, pp. 1–343.

[73] Z. Zou, L. Fu, X. Song, Y. Zhang and Z. Liu, *Nano Letters*, 2014, **14**, 3832–3839.

[74] K. De Jong and J. Geus, *Catalysis Reviews*, 2000, **42**, 481–510.

[75] A. Reina, X. Jia, J. Ho, D. Nezich, H. Son, V. Bulovic, M. S. Dresselhaus, K. Jing and J. Kong, *Nano Letters*, 2009, **9**, 30–35.

[76] S. Bae, H. Kim, Y. Lee, X. Xu, J.-S. Park, Y. Zheng, J. Balakrishnan, T. Lei, H. R. Kim, Y. I. Song, Y.-J. Kim, K. S. Kim, B. Ozyilmaz, J.-H. Ahn, B. H. Hong and S. Iijima, *Nature nanotechnology*, 2010, **5**, 574–8.

[77] X. Li, W. Cai, J. An, S. Kim, J. Nah, D. Yang, R. Piner, A. Velamakanni, I. Jung, E. Tutuc, S. K. Banerjee, L. Colombo and R. S. Ruoff, *Science (New York, N.Y.)*, 2009, **324**, 1312–1314.

[78] X. Li, W. Cai, L. Colombo and R. S. Ruoff, *Nano letters*, 2009, **9**, 4268–4272.

[79] X. Li, W. Cai, J. An, S. Kim, J. Nah, D. Yang, R. Piner, A. Velamakanni, I. Jung, E. Tutuc, S. K. Banerjee, L. Colombo and R. S. Ruoff, *Science (New York, N.Y.)*, 2009, **324**, 1312–1314.

[80] H. J. Park, J. Meyer, S. Roth and V. Skakalova, *Carbon*, 2010, **48**, 1088–1094.

[81] X. Zhang, L. Wang, J. H. Xin, B. I. Yakobson and F. Ding, *Journal of the American Chemical Society*, 2014, **136**, 1 – 9.

[82] S. Nie, W. Wu, S. Xing, Q. Yu, J. Bao, S.-s. Pei and K. F. McCarty, *New Journal of Physics*, 2012, **14**, 93028.

[83] M. Losurdo, M. M. Giangregorio, P. Capezzuto and G. Bruno, *Physical chemistry chemical physics : PCCP*, 2011, **13**, 20836–20843.

[84] I. Vlassiouk, M. Regmi, P. Fulvio and S. Dai, *ACS nano*, 2011, **5**, 6069–6076.

[85] W. Zhang, P. Wu, Z. Li and J. Yang, *Journal of Physical Chemistry C*, 2011, **115**, 17782–17787.

[86] M. L. Toebes, J. H. Bitter, A. J. van Dillen and K. P. de Jong, *Catalysis Today*, 2002, **76**, 33–42.

[87] M. Losurdo, M. M. Giangregorio, P. Capezzuto and G. Bruno, *Physical chemistry chemical physics : PCCP*, 2011, **13**, 20836–20843.

[88] Y. C. Shin and J. Kong, *Carbon*, 2013, **59**, 439–447.

[89] Y. Lee, S. Bae, H. Jang, S. Jang, S.-E. Zhu, S. H. Sim, Y. I. Song, B. H. Hong and J.-H. Ahn, *Nano letters*, 2010, **10**, 490–493.

[90] A. T. Murdock, A. Koos, T. B. Britton, L. Houben, T. Batten, T. Zhang, A. J. Wilkinson, R. E. Dunin-Borkowski, C. E. Lekka and N. Grobert, *ACS nano*, 2013, **7**, 1351–1359.

[91] L. Gan and Z. Luo, *ACS nano*, 2013, **7**, 9480–9488.

[92] Y. a. Wu, Y. Fan, S. Speller, G. L. Creeth, J. T. Sadowski, K. He, A. W. Robertson, C. S. Allen and J. H. Warner, *ACS nano*, 2012, **6**, 5010–5017.

[93] Y.-P. Hsieh, M. Hofmann and J. Kong, *Carbon*, 2013, **67**, 417–423.

[94] C. Wang, W. Chen, C. Han, G. Wang, B. Tang, C. Tang, Y. Wang, W. Zou, X.-A. Zhang, S. Qin, S. Chang and L. Wang, *Scientific reports*, 2014, **4**, 4537.

[95] S. Chen, H. Ji, H. Chou, Q. Li, H. Li, J. W. Suk, R. Piner, L. Liao, W. Cai and R. S. Ruoff, *Advanced materials (Deerfield Beach, Fla.)*, 2013, **25**, 2062–2065.

[96] Y. Hao, M. S. Bharathi, L. Wang, Y. Liu, H. Chen, S. Nie, X. Wang, H. Chou, C. Tan, B. Fallahazad, H. Ramanarayan, C. W. Magnuson, E. Tutuc, B. I. Yakobson, K. F. McCarty, Y.-W. Zhang, P. Kim, J. Hone, L. Colombo and R. S. Ruoff, *Science (New York, N.Y.)*, 2013, **342**, 720.

[97] A. Ismach, C. Druzgalski, S. Penwell, A. Schwartzberg, M. Zheng, A. Javey, J. Bokor and Y. Zhang, *Nano letters*, 2010, **10**, 1542–1548.

[98] Y. H. Lee and J. H. Lee, *Applied Physics Letters*, 2010, **96**, 083101.

[99] S. Y. Kwon, C. V. Ciobanu, V. Petrova, V. B. Shenoy, J. Bareño, V. Gambin, I. Petrov and S. Kodambaka, *Nano Letters*, 2009, **9**, 3985–3990.

[100] P. W. Sutter, J.-I. Flege and E. a. Sutter, *Nature materials*, 2008, **7**, 406–411.

[101] C. A. Di, D. Wei, G. Yu, Y. Liu, Y. Guo and D. Zhu, *Advanced Materials*, 2008, **20**, 3289–3293.

[102] J. Coraux, A. T. N'Diaye, M. Engler, C. Busse, D. Wall, N. Buckanie, F. J. Meyer Zu Heringdorf, R. Van Gastel, B. Poelsema and T. Michely, *New Journal of Physics*, 2009, **11**, 023006.

[103] B. J. Kang, J. H. Mun, C. Y. Hwang and B. J. Cho, *Journal of Applied Physics*, 2009, **106**, 104309.

[104] E. V. Rut'kov, a. V. Kuz'michev, N. R. Gall', E. V. Rut'kov, a. V. Kuz'michev and N. R. Gall', *Phys. Solid State*, 2011, **53**, 1092–1098.

[105] M. E. Ayhan, G. Kalita, S. Sharma and M. Tanemura, *physica status solidi (RRL) – Rapid Research Letters*, 2013, **7**, 1076–1079.

[106] Y. Shen and A. C. Lua, *Scientific reports*, 2013, **3**, 3037.

[107] M. E. Ramón, A. Gupta, C. Corbet, D. A. Ferrer, H. C. Movva, G. Carpenter, L. Colombo, G. Bourianoff, M. Doczy, D. Akinwande, E. Tutuc and S. K. Banerjee, *ACS Nano*, 2011, **5**, 7198–7204.

[108] T. Oznuluer, E. Pince, E. O. Polat, O. Balci, O. Salihoglu and C. Kocabas, *Applied Physics Letters*, 2011, **98**, 183101.

[109] R. Balog, B. Jørgensen, L. Nilsson, M. Andersen, E. Rienks, M. Bianchi, M. Fanetti, E. Lægsgaard, A. Baraldi, S. Lizzit, Z. Sljivancanin, F. Besenbacher, B. Hammer, T. G. Pedersen, P. Hofmann and L. Hornekær, *Nature Materials*, 2010, **9**, 315–319.

[110] M. Kumar, *Nanotechnology Perceptions*, 2010, **6**, 7–28.

[111] G. Nandamuri, S. Roumimov and R. Solanki, *Nanotechnology*, 2010, **21**, 145604.

[112] Z. Li, P. Wu, C. Wang, X. Fan, W. Zhang, X. Zhai, C. Zeng, Z. Li, J. Yang and J. Hou, *ACS nano*, 2011, **5**, 3385–3390.

[113] J. Jang, M. Son, S. Chung, K. Kim, C. Cho, B. H. Lee and M.-h. Ham, *Nature Publishing Group*, 2015, 1–7.

[114] B. Zhang, W. H. Lee, R. Piner, I. Kholmanov, Y. Wu, H. Li, H. Ji and R. S. Ruoff, *ACS nano*, 2012, **6**, 2471–2476.

[115] A. Srivastava, C. Galande, L. Ci, L. Song, C. Rai, D. Jariwala, K. F. Kelly and P. M. Ajayan, *Chemistry of Materials*, 2010, **22**, 3457–3461.

[116] A. Guermoune, T. Chari, F. Popescu, S. S. Sabri, J. Guillemette, H. S. Skulason, T. Szkopek and M. Siaj, *Carbon*, 2011, **49**, 4204–4210.

[117] a. Delamoreanu, C. Rabot, C. Vallee and a. Zenasni, *Carbon*, 2014, **66**, 48–56.

[118] G. Ruan, Z. Sun, Z. Peng and J. M. Tour, *ACS nano*, 2011, **5**, 7601–7607.

[119] X. Li, C. W. Magnuson, A. Venugopal, R. M. Tromp, J. B. Hannon, E. M. Vogel, L. Colombo, R. S. Ruoff and R. S. Ruo, *Journal of the American Chemical Society*, 2011, **133**, 2816–2819.

[120] W. Liu, H. Li, C. Xu, Y. Khatami and K. Banerjee, *Carbon*, 2011, **49**, 4122–4130.

[121] K. S. Kim, Y. Zhao, H. Jang, S. Y. Lee, J. M. Kim, K. S. Kim, J.-H. Ahn, P. Kim, J.-Y. Choi and B. H. Hong, *Nature*, 2009, **457**, 706–710.

[122] Y. Fan, K. He, H. Tan, S. Speller and J. H. Warner, *Chemistry of Materials*, 2014, **26**, 4984–4991.

[123] D. Sukhdeo, *Electrical Engineering*, 2009, **324**, 1312–1314.

[124] Z. Luo, Y. Lu, D. W. Singer, M. E. Berck, L. a. Somers, B. R. Goldsmith and a. T. C. Johnson, *Chemistry of Materials*, 2011, **23**, 1441–1447.

[125] S. M. Kim, A. Hsu, Y.-H. Lee, M. Dresselhaus, T. Palacios, K. K. Kim and J. Kong, *Nanotechnology*, 2013, **24**, 365602.

[126] G. H. Han, F. Güneş, J. J. Bae, E. S. Kim, S. J. Chae, H.-J. Shin, J.-Y. Choi, D. Pribat and Y. H. Lee, *Nano letters*, 2011, **11**, 4144–4148.

[127] N. Reckinger, A. Felten, C. N. Santos, B. Hackens and J.-F. Colomer, *Carbon*, 2013, **63**, 84–91.

[128] A. Mohsin, L. Liu, P. Liu, W. Deng, I. N. Ivanov, G. Li, O. E. Dyck, G. Duscher, J. R. Dunlap, K. Xiao and G. Gu, *ACS nano*, 2013, **7**, 8924–8931.

[129] I. Vlassiouk, P. Fulvio, H. Meyer, N. Lavrik, S. Dai, P. Datskos and S. Smirnov, *Carbon*, 2013, **54**, 58–67.

[130] T. Kato and R. Hatakeyama, *Nature Nanotechnology*, 2012, **7**, 651–656.

[131] J. Zhang, L. Huang, Y. Zhang, Y. Xue and E. Zhang, *Journal of Alloys and Compounds*, 2015, **649**, 933–938.

[132] D. Wei, Y. Liu, H. Zhang, L. Huang, B. Wu, J. Chen and G. Yu, *Journal of the American Chemical Society*, 2009, **131**, 11147–11154.

[133] G. Ouyang, X. Tan, C. X. Wang and G. W. Yang, *Nanotechnology*, 2006, **17**, 4257–4262.

[134] M. T. Pettes, H. Ji, R. S. Ruoff and L. Shi, *Nano Letters*, 2012, **12**, 2959–2964.

[135] Z. Chen, C. Xu, C. Ma, W. Ren and H.-M. Cheng, *Advanced materials (Deerfield Beach, Fla.)*, 2013, **25**, 1296–1300.

[136] M. Lotya, Y. Hernandez, P. J. King, R. J. Smith, V. Nicolosi, L. S. Karlsson, F. M. Blighe, S. De, Z. Wang, I. T. McGovern, G. S. Duesberg and J. N. Coleman, *Journal of the American Chemical Society*, 2009, **131**, 3611–3620.

[137] Y. Hernandez, V. Nicolosi, M. Lotya, F. M. Blighe, Z. Sun, S. De, I. T. McGovern, B. Holland, M. Byrne, Y. K. Gun'Ko, J. J. Boland, P. Niraj, G. Duesberg, S. Krishnamurthy, R. Goodhue, J. Hutchison, V. Scardaci, A. C. Ferrari and J. N. Coleman, *Nature nanotechnology*, 2008, **3**, 563–568.

[138] K. R. Paton, E. Varrla, C. Backes, R. J. Smith, U. Khan, A. O'Neill, C. Boland, M. Lotya, O. M. Istrate, P. King, T. Higgins, S. Barwich, P. May, P. Puczkarski, I. Ahmed, M. Moebius, H. Pettersson, E. Long, J. Coelho, S. E. O'Brien, E. K. McGuire, B. M. Sanchez, G. S. Duesberg, N. McEvoy, T. J. Pennycook, C. Downing, A. Crossley, V. Nicolosi and J. N. Coleman, *Nature Materials*, 2014, **13**, 624–630.

[139] S. Stankovich, D. a. Dikin, G. H. Dommett, K. M. Kohlhaas, E. J. Zimney, E. a. Stach, R. D. Piner, S. T. Nguyen and R. S. Ruoff, *Nature*, 2006, **442**, 282–286.

[140] G. Eda, G. Fanchini and M. Chhowalla, *Nature Nanotechnology*, 2008, **3**, 270–274.

[141] Y. Hernandez, M. Lotya, D. Rickard, S. D. Bergin and J. N. Coleman, *Langmuir : the ACS journal of surfaces and colloids*, 2010, **26**, 3208–3213.

[142] C. Mattevi, G. Eda, S. Agnoli, S. Miller, K. A. Mkhoyan, O. Celik, D. Mastrogiovanni, G. Granozzi, E. Carfunkel and M. Chhowalla, *Advanced Functional Materials*, 2009, **19**, 2577–2583.

[143] G. Eda and M. Chhowalla, *Advanced Materials*, 2010, **22**, 2392–2415.

[144] W. S. H. Jr and R. E. Offeman, *Journal of the American Chemical Society*, 1958, **208**, 1937.

[145] H. He, J. Klinowski, M. Forster and A. Lerf, *Chemical physics letters*, 1998, **287**, 53–56.

[146] H. C. Schniepp, J.-L. Li, M. J. McAllister, H. Sai, M. Herrera-Alonso, D. H. Adamson, R. K. Prud'homme, R. Car, D. a. Saville and I. a. Aksay, *The journal of physical chemistry. B*, 2006, **110**, 8535–8539.

[147] S. Park and R. S. Ruoff, *Nature nanotechnology*, 2009, **4**, 217–224.

[148] S. Gilje, S. Han, M. Wang, K. L. Wang and R. B. Kaner, *Nano letters*, 2007, **7**, 3394–3398.

[149] M. J. Fernández-Merino, L. Guardia, J. I. Paredes, S. Villar-Rodil, P. Solís-Fernández, A. Martínez-Alonso and J. M. D. Tascón, *The Journal of Physical Chemistry C*, 2010, **114**, 6426–6432.

[150] S. Pei, J. Zhao, J. Du, W. Ren and H.-M. Cheng, *Carbon*, 2010, **48**, 4466–4474.

[151] S. Pei and H.-M. Cheng, *Carbon*, 2012, **50**, 3210–3228.

[152] R. S. Edwards and K. S. Coleman, *Nanoscale*, 2013, **5**, 38–51.

[153] H. Bai, C. Li, X. Wang and G. Shi, *Journal of Physical Chemistry C*, 2011, **115**, 5545–5551.

[154] Y. Xu, K. Sheng, C. Li and G. Shi, *ACS Nano*, 2010, **4**, 4324–4330.

[155] Z. S. Wu, A. Winter, L. Chen, Y. Sun, A. Turchanin, X. Feng and K. Müllen, *Advanced Materials*, 2012, **24**, 5130–5135.

[156] D. a. Dikin, E. J. Zimney, S. T. Nguyen and R. S. Ruoff, *Nature Mater.*, 2007, **448**, 457–460.

[157] X. Li, G. Zhang, X. Bai, X. Sun, X. Wang, E. Wang and H. Dai, *Nature nanotechnology*, 2008, **3**, 538–542.

[158] C. Vallés, C. Drummond, H. Saadaoui, C. a. Furtado, M. He, O. Roubeau, L. Ortolani, M. Monthioux and A. Pénicaud, *Journal of the American Chemical Society*, 2008, **130**, 15802–15804.

[159] G. Wang, B. Wang, J. Park, Y. Wang, B. Sun and J. Yao, *Carbon*, 2009, **47**, 3242–3246.

[160] J. Wang, K. K. Manga, Q. Bao and K. P. Loh, *Journal of the American ...*, 2011, **133**, 8888–8891.

[161] P. Parent, C. Laffon, I. Marhaba, D. Ferry, T. Z. Regier, I. K. Ortega, B. Chazallon, Y. Carpentier and C. Focsa, *Carbon*, 2016, **101**, 86–100.

[162] J. Ding, W. Yan, W. Xie, S. Sun, J. Bao and C. Gao, *Nanoscale*, 2014, **6**, 2299.

[163] Y. Zhang, W. Ren, Z. Jiang, S. Yang, W. Jing, P. Shi, X. Wu and Z.-G. Ye, *J. Mater. Chem. C*, 2014, **2**, 7570–7574.

[164] Z. Czigány and L. Hultman, *Ultramicroscopy*, 2010, **110**, 815–819.

[165] J. Filik, J. Hodkiewicz, T. F. Scientific, T. R. Society, P. Transactions, E. Sciences, I. Childres, L. Jauregui, W. Park, H. Cao, Y. Chen and J. B. Lambert, *Spectroscopy Europe*, 2005, **17**, 10–16.

[166] Y. Bai, X. Zhao, T. Li, Z. Lv, S. Lv, H. Han, Y. Yin and H. Wang, *Carbon*, 2014, **78**, 70–78.

[167] a. C. Ferrari, J. C. Meyer, V. Scardaci, C. Casiraghi, M. Lazzeri, F. Mauri, S. Piscanec, D. Jiang, K. S. Novoselov, S. Roth and a. K. Geim, *Physical Review Letters*, 2006, **97**, 1–4.

[168] a. Ferrari and J. Robertson, *Physical Review B*, 2000, **61**, 14095–14107.

[169] D. R. Lenski and M. S. Fuhrer, *Journal of Applied Physics*, 2011, **110**, 013720.

[170] Z. Tu, Z. Liu, Y. Li, F. Yang, L. Zhang, Z. Zhao, C. Xu, S. Wu, H. Liu, H. Yang and P. Richard, *Carbon*, 2014, **73**, 252–258.

[171] A. C. Ferrari and D. M. Basko, *Nature nanotechnology*, 2013, **8**, 235–246.

[172] A. C. Ferrari, *Solid State Communications*, 2007, **143**, 47–57.

[173] A. G. Souza Filho, S. G. Chou, G. G. Samsonidze, G. Dresselhaus, M. S. Dresselhaus, L. An, J. Liu, A. K. Swan, M. S. Ünlü, B. B. Goldberg, A. Jorio, A. Grüneis and R. Saito, *Physical Review B - Condensed Matter and Materials Physics*, 2004, **69**, 1–8.

[174] M. S. Dresselhaus, G. Dresselhaus, R. Saito and a. Jorio, *Physics Reports*, 2005, **409**, 47–99.

[175] S. Eigler, *Chemical communications (Cambridge, England)*, 2015, **51**, 3162–3165.

[176] D. A. C. Brownson and C. E. Banks, *Physical Chemistry Chemical Physics*, 2012, **14**, 8264.

[177] S. C. Tjong, Y. C. Li and R. K. Y. Li, *Journal of Nanomaterials*, 2010, **2010**, 1155.

[178] Z. Chen, W. Ren, L. Gao, B. Liu, S. Pei and H.-M. Cheng, *Nature materials*, 2011, **10**, 424–428.

[179] S. Stankovich, D. a. Dikin, R. D. Piner, K. a. Kohlhaas, A. Kleinhammes, Y. Jia, Y. Wu, S. T. Nguyen and R. S. Ruoff, *Carbon*, 2007, **45**, 1558–1565.

[180] A. W. Robertson and J. H. Warner, *Nanoscale*, 2013, **5**, 4079.

[181] R. F. Egerton and M. Malac, *Journal of Electron Spectroscopy and Related Phenomena*, 2005, **143**, 43–50.

[182] D. Bom, R. Andrews, D. Jacques, J. Anthony, B. Chen, M. S. Meier and J. P. Selegue, *Nano Letters*, 2002, **2**, 615–619.

[183] L. M. Viculis, J. J. Mack, O. M. Mayer, H. T. Hahn and R. B. Kaner, *Journal of Materials Chemistry*, 2005, **15**, 974.

[184] J. D. Saxby, S. P. Chatfield, A. J. Palmisano, A. M. Vassallo, M. A. Wilson and L. S. K. Pang, *The Journal of Physical Chemistry*, 1992, **96**, 17–18.

[185] P. Song, Z. Cao, Y. Cai, L. Zhao, Z. Fang and S. Fu, *Polymer*, 2011, **52**, 4001–4010.

[186] X.-q. Zhang, W.-c. Li and A.-h. Lu, *New Carbon Materials*, 2015, **30**, 481–501.

[187] M. Sevilla and A. B. Fuertes, *Energy Environ. Sci.,*, 2011, **4**, 1765.

[188] J. Lee, J. Kim and T. Hyeon, *Advanced Materials*, 2006, **18**, 2073–2094.

[189] D. Fairén-Jiménez, F. Carrasco-Marín and C. Moreno-Castilla, *Langmuir*, 2008, **24**, 2820–2825.

[190] R. Wang, P. Wang, X. Yan, J. Lang, C. Peng and Q. Xue, *ACS Applied Materials and Interfaces*, 2012, **4**, 5800–5806.

[191] M. Kruk, K. M. Kohlhaas, B. Dufour, E. B. Celer, M. Jaroniec, K. Matyjaszewski, R. S. Ruoff and T. Kowalewski, *Microporous and Mesoporous Materials*, 2007, **102**, 178–187.

[192] W. Kicinski, M. Bystrzejewski, M. H. Ruemmeli and T. Gemming, *Bulletin of Materials Science*, 2014, **37**, 141–150.

[193] N. Job, R. Pirard, J. Marien and J. P. Pirard, *Carbon*, 2004, **42**, 3217–3227.

[194] Z. Wang, X. Zhang, X. Liu, M. Lv, K. Yang and J. Meng, *Carbon*, 2011, **49**, 161–169.

[195] M. Sevilla, C. Sanchís, T. Valdés-Solís, E. Morallón and a.B. Fuertes, *Carbon*, 2008, **46**, 931–939.

[196] J. W. Long, M. Laskoski, T. M. Keller, K. a. Pettigrew, T. N. Zimmerman, S. B. Qadri and G. W. Peterson, *Carbon*, 2010, **48**, 501–508.

[197] F. J. Maldonado-Hodar, C. Moreno-Castilla, J. Rivera-Utrilla, Y. Hanzawa and Y. Yamada, *Langmuir*, 2000, **16**, 4367–4373.

[198] R. Fu, T. F. Baumann, S. Cronin, G. Dresselhaus, M. S. Dresselhaus and J. H. Satcher, *Langmuir*, 2005, **21**, 2647–2651.

[199] J. Qi, L. Jiang, Q. Tang, S. Zhu, S. Wang, B. Yi and G. Sun, *Carbon*, 2012, **50**, 2824–2831.

[200] M. Sevilla, C. Sanchís, T. Valdés-Soh, E. Morallón and A. B. Fuertes, *Journal of Physical Chemistry C*, 2007, **111**, 9749–9756.

[201] W. Meng, W. Chen, L. Zhao, Y. Huang, M. Zhu, Y. Huang, Y. Fu, F. Geng, J. Yu, X. Chen and C. Zhi, *Nano Energy*, 2014, **8**, 133–140.

[202] B. G. Choi, M. Yang, W. H. Hong, J. W. Choi and Y. S. Huh, *ACS Nano*, 2012, **6**, 4020–4028.

[203] H. Bi, X. Xie, K. Yin, Y. Zhou, S. Wan, L. He, F. Xu, F. Banhart, L. Sun and R. S. Ruoff, *Advanced Functional Materials*, 2012, **22**, 4421–4425.

[204] S. Park, S.-O. Kang, E. Jung, S. Park and H. S. Park, *RSC Advances*, 2014, **4**, 899–902.

[205] X. Cao, Y. Shi, W. Shi, G. Lu, X. Huang, Q. Yan, Q. Zhang and H. Zhang, *Small (Weinheim an der Bergstrasse, Germany)*, 2011, **7**, 3163–3168.

[206] Y. He, W. Chen, X. Li, Z. Zhang, J. Fu, C. Zhao and E. Xie, *ACS Nano*, 2013, **7**, 174–182.

[207] P. Trinsoutrot, H. Vergnes and B. Caussat, *Materials Science and Engineering: B*, 2014, **179**, 12–16.

[208] C. Tang, B. Q. Li, Q. Zhang, L. Zhu, H. F. Wang, J. L. Shi and F. Wei, *Advanced Functional Materials*, 2016, **26**, 577–585.

[209] M. Mecklenburg, A. Schuchardt, Y. K. Mishra, S. Kaps, R. Adelung, A. Lotnyk, L. Kienle and K. Schulte, *Advanced Materials*, 2012, **24**, 3486–3490.

[210] W. Li, S. Gao, L. Wu, S. Qiu, Y. Guo, X. Geng, M. Chen, S. Liao, C. Zhu, Y. Gong, M. Long, J. Xu, X. Wei, M. Sun and L. Liu, *Scientific reports*, 2013, **3**, 2125.

[211] D. Walsh, L. Arcelli, T. Ikoma, J. Tanaka and S. Mann, *Nature materials*, 2003, **2**, 386–390.

[212] F. Khan and S. Mann, *Journal of Physical Chemistry C*, 2009, **113**, 19871–19874.

[213] X. Jin, L. Zhuang and J. Lu, *Journal of Electroanalytical Chemistry*, 2002, **519**, 137–144.

[214] M. Hieda, R. Garcia, M. Dixon, T. Daniel, D. Allara and M. H. W. Chan, *Applied Physics Letters*, 2004, **84**, 628–630.

[215] S. Y. Gao, H. J. Zhang, X. M. Wang, J. H. Yang, L. Zhou, C. Y. Peng, D. H. Sun and M. Y. Li, *Nanotechnology*, 2005, **16**, 2530–2535.

[216] J. R. Hayes, G. W. Nyce, J. D. Kuntz, J. H. Satcher and A. V. Hamza, *Nanotechnology*, 2007, **18**, 275602.

[217] X.-Y. Yang, A. Léonard, A. Lemaire, G. Tian and B.-L. Su, *Chemical Communications*, 2011, **47**, 2763.

[218] Y. Liu, J. Goebl and Y. Yin, *Chemical Society reviews*, 2013, **42**, 2610–2653.

[219] R.-H. Jin and J.-J. Yuan, *Journal of Materials Chemistry*, 2005, **15**, 4513–4517.

[220] M. Iwasaki, S. A. Davis and S. Mann, Journal of Sol-Gel Science and Technology, 2004, pp. 99–105.

[221] C. M. Orofeo, H. Hibino, K. Kawahara, Y. Ogawa, M. Tsuji, K.-i. Ikeda, S. Mizuno and H. Ago, *Carbon*, 2012, **50**, 2189–2196.

[222] Y. Xue, B. Wu, Y. Guo, L. Huang, L. Jiang, J. Chen, D. Geng, Y. Liu, W. Hu and G. Yu, *Nano Research*, 2011, **4**, 1208–1214.

[223] A. Yahyazadeh and B. Khoshandam, *Results in Physics*, 2017, **7**, 3826–3837.

[224] Y. Ishikawa, H. Jinbo and H. Yamanaka, *Japanese Journal of Applied Physics*, 2006, **45**, 50.

[225] S. A. Manafi and S. H. Badiee, *Research Letters in Materials Science*, 2008, **2008**, 1–5.

[226] I. Martin-Gullon, J. Vera, J. A. Conesa, J. L. González and C. Merino, *Carbon*, 2006, **44**, 1572–1580.

[227] M. a. Pimenta, G. Dresselhaus, M. S. Dresselhaus, L. G. Cançado, a. Jorio and R. Saito, *Physical chemistry chemical physics : PCCP*, 2007, **9**, 1276–1291.

[228] Z. Yan, J. Lin, Z. Peng, Z. Sun, Y. Zhu, L. Li, C. Xiang, E. L. Samuel, C. Kittrell and J. M. Tour, *ACS Nano*, 2012, **6**, 9110–9117.

[229] S. Thiele, A. Reina, P. Healey, J. Kedzierski, P. Wyatt, P.-L. Hsu, C. Keast, J. Schaefer and J. Kong, *Nanotechnology*, 2010, **21**, 15601.

[230] S. J. Chae, F. Günes, K. K. Kim, E. S. Kim, G. H. Han, S. M. Kim, H.-J. Shin, S.-M. Yoon, J.-Y. Choi, M. H. Park, C. W. Yang, D. Pribat and Y. H. Lee, *Advanced Materials*, 2009, **21**, 2328–2333.

[231] J.-S. Lee, H.-J. Ahn, J.-C. Yoon and J.-H. Jang, *Physical chemistry chemical physics : PCCP*, 2012, **14**, 7938–7943.

[232] X. Wang, Y. Zhang, C. Zhi, X. Wang, D. Tang, Y. Xu, Q. Weng, X. Jiang, M. Mitome, D. Golberg and Y. Bando, *Nature communications*, 2013, **4**, 2905.

[233] M. Sevilla and A. B. Fuertes, *Materials Chemistry and Physics*, 2009, **113**, 208–214.

[234] A. Oya and H. Marsh, *Journal of Materials Science*, 1982, **17**, 309–322.

[235] Y. Wang, D. C. Alsmeyer and R. L. Mccreery, *Carbon*, 1990, 557–563.

[236] F. Tuinstra, *The Journal of Chemical Physics*, 1970, **53**, 1126.

[237] A. Muhammad, *Surface modification and characterization of Carbon Black ; UV - cured colored Epoxy Composites*, 2014.

[238] X. Lu, J. Shen, H. Ma, B. Yan, Z. Li, M. Shi and M. Ye, *Journal of Power Sources*, 2012, **201**, 340–346.

[239] A. Mohsin, L. Liu, P. Liu, W. Deng, I. N. Ivanov, G. Li, O. E. Dyck, G. Duscher, J. R. Dunlap, K. Xiao and G. Gu, *ACS Nano*, 2013, **7**, 8924–8931.

[240] R. T. Woodward, D. W. H. Fam, D. B. Anthony, J. Hong, T. O. McDonald, C. Petit, M. S. P. Shaffer and A. Bismarck, *Carbon*, 2016, **101**, 253–260.

[241] N. R. Cameron, *Polymer*, 2005, **46**, 1439–1449.

[242] A. Gross and A. Nowak, *Langmuir*, 2010, **26**, 11378–11383.

[243] U. M. Patil, R. V. Ghorpade, M. S. Nam, A. C. Nalawade, S. Lee, H. Han and S. C. Jun, *Scientific Reports*, 2016, **6**, 35490.

[244] H. D. Asfaw, M. Roberts, R. Younesi and K. Edström, *Journal of Materials Chemistry A*, 2013, **1**, 13750.

[245] Y. Ma, H. D. Asfaw and K. Edström, *Chemistry of Materials*, 2015, **27**, 3957–3965.

[246] A. Menner, K. Haibach, R. Powell and A. Bismarck, *Polymer*, 2006, **47**, 7628–7635.

[247] R. T. Woodward, F. De Luca, A. D. Roberts and A. Bismarck, *Materials*, 2016, **9**, 776.

[248] A. Szczurek, V. Fierro, A. Pizzi and A. Celzard, *Carbon*, 2014, **74**, 352–362.

[249] D. Wang, N. L. Smith and P. M. Budd, *Polymer International*, 2005, **54**, 297–303.

[250] S. Ungureanu, M. Birot, H. Deleuze, V. Schmitt, N. Mano and R. Backov, *Carbon*, 2015, **91**, 311–320.

[251] N. Cohen and M. S. Silverstein, *Polymer*, 2011, **52**, 282–287.

[252] S. Vílchez, L. A. Pérez-Carrillo, J. Miras, C. Solans and J. Esquena, *Langmuir*, 2012, **28**, 7614–7621.

[253] N. Thongprachan, T. Yamamoto, J. Chaichanawong, T. Ohmori and A. Endo, *Adsorption*, 2011, **17**, 205–210.

[254] N. R. Cameron, D. C. Sherrington, L. Albiston and D. P. Gregory, *Colloid & Polymer Science*, 1996, **274**, 592–595.

[255] A. Barbetta and N. R. Cameron, *Macromolecules*, 2004, **37**, 3202–3213.

[256] K. Hernadi, A. Fonseca, J. B. Nagy, A. Siska and I. Kiricsi, 2000, **199**, 245–255.

[257] J. Baringhaus, M. Ruan, F. Edler, A. Tejeda, M. Sicot, A. Taleb-Ibrahimi, A.-P. Li, Z. Jiang, E. H. Conrad, C. Berger, C. Tegenkamp and W. a. de Heer, *Nature*, 2014, **506**, 349–354.

[258] C. Vallés, A. M. Abdelkader, R. J. Young and I. a. Kinloch, *Faraday Discuss.*, 2014, **44**, 379–390.

[259] J.-S. Lee, S.-I. Kim, J.-C. Yoon and J.-H. Jang, *ACS nano*, 2013, **7**, 6047–6055.

[260] W.-C. Yen, Y.-Z. Chen, C.-H. Yeh, J.-H. He, P.-W. Chiu and Y.-L. Chueh, *Scientific reports*, 2014, **4**, 4739.

[261] R. Wang, Y. Hao, Z. Wang, H. Gong and J. T. L. Thong, *Nano letters*, 2010, **10**, 4844–4850.

[262] J. Liu, X. Li and L. Dai, *Advanced Materials*, 2006, **18**, 1740–1744.

[263] K. K. Nanda, A. Maisels, F. E. Kruis, H. Fissan and S. Stappert, *Physical Review Letters*, 2003, **91**, 1–4.

[264] D. Wang, H. Tian, Y. Yang, D. Xie, T.-L. Ren and Y. Zhang, *Scientific Reports*, 2013, **3**, 1348.

[265] S.-m. Yoon, W. M. Choi, H. Baik, H.-j. Shin, I. Song and M.-s. Kwon, *ACS nano*, 2012, **6**, 6803–6811.

[266] C. Mattevi, H. Kim and M. Chhowalla, *Journal of Materials Chemistry*, 2011, **21**, 3324.

[267] S. Sun, F. Zhou, L. Wang, X. Song and Z. Yang, *Crystal Growth & Design*, 2010, **10**, 541–547.

[268] J. M. Wofford, S. Nie, K. F. McCarty, N. C. Bartelt and O. D. Dubon, *Nano letters*, 2010, **10**, 4890–4896.

[269] J. Park, R. S. Zhu and M. C. Lin, *Journal of Chemical Physics*, 2002, **117**, 3224–3231.

[270] J. Zhu, J. Jia, F.-l. Kwong and D. H. L. Ng, *Carbon*, 2012, **50**, 2504–2512.

[271] P. Zhao, A. Kumamoto, S. Kim, X. Chen, B. Hou, S. Chiashi, E. Einarsson, Y. Ikuhara and S. Maruyama, *The Journal of Physical Chemistry C*, 2013, **117**, 10755–10763.

[272] G. Faggio, A. Capasso, G. Messina, S. Santangelo, T. Dikonimos, S. Gagliardi, R. Giorgi, V. Morandi, L. Ortolani and N. Lisi, *Journal of Physical Chemistry C*, 2013, **117**, 21569–21576.

[273] Y. Liu, C. Pan and J. Wang, *Journal of Materials Science*, 2004, **39**, 1091–1094.

[274] S. Jankhah, N. Abatzoglou and F. Gitzhofer, *International Journal of Hydrogen Energy*, 2008, **33**, 4769–4779.

[275] F. J. Mariño, E. G. Cerrella, S. Duhalde, M. Jobbagy and M. A. Laborde, *International Journal of Hydrogen Energy*, 1998, **23**, 1095–1101.

[276] M. a. Bissett, S. Konabe, S. Okada, M. Tsuji and H. Ago, *ACS nano*, 2013, **7**, 10335.

[277] S. Lee, J. Hong, J. H. Koo, H. Lee, S. Lee, T. Choi, H. Jung, B. Koo, J. Park, H. Kim, Y.-W. Kim and T. Lee, *ACS applied materials & interfaces*, 2013, **5**, 2432–2437.

[278] S. Wang, X. Huang, Y. He, H. Huang, Y. Wu, L. Hou, X. Liu, T. Yang, J. Zou and B. Huang, *Carbon*, 2012, **50**, 2119–2125.

[279] P. Tan, S. Dimovski and Y. Gogotsi, *Philosophical transactions. Series A, Mathematical, physical, and engineering sciences*, 2004, **362**, 2289–2310.

[280] A. Rinaldi, N. Abdullah, M. Ali, A. Furche, S. B. A. Hamid, D. S. Su and R. Schlögl, *Carbon*, 2009, **47**, 3023–3033.

[281] H. Ba, L. Truong-Phuoc, Y. Liu, C. Duong-Viet, J. M. Nhut, L. Nguyen-Dinh, P. Granger and C. Pham-Huu, *Carbon*, 2016, **96**, 1060–1069.

[282] D. Pan, M. Ombaba, Z. Y. Zhou, Y. Liu, S. Chen and J. Lu, *ACS Nano*, 2012, **6**, 10720–10726.

[283] M. Hikita, R. L. Bradford and K. Lafdi, *Crystals*, 2014, **4**, 466–489.

[284] Y. Saito, *Carbon*, 1995, **33**, 979–988.

[285] R. S. Wagner and W. C. Ellis, *Applied Physics Letters*, 1964, **4**, 89.

[286] X. Jiang, *Physica Status Solidi (a)*, 2014, **211**, 2679–2687.

[287] R. Baker, R. Barber, M. Harris, P. Feates and F. Waite, *Journal of Catalysis*, 1972, **26**, 51–62.

[288] G. Tibbetts, *Applied Physics Letters*, 1983, **42**, 666.

[289] K. B. K. Teo, C. Singh, M. Chhowalla and W. I. Milne, *Encyclopedia of Nanoscience and Nanotechnology*, 2003, **63**, 1–22.

[290] B. Louis, R. Vieira, A. Carvalho, J. Amadou, M. J. Ledoux and C. Pham-Huua, *Topics in Catalysis*, 2007, **45**, 75–80.

[291] W. Zhou, Z. Han, J. Wang, Y. Zhang, Z. Jin, X. Sun, Y. Zhang, C. Yan and Y. Li, *Nano letters*, 2006, **6**, 2987–2990.

[292] N. Xiao, Z. Ling, Y. Zhou and J. Qiu, *Carbon*, 2013, **61**, 386–394.

[293] N. Cherkasov, S. V. Savilov, A. S. Ivanov, A. V. Egorov, V. V. Lunin and A. O. Ibhadon, *Applied Surface Science*, 2014, **308**, 388–395.

[294] X. Jian, M. Jiang, Z. Zhou, M. Yang, J. Lu, S. Hu, Y. Wang and D. Hui, *Carbon*, 2010, **48**, 4535–4541.

[295] Y. Qin, Z. Zhang and Z. Cui, *Carbon*, 2003, **41**, 3072–3074.

[296] Y. Qin, Z. Zhang and Z. Cui, *Carbon*, 2004, **42**, 1917–1922.

[297] A. Shaikjee and N. J. Coville, *Materials Chemistry and Physics*, 2011, **125**, 899–907.

[298] Y. Qin, X. Jiang and Z. Cui, *Journal of Physical Chemistry B*, 2005, **109**, 21749–21754.

[299] C.-W. Huang, H.-C. Wu, W.-H. Lin and Y.-Y. Li, *Carbon*, 2009, **47**, 795–803.

[300] A. Rinaldi, N. Abdullah, M. Ali, A. Furche, S. B. A. Hamid, D. S. Su and R. Schlögl, *Carbon*, 2009, **47**, 3023–3033.

[301] S.-H. Yoon, S. Lim, S.-h. Hong, I. Mochida, B. An and K. Yokogawa, *Carbon*, 2004, **42**, 3087–3095.

[302] F. Nitze, E. Abou-Hamad and T. Wgberg, *Carbon*, 2011, **49**, 1101–1107.

[303] A. Shaikjee, P. J. Franklyn and N. J. Coville, *Carbon*, 2011, **49**, 2950–2959.

[304] J. I. Paredes, M. Burghard, A. Martínez-Alonso and J. M. D. Tascón, *Applied Physics A: Materials Science and Processing*, 2005, **80**, 675–682.

[305] J. Sehested, P. L. Hansen, S. Helveg, C. Lo, B. S. Clausen, J. R. Rostrup-nielsen and F. Abild-pedersen, *Nature*, 2004, **427**, 5–8.

[306] G. Xu, W.-T. Wu, Y. Wang, W. Pang, Q. Zhu, P. Wang and Y. You, *Polymer*, 2006, **47**, 5909–5918.

[307] Meng.N, *Energy Explore. Exploit.*, 2006, **24**, 197–209.

[308] C. A. Bessel, K. Laubernds, N. M. Rodriguez and R. T. K. Baker, *Journal of Physical Chemistry B*, 2001, **105**, 1115–1118.

[309] F. Salman, C. Park and R. T. K. Baker, *Catalysis Today*, 1999, **53**, 385–394.

[310] M. J. Ledoux, R. Vieira, C. Pham-Huu and N. Keller, *Journal of Catalysis*, 2003, **216**, 333–342.

[311] S. Jankhah, N. Abatzoglou, F. Gitzhofer, J. Blanchard and H. Oudghiri-Hassani, *Chemical Engineering Journal*, 2008, **139**, 532–539.

[312] Z. Liu, R. Ma, M. Osada, K. Takada and T. Sasaki, *Selective and controlled synthesis of alpha- and beta-cobalt hydroxides in highly developed hexagonal platelets.*, 2005, http://www.ncbi.nlm.nih.gov/pubmed/16201808.

[313] Y. Miyata, K. Kamon, K. Ohashi, R. Kitaura, M. Yoshimura and H. Shinohara, *Applied Physics Letters*, 2010, **96**, 1–4.

[314] Y. Miyasaka, A. Matsuyama, A. Nakamura and J. Temmyo, *Physica Status Solidi (C) Current Topics in Solid State Physics*, 2011, **8**, 577–579.

[315] J. K. Wassei, M. Mecklenburg, J. A. Torres, J. D. Fowler, B. C. Regan, R. B. Kaner and B. H. Weiller, *Small*, 2012, **8**, 1415–1422.

[316] Y. Zhao, D. Huang and Y. Saito, *Nanotechnology*, 2007, **18**, 445608.

[317] M. H. Rümmeli, A. Bachmatiuk, F. Börrnert, F. Schäffel, I. Ibrahim, K. Cendrowski, G. Simha-Martynkova, D. Plachá, E. Borowiak-Palen, G. Cuniberti and B. Büchner, *Nanoscale research letters*, 2011, **6**, 303.

[318] O. Nakagoe, N. Takagi and Y. Matsumoto, *Surface Science*, 2002, **514**, 414–419.

[319] R. T. Vang, K. Honkala, S. Dahl, E. K. Vestergaard, J. Schnadt, E. Lægsgaard, B. S. Clausen, J. K. Nørskov and F. Besenbacher, *Nature Materials*, 2005, **4**, 160–162.

[320] Q. Yu, J. Lian, S. Siriponglert, H. Li, Y. P. Chen and S. S. Pei, *Applied Physics Letters*, 2008, **93**, 1–4.

[321] S. A. Tikhomirov, M. I. Alymov, I. V. Tregubova and V. S. Shustov, *Nanotechnologies in Russia*, 2011, **6**, 268–271.

[322] M. K. Tynan, D. W. Johnson, B. P. Dobson and K. S. Coleman, 2016, **8**, 13303–13310.

Appendices

Associated publications:

Formation of 3D graphene foams on soft templated metal monoliths.[322]

8.3 Appendix A - Supporting Information for Chapter 3

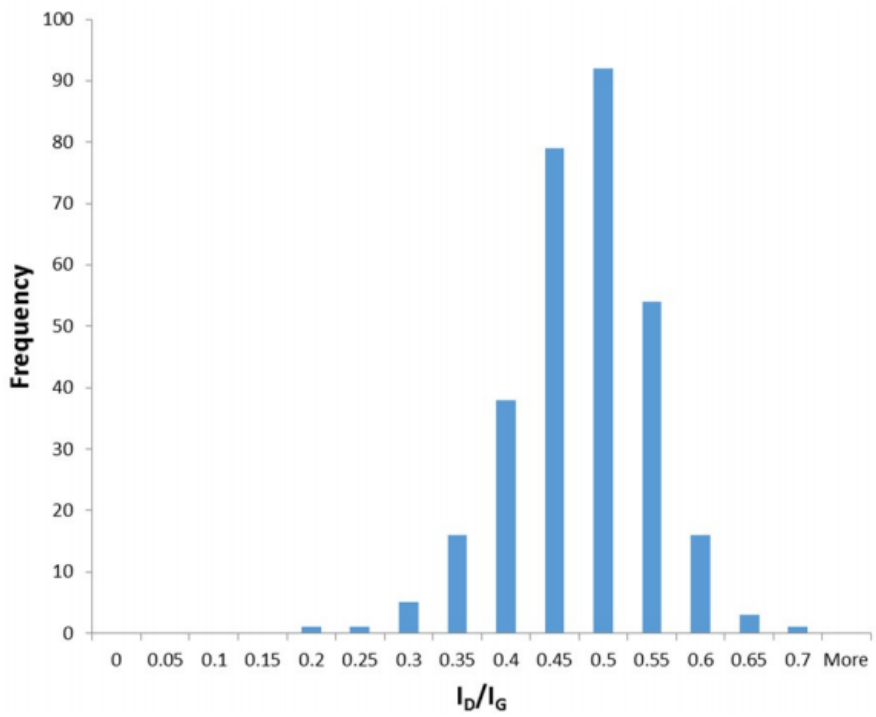

Figure 8.1: Histogram of I_D/I_G for CuGF over 307 spectra. Used to work out crystallite size in equation 3.1

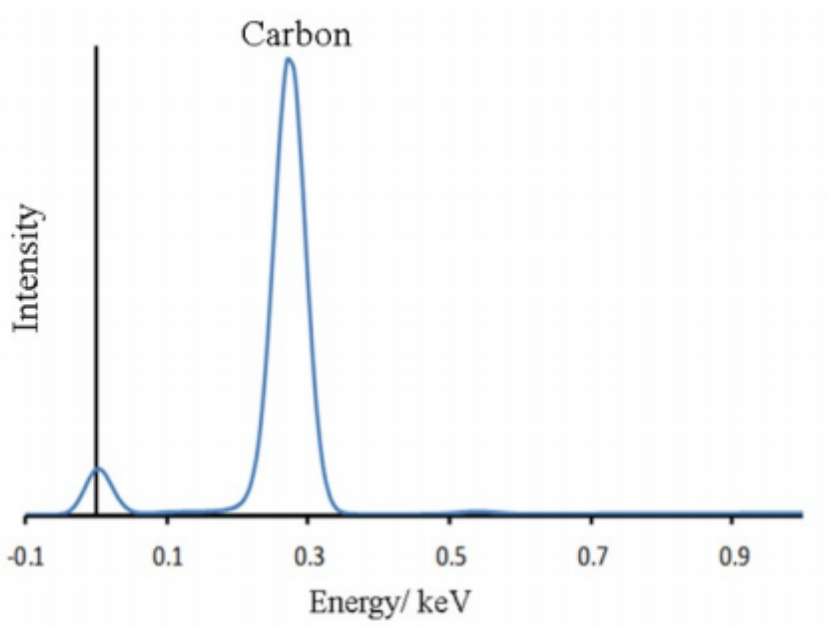

Figure 8.2: EDX spectra taken from figure 3.13 A at 15 kV showing the presence of carbon and no cobalt

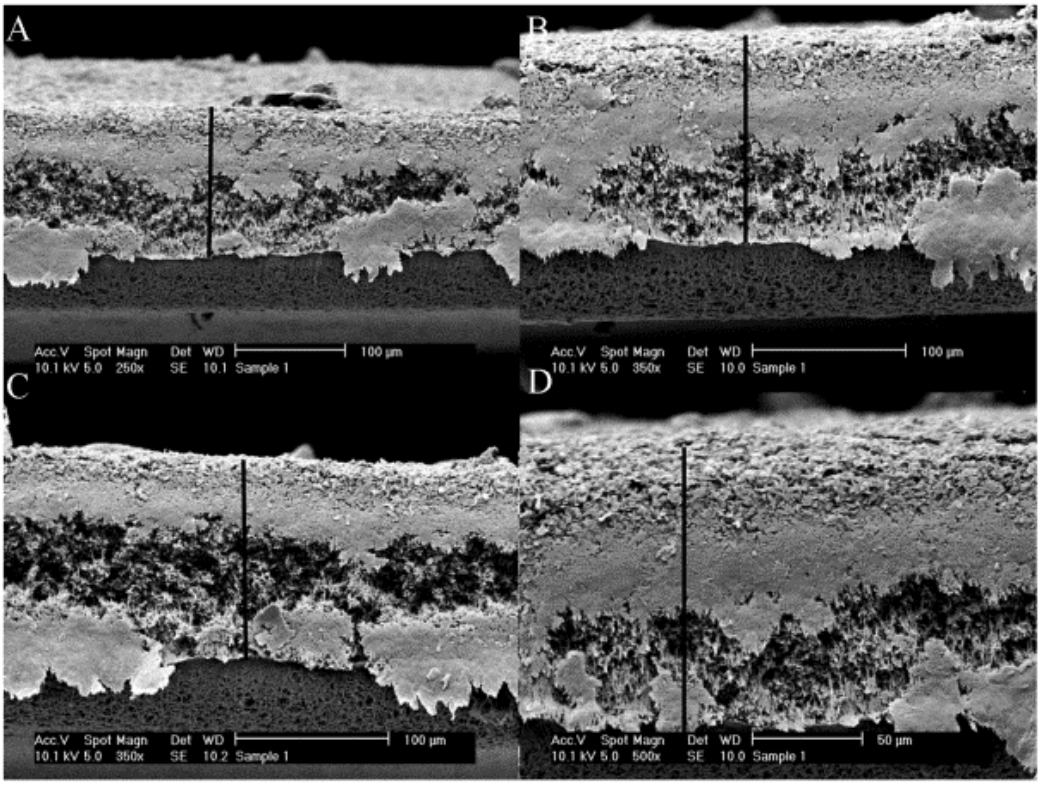

Figure 8.3: SEM images showing thickness of films used for conductivity measurement of cobalt graphene foam.

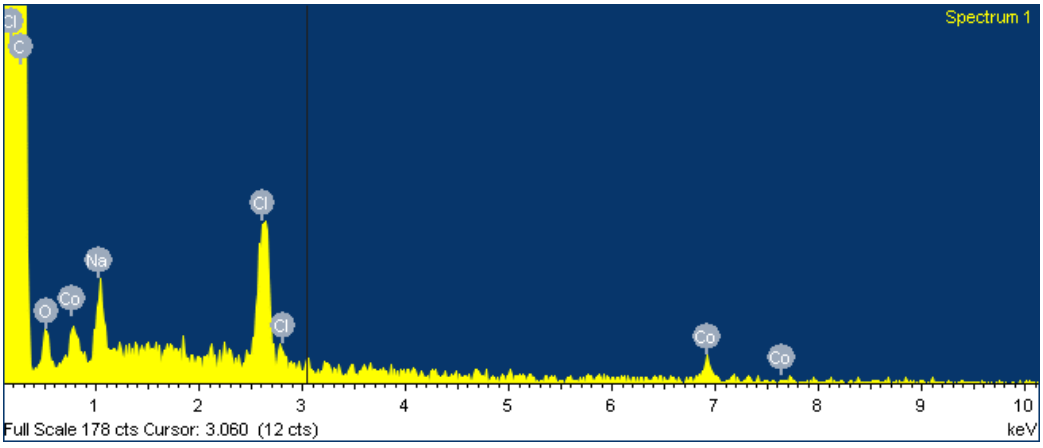

Figure 8.4: EDX of the area shown in figure 3.17 (D) showing the presence of cobalt. The Na and Cl are likely due to contaminants.

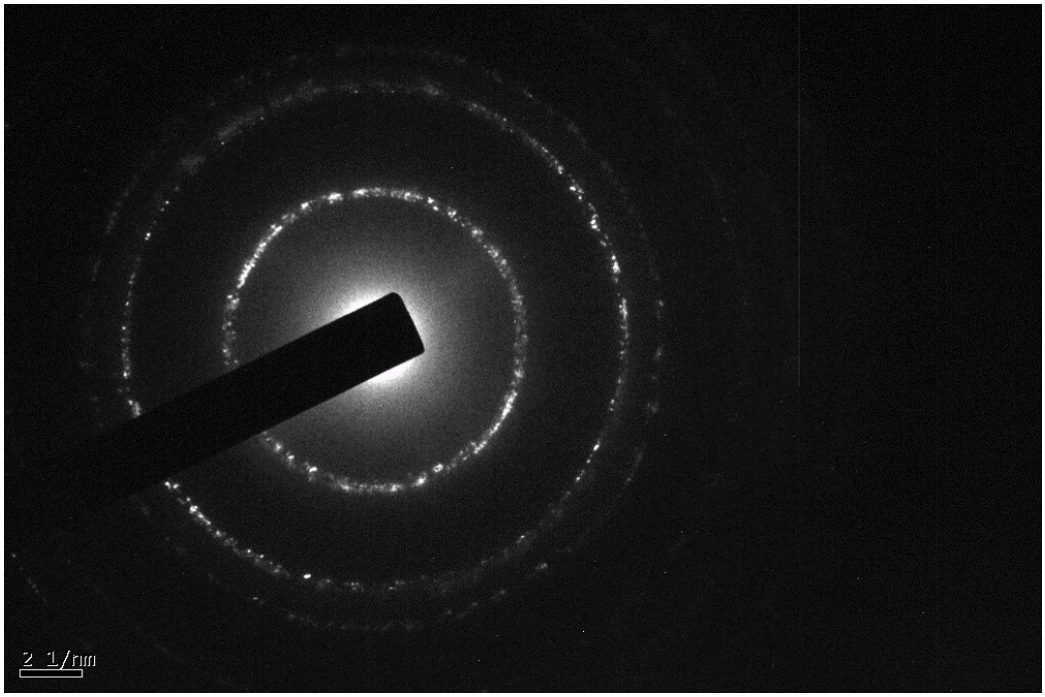

Figure 8.5: ED showing copper derived carbon material. d spacing calculated to be 0.21 nm and 0.12 nm.

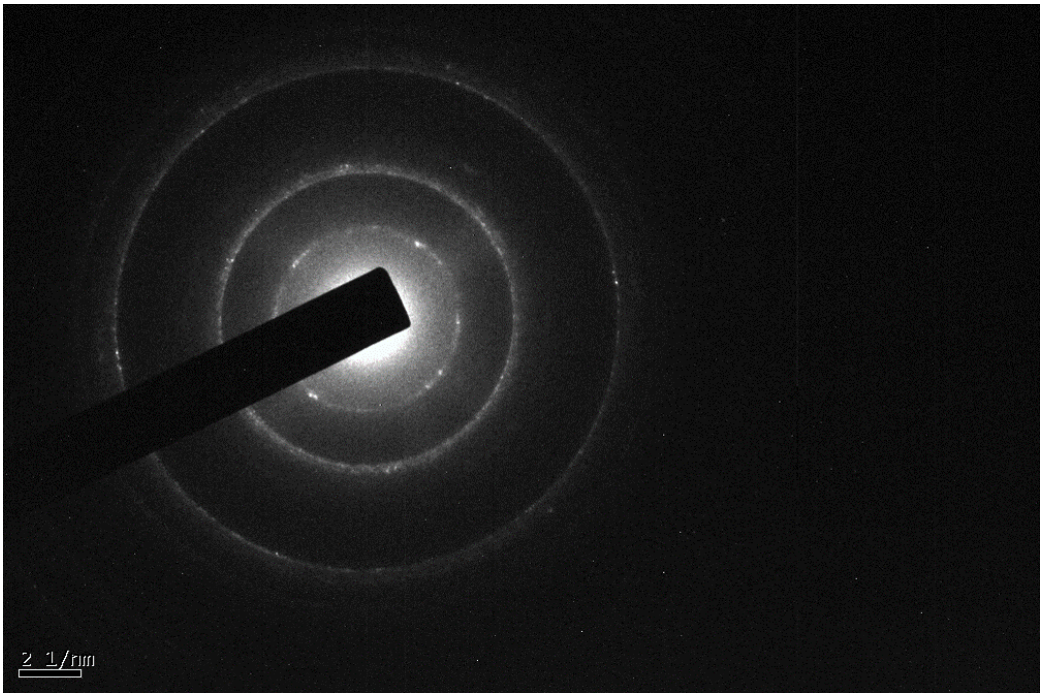

Figure 8.6: ED showing iron derived carbon material. d spacing calculated to be 0.34, 0.21 nm and 0.12 nm.

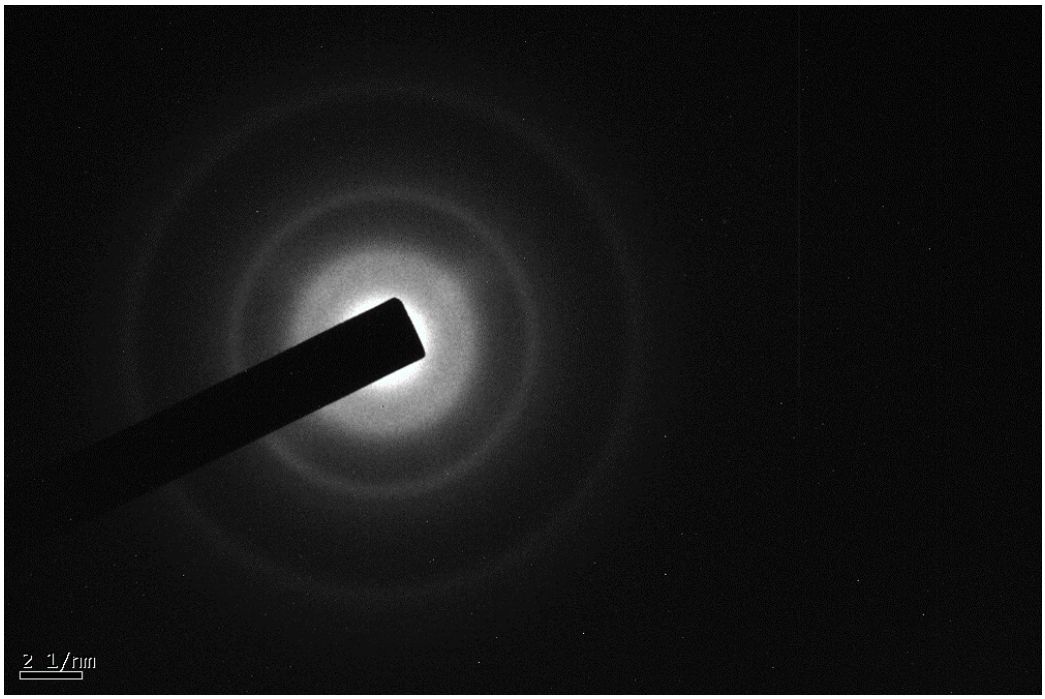

Figure 8.7: ED showing nickel derived carbon material. d spacing calculated to be 0.37, 0.22 nm and 0.13 nm.

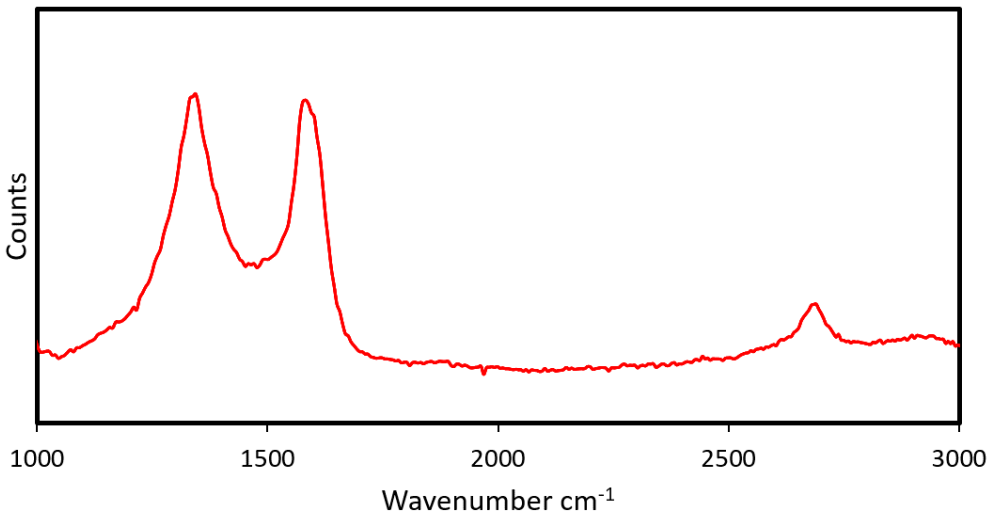

Figure 8.8: Raman spectrosopy of one pot synthesis of cobalt graphitic foam performed at 800 °C.

8.4 Appendix B - Supporting Information for Chapter 5

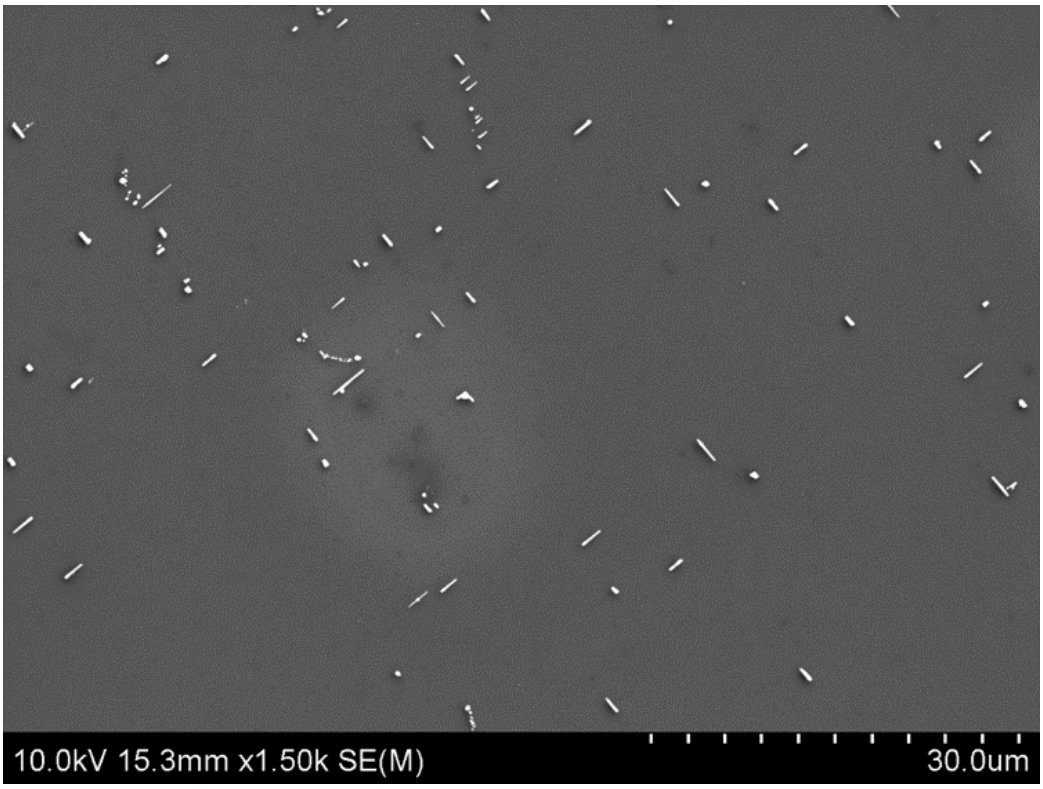

Figure 8.9: SEM image of Cu_2O heated to 1000 °C.

8.5 Appendix C - Supporting Information for Chapter 6

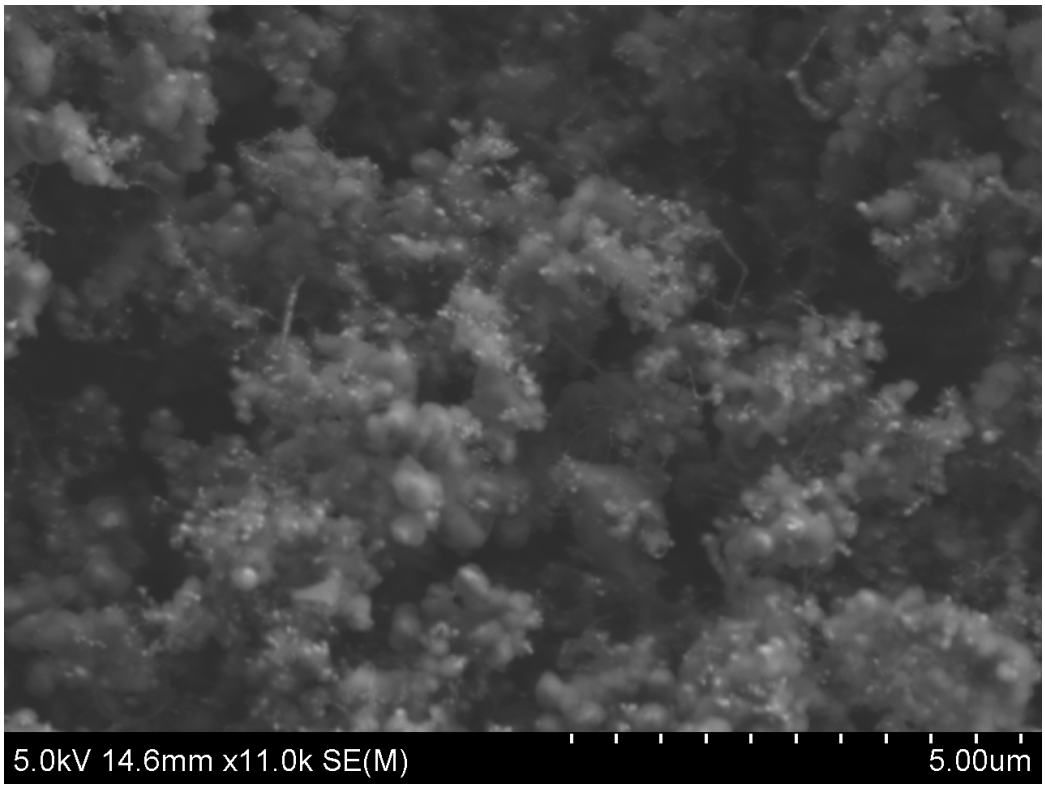

Figure 8.10: SEM image of APCVD with acetylene on CoOH catalysts at 800 ℃ for 1 minute.